ACHIEVING BRIGHT BLUE PHOSPHORESCENT PLATINUM(II) COMPOUNDS WITH CYCLOMETALLATING PHENYL-1,2,3-TRIAZOLE LIGANDS

by

Xiang Wang

A thesis submitted to the Department of Chemistry

In conformity with the requirements for

the degree of Doctor of Philosophy

Queen's University

Kingston, Ontario, Canada

January, 2017

Copyright ©Xiang Wang, 2017

Abstract

Although tremendous progress has been made in the research and commercialization of organic light emitting diodes (OLEDs), the development of efficient and stable deep blue OLEDs remains one of the greatest challenges. This thesis describes our approach to achieve highly efficient deep-blue phosphorescent emitters based on cyclometalated Pt(II) compounds bearing 1,2,3-triazole moieties. The influence of different ancillary ligands and the impact of various substituent groups and ligand denticity on phosphorescent emission color, phosphorescent quantum efficiency, excimer emission, thermal and UV stability of these molecules were carefully examined. Their performance in OLED devices has also been evaluated.

A series of dimesitylboron($BMes_2$)-functionalized Pt(II) complexes based on $N^{\wedge}C$-chelate phenyl-1,2,3-triazolyl backbones and acetylacetonate, picolinate or pyridyl-1,2,4-triazolyl ancillary ligands have been synthesized and their use as emitters in efficient greenish-blue and white phosphorescent OLED devices were demonstrated. This was the first example of using phenyl-1,2,3-triazoles as the cyclometallating ligand in Pt(II) complexes and revealed that this was a viable approach to achieve bright blue phosphorescent Pt(II) compounds.

We then synthesized a class of brightly phosphorescent Pt(II) compounds that contain an N^C-chelate phenyl-1,2,3-triazolyl ligand (ptrz) and an N^C-chelate pyridyl-1,2,4-triazolyl ligand (pytrz) with different substituent groups. When the bulky trityl group (Ph_3C) was introduced, the thermal stability of the molecule was improved and the excimer emission was reduced. Efficient

greenish-blue phosphorescent OLED devices with no excimer emission were successfully fabricated using the Ph_3C-contining compounds.

Finally, by using tetradentate or macrocyclic cyclometallating ligands, the photostability of the corresponding Pt(II) complexes was greatly enhanced as they undergo less structural distortion at the excited state. Bright and efficient deep blue OLEDs with high color purity were successfully fabricated using the macrocyclic Pt(II) complex, demonstrating a new route to stable and highly luminescent deep blue Pt(II) emitters.

Co-Authorship

Chapter 2: The single crystals of **2.1** and **2.4** and the ROESY NMR spectrum of compound **2.8** were obtained by Jia-Sheng Lu. Electroluminescent devices were fabricated by Yi-Lu Chang at the University of Toronto and Tao Zhang at the Yunnan University in the laboratories of Prof. Zheng-Hong Lu.

Chapter 3: Electroluminescent devices were fabricated by Dr. Shao-Long Gong at the University of Toronto in the laboratory of Prof. Zheng-Hong Lu and Prof. Datong Song.

Chapter 4: Electroluminescent devices were fabricated by Prof. Tai Peng at the Beijing Institute of Technology of China and Carmen Nguyen at the University of Toronto in the laboratory of Prof. Zheng-Hong Lu. Root mean square deviation calculations of compounds **4.1-4.7** and the excited state geometry calculation of **3.8** were performed by Wenjie Wu at the Beijing Institute of Technology of China in the laboratory of Prof. Quansong Li. The decay life at 77K of compounds **4.1-4.7** were measured by Prof. Tai Peng and Prof. Nan Wang at the Beijing Institute of Technology of China.

Acknowledgements

First, I would like to express my deepest gratitude to my supervisor Prof. Suning Wang for accepting me as one of her graduate students. That was my second time applying for graduate school and her offer was one of the only two I received in two years. When I first came to the lab I knew little about organic synthesis. I still remember my first seven Sonogashira coupling reactions were all unsuccessful and I almost lost hope in organic synthesis. It was her patience, advice and the help of the labmates that uncovered the source of the failure was a leak in schlenk line. She treats her students like her own children, caring about not only their studies but also their everyday life. She can get very excited if the student has discovered something interesting; She can also become angry if the student presented something unthoughtful. Most importantly, she never gave up on her students. During my graduate studies, there were several times I got slack at study due to my lack of self-control and some frustration in the research. Without her encouragement and push I would never finish the work in this thesis. It is fortunate for me to meet such a great supervisor during the graduate studies.

Further, many thanks to the excellent chemists in the chemistry department at Queen's University. I would like to thank my committee members Prof. Anne Petitjean and Prof. Jean-Michel Nunzi for their valuable suggestions and help. I also want to appreciate Dr. Jiaxi Wang for his help with mass spectrometric analyses, Dr. Gabriele Schatte for her help with X-ray crystallographic analyses, and Dr. Françoise Sauriol for her help with NMR spectroscopic analyses.

None of my work could be done without the excellent collaborations outside the Queen's University. I gratefully acknowledge Prof. Zheng-Hong Lu and his group members Dr. Yi-Lu

Chang, Dr. Shaolong Gong and Carmen Nguyen at the University of Toronto for their hard effort and valuable suggestions on OLED fabrication. I also greatly appreciate Prof. Tai Peng in the Beijing Institute of Technology of China for making OLED devices and Prof. Quansong Li and his student Wenjie Wu at the same university for their help with DFT calculations.

I am also grateful for the wonderful time with many knowledgeable visiting professors, postdoctoral fellows and young talented chemists in the Wang group. First, I would like to thank Dr. Jiasheng Lu and Prof. Young-Jin Kang, for their training and guidance when I first came to the Wang lab. Also, I sincerely appreciate Dr. Barry Blight, Dr. Soo-Byung Ko, Dr. Hee-Jun Park and Dr. Jin-bao Peng for their assistance and suggestions on synthesis and material characterizations. I always appreciate the friendship and help from all the past and current members of Wang group, especially Yufei Li, Dengtao Yang and Kang Yuan.

Last but not the least, I want to thank my father and mother for their financial and spiritual support. They always believe in me and have tried all their best to support me no matter what happened. I wish to become more outgoing and they can worry less about me.

Statement of Originality

I hereby certify that all of the work described within this thesis is the original work of the author. Any published (or unpublished) ideas and/or techniques from the work of others are fully acknowledged in accordance with the standard referencing practices.

(Xiang Wang)

(11, 2016)

Table of Contents

Abstract ii

Co-Authorship iv

Acknowledgements v

Statement of Originality vii

List of Figures xii

List of Tables xvii

List of Abbreviations xviii

Chapter 1 Introduction 1

1.1 OLEDs 3

1.1.1 Device Architecture 3

1.1.2 Working Principle 5

1.1.3 Performance Characterization 10

1.2 Introduction to Cyclometalated Complexes 13

1.3 Design of Highly Luminescent Cyclometalated Pt(II) Compounds 15

1.3.1 Advantages of Using Pt-based Luminescent Materials 15

1.3.2 Strategies for Emission Color Tuning 15

1.3.3 Strategies to Improve Phosphorescent Quantum Yields 17

1.4 Recent Development of Highly Efficient Phosphorescent Pt(II) Compounds 21

1.4.1 Type **I** Complexes 22

1.4.2 Type **II** Complexes 23

1.4.3 Type **III** Complexes 28

1.4.4 Type **IV** Complexes 34

1.4.5 Type **V** Complexes 40

1.5 Click Chemistry and 1,2,3-Triazoles 41

1.6 Scope of the Thesis 43

1.7 References: 44

Chapter 2 Achieving Bright Blue Phosphorescent Pt(II) Compounds with Triarylboryl-Functionalized Cyclometallating Phenyl-1,2,3-Triazole Ligands 50

2.1 Introduction 50

2.2 Results and Discussion 54

2.2.1 Synthesis 54

2.2.2 Structures 57

2.2.2.1 Structural Isomers 65

2.2.2.2 Intermolecular Interactions 66

2.2.3 Luminescent Properties 67

2.2.3.1 The Impact of the Bptrz Chelate Ligands and the Location of the $BMes_2$ Group on Luminescence 71

2.2.3.2 The Impact of Ancillary Ligands on Luminescence 73

2.2.3.3 The Impact of the Substituent Groups on Luminescence 75

2.2.3.4 The Impact of Isomerism on Luminescence 77

2.2.4 Computational study 78

2.2.5 Electrophosphorescence of **2.9** and **2.10** 82

2.2.6 Improved EL Devices for **2.9** with External Quantum Efficiency of 24.0% 86

2.3 Experimental 90

2.3.1 General Procedures 90

2.3.2 Synthesis of Ligands 91

2.3.3 Synthesis of Pt(II) complexes 94

2.3.3.1 General Procedure to Synthesize Pt(II) Complexes **2.1**-**2.3** 94

2.3.3.2 General Procedure to Synthesize Pl(II) Complexes **2.4**-**2.7** 96

2.3.3.3 General Procedure to Synthesize Pl(II) Complexes **2.8-2.11** 98

2.3.4 X-Ray Diffraction Analysis 100

2.3.5 EL Device Fabrication 100

2.4 Conclusions 101

2.5 Notes and References 102

Chapter 3 Bright Phosphorescent and Thermally Stable Pt(II) Compounds Based on a Phenyl-1,2,3-triazolyl and a Pyridyl-1,2,4-triazolyl Chelate Core 106

3.1 Introduction 106

3.2 Results and Discussion 108

3.2.1 Synthesis 108

3.2.2 Crystal Structures 110

3.2.3 Thermal stability 114

3.2.4 Luminescent Properties 115

3.2.5 Computational study 123

3.2.6 Electrophosphorescence of **3.7-3.9** 126

3.3 Experimental 134

3.3.1 General Procedures 134

3.3.2 Synthesis of Ligands 135

3.3.3 Synthesis of Pt(II) complexes 137

3.3.4 X-Ray Diffraction Analysis 141

3.3.5 EL Device Fabrication 142

3.4 Conclusion 142

3.5 Notes and References 143

Chapter 4 Stable and Efficient Deep Blue Phosphorescent Pt(II) Compounds Based on Tetradentate and Macrocyclic Phenyltriazole Ligands 146

4.1 Introduction 146

4.2 Results and Discussion 150

4.2.1 Synthesis 150

4.2.2 Crystal Structures 153

4.2.3 Thermal stability 157

4.2.4 Luminescent Properties 158

4.2.5 Stability towards UV Irradiation 164

4.2.6 Computational Studies 166

4.2.7 Electroluminescence 174

4.3 Experimental 178

4.3.1 General Procedures 178

4.3.2 Synthesis of Ligands 179

4.3.3 Synthesis of Pt(II) complexes 185

4.3.4 X-Ray Diffraction Analysis 187

4.3.5 EL Device Fabrication 188

4.4 Conclusion 189

4.5 Notes and References 190

Chapter 5 Conclusion and Future Work 195

List of Figures

Figure 1.1 Device structure of a three-layer OLED.....4

Figure 1.2 The energy diagrams and working mechanism of a three-layer OLED (left) and a seven-layer OLED (right).....6

Figure 1.3 Jablonski diagram showing various energy transfer pathways.....7

Figure 1.4 Charge trapping process in OLEDs. 8

Figure 1.5 Förster energy transfer mechanisms. 9

Figure 1.6 Dexter transfer mechanisms. 9

Figure 1.7 Triplet-triplet annihilation mechanism.....10

Figure 1.8 Normalized sensitivity curves of rod cells and cone cells. (adapted from Ref. 17).....12

Figure 1.9 Some common examples of cyclometalating ligands. 13

Figure 1.10 Examples of common ancillary ligands. 14

Figure 1.11 A diagram showing different excited state transitions in cyclometalated compounds.....14

Figure 1.12 A diagram demonstrating emission color tuning of Pt(II) compounds. 16

Figure 1.13 Ligand field splitting diagram of square-planar Pt(II) complexes. 18

Figure 1.14 Energy diagram showing potential energy surfaces of the ground state (S_0), first triplet excited state (T_1) and metal d-d state of a cyclometalated Pt(II) complex. Curved arrows represent non-radiative decay. 19

Figure 1.15 Diagrams showing the relationship between the Huang-Rhys parameter S and emission curve. Top: single emission peak when S=0; Middle: narrow emission spectrum when S is small. Bottom: broad emission curve when S is large. 20

Figure 1.16 Diagram showing five types of coordination modes of Pt(II) complexes. 22

Figure 1.17 Chemical structures and photophysical properties of complexes **1.1** and **1.2**. 23

Figure 1.18 Chemical structures and photophysical properties of complexes **1.3-1.5**. 23

Figure 1.19 Chemical structures and photophysical properties of complexes **1.6-1.12**. Inset: The crystal packing diagram of **1.10**. 24

Figure 1.20 Chemical structures and photophysical properties of complexes **1.13-1.16**.....25

Figure 1.21 Chemical structures and photophysical properties of complexes **1.17-1.19**.....26

Figure 1.22 Chemical structures and photophysical properties of complexes **1.20-1.23**.....27

Figure 1.23 Chemical structures and photophysical properties of complexes **1.24** and **1.25**. 27

Figure 1.24 Chemical structures and photophysical properties of complexes **1.26-1.32**. Inset: The optimized structure of **1.26**, **1.27**, **1.29** and **1.30** at the ground and first triplet excited state. 29

Figure 1.25 Chemical structures and photophysical properties of complexes **1.33-1.38**..... 31
Figure 1.26 Normalized emission spectra of **1.4** and **1.35** in dichloromethane at T=300 K. (adapted from Ref. 38)..... 31
Figure 1.27 Chemical structures and photophysical properties of complexes **1.39-1.44**..... 33
Figure 1.28 Chemical structure, photophysical properties and molecular orbitals of the optimized ground state and excited state of **1.45**. 34
Figure 1.29 Chemical structures and photophysical properties of complexes **1.46-1.48**. Inset: The optimized structure of **1.47** at the ground and first triplet excited state. 35
Figure 1.30 Chemical structures and photophysical properties of complexes **1.49-1.51**..... 36
Figure 1.31 Chemical structures and photophysical properties of complexes **1.52-1.56**..... 37
Figure 1.32 Chemical structures and photophysical properties of complexes **1.58-1.60**..... 39
Figure 1.33 Optimized structure of **1.58** (top) and **1.60** (bottom). Left: Top view; Right: Side view. (adapted from Ref. 53)..... 39
Figure 1.34 Top: Chemical structures and photophysical properties of complexes **1.61-1.63**. Bottom: Crystal structures showing the dimeric packing of **1.61** and **1.62** and that of **1.63**. The fluorine atoms in **1.61** and **1.62** are omitted for clarity. (adapted from Ref. 55) 40
Figure 1.35 The structure of **1.64**. 41
Figure 1.36 Molecular structures of **1.62-1.64**. 43
Figure 2.1 Structures of dimesitylboron-functionalized Pt(II) acetylacetonates synthesized in our group. 51
Figure 2.2 Structures of $BMes_2$-functionalized phenyl-1,2,3-triazole chelated Pt(II) compounds described in this chapter. 53
Figure 2.3 ^{1}H NMR spectrum of N^1-trans isomer of **2.8** in CD_2Cl_2..... 59
Figure 2.4 ^{1}H NMR spectrum of the N^4-trans isomer of **2.8** in CD_2Cl_2..... 60
Figure 2.5 Top left: COSY NMR spectrum of of the N^4-trans isomer of **2.8** in CD_2Cl_2. Bottom left: ROESY NMR spectrum of the N^4-trans isomer of **2.8** in CD_2Cl_2..... 60
Figure 2.6 Crystal structures of **2.1** (left) and **2.4** (right) with 35% thermal ellipsoids and labeling schemes for key atoms..... 61
Figure 2.7 Crystal structures of **2.6** (left) and **2.7a** (right) with 35% thermal ellipsoids and labeling schemes for key atoms..... 62
Figure 2.8 Crystal structures of **2.9** (left) and **2.10** (right) with 35% thermal ellipsoids and labeling schemes for key atoms..... 62

Figure 2.9 (a): A diagram showing the π-stacked dimer of **2.5** in the crystal lattice. (b): A diagram showing the π-stacked dimer of **2.7a** in the crystal lattice. 63
Figure 2.10 (a) A diagram showing the 1D extended π-stacking interactions of **2.8** in the crystal lattice. (b): A diagram showing the π-stacked dimer of **2.9** in the crystal lattice. (c): A diagram showing the π-stacked dimer of **2.10** in the crystal lattice..... 64
Figure 2.11 Photographs showing the emission colors of compounds **2.1**-**2.11** in 10 wt% PMMA films (top), as neat solids (middle) and in Me-THF glass (~1.0 x 10^{-5} M, bottom) at 77 K. 68
Figure 2.12 Normalized phosphorescent emission spectra of compounds **2.1**-**2.7** (~10^{-6} M in Me-THF) at ambient temperature. 68
Figure 2.13 Phosphorescent spectra of compounds **2.8**-**2.11** (~10^{-6} M in Me-THF) at ambient temperature. 69
Figure 2.14 Absorption (left, recorded in THF) and phosphorescent spectra (right, in PMMA film with the doping level indicated) of compounds **2.1**-**2.3** at ambient temperature. 72
Figure 2.15 Absorption (left, recorded in THF) and phosphorescent spectra (right, in PMMA film with the doping level indicated) of compounds **2.4**-**2.7** at ambient temperature. 72
Figure 2.16 Absorption (left, recorded in THF) and phosphorescent spectra (right, in PMMA film with the doping level indicated) of compounds **2.8**-**2.11** at ambient temperature. 74
Figure 2.17 Photographs showing the emission colors of compounds **2.8**-**2.11** (N^1-trans isomers) in PMMA films at 2 wt%, 5 wt% and 10 wt% PMMA films. 76
Figure 2.18 The phosphorescent spectra of the N^1-trans (A) and N^4-trans (B) isomers of compound **2.8** in 5 wt% and 10 wt% PMMA films. 78
Figure 2.19 The experimental (blue) and calculated (red) HOMO and LUMO energies for selected Pt (II) compounds. 79
Figure 2.20 EL device structure and materials used. 83
Figure 2.21 EL spectra, L-J-V and EQE-L diagrams of EL devices using **2.9** or **2.10** as the dopant. 86
Figure 2.22 Device structures and energy diagrams of the EL devices and molecular structure of POPCPA and TP3PO. 88
Figure 2.23 (a) Normalized emission spectra of POPCPA and TP3PO and ^{3}MLCT absorption band of **2.9**. Inset: The absorption spectrum of **2.9**. (b) EQE-L diagrams of EL devices. (c) P-L diagrams of EL devices. Inset: Photograph showing device 7% B at 500 cd/m^2. (adapted from Ref. 33)..... 89
Figure 3.1 The crystal structure of compound **3.4**, showing the stacked dimer (left: top view, right: side view), with labeling schemes and 50% thermal ellipsoids. H atoms are omitted for clarity. 112

Figure 3.2 The crystal structures of compound **3.5** (left) and **3.7** (right) with labeling schemes and 50% thermal ellipsoids. H atoms are omitted for clarity. 113
Figure 3.3 The crystal structures of compound **3.8** (left) and **3.9** (right) with labeling schemes and 50% thermal ellipsoids. H atoms are omitted for clarity. 113
Figure 3.4 Diagram showing intermolecular π stacking interactions in the crystal lattice of **3.7** (left), **3.8** (middle) and **3.9** (right)..... 114
Figure 3.5 TGA diagrams for compounds **3.7-3.9** and **2.9**. 115
Figure 3.6 Photographs showing the emission colors of compounds **3.1-3.9** in 5 wt% PMMA films (top), as neat solids (middle) and in frozen CH_2Cl_2 glass (~2.0 x 10^{-5} M, bottom) at 77K..... 116
Figure 3.7 Absorption spectra of compounds **3.1-3.9** in CH_2Cl_2 at ambient temperature. 118
Figure 3.8 The phosphorescent emission spectra of **3.1** and **3.2** in PMMA at ambient temperature (left) and in frozen CH_2Cl_2 glass at 77 K (right)..... 119
Figure 3.9 The phosphorescent emission spectra of **3.3** and **3.4** in PMMA at ambient temperature (left) and in frozen CH_2Cl_2 glass at 77 K (right)..... 121
Figure 3.10 The phosphorescent emission spectra of **3.5** and **3.6** in PMMA at ambient temperature (left) and in frozen CH_2Cl_2 glass at 77 K (right)..... 122
Figure 3.11 The phosphorescent emission spectra of **3.7-3.9** in PMMA at ambient temperature (left) and in frozen CH_2Cl_2 glass at 77 K (right). 123
Figure 3.12 The experimental (black) and calculated (gray) HOMO and LUMO energies for compound **3.1-3.9**..... 125
Figure 3.13 HOMO and LUMO diagrams of selected compounds (isocontour value = 0.03). 126
Figure 3.14 The structure A for the EL devices using POPCPA as host material..... 128
Figure 3.15 The structure B for the EL devices using 26mCPy as host material..... 128
Figure 3.16 L-J-V and current efficiency, power efficiency, EL spectra of EL devices based on **3.7** and device structure B..... 129
Figure 3.17 L-J-V and current efficiency, power efficiency, EL spectra of EL devices based on **3.9** and device structure B..... 129
Figure 3.18 L-J-V and current efficiency, power efficiency, EL spectra of EL devices based on **3.7** and device structure A..... 130
Figure 3.19 L-J-V and current efficiency, power efficiency, EL spectra and EQE-L diagram of EL devices based on **3.9** and device structure A..... 130
Figure 3.20 L-J-V and current efficiency, power efficiency, EL spectra of EL devices based on **3.8** and device structure A..... 131

Figure 3.21 L-J-V and current efficiency, power efficiency, EL spectra and EQE-L diagrams of EL devices based on **3.8** device structure B. 133
Figure 4.1 Top view and side view of the crystal structures of compounds **4.1**-**4.3** and **4.5**-**4.7**. For **4.3**, the side view shows the puckering of the CH_2 linker. 155
Figure 4.2 Diagrams showing the stacking of compound **4.1**, **4.5** and **4.6** in the crystal lattice. Top left: extended π-stacking of compound **4.5**; Top right: partially stacked discrete dimer of **4.1**; Bottom: partially stacked discrete dimer of **4.6**. 156
Figure 4.3 TGA diagrams for compounds **4.2** and **4.6**. 157
Figure 4.4 UV-Vis (solid lines) and phosphorescent (dashed lines) spectra of compounds **4.1**-**4.7** in CH_2Cl_2 at ambient temperature. 159
Figure 4.5 Photographs showing the emission colours of compounds **4.1**-**4.7** as neat solid (top), in CH_2Cl_2 (middle) and in 5% PMMA film at ambient temperature. 160
Figure 4.6 (a)-(g): Phosphorescent emission spectra of **4.1**-**4.7** in doped PMMA films; (h) Phosphorescent emission spectra of **4.6**, **2.10** and **3.9** in 5% PMMA films. 161
Figure 4.7 Phosphorescent emission spectra of **4.4**, **4.5** and **4.7** as neat powder. 164
Figure 4.8 A diagram showing the emission intensity decay of the peak at λ_{max} with time for representative compounds in 5 wt% PMMA films under continuous UV irradiation under air and at ambient temperature. Inset: photographs showing the emission color of the PMMA films before and after UV exposure. 166
Figure 4.9 EL spectra of devices C1 and E1 at various driving voltages, L-J-V diagrams of all devices, and EQE-L diagrams of all devices. Inset: a photograph showing the emission color of the EL device. 176
Figure 5.1 (a) Photograph showing the piezochromic property of compound **3.7**; (b) Photographs showing the thermochromic property of compound **3.4** in THF. 197

List of Tables

Table 1.1 Performances of PhOLEDs developed by UDC. (adapted from Ref. 9) 3
Table 2.1 Key bond lengths and short contact distances (Å) 65
Table 2.2 Photophysical data of Pt(II) Compounds 70
Table 2.3 Experimental HOMO–LUMO energy and TD-DFT calculation results for selected compounds. 79
Table 2.4 The HOMO and LUMO diagrams of selected Pt(II) compounds. (isocontour value = 0.03).... 80
Table 2.5 EL device data for **2.9** and **2.10**. 85
Table 3.1 Important bond lengths and angles of the Pt(II) compounds 111
Table 3.2 Photophysical data of Compounds **3.1-3.9** 117
Table 3.3 Experimental HOMO–LUMO energy and TD-DFT data for compound **3.1-3.9**. 124
Table 3.4 EL device data for **3.8**. 132
Table 4.1 Important Bond Lengths (Å) and Angles (°) for compounds **4.1-4.7** (except **4.4**) 156
Table 4.2 Photophysical Data of Compounds **4.1-4.7** 158
Table 4.3 TD-DFT data for compounds **4.1-4.7** 168
Table 4.4 MO diagrams of **4.1-4.7** (isocontour value = 0.03). 169
Table 4.5 Optimized S_0 and T_1 structures and RMSD values of **4.1-4.7** and **3.8** 172
Table 4.6 Six stable geometries of **3.8** at the T_1 state 173
Table 4.7 EL device data of Compound **4.6** 175
Table 5.1 Luminous efficiency of various light sources. (adapted from Ref. 1) 197

List of Abbreviations

°	degrees
°C	degrees Celsius
$^1D^*$	singlet excited dopant molecule
$^3D^*$	triplet excited dopant molecule
$^1H^*$	singlet excited host molecule
$^3H^*$	triplet excited host molecule
η_{out}	light outcoupling factor
χ	electroexcitation efficiency
δ	chemical shift
Δ	change/difference; heat
ε	molar extinction coefficient
η_{ext}	external quantum efficiency
η_{int}	internal quantum efficiency
η_{CE}/η_c	current efficiency
η_{PE}/η_p	power efficiency
η_r	charge recombination efficiency
θ	angle
λ	wavelength
λ_{max}	emission maximum
μs	microsecond
Σ	sum
τ_P	phosphorescent decay lifetime

Φ_{PL}	photoluminescence quantum efficiency
Ω	ohms
26mCPy	2,6-bis(N-carbazolyl)pyridine
Å	angstrom
A	device active area
A	amp; absorbance; acceptor
acac	acetylacetonate
Ad	adamantyl
Alq3	tris(8-hydroxyquinolate)aluminum(III)
Anal. calcd.	elemental analysis calculated
Ar	aromatic
BCPO	9,9′-(4,4′-(phenylphosphoryl)bis-(4,1-phenylene))bis(9H-carbazole)
Bn	benzyl
Bp	$BMes_2$-phenyl
Bptrz	$BMes_2$-functionalized phenyl-1,2,3-triazole
br	broad
C	Ph_3C-functionalized
CBP	4,4*'*-*N,N'*-dicarbazolebiphenyl
cd	candelas
CDBP	4,4'-bis(9-carbazolyl)-2,2'-dimethylbiphenyl
CIE	Commision Internationale de l"Éclairage
cm	centimetres

Cp	cyclopentadienyl
CT	charge-transfer
CuAAC	copper catalyzed azide-alkyne cycloaddition
CV	cyclic voltammetry
D	dopant molecule; donor
d	doublet; d orbital
dd	doublet of doublets
DFT	density functional theory
DIEPA	diisopropylethylamine
DMF	dimethylformamide
DMSO	dimethylsulfoxide
DPEPO	bis[2-(diphenylphosphino)phenyl] ether oxide
dpm	dipivaloylmethane anion
E	energy
e^-	electron
EBL	electron blocking layer
EIL	electron injection layer
EL	electroluminescent
EML	emissive layer
EQE	external quantum efficiency
equiv.	equivalents
E_{red}	reduction potential
Et	ethyl

ETL	electron transport layer
eV	electronvolts
ExBL	exciton blocking layer
f	oscillator strength
F	fluorescence
Firpic	bis[2-(4,6-difluorophenyl)pyridinato C^2,N](picolinato)iridium(III)
FW	formula weight
g	grams
H	HOMO
h/hr	hours
h^+	hole
hν	light
HBL	hole blocking layer
HIL	hole injection layer
HOMO	highest occupied molecular orbital
HPCVL	High Performance Computing Virtual Laboratory
HRMS	high-resolution mass spectrometry
HTL	hole transport layer
Hz	hertz
I	intensity
ILCT	intra-ligand charge transfer
I_{OLED}	operating current
IQE	internal quantum efficiency

$Ir(ppy_3)$	tris[2-phenylpyridinato-C^2,N]iridium(III)
ITO	indium tin oxide
J	coupling constant
J	current density
K	Kelvin
k	Boltzmann constant
kJ	kilojoules
k_{nr}	nonradiative decay rate
k_r	radiative decay rate
kV	kilovolts
L	Luminance; ligand; LUMO
LC	ligand-centered
LCD	liquid crystal display
LLCT	ligand to ligand charge transfer
lm	lumens
LMCT	ligand-to-metal charge transfer
L_P	light power of OLED as perceived by the human eye
LUMO	lowest unoccupied molecular orbital
m	meta
m	meters
m^2	square meters
M	molar; metal
mA	milliamps

MC	metal centered
mCP	*N*,*N*′-dicarbazolyl-3,5-benzene
Me	methyl
MeCN	acetonitrile
Mes	mesityl
mg	milligrams
MHz	megahertz
min	minutes
mL	millilitre
MLCT	metal-to-ligand charge-transfer
MO	molecular orbital
mol	mole
mV	millivolts
N	Ph_2N-functionalized
NHC	*N*-heterocyclic carbene
nm	nanometres
NMR	nuclear magnetic resonance
NPB	*N,N'*-di-[(1-naphthyl)-*N,N'*-diphenyl]-(1,1'-biphenyl)-4,4'-diamine
OLED	organic light-emitting diode
p	para
Pa	pascal
pic	picolinate

Ph	phenyl
PhOLED	phosphorescent organic light-emitting diode
PL	photoluminescence
PMMA	poly(methyl methacrylate)
POPCPA	[(4-{1-[4-(diphenylphosphoryl)phenyl] cyclohexyl}phenyl)bis(4-methylphenyl)amine]
ppm	parts per million
ppy	2-phenylpyridine
py	pyridyl
RMSD	root-mean-square deviation
ROSEY	rotating-frame overhauser effect spectroscopy
RT	room temperature
S	spin; Huang-Rhys parameter
s	second
S_0	ground state
S_n, (n > 0)	nth singlet excited state
t	time
T	temperature
tBu	*tert*-butyl
TBTA	tris[(1-benzyl-1*H*-1,2,3-triazol-4-yl)methyl]amine
T_n (n > 0)	nth triplet excited state
TAPc	4,4′-cyclohexylidenebis[*N,N*-bis(4-methylphenyl)benzene-amine]

TBAF	tetrabutylammonium fluoride
TD-DFT	time-dependent density functional theory
TGA	thermogravimetric analysis
THF	tetrahydrofuran
TLC	thin layer chromatography
TmPyPb	1,3,5-tris(3-pyridyl-3-phenyl)benzene
TP3PO	1,3,5-tri[3-(diphenylphosphoryl)phenyl]benzene
TPBI	1,3,5-tris(*N*-phenylbenzimidazole-2-yl)benzene
trz	triazole
TsOH	tosylic acid
UV	ultraviolet
V	volt
ν	vibrational level
V_{on}	turn-on voltage
W	watt
wt	weight

Chapter 1

Introduction

Electroluminescence (EL) of organic molecules was first observed and studied at 1960s, but attempts to fabricate organic electroluminescence devices for practical applications were not successful due to the high voltage (hundreds of volts) needed for charge injection.[1-2] It was not until 1987 that an organic electroluminescent diode comprised of a novel double-layer structure with a low driving voltage and promising luminescence efficiency was demonstrated by Tang and VanSlyke.[3] Since then, tremendous research efforts have been devoted to the development of organic light-emitting diodes (OLEDs) in order to achieve high luminescence efficiency, long device life time, low manufacturing cost and good color purity. OLED technology has been commercialized and is extensively used in the production of flat panel displays devices such as computer monitors, cellular phone displays and television screens.[4]

Compared to conventional liquid crystal displays (LCDs), OLEDs provide several advantages. As OLEDs are self-luminous, the use of backlight is not needed, which not only greatly reduces the size and manufacturing cost of OLED displays but also offers better contrast and wider viewing angle. OLEDs can even be deposited on flexible substrates which enables the construction of ultra-thin, bendable displays. The response time for OLED displays is also much shorter, because the generation of electroluminescence is substantially faster than the response of liquid crystals to applied electric field. Though the current manufacturing procedures for OLEDs are sophisticated, inkjet printing or screen printing methods have been utilized to simplify the fabrication process, which may lead to significant reduction in production cost in the future.[5-7]

Although tremendous progress has been made in the research and commercialization of OLED technology in both academic and industrial sectors, the development of efficient and stable deep blue phosphorescent OLEDs (PhOLEDs) remains one of the greatest challenges.[8] Compared to OLEDs based on fluorescent materials which can only harvest singlet excitons, PhOLEDs are able to harvest both singlet and triplet excitons and can reach an internal quantum yield four times higher. Table 1.1 shows the performances of PhOLEDs developed by Universal Display Corporation in 2012, which remain as the state of the art in OLED industry at present.[9] While green and red PhOLEDs with high quantum efficiency and long lifetime have already entered the market, deep blue PhOLEDs with similar performance are not even realized in laboratories. The half-life (LT 50%) of the most stable blue PhOLED device reported in the literature was 3500 hours at the initial luminance of 1000 cd/m^2 with Commission Internationale de l'Eclairage (CIE) coordinates of (0.15, 0.29), which are much shorter compared to those of the industrial green (400,000 hours) and red (600,000-900,000 hours) PhOLEDs.[10]

Table 1.1 Performances of PhOLEDs developed by UDC. (adapted from Ref. 9)

PhOLED Performance (at 1000 cd/m^2)	1931 Color Coordinates	Current Efficiency (cd/A)	Operating Lifetime (hrs)	
			LT 95%	LT 50%
Deep Red	(0.69, 0.31)	17	14,000	250,000
Red	(0.66, 0.34)	29	23,000	600,000
Red	(0.64, 0.36)	30	50,000	900,000
Yellow	(0.44, 0.54)	81	85,000	1,450,000
Green	(0.31, 0.63)	85	18,000	400,000
Light Blue	(0.18, 0.42)	50	700	20,000

In this thesis, we aim to improve the efficiency and stability of deep blue OLEDS by developing highly efficient deep-blue phosphorescent emitters. In this chapter, a short introduction about OLED structure and its working principle will be presented, followed by a brief review about cyclometalated Pt(II) compounds and their applications in OLEDs. Copper catalyzed azide-alkyne cycloaddition (CuAAC) reaction, which is used to synthesize 1,2,3-triazoles, will be mentioned at the end.

1.1 OLEDs

1.1.1 Device Architecture

A typical device structure for a three-layer OLED is shown in Figure 1.1. The electroluminescent material is doped in the host material to form the emissive layer (EML), which is sandwiched between the electron transport layer (ETL) and the hole transport layer (HTL). The incorporation

of ETL and HTL is to facilitate electron and hole transport, respectively. The electrons are injected from the cathode, which is made of a low work function metal such as Mg or Al, and holes are injected from the anode, which is usually comprised of a transparent layer of indium tin oxide (ITO). The organic layers and the cathode material are usually thermally evaporated under high vacuum (10^{-4} Pa or less) until a thickness of several tens of nanometers is reached.

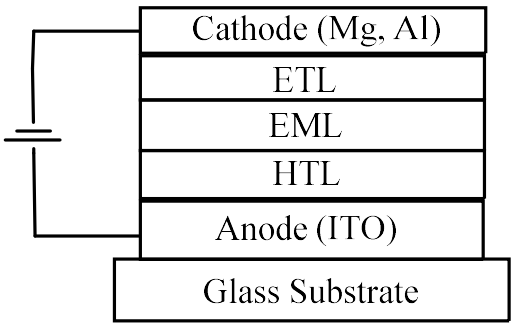

Figure 1.1 Device structure of a three-layer OLED.

The materials used in OLEDs must be chosen carefully in order to optimize the device performance. The hole and electron injection barriers are defined as the energy difference between the highest occupied molecular orbital (HOMO) level of the HTL and the Fermi level of ITO, and the lowest unoccupied molecular orbital (LUMO) level of the ETL and the work function of the cathode, respectively. Small injection barriers are beneficial to the efficiency and lifetime of an OLED device, as they lead to a good charge balance and low driving voltages. In practice, the injection barriers can be decreased by adding charge injection layers between anode/HTL and cathode/ETL. MoO_3 and *N,N′*-di(1-naphthyl)-*N,N′*-diphenyl-(1,1′-biphenyl)-4,4′-diamine (NPB) are commonly used as hole injection layer (HIL) and LiF is frequently used as electron injection layer (EIL). Typical HTL and ETL contain electron rich arylamine or carbazole groups, and electron deficient heterocyclic groups, respectively, to achieve high carrier mobility. In addition, the HOMO of the

hole transport material and the LUMO of the electron transport material are close to those of the HIL and EIL, respectively, for efficient charge injection. Most modern OLED devices also have extra blocking layers between the charge transport layers and the emissive layer, to prevent charge or exciton leakage from the EML. The electron blocking layer (EBL) that has a LUMO level much higher than the LUMO level of EML could be inserted between the HTL and EML. A hole blocking layer (HBL) that has a considerably lower HOMO than that of the EML could be inserted between the ETL and EML. The exciton blocking layer (ExBL) is commonly seen in deep blue PhOLEDs, which contain phosphorescent dopants that emit light near 450 nm. To confine the high energy triplet excitons within the emissive layer, the triplet energy of the ExBL should be larger than 2.8 eV.[11]

1.1.2 Working Principle

As depicted in Figure 1.2, when a voltage is applied between the cathode and the anode, electrons and holes are generated and migrate towards the opposing electrodes. The electrons and holes are transferred through the LUMO of the electron transporting material and the HOMO of the hole transporting material, respectively. When electrons and holes approach each other in the emitting layer, they recombine to give electron-hole pairs, also known as excitons. The energy could be transferred to the dopant molecule via energy transfer process or charge trappinng process, which will be discussed shortly after. Light is then released from the dopant when the excited molecules go back to the ground state radiatively.

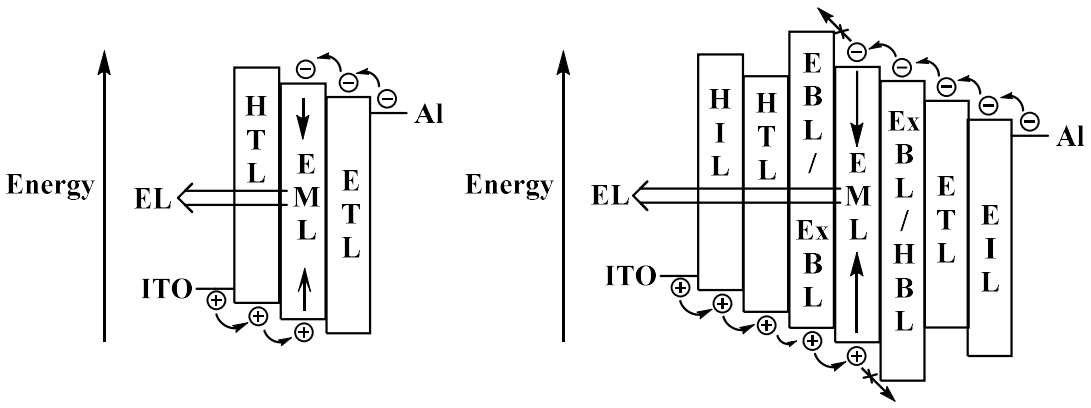

Figure 1.2 The energy diagrams and working mechanism of a three-layer OLED (left) and a seven-layer OLED (right).

During the recombination process, both singlet excitons (S = 0) and triplet excitons (S =1) are generated as the electrons and holes are injected from different sources. According to quantum mechanics, about three times more triplet excitons are created than the singlet excitons. OLEDs based on fluorescent materials can only harvest singlet excitons as the $T_1 \rightarrow S_0$ transition is spin-forbidden, leading to a maximum internal quantum yield of 25%. PhOLEDs, however, are able to harvest both singlet and triplet excitons thus a theoretical internal quantum yield of 100% could be obtained.[12] Most PhOLEDs employ phosphorescent organometallic complexes as the emitting materials, which usually contain third-row transitional metals such as iridium or platinum that exhibit strong spin-orbital coupling to facilitate intersystem crossing process. The various photophysical processes involved in phosphorescence is illustrated with the help of the Jablonski diagram, as depicted in Figure 1.3.[13] After the absorption of a photon, the molecule is excited to a higher electronic state. This process is very fast (10^{-15} s) and during which the electron spin is preserved. The molecule will then quickly (10^{-14} s -10^{-11} s) drop to its first singlet excited state (S_1) via two non-radiative processes, namely vibrational relaxation (from higher vibrational state to

lower vibrational state) and internal conversion (from higher electronic state to lower electronic state). At the lowest singlet excited state, the molecule can return to its ground state (S_0) via the emission of light by fluorescence on the time scale of 10^{-9} s. It can also relax via intersystem crossing to a triplet state in which the excited electron and the electron at the ground state are parallel, followed by the emission of light as phosphorescence. In most common organic molecules, the intersystem crossing and phosphorescent processes, which involve spin-flip, are unlikely to happen due to the violation of the selection rule. Compared to the fast fluorescent process (10^{-12} - 10^{-9} s), intersystem crossing and phosphorescence occur much more slowly, typically on the time scale of 10^{-8} - 10^{-4} s and 10^{-6} - 10^{0} s, respectively. However, when a heavy atom is incorporated, intersystem crossing is enhanced substantially as the heavy atom nucleus induces large spin-orbit coupling which enhances the mixing of singlet and triplet states, and efficient phosphorescence is produced.

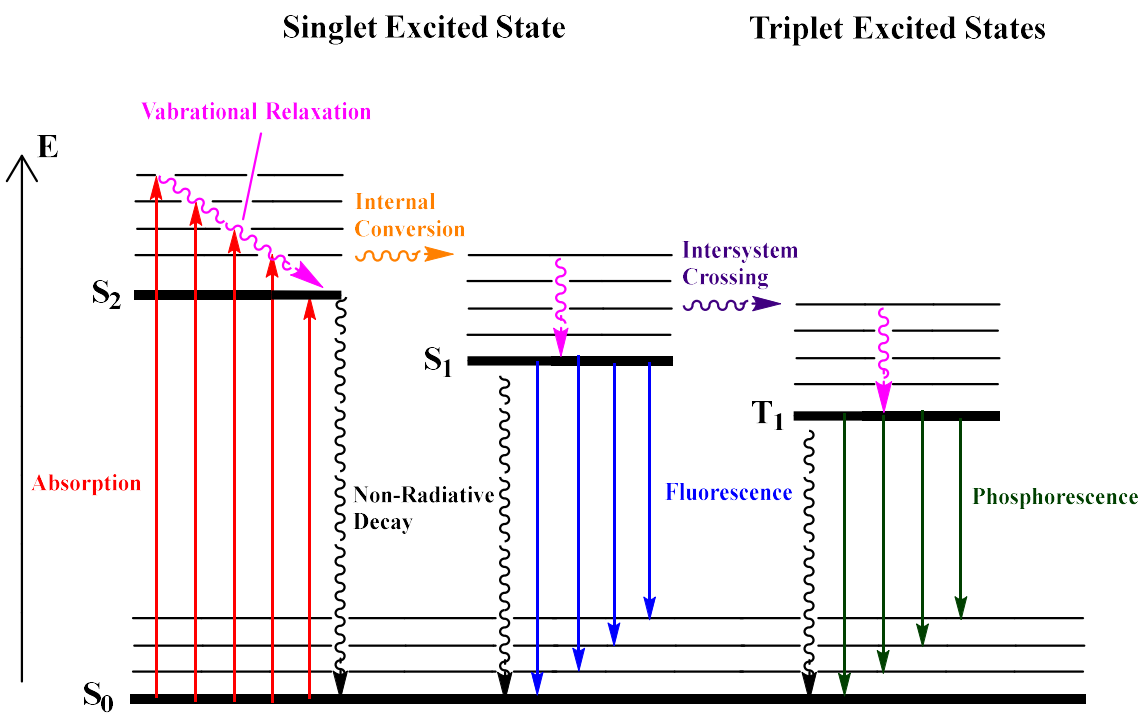

Figure 1.3 Jablonski diagram showing various energy transfer pathways.

In the Jablonski diagram, molecules are excited via photon absorption. As mentioned earlier, the dopant molecules in OLEDs are excited via either energy transfer from the host or charge trapping and recombination on the dopant.[14,15]

The charge trapping process is shown in Figure 1.4. If the HOMO and LUMO levels of the dopant molecule are within the HOMO and LUMO levels of the host molecule, the electrons and holes generated on the host molecule will be transferred and trapped in the LUMO and HOMO of the dopant molecule, respectively. The efficiency of this process depends highly on the energy gaps of the HOMOs and LUMOs of the host and dopant. The higher the energy gap, the more efficient the charge trapping process will be.

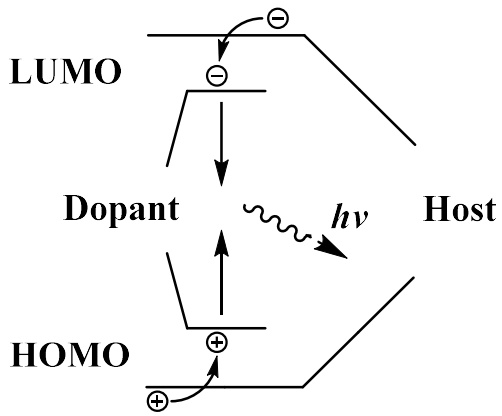

Figure 1.4 Charge trapping process in OLEDs.

The Förster resonance energy transfer and the Dexter electron transfer account for the energy transfer process in the emitting layer. For Förster energy transfer (Figure 1.5), the energy of a singlet excited host molecule (^{1}H*) will be transferred to a dopant molecule (D) through non-radiative dipole–dipole coupling, and its efficiency is proportional to the spectral overlap of the

host emission band and the dopant absorption band. Typical Förster transfer distance can be up to 10 nm.

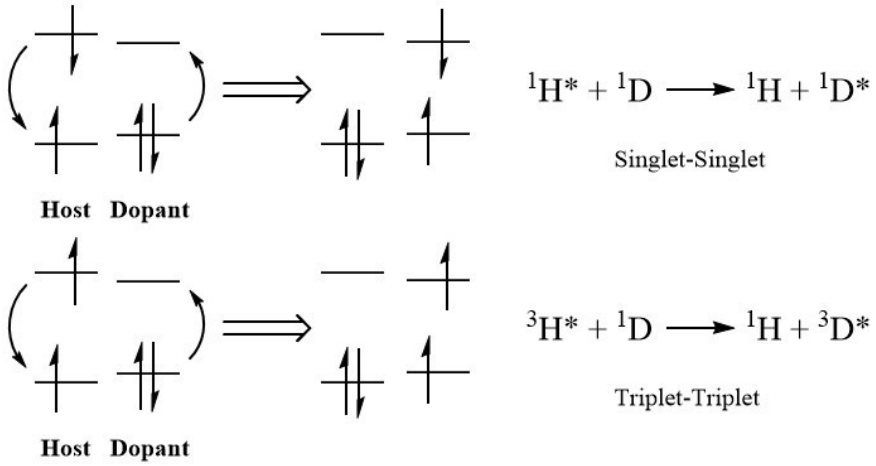

Figure 1.5 Förster energy transfer mechanisms.

For Dexter electron transfer (Figure 1.6), the excited electron of a host molecule will exchange with an electron of a dopant molecule in the ground state. Dexter transfer requires a wavefunction overlap between the host and dopant molecules, which means it can only occur between neighboring molecules (within 2 nm).

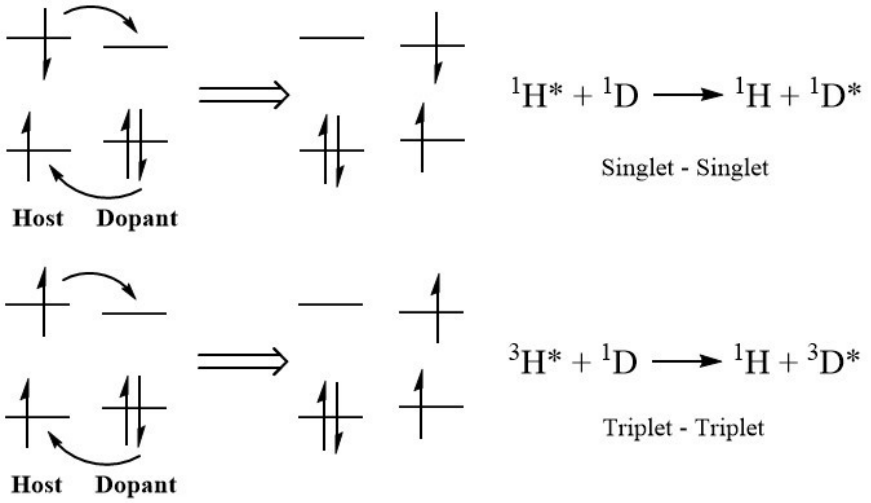

Figure 1.6 Dexter transfer mechanisms.

A special case following Dexter electron transfer pathway is triplet-triplet annihilation (Figure 1.7), in which two triplet excited states interact to form one singlet ground state and one excited singlet state, resulting in a loss of one exciton.

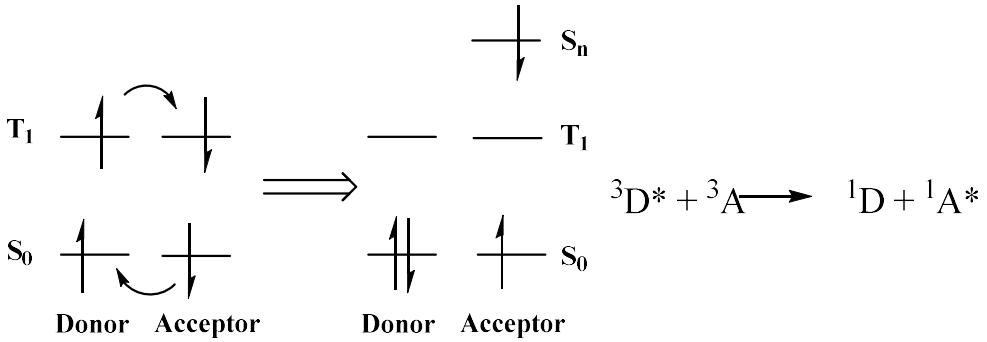

Figure 1.7 Triplet-triplet annihilation mechanism.

In PhOLEDs, the predominant energy transfer processes are the singlet–singlet Förster transfer and triplet–triplet Dexter transfer, as the singlet–singlet Dexter transfer rate is much smaller than that of the Förster transfer, and the triplet-triplet Förster transfer is unlikely to happen as the emission from the triplet state of the host molecule (which is most likely to be organic molecule) is very weak. Triplet-triplet annihilation, on the other hand, is one major source of efficiency loss at high brightness.

1.1.3 Performance Characterization

Among several parameters that are used to determine the efficiency of an OLED device, the device external quantum efficiency η_{ext}, defined as the ratio of the number of photons left the device to the number of electron injected, is the most important.[16] It can be described as:

$$\eta_{ext} = \chi \times \eta_r \times \Phi_{PL} \times \eta_{out} = \eta_{int} \times \eta_{out}$$

where χ is the fraction of excitons transferred to the emitter which could lead to fluorescence or phosphorescence, η_r is a charge recombination efficiency, η_{out} represents the light out-coupling efficiency, and Φ_{PL} is the photoluminescence quantum yield of the emitter. As discussed above, χ is 25% for fluorescent OLEDs and 100% for phosphorescent OLEDs. η_r can be defined as the fraction of charge that forms excitons. For a device with balanced charge injection and transport rate, η_r could be close to unity. Φ_{PL} is the fraction of emitted photons among all absorbed photons. Φ_{PL} equals to 1 means every photon absorbed by the emitting material will be emitted. The internal quantum efficiency (η_{int}) is defined as the combination of χ, η_r and Φ_{PL}, which determines the ratio of the number of photons generated in the device to the number of electron injected and could be as high as 100%. Unfortunately, only a small portion of these photons can escape the device. The light out-coupling efficiency in an OLED device is 0.2-0.3, due to the refraction index mismatch between the organic layers, the ITO layer, the glass substrate and air.

The current efficiency η_{CE} and power efficiency η_{PE} of the OLED device are also presented in most literatures reports. Compared to η_{ext} which treat photons of all wavelengths equally, η_{CE} and power efficiency η_{PE} take the photopic response of human eyes into consideration. There are two photoreceptors in human eyes, the rod cells and the cone cells, named after their corresponding shapes. The cone cells have three types, each has their own sensitivity which peaks at 437 nm (blue), 534 nm (bluish-green), and 564 nm (yellowish-green), respectively (Figure 1.8).[17]

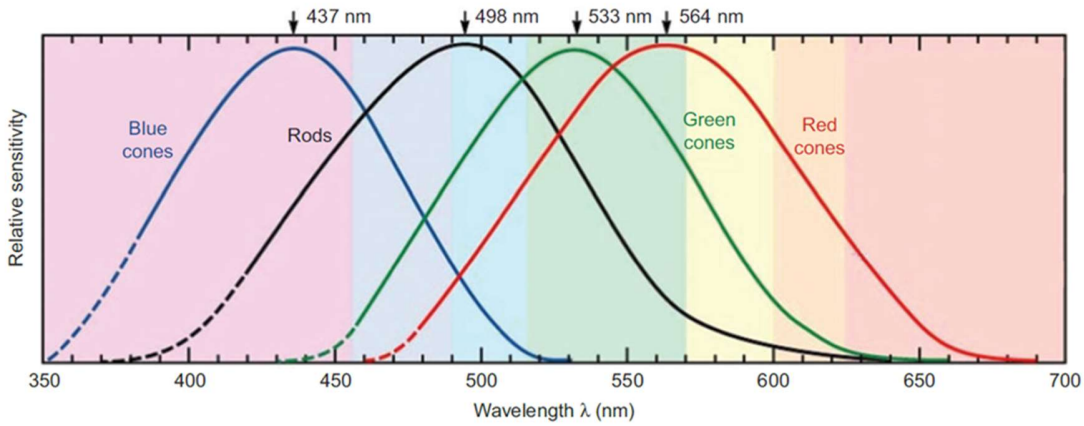

Figure 1.8 Normalized sensitivity curves of rod cells and cone cells. (adapted from Ref. 17)

The rod cells are responsible for our vision at low brightness (< 0.005 cd/m^2, scotopic vision) and the cone cells are responsible for the vision at high light level (>5 cd/m^2, photopic vision). As for display applications, the brightness needs to be higher than 100 cd//m^2, the photopic sensitivity of human eyes needs to be considered for display purposes.

The current efficiency η_{CE} is defined as:

$$\eta_{CE} = A \times L / I_{OLED}$$

Where A is the device active area, L is the luminance of the OLED in cd/m^2 and I_{OLED} is the operating current.

The power efficiency η_{PE} is defined as:

$$\eta_{PE} = L_P / I_{OLED} V = \pi \times \eta_{CE} / V$$

Where L_P is the light power of OLED as perceived by the human eye in lumen (lm) and V is the operating voltage.

1.2 Introduction to Cyclometalated Complexes

Due to the higher theoretical internal quantum yield of PhOLEDs relative to fluorescent OLEDs, recent research efforts have been devoted to the synthesis of phosphorescent materials with high quantum efficiency, good thermal stability and high color purity. Most of the compounds investigated for PhOLEDs are cyclometalated complexes. Cyclometalating ligands are capable of chelating the metal center via at least one carbon atom forming a C-M σ bond, and one or more heteroatoms, forming X-M dative bonds (e.g. N-M, S-M, P-M) (Figure 1.9). If a ligand forms a 5-membered metallacycle through the binding of a carbon atom and a nitrogen atom, it can also be described as a C^N chelate ligand.

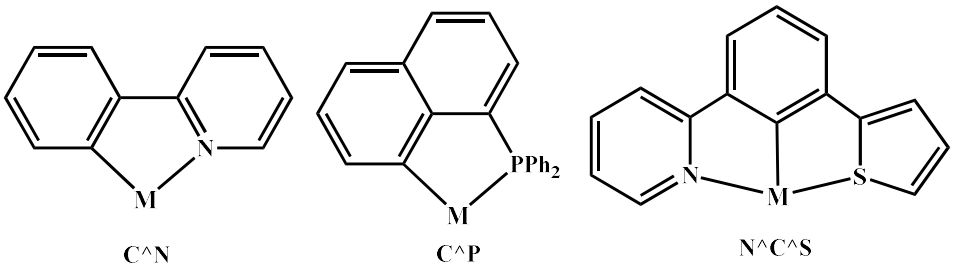

Figure 1.9 Some common examples of cyclometalating ligands.

In luminescent cyclometalated molecules, ligands other than the cyclometalating ligand are called ancillary ligands, which are introduced to modify steric or electronic properties. The common ancillary ligands are β-diketonates (i.e. acetylacetonate (acac), dipivaloylmethane anion (dpm)), picolinate (pic) and its derivatives, which are shown in Figure 1.10. The choice of ancillary ligands can have a profound impact on properties such as emission color and quantum efficiency, which will be discussed in detail in Chapter 2.

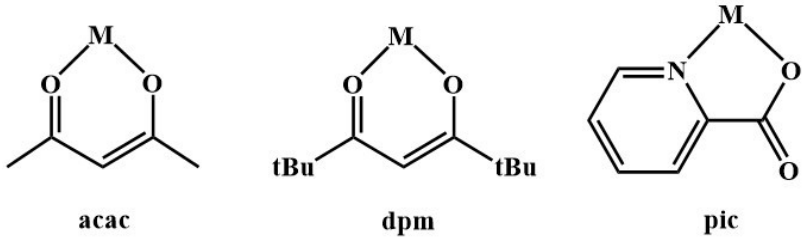

Figure 1.10 Examples of common ancillary ligands.

Depending on the composition of the frontier orbitals involved in the excitation process, there are mainly four types of excited states in cyclometalated complexes, as shown in Figure 1.11.[18] If the transition originates from the ligand π orbital to the empty metal d orbital, it is called ligand to metal charge transfer (LMCT) transition. If the transition involves metal d orbital and ligand π^* orbital, it is a metal to ligand charge transfer (MLCT) transition. If the transition only involves the metal d-d states, it is a metal centered (MC) transition. Ligand centered (LC) transitions or ligand to ligand charge transfer (LLCT) transitions, on the contrary, involve intramolecular π-π^* transitions on the same ligand or between different ligands, respectively. The excited state can be an admixture of two or more states, such as a LC state with MLCT character.

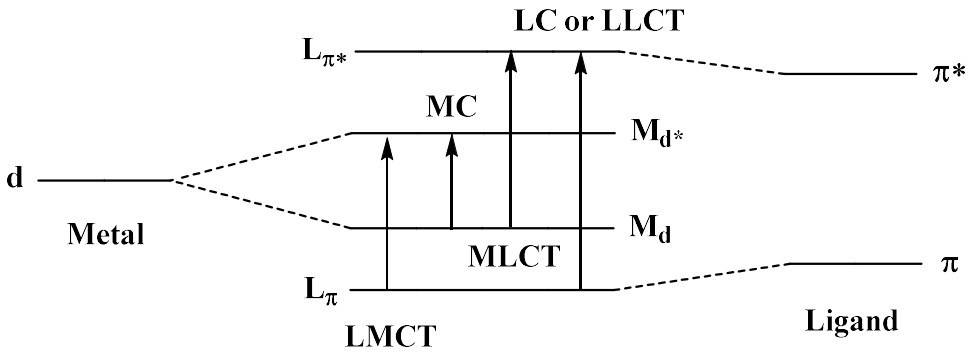

Figure 1.11 A diagram showing different excited state transitions in cyclometalated compounds

1.3 Design of Highly Luminescent Cyclometalated Pt(II) Compounds

1.3.1 Advantages of Using Pt-based Luminescent Materials

Luminescent Pt(II) compounds have attracted tremendous research efforts in the field of OLED. The strong spin-orbital coupling provided by the platinum atom readily promotes the rate of intersystem crossing to around 10^{12} s^{-1} to allow efficient phosphorescence.[19] When chelated by cyclometalating ligands, the strong ligand field of the cyclometalating ligands can raise the energy level of the unoccupied metal d orbitals, reducing the probability of quenching by nonradiative metal d-d transitions. Due to the chelation effect, most cyclometalated Pt(II) complexes are in general chemically stable and charge-neutral, which is beneficial to the OLED device stability. Emission color tuning can be achieved by introducing various substituent groups or heterocyclic rings. With the help of density functional theory (DFT) or time-dependent density functional theory (TD-DFT) calculations, the band gaps, which relates to the emission color of Pt compounds, can be predicted with relative accuracy. The synthetic methods are also well-established and relatively simple.[8e]

1.3.2 Strategies for Emission Color Tuning

Mixing red, green and blue light is the most common way to obtain white light. Thus to achieve white light emission, OLEDs with red, green and blue emitting materials are required. One of the advantages of OLEDs over inorganic LEDs is that color tuning can be done by modifying the molecular structure of the emissive molecules. As phosphorescence originates from the $T_1 \rightarrow S_0$ transition, the HOMO-LUMO energy gap is a good indicator for emission color. As a result, tuning the emission color usually involves the manipulation of the HOMO and LUMO levels of the cyclometalated complex, which will be illustrated in Figure 1.12 using ppyPt(acac) as an example

(ppy = 2-phenylpyridine). It has been reported that in ppyPt(acac), the HOMO is located on the phenyl ring, Pt and acac group while the LUMO is mainly located on the pyridine moietiy.[20] If electron withdrawing/donating groups are introduced on the phenyl ring, the HOMO will be stabilized/destabilized and shifted to lower/higher energy, respectively, resulting in hypochromic/bathochromic shift of the luminescence color. If the π-conjugated system is expanded (i.e. 2-phenylquinoline is used instead of 2-phenylpyridine), the emission wavelength will shift to a longer wavelength as the HOMO-LUMO energy gap decreases. If heterocyclic rings with higher/lower triplet energies are used instead of pyridine, the luminescence will be shifted to a shorter/longer wavelength, respectively.

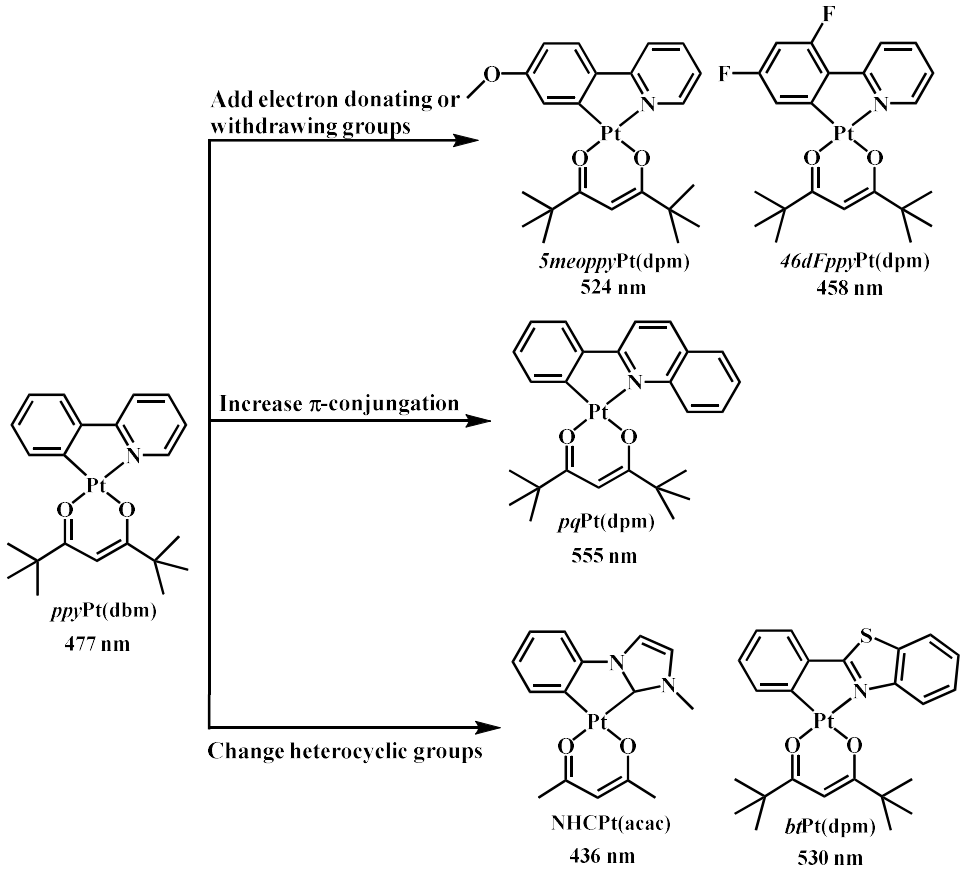

Figure 1.12 A diagram demonstrating emission color tuning of Pt(II) compounds.[20,21]

1.3.3 Strategies to Improve Phosphorescent Quantum Yields

One of the top priorities in the development of phosphorescent materials is to achieve high luminescence quantum yield, which is defined as the ratio of the radiative rate (k_r) over the sum of radiative and all nonradiative rates:

$$\Phi_{PL} = k_r / (k_r + \sum k_{nr})$$

Several strategies can be used to obtain high Φ_{PL}, with the general idea to either increase k_r, or decrease k_{nr}, or do both at the same time.[8d] Enhancing the mixing of the MLCT state and LC state is an effective way to increase k_r, as the spin-orbit coupling is more effective when there is more MLCT character in the excited state. It has been reported that the degree of mixing is inversely proportional to the energy gap between the two states, thus a small energy difference between the MLCT state and LC state is beneficial to obtain higher k_r.[8e] In order to decrease k_{nr}, two methods are often used: 1) deactivate the non-radiative metal d-d state; 2) decrease structural distortion in the excited state. A brief discussion will be given below.

In most Pt coordination complexes, the oxidation state of platinum is + 2, with 8 electrons in its d orbitals. According to the crystal field theory, Pt(II) complexes almost always adopt the square planar geometry. The ligand field splitting diagram is shown in Figure 1.13.

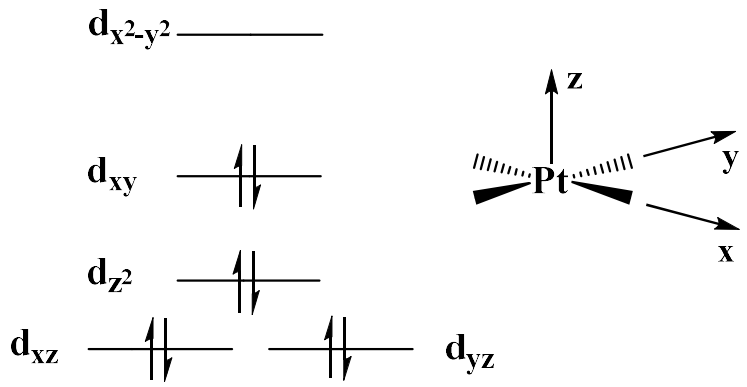

Figure 1.13 Ligand field splitting diagram of square-planar Pt(II) complexes.

The population to the d(x^2–y^2) orbital would weaken the Pt-ligand bonds in the excited state, causing a severe geometry distortion. The excitation energy could be easily dissipated through the isoenergetic crossing point as the molecule returns to the ground state non-radiatively. For most cyclometalated Pt(II) complexes, the first triplet excited state, which usually is a LC or LLCT state with MLCT character, lies below the metal d-d state. Thermal population from the T_1 state to the metal d-d state is still possible if the energy difference (ΔE in Figure 1.14) of these two states is comparable to thermal energy *kT* (*k* is Boltzmann constant), as shown in Figure 1.14. To avoid this thermal quenching process, ΔE should be reasonably large, which could be achieved by raising the d-d state or decreasing the excited state. However, due to the requirement of high triplet energy for deep blue emitters, raising the metal d-d state becomes the sole option.

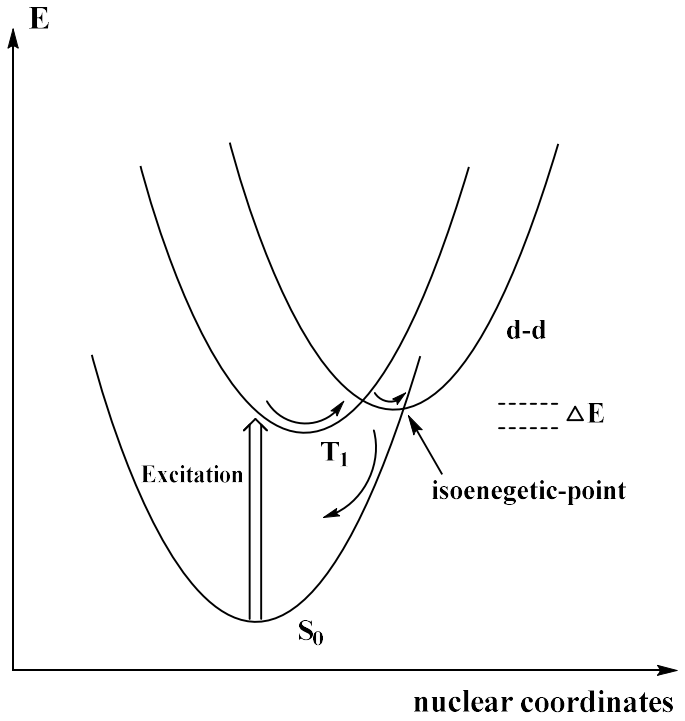

Figure 1.14 Energy diagram showing potential energy surfaces of the ground state (S_0), first triplet excited state (T_1) and metal d-d state of a cyclometalated Pt(II) complex. Curved arrows represent non-radiative decay.

The offset between the ground state structure and the excited state structure ΔQ can be quantified by the Huang-Rhys parameter S, which can be roughly estimated as:

$$S = I_{0\text{-}1} / I_{0\text{-}0}$$

Where $I_{0\text{-}1}$ and $I_{0\text{-}0}$ denote the phosphorescence intensity of the 0-1 band ($\nu = 0$ of the T_1 state to $\nu = 1$ of the S_0 state) and 0-0 band ($\nu = 0$ of the T_1 state to $\nu = 0$ of the S_0 state), respectively.[22] When S = 0, the structure in the first excited state is exactly the same as the ground state structure and only one emission peak will be seen in the emission spectrum. A lager S value indicates greater structural difference between the ground state and the excited state, as shown in Figure 1.15,[23] resulting in the appearance of additional emission bands and broad emission spectra.

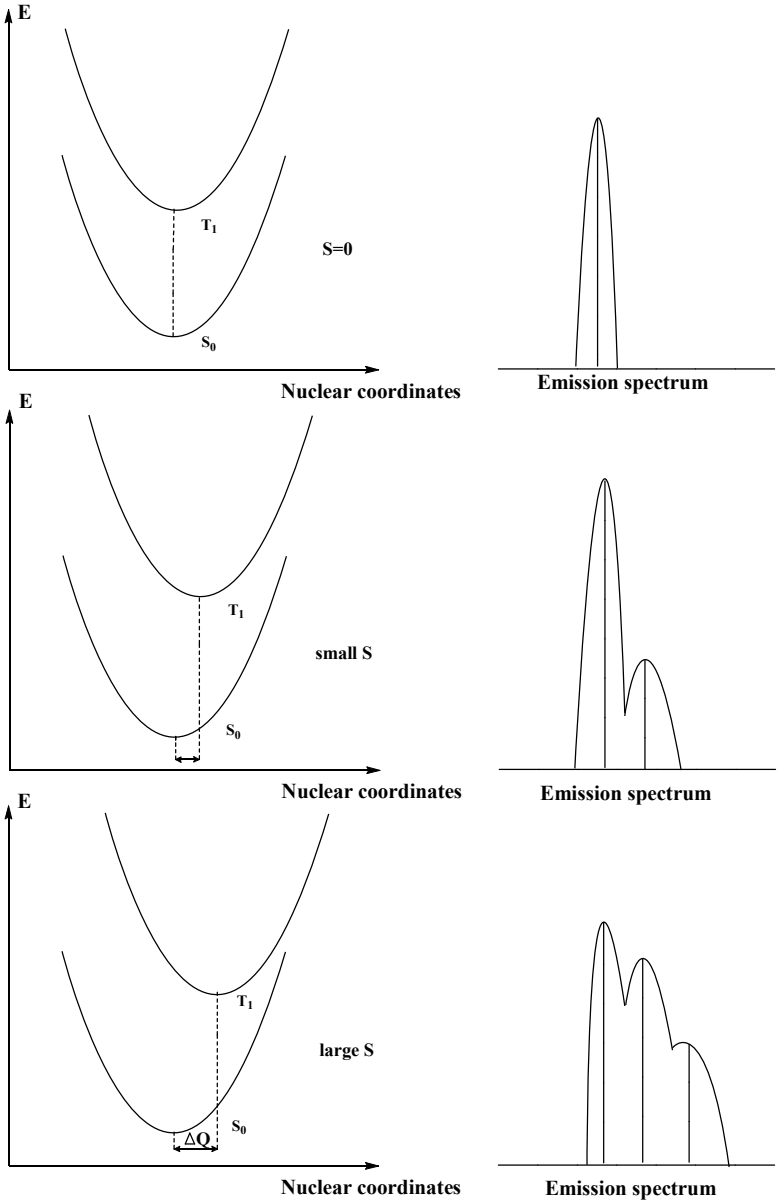

Figure 1.15 Diagrams showing the relationship between the Huang-Rhys parameter S and emission curve. Top: single emission peak when S=0; Middle: narrow emission spectrum when S is small. Bottom: broad emission curve when S is large.

For Pt(II) complexes chelated by a terdentate or tetradentate cyclometalating ligand, emission spectra with narrow peaks and small $I_{0\text{-}1}$ / $I_{0\text{-}0}$ ratio are often noticed, indicating minor structure deformation in the excited state.

Cyclometalated Pt(II) compounds without bulky functional groups are usually flat, which offers the opportunity for intermolecular interactions such as Pt-Pt interactions or ligand π-π interactions. This would facilitate the formation of excimers, which is a dimeric species composed of an excited state and a ground state molecule. The emission produced by excimers is red-shifted and usually less efficient compared to the excited monomer. Generally, except to get white light from the combination of monomer and excimer emission, the formation of excimer should be prevented to avoid loss of quantum efficiency and color purity.[16b]

With the above points in mind, the general approaches to design cyclometalated Pt(II) complexes with high quantum efficiency include: 1) increasing the rigidity of the cyclometalating ligand to reduce geometric distortion in the excited state, which is usually accomplished using multidentate ligands, 2) applying dendrimer structures or using sterically demanding functional groups to minimize intermolecular interactions in the solid state, in order to avoid aggregation or excimer formation, 3) using ligands with high ligand fields (i.e. carbenes) to prevent quenching via nonradiative metal d-d transitions, which is particularly important for the design of deep blue phosphors, 4) adjusting the energy level of MLCT and LC states by functionalizing the cyclometalating ligand, such as introducing the electron deficient triarylboron group, to achieve well-mixed MLCT and LC states.

1.4 Recent Development of Highly Efficient Phosphorescent Pt(II) Compounds

Depending on the number of binding sites on the chelating ligand, there are mainly five types of Pt (II) complexes, as shown in Figure 1.16.[24] Type **I** involves one bidentate ligand and two monodentate ligands. In Type **II** the platinum center is chelated by two bidentate ligands. Type **III**

contains one terdentate ligand and one monodentate ligand. Type **IV** and **V** both contain only one tetradentate ligand. The difference being that the one in Type **V** is cyclic while the one in Type **IV** is not. This section will give some representative examples for each type with discussion on their quantum yields.

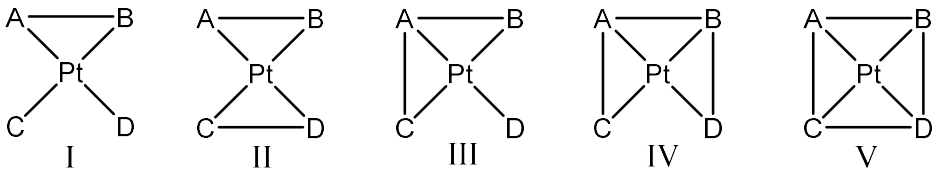

Figure 1.16 Diagram showing five types of coordination modes of Pt(II) complexes.

1.4.1 Type I Complexes

Type **I** complexes are generally non-emissive or only weakly emissive, which could be rationalized with the combination of insufficient ligand strength to push the metal d-d state up high enough, free rotation of the monodentate ligands which opens up non-radiative decay pathways in the excited states and the lability of the monodentate ligands due to the lack of chelation effect. As presented in Figure 1.17, the simple addition of an alkyne linkage between the two phenyl rings almost doubles the quantum yield, which is mainly due to the suppression of k_{nr} (4.8×10^5 s^{-1} and 1.9×10^5 s^{-1} for **1.1** and **1.2**, respectively).[25]

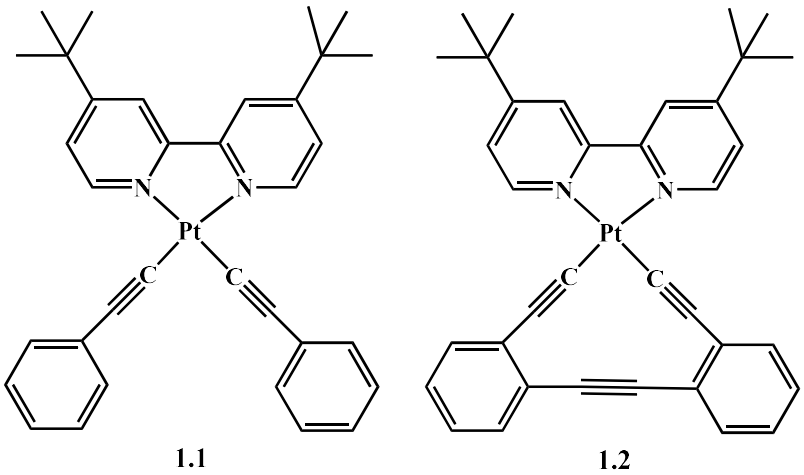

	λ_{max} (nm)	ϕ_P
1.1	562	0.52
1.2	560	0.34

Measured in CH_2Cl_2

Figure 1.17 Chemical structures and photophysical properties of complexes **1.1** and **1.2**.

1.4.2 Type II Complexes

In 2002, Brooks et al. carried out an extensive study on cyclometalated Pt(II) complexes with β-diketonate based ancillary ligands.[20] By introducing different electron donating and accepting groups and heterocycles they successfully tuned the emission color from 456 to 600 nm with quantum yields varying from 0.02-0.25. Compounds **1.3**-**1.5**, together with their emission λ_{max} and Φ_P, are listed in Figure 1.18. As discussed above, emission color can be blue shifted when electron withdrawing group and electron donation group are introduced to the phenyl ring and pyridine, respectively. The luminescence efficiency decrease is likely due to thermal quenching to metal d-d state, as the energy of the LC state gets higher from **1.3** to **1.5**.

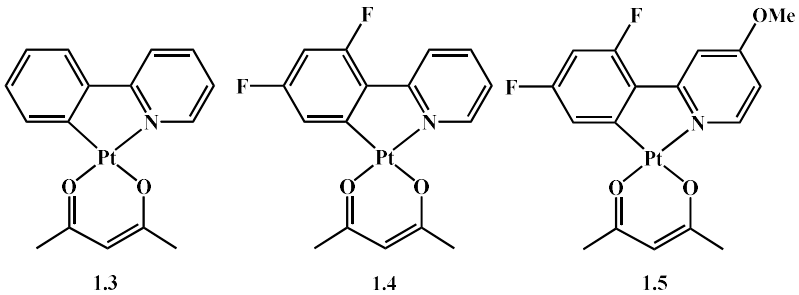

	λ_{max} (nm)	ϕ_P
1.3	486	0.15
1.4	466	0.02
1.5	456	< 0.1%

Measured in 2-Methyltetrahydrofuran

Figure 1.18 Chemical structures and photophysical properties of complexes **1.3**-**1.5**.

Velusamy et al. reported a series of bidentate Pt(II) complexes of lepidine-based ligands with high quantum yields (Figure 1.19).[26] The low Φ_P of **1.10** is mainly due to the distortion caused by the steric interaction between the hydrogens on the lepidine and naphthalene, which is confirmed by its crystal packing diagram. Yellow OLEDs based on **1.8** shows an impressive maximum external quantum efficiency value of 15.21%.

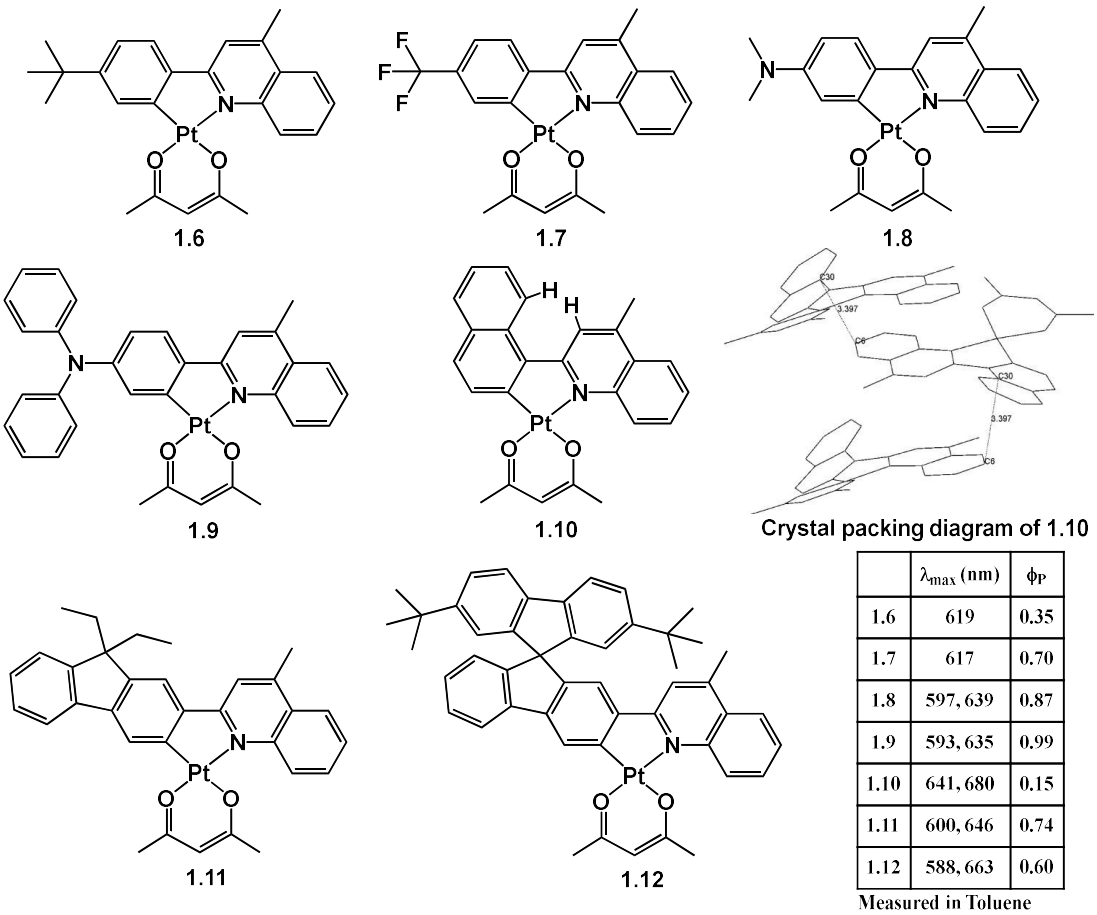

	λ_{max} (nm)	ϕ_P
1.6	619	0.35
1.7	617	0.70
1.8	597, 639	0.87
1.9	593, 635	0.99
1.10	641, 680	0.15
1.11	600, 646	0.74
1.12	588, 663	0.60

Figure 1.19 Chemical structures and photophysical properties of complexes **1.6-1.12**. Inset: The crystal packing diagram of **1.10**.

Zhou et.al attached main group moieties to the para-position of the phenyl ring in **1.3** and systematically studied the photophysical and electroluminescent properties of the resulting

compounds. The structure and photophysical data of four of the compounds are shown in Figure 1.20.[27] One would expect that the attachment of the strongly electron withdrawing SO_2Ph and $POPh_2$ groups would shift the emission energy to shorter wavelength, compared to **1.3**. However, red-shifts of 14-17 nm were observed and rationalized by the stronger stabilization of the LUMO level compared to the HOMO level by the SO_2Ph and $POPh_2$ groups, according to TD-DFT calculation. The substantially smaller Φ_P for **1.13** is due to the little contribution of the Pt d orbital to the HOMO (1%) level as the electron rich NPh_2 group destabilized the ligand LC state.

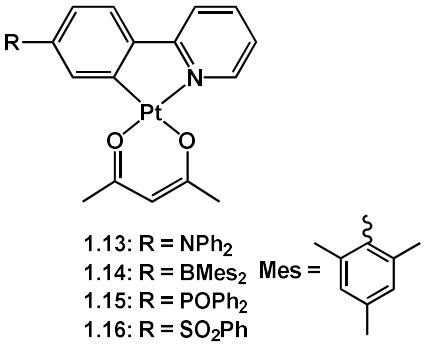

	λ_{max} (nm)	ϕ_P
1.13	540	0.07
1.14	542	0.42
1.15	500	0.93
1.16	503	0.95

Measured in CH_2Cl_2

Figure 1.20 Chemical structures and photophysical properties of complexes **1.13-1.16.**

Unger et al. investigated cyclometalated Pt(II) complexes based on NHCs (Figure 1.21).[21] Again for **1.17-1.19** the decrease of Φ_P with respect to the increase of the emission energy can be explained by thermal quenching via the metal d-d states. The rigid structure of the cyclometalating ligand in **1.19** also contributes to its outstanding Φ_P. OLED devices using **1.19** as emitter have been fabricated with maximum external quantum efficiency of 6.2%.

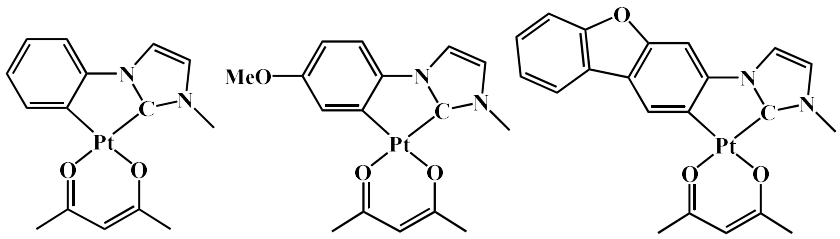

	λ_{max} (nm)	ϕ_P
1.17	416, 441	0.07
1.18	~430, 456	0.32
1.19	463	0.90

In 2% PMMA films

Figure 1.21 Chemical structures and photophysical properties of complexes **1.17-1.19.**

Our group investigated a series of $BMes_2$-functionailzed Pt(II) complexes and four of them are shown in Figure 1.22.[28,29] The position of the $BMes_2$ group has substantial influence on emission energy and quantum efficiency. The higher quantum efficiency of **1.20** compared to **1.14** can be attributed to the synergetic coupling of the electron deficient boron center and pyridine moiety which enhances the mixing of LC and MLCT states. The blueshifted emission energy of **1.22** relative to **1.14** is due to the LUMO level of **1.14** which is more stabilized owing to a larger contribution from the boron group at the position meta to the platinum binding site. Compared to **1.14**, **1.22** is more prone to excimer formation, as the platinum core is less shielded when the $BMes_2$ group is at the para-position to it. The much smaller Φ_P value of **1.23** than that of **1.22** is because the excited state of **1.23** is dominated by ILCT and LLCT transitions with little or no contribution from the $BMes_2$ group. The phosphorescent life time of **1.21** (67.4 μs) is much longer than that of **1.14** (10.2 μs), as the emission of **1.21** is dominated by the intramolecular charge transfer (NPh_2 group to $BMes_2$ group) with very little contribution from Pt center. After optimization, OLEDs based on **1.20** show peak current efficiency, power efficiency and external quantum efficiency of 64.8 cd/A, 79.3 lm/W and 20.9%, respectively, which was the highest at that time.[30] The current density in electron-only device containing **1.20** is 3-4 orders of magnitude

greater than that in device with **1.3**, which clearly demonstrated electron mobility enhancement by the incorporation of triarylboron group.

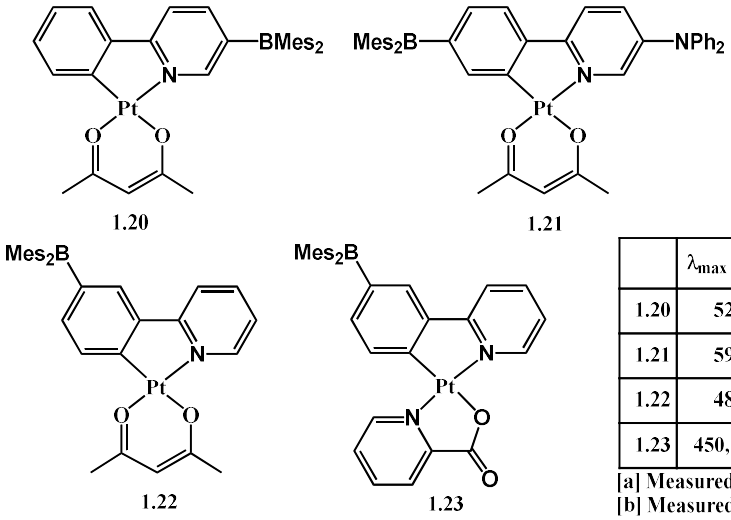

	λ_{max} (nm)	ϕ_P[a]	ϕ_P[b]
1.20	527	0.98	0.57
1.21	596	0.79	0.42
1.22	481	0.43	0.35
1.23	450, 453	0.013	N/A

[a] Measured in CH_2Cl_2
[b] Measured in PMMA films

Figure 1.22 Chemical structures and photophysical properties of complexes **1.20-1.23.**

In 2012, the first examples of $BMes_2$-functionalized Pt(II) compounds using N-heterocyclic carbenes as cyclometalating ligand have been synthesized in our lab (Figure 1.23).[31] EL devices based on **1.24** and **1.25** showed EQE as high as 9.8% and 17.9%, respectively, which was the highest for NHC based Pt(II) compounds.

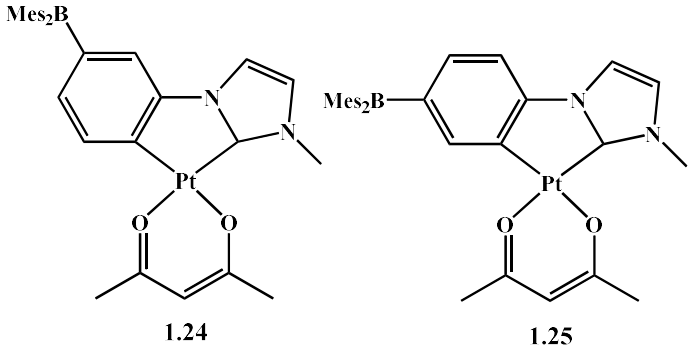

	λ_{max}(nm)	ϕ_P[a]	ϕ_P[b]
1.24	462	0.41	0.86
1.25	478	0.87	0.90

[a] Measured in CH_2Cl_2
[b] Measured in PMMA films

Figure 1.23 Chemical structures and photophysical properties of complexes **1.24** and **1.25**.

1.4.3 Type III Complexes

Che and co-workers have done extensive research on *C^N^N*-coordinated Pt complexes and some of the molecules they made are listed in Figure 1.24.[32-34] The quantum yield of the simple compound **1.26** is very low in dichloromethane. According to DFT calculation, **1.26** undergoes substantial structural distortion after excitation as the two side-arms are non-planar in the optimized T_1 structure, which would lead to a fast nonradiative decay rate.[33] Similarly, the weak luminescence of **1.29** and **1.30** can be attributed to their distorted geometries, at both the ground and excited states, owing to the intramolecular interaction between the hydrogens on the isoquinoline and pyridine and the hydrogen on the quinoline and the chlorine atom, respectively. On the contrary, the planar geometry of **1.27** remains after excitation, giving rise to its small k_{nr} of 2.9×10^4 S^{-1} and high Φ_P of 0.78. The smaller Φ_P of **1.28** (0.10) compared to that of **1.27** is due to its large k_{nr} of 1.3×10^6 s^{-1}. The large non-radiative rate of **1.28** is caused by the structural distortion of the cyclometalating ligand in the excited state where a large amount of electron density is transferred from the naphthalene part to the pyridines. Compound **1.31** has quantum yield reaching unity in dichloromethane solution, which is markably larger than that of **1.32** (0.27). OLED device incorporating **1.31** showed impressive EQE value of 22.1%.[34]

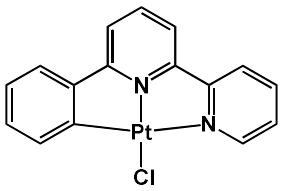

1.26

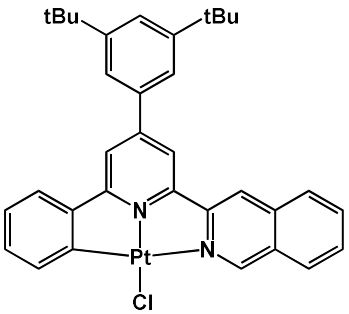

1.27

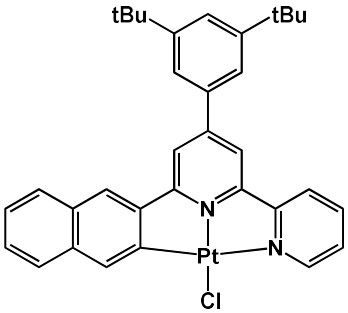

1.28

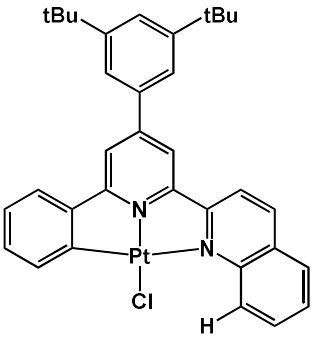

1.29

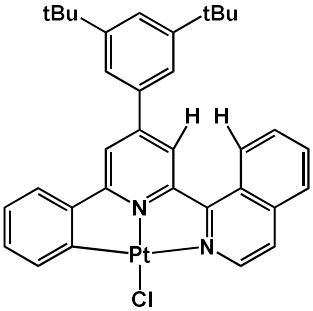

1.30

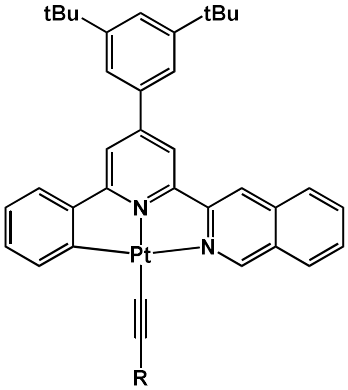

1.31: R = C_6F_5
1.32: R = 4-tolyl

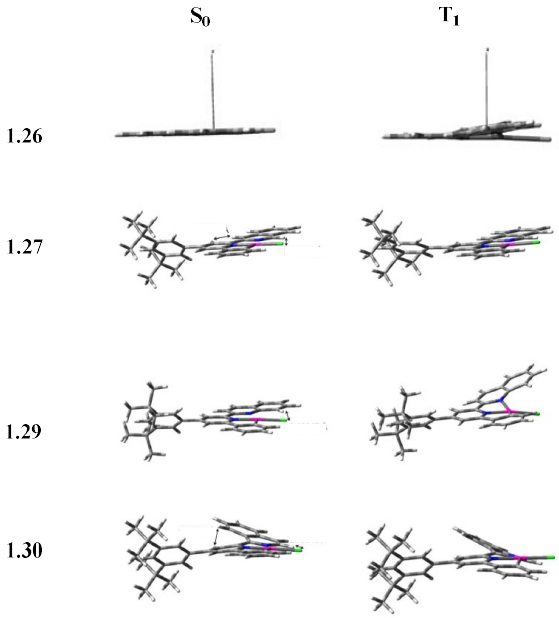

	λ_{max} (nm)	ϕ_P
1.26	565	0.025
1.27	530	0.78
1.28	561	0.10
1.29	624	<0.1%
1.30	621	< 0.1%
1.31	521	0.99
1.32	573	0.27

Measured in CH_2Cl_2

Figure 1.24 Chemical structures and photophysical properties of complexes **1.26-1.32**. Inset: The optimized structure of **1.26**, **1.27**, **1.29** and **1.30** at the ground and first triplet excited state.[33]

Williams et al. have reported a series of cyclometalated Pt(II) complex with *N^C^N* ligands (Figure 1.25).[35-39] Most of this type of tridentate complexes are bright phosphors thanks to their rigid structures. The room temperature emission spectra of **1.4** and **1.35** in dichloromethane are shown in Figure 1.26.[38] The smaller Huang−Rhys factor of **1.35** relative to that of **1.4** is indicative of less structural change going from ground state to excited state, demonstrating the superiority of tridentate ligands over bidentate ligands in structural rigidity. The smaller Φ_P of **1.34** compared to that of **1.33** is a combination of reduced k_r (5.0×10^3 s^{-1} vs. 8.3×10^4 s^{-1}) and increased k_{nr} (2.5×10^5 s^{-1} vs. 5.6×10^4 s^{-1}), implying that the structure of **1.34** is less rigid than **1.33**.[36] Color tuning can be easily achieved via introducing different functionalities onto the cyclometalating ligands. For example, introducing two electron withdrawing fluorine atoms on the central phenyl ring of **1.33** blueshifts the emission energy by 19 nm (**1.35**). With two more electron donating dimethylaminno group on the pyridyl rings of **1.35**, a further 19 nm shift in the blue region is obtained (**1.36**).[37] The quantum efficiency of **1.36** is still as high as 0.6, which suggests the non-radiative metal d-d state is thermally inaccessible. When the monodentate ligand is changed to acetylide, an increase in Φ_P can usually be observed. Compound **1.37** and **1.38** display bright green phosphorescence in dichloromethane solution. The mesityl group in **1.37** greatly inhibits self-quenching via excimer or aggregation formation, leading to an EQE_{max} of 12% in a 5% doped OLED device, which is much better than the EQE_{max} of 5% in the device with 5% **1.38**.[39]

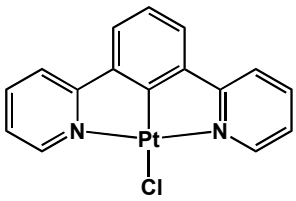

1.33

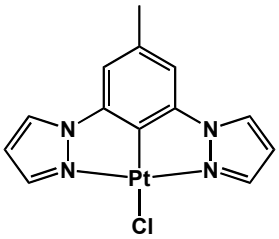

1.34

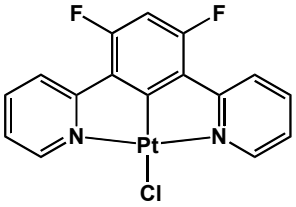

1.35

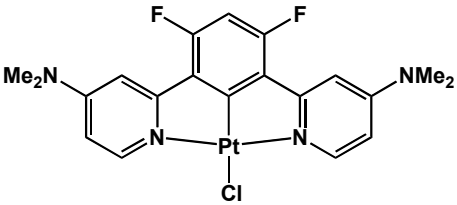

1.36

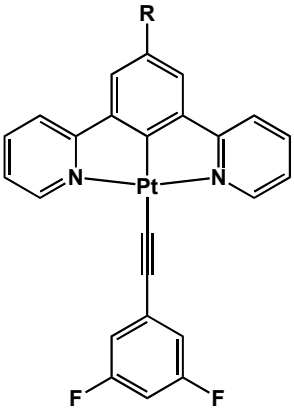

1.37: R = Me
1.38: R = Mes

	λ_{max} (nm)	ϕ_P
1.33	491	0.6
1.34	453	0.02
1.35	472	0.80
1.36	453	0.60
1.37	508	0.77
1.38	500	0.66

Measured in CH_2Cl_2

Figure 1.25 Chemical structures and photophysical properties of complexes **1.33-1.38**.

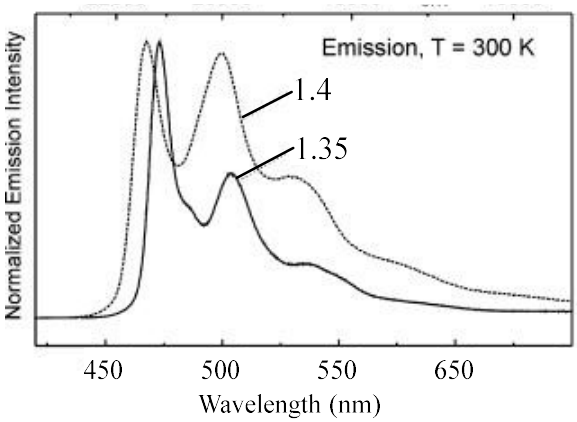

Figure 1.26 Normalized emission spectra of **1.4** and **1.35** in dichloromethane at T=300 K. (adapted from Ref. 38)

Most terdentate Pt(II) complexes reported so far contains two five-membered chelate rings. As a result, the biting angles in those complexes are around 160°, being 20° less compared to that in the ideal square planar complex. In order to release the distortion due to the smaller biting angle, Huo and coworkers synthesized a group of tridentate Pt complexes with one five-membered and one six-membered chelate rings by inserting an amino group between the central ring and one side arm (Figure 1.27).[40-42] The biting angles in compounds **1.39**-**1.43** were successfully enlarged to 170°-175° and very interesting photophysical properties were observed. Compound **1.39** emits at longer wavelength (15 nm) with a slight higher efficiency compared to **1.33**. The Huang-Rhys ratio of **1.39** is larger than that of **1.33**, indicating a larger structural distortion in the excited state. The self-quenching effect of **1.39** is less than that of **1.33**, which is due to the steric hindrance of the N-phenyl ring that is almost perpendicular to the coordination plane.[40] The emission quantum efficiency of **1.40** is much inferior to its counterpart with two five-membered chelate rings, which emits at 487 nm with a Φ_P of 0.64. A possible explanation is the higher emission energy and less rigid structure of **1.40** makes it vulnerable to thermal quenching via the metal d-d state. For the C^N*N type compounds (* means the metallacycle is a six-membered ring), ancillary ligands have a huge impact on their quantum yields. Compounds with chloride ancillary ligand (**1.41a** and **1.42a**) are nearly non-emissive, while those with acetylides (**1.41b** and **1.42b**) display intense emission. The Φ_P of 56% for **1.41b** greatly surpass that of its C^N^N counterpart, which is only 4%.[41] However, the quantum efficiency of the N^N*C complex **1.43** is less than that of the corresponding N^N^C compound **1.44**.[42] The results imply that the use of the 5-6-membered chelate ring system would lead to better square-planar geometry at the cost of losing structural rigidity and reducing ligand field strength, which is not suitable in the design of deep blue emitters.

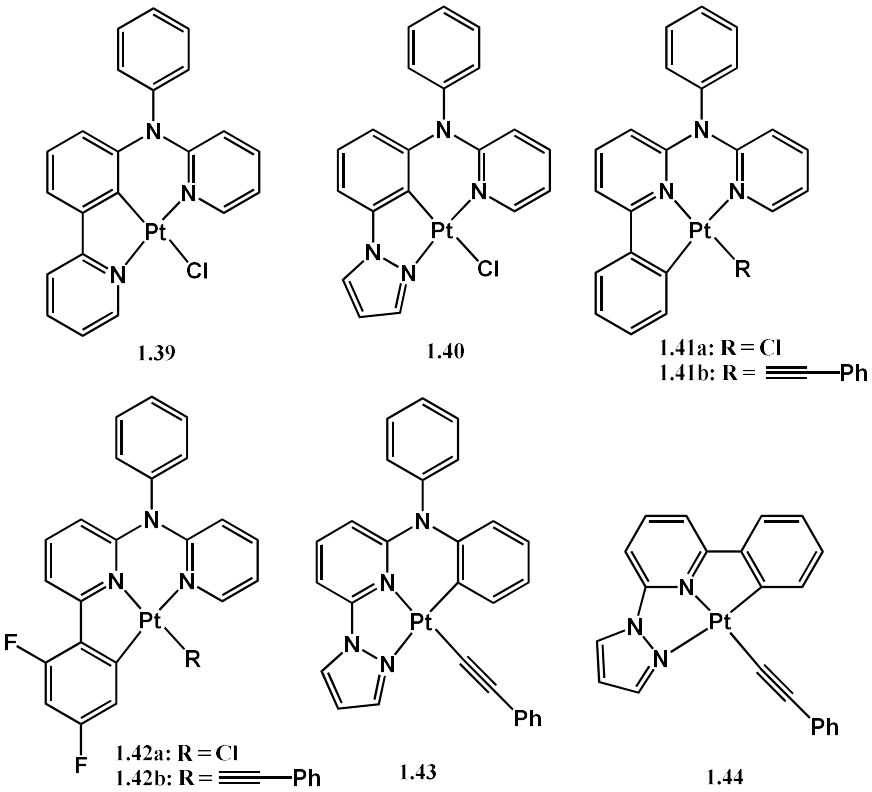

	λ_{max} (nm)	ϕ_P
1.39	506	0.65
1.40	467	0.038
1.41a	non-emissive	
1.41b	492	0.56
1.42a	non-emissive	
1.42b	480	0.22
1.43	521	0.43
1.44	511	0.62

Measured in CH_2Cl_2

Figure 1.27 Chemical structures and photophysical properties of complexes **1.39-1.44**.

Zhang et al. reported C^C^C-coordinated Pt complex **1.45** based on NHCs.[43] While this compound emits in the deep blue region, its quantum efficiency is quite low. DFT calculations revealed that in the first excited state, the chlorine atom bends out of the coordination plane, resulting a C_{aryl}-Pt-Cl angle of 93° (Figure 1.28). Interestingly, this geometric distortion in the excited state might be the reason why **1.45** is surprisingly photostable under ambient conditions, losing only 1% of its initial emission intensity after being continuously irradiated at 355 nm or 6 hours.

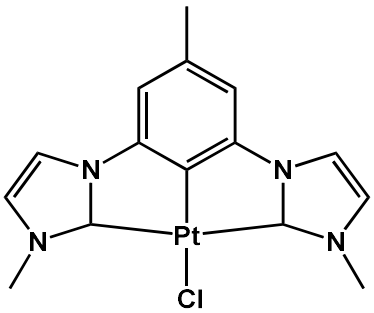

1.45

	λ_{max} (nm)	ϕ_P
1.33	**449, 474**	**0.013**

Measured in MeOH

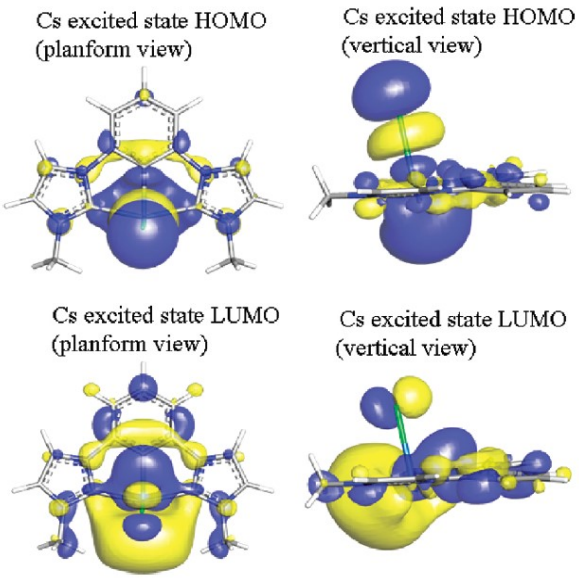

Figure 1.28 Chemical structure, photophysical properties and molecular orbitals of the optimized ground state and excited state of **1.45**.[43]

1.4.4 Type IV Complexes

Che and co-worker prepared various tetradentate O*C*C*O-coordinated Pt complexes (Figure 1.29).[44, 45] The fairly low Φ_P of compounds **1.46-1.48** is mainly due to their bent geometry in the ground state and the symmetry-breaking distortion in the first excited state, which could be attributed to the low rigidity of the 6-6-6-membered chelate ring system.

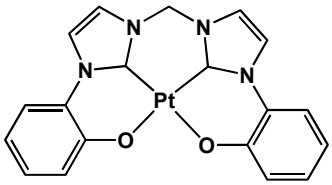

1.46

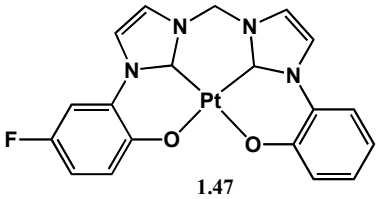

1.47

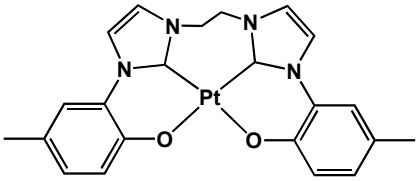

1.48

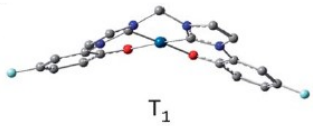

1.47

	λ_{max} (nm)	ϕ_P[a]	ϕ_P[b]
1.46	457[a]/443[b]	0.03	0.29
1.47	443[a]/434[b]	0.18	0.26
1.48	non-emissive		

[a] Measured in THF-DMF(19:1, v/v)
[b] Measured in PMMA films

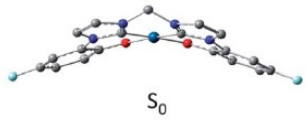

1.47

Figure 1.29 Chemical structures and photophysical properties of complexes **1.46-1.48**. Inset: The optimized structure of **1.47** at the ground and first triplet excited state.[45]

The same group also developed another type of tetradentate Pt complexes with O*N^C^N-coordinating ligands (Figure 1.30).[46-48] The structural rigidity of compounds **1.49-1.51** is improved substantially compared to that of **1.46-1.48**, as indicated by smaller Huang-Rhys ratios and much greater solution quantum yields. The biting angles of O_{phenol}-Pt-C_{aryl} and N-Pt-N are around 175° and 162°, respectively, which resemble those of the tridentate compounds with 5-6-membered rings and 5-5-membered rings. OLED devices with EQE_{max} of 15.55% have been fabricated using **1.49** as emitting material.[47] In another OLED device based on **1.51**, peak current efficiency, power efficiency and external quantum efficiency of 104.2 cd/A, 109.4 lm/W and 27.6%, were achieved.[48]

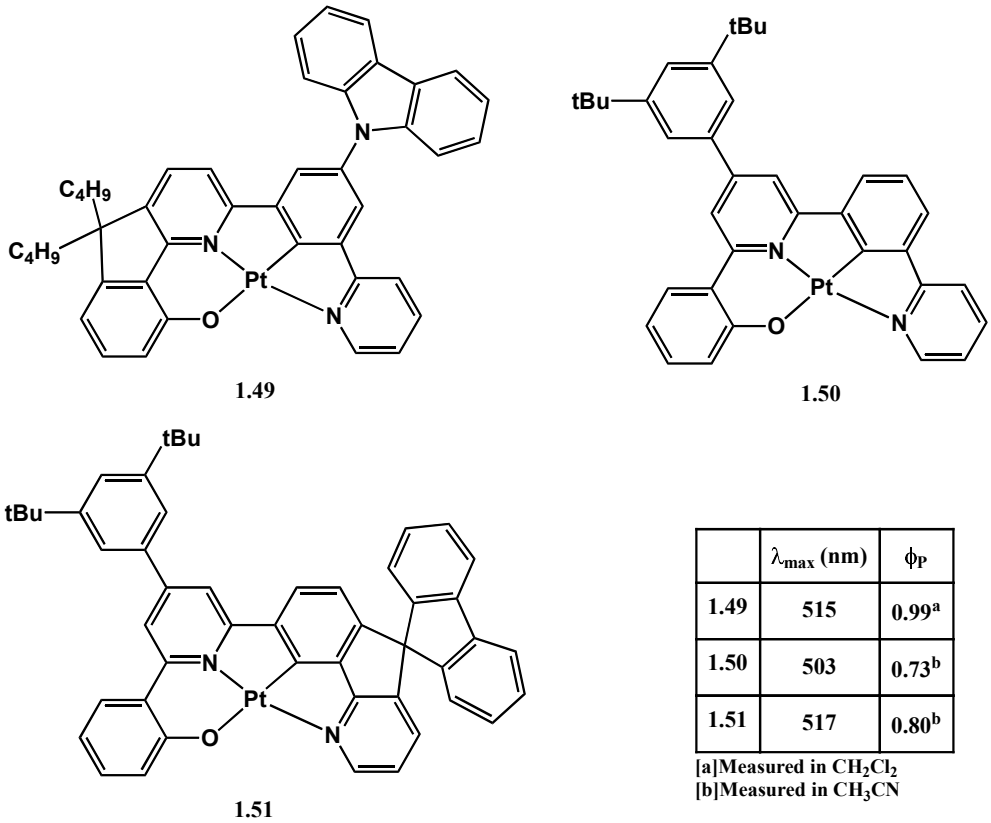

	λ_{max} (nm)	ϕ_P
1.49	515	0.99[a]
1.50	503	0.73[b]
1.51	517	0.80[b]

[a]Measured in CH_2Cl_2
[b]Measured in CH_3CN

Figure 1.30 Chemical structures and photophysical properties of complexes **1.49-1.51**.

Huo and co-workers synthesized tetradentate Pt complexes **1.52-1.55** (Figure 1.31) with C^N*N^C, N^C*C^N and C^C*N^N-coordinating ligands and thoroughly studied their photophysical properties.[49-51] The quantum efficiencies of these compounds generally follow the energy gap law, which states the k_{nr} increases with the decrease of the emission energy. Huang-Rhys ratios of around 0.4 were estimated for **1.52-1.55**, suggesting very small structural displacement in the excited state. Recently, compound **1.56** was utilized as efficient red emitters in OLED devices, giving maximum EQE of 19.3%.[50] It worth noting that the attempt to make **1.57** always gives the corresponding tridentate Pt(II) complex with chlorine atom as the ancillary ligand,

as shown in Scheme 1.1.[51] It is clever that the Huo's group developed the cyclometalating ligand in **1.55** which forces the tetradentate binding mode.

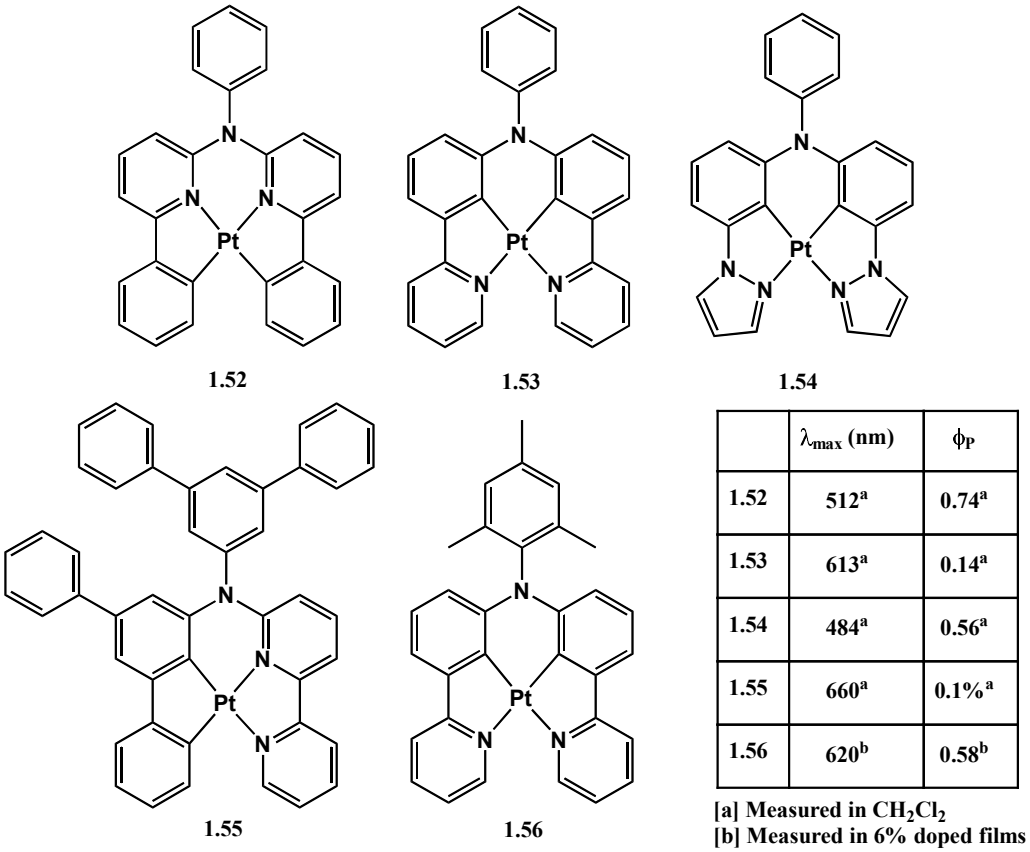

	λ_{max} (nm)	ϕ_P
1.52	512[a]	0.74[a]
1.53	613[a]	0.14[a]
1.54	484[a]	0.56[a]
1.55	660[a]	0.1%[a]
1.56	620[b]	0.58[b]

[a] Measured in CH_2Cl_2
[b] Measured in 6% doped films

Figure 1.31 Chemical structures and photophysical properties of complexes **1.52-1.56**.

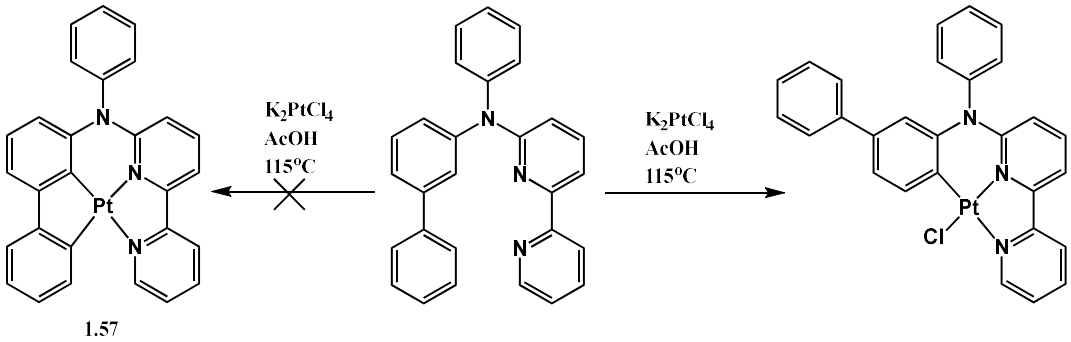

Scheme 1.1 Attempted Synthesis of **1.57** and the observed product.

Li's group reported recently that by using a novel ligand design strategy, highly efficient phosphorescent Pt(II) compounds **1.58-1.60** can be obtained (Figure 1.32).[52-54] Although **1.58** and **1.60** adopt highly twisted conformation, as shown in Figure 1.33, their high photoluminescence quantum yields and low Huang-Rhys ratios indicate their structures are indeed quite rigid and stable.[53] This distorted geometry also reduces intermolecular interactions and excimer formation. An OLED based on **1.58** was reported in 2013 to have maximum external quantum efficiency of 25.2% with CIE coordinates of (0.15, 0.13).[52] In 2014, another OLED containing **1.60** with an EQE_{max} of 24.8% and CIE coordinates of (0.147, 0.079).[53] The molecular plane of **1.59** is much more flat compared to **1.58** and **1.60**, which makes it prone to excimer formation. However, the excimer emission from **1.59** is very efficient and was exploited to make single-doped white OLEDs. A series of white OLED devices with EQE_{max} over 24% were successfully fabricated using **1.59** as the only dopant material.[54]

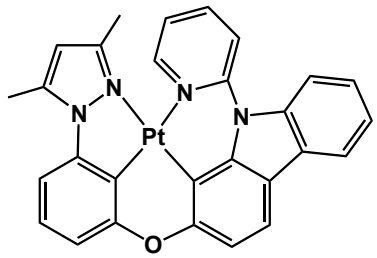

1.58

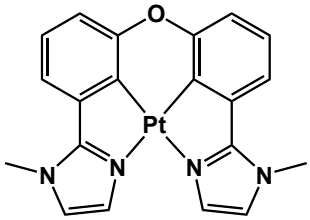

1.59

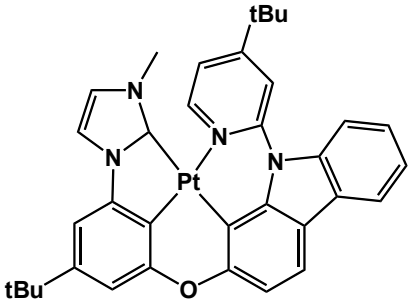

1.60

	λ_{max} (nm)	ϕ_P
1.58	**449**	**0.85**
1.59	**not reported**	
1.60	**446**	**0.91**

Measured in PMMA films

Figure 1.32 Chemical structures and photophysical properties of complexes **1.58-1.60**.

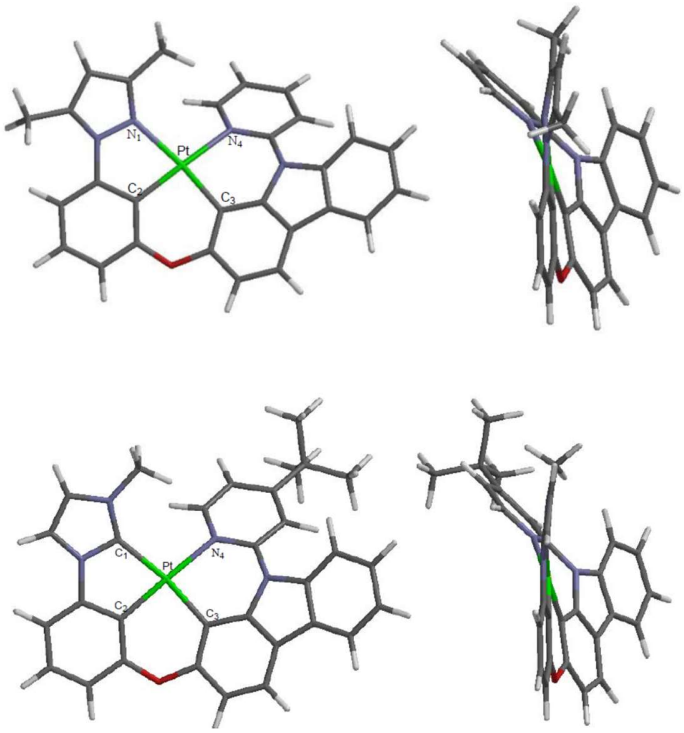

Figure 1.33 Optimized structure of **1.58** (top) and **1.60** (bottom). Left: Top view; Right: Side view. (adapted from Ref. 53)

Chi and co-worker prepared various tetradentate N*N*N*N-coordinated Pt complexes (Figure 1.34).[55] The high Φ_{PL} (0.60 and 0.82) and high emission energy (2.74 eV and 2.69 eV) of compounds **1.61-1.62** make them good candidates as blue emitters in OLED. However, they are prone to excimer formation, as indicated by their crystal structures in Figure 1.34. When the fluorene is replaced with the dihydroacridine in compound **1.63**, excimer emission is reduced substantially, at the cost of redshifted emission energy (2.38 eV). OLED devices based on **1.63** showed maximum external quantum efficiency of 15.3% with CIE coordinates of (0.19, 0.34).

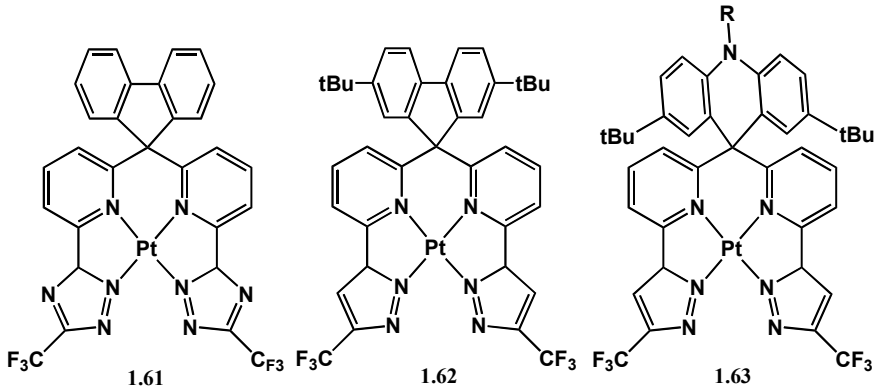

	λ_{max} (nm)	ϕ_P
1.61	452	0.60
1.62	461	0.82
1.63	520	0.88

Measured in CH_2Cl_2

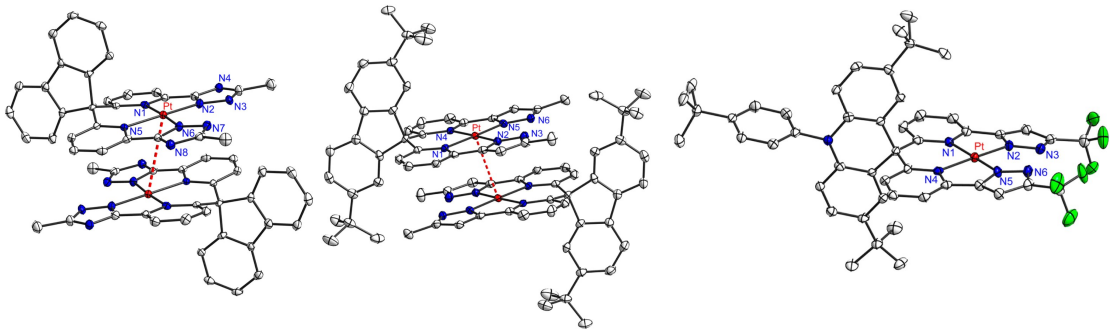

Figure 1.34 Top: Chemical structures and photophysical properties of complexes **1.61-1.63**. Bottom: Crystal structures showing the dimeric packing of **1.61** and **1.62** and that of **1.63**. The fluorine atoms in **1.61** and **1.62** are omitted for clarity. (adapted from Ref. 55)

1.4.5 Type V Complexes

One of the pioneer work in the study of PhOLEDs based on luminescent Pt(II) compounds was reported by Baldo et al. in which a porphyrin based Pt(II) compound **1.64** was used as the emitter (Figure 1.35).[56] **1.64** shows red emission (λ = 650 nm) with high quantum yield (Φ_P=0.6). By doping **1.64** into tris(8-hydroxyquinolinato)aluminium (Alq_3), a maximum external quantum efficiency of 4% was obtained. However, the long decay lifetime (65 us) of **1.64** causes very severe efficiency drop at high exciton density.

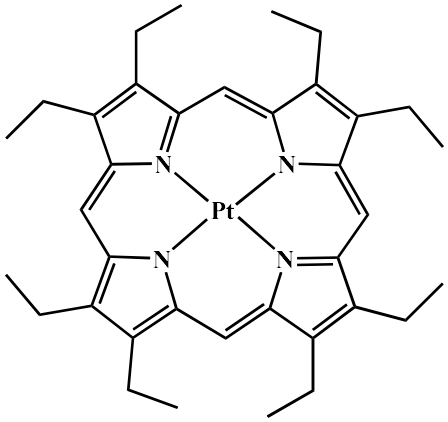

1.64

Figure 1.35 The structure of **1.64**.

Type **V** Pt complexes based on cyclometalating ligands are still missing in scientific reports so far. In this thesis, the syntheses, structures, photophysical and electroluminescence properties of two Type **V** cyclometalated Pt compounds based on macrocyclic ligands will be presented in details.

1.5 Click Chemistry and 1,2,3-Triazoles

The idea of "Click" chemistry, to mimic nature's ability to assemble molecules with complex structures using simple starting materials in an efficient way, was first formally introduced by Sharpless et al. in 2001.[57] "Click" chemistry is composed of several "click" reactions, which by

definition, are chemical reactions that 1) have high yields, 2) are atom efficient, 3) are not oxygen or water sensitive, 4) exhibit high regioselectivity, 5) generate only environmental friendly byproducts (such as water). One of the most well-known "Click" reactions is the Cu(I)-catalyzed azide-alkyne cycloaddition reaction, where 1,4-disubstituted 1,2,3-triazoles with various functional groups can be generated in high yields under mild conditions[58] (Scheme 1.2). When Ru(II) catalyst is used instead of the Cu(I) catalyst, 1,5-disubstituted 1,2,3-triazoles are synthesized regioselectively. Because both acetylene and azide functionalities are easy to introduce, this "click" reaction has been widely used in many areas of chemistry and biochemistry, such as drug delivery[59], medical applications[60] and materials chemistry[61].

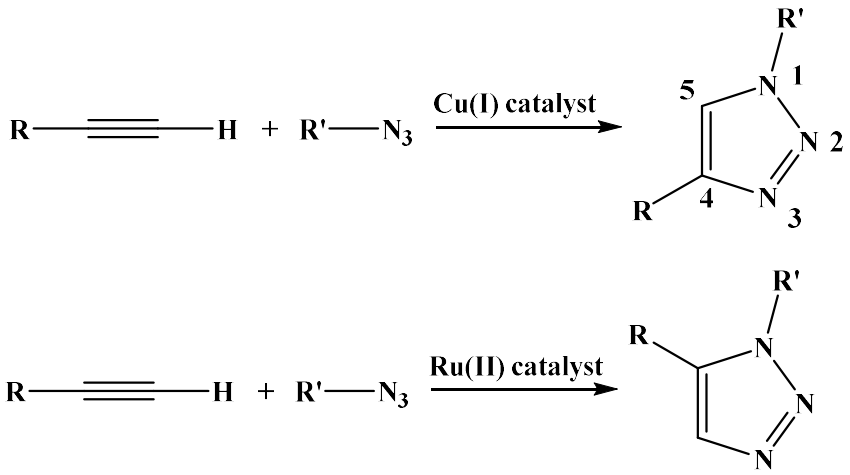

Scheme 1.2 The Cu(I)- and Ru(II)-catalyzed azide-alkyne cycloaddition reaction.

Unlike the 1,2,4-triazoles, which have been extensively studied as either the chelate chromophore or ancillary ligands in phosphorescent organometallic complexes,[62-67] only a few examples with 1,2,3-triazole moieties were reported. Cola et. al. reported the use of pyridyl-1,2,3-triazoyl as the ancillary ligand in cyclometallated Ir(III) complex **1.62**, which emits at 460 nm in CH_2Cl_2 with a Φ_{PL} of 0.32.[68] Schubert et. al. synthesized Ir(III) complex **1.63** and **1.64** with cyclometallating

phenyl-1,2,3-triazoyl chromophores.[69] Compounds **1.63** and **1.64** show weak phosphorescence (Φ_{PL} =0.11 for **1.63**, Φ_{PL}= 0.02 for **1.64**) in degassed CH_2Cl_2 at room temperature, with λ_{max} at 527 nm and 435 nm respectively. Although the quantum efficiency of **1.64** is low, its deep blue emission color indicates that the triplet energy of the phenyl-1,2,3-triazoyl chromophore is high enough for the design of deep blue phosphorescent emitters. To the best of our knowledge, no other group has used phenyl-1,2,3-triazoles as the chelating ligands in phosphorescent cyclometallating Pt(II) complexes, which drives us to evaluate the performance of phenyl-1,2,3-triazole containing Pt(II) complexes in OLEDs.

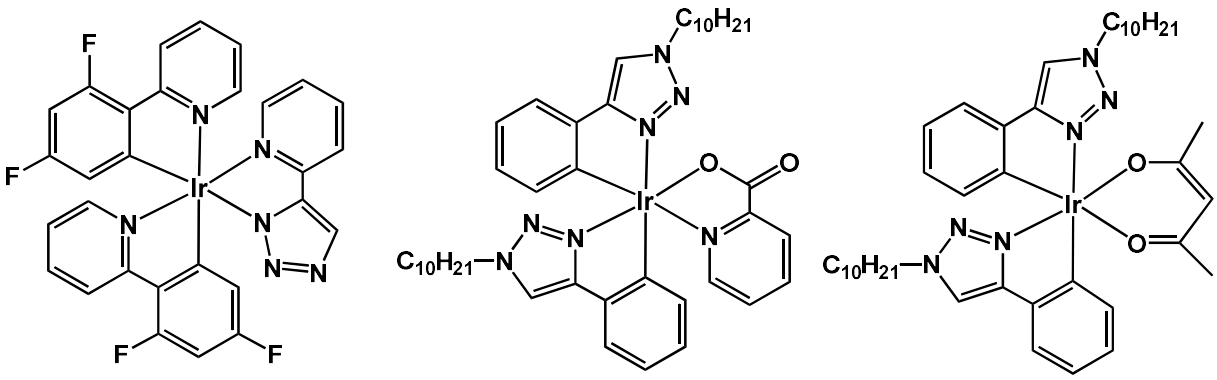

1.62 1.63 1.64

Figure 1.36 Molecular structures of **1.62-1.64**.

1.6 Scope of the Thesis

This thesis describes our approach to achieve highly efficient deep-blue phosphorescent emitters based on cyclometalated platinum compounds bearing 1,2,3-triazole moieties.

Chapter 2 describes the synthesis and characterization of a series of triarylboron-functionalized Pt(II) complexes based on $N^{\wedge}C$-chelate phenyl-1,2,3-triazolyl backbones and acetylacetonate,

picolinate or pyridyl-1,2,4-triazolyl ancillary ligands and their use as emitters in efficient sky blue and white PhOLED devices.

Chapter 3 describes the preparation and photophysical properties of a new kind of Pt(II) compounds with functional groups of various steric and electronic properties. Introduction of the bulky trityl group is found to not only enhance the thermal stability of the molecule but also reduce excimer emission in both photoluminescence and electroluminescence.

Chaper 4 shows that by using tetradentate or macrocyclic cyclometalating ligands the photostability of the corresponding Pt(II) complexes is greatly enhanced as they undergo less structural distortion in the excited state. Bright and efficient deep blue OLEDs based on the macrocyclic complex were successfully fabricated.

1.7 References:

(1) A. Bernanose, M. Comte, P. Vouaux, *J. Chem. Phys.* **1953**, *50*, 64.

(2) M. Pope, H. Kallman, P. Magnante, *J. Chem. Phys*. **1963**, *38*, 2042.

(3) C. W. Tang, S. A. VanSlyke, *Appl. Phys. Lett*. **1987**, *51*, 913.

(4) http://www.oled-info.com/devices last access date: 2016/11/13

(5) http://en.wikipedia.org/wiki/OLED last access date: 2016/11/13

(6) http://en.wikipedia.org/wiki/Comparison_of_CRT,_LCD,_Plasma,_and_OLED last access date: 2016/11/13

(7) D. A. Pardo, G. E. Jabbour, N. Peyghambarian, *Adv. Mater.* **2000**, *12*, 1249.

(8) (a) M. Cocchi, D. Virgili, V. Fattori, D. L. Rochester, J. A. G. Williams, *Adv. Funct. Mater.* **2007**, *17*, 285; (b) N. C. Giebink, B. W. D'Andrade, M. S. Weaver, P. B. Mackenzie, J. J.

Brown, M. E. Thompson and S. R. Forrest, *J. Appl. Phys.* **2008**, *103*, 044509; (c) G. J. Zhou, C. L. Ho, W. Y. Wong, Q. Wang, D. G. Ma, L. X. Wang, Z. Y. Lin, T. B. Marder, A. Beeby, *Adv. Funct. Mater.* **2008**, *18*, 499; (d) Y. You. S. Y. Park, *Dalton Trans.* **2009**, 1267; (e) Y. Chi, P. T. Chou, *Chem. Soc. Rev*. **2010**, *39*, 638, and references therein; (f) C.-L. Ho, W.-Y. Wong, *New. J. Chem*. **2013**, *37*, 1665.

(9) http://www.oled.com/default.asp?contentID=604 last access date: 2016/11/13

(10) Y. Zhang, J. Lee and S. R. Forrest, *Nat. Commun.*, **2014**, *5*, 5008.

(11) K. S. Yook and J. Y. Lee, *Adv. Mater*., **2012**, *24*, 3169.

(12) L. S. Hung, C. H. Chen, *Mater. Sci. Eng. R-Rep.* **2002**, *39*, 143.

(13) http://www.olympusmicro.com/primer/java/jablonski/jabintro/ last access date: 2016/11/13

(14) http://chem.libretexts.org/Core/Physical_and_Theoretical_Chemistry/Fundamentals/Dexter_Energy_Transfer last access date: 2016/11/13

(15) http://ppt.asaha.com/e/energy-and-electron-transfer---columbia-university-w8896-ppt.ppt last access date: 2016/11/13

(16) (a) S. R. Forrest, D. D. C. Bradley and M. E. Thompson, *Adv. Mater.*, **2003**, *15*, 1043; (b) J. A. Gareth Williams, S. Develay, D. L. Rochester and L. Murphy, *Coord. Chem. Rev.*, **2008**, *252*, 2596.

(17) T. Erdem and H. V. Demir, *Nanophotonics*, **2013**, *2*, 57.

(18) http://photonicswiki.org/index.php?title=Fluorescent/Phosphorescent_Dopants last access date: 2016/11/13

(19) J. A. G. Williams, *Top. Curr. Chem.,* **2007**, *281*, 205.

(20) J. Brooks, Y. Babayan, S. Lamansky, P. I. Djurovich, I. Tsyba, R. Bau, M. E. Thompson, *Inorg. Chem.* **2002**, *41*, 3055.

(21) Y. Unger, D. Meyer, O. Molt, C. Schildknecht, I. Münster, G. Wagenblast, T. Strassner, *Angew. Chem. Int. Ed.*, **2010**, *49*, 10214.

(22) J. Li, P. I. Djurovich, B. D. Alleyne, M. Yousufuddin, N. N. Ho, J. C. Thomas, J. C. Peters, R. Bau and M. E. Thompson, *Inorg. Chem.*, **2005**, *44*, 1713.

(23) K. Li, G. S. Ming Tong, Q. Wan, G. Cheng, W.-Y. Tong, W.-H. Ang, W.-L. Kwong and C.-M. Che, *Chem. Sci.*, **2016**, *7*, 1653.

(24) S. Huo, J. Carroll and D. A. K. Vezzu, *Asian J. Org. Chem.*, **2015**, *4*, 1210.

(25) F. Hua, S. Kinayyigit, J. R. Cable and F. N. Castellano, *Inorg. Chem.*, **2006**, *45*, 4304.

(26) M. Velusamy, C.-H. Chen, Y. S. Wen, J. T. Lin, C.-C. Lin, C.-H. Lai and P.-T. Chou, *Organometallics*, **2010**, *29*, 3912.

(27) G. Zhou, Q. Wang, X. Wang, C.-L. Ho, W.-Y. Wong, D. Ma, L. Wang and Z. Lin, *J. Mater. Chem.*, **2010**, *20*, 7472.

(28) Z. M. Hudson, C. Sun, M. G. Helander, H. Amarne, Z.-H. Lu and S. Wang, *Adv. Funct. Mater.*, **2010**, *20*, 3426.

(29) S.-B. Ko, J.-S. Lu, Y. Kang and S. Wang, *Organometallics*, **2013**, *32*, 599.

(30) Z. B. Wang, M. G. Helander, Z. M. Hudson, J. Qiu, S. Wang and Z.-H. Lu. *Appl. Phys. Lett.,* **2011**, *98*, 213301.

(31) Z. M. Hudson, C. Sun, M. G. Helander, Y.-L. Chang, Z.-H. Lu, S. Wang, *J. Am. Chem. Soc.* **2012**, *134*, 13930.

(32) T.-C. Cheung, K.-K. Cheung, S.-M. Peng and C.-M. Che, *J. Chem. Soc., Dalton Trans.*, **1996**, 1645.

(33) G. S.-M. Tong and C.-M. Che, *Chem.-Eur. J.*, **2009**, *15*, 7225.

(34) P.-K. Chow, G. Cheng, G. S. M. Tong, W.-P. To, W.-L. Kwong, K.-H. Low, C.-C. Kwok,

C. Ma and C.-M. Che, *Angew. Chem. Int. Ed.*, **2015**, *54*, 2084.

(35) J. A. G. Williams, A. Beeby, E. S. Davies, J. A. Weinstein and C. Wilson, *Inorg. Chem.*, **2003**, *42*, 8609.

(36) S. Develay, O. Blackburn, A. L. Thompson and J. A. G. Williams, *Inorg. Chem.*, **2008**, *47*, 11129.

(37) L. Murphy, P. Brulatti, V. Fattori, M. Cocchi and J. A. G. Williams, *Chem. Commun.*, **2012**, *48*, 5817.

(38) A. F. Rausch, L. Murphy, J. A. G. Williams and H. Yersin, *Inorg. Chem.*, **2012**, *51*, 312.

(39) E. Rossi, A. Colombo, C. Dragonetti, D. Roberto, R. Ugo, A. Valore, L. Falciola, P. Brulatti, M. Cocchi and J. A. G. Williams, *J. Mater. Chem.*, **2012**, *22*, 10650.

(40) D. A. K. Vezzu, D. Ravindranathan, A. W. Garner, L. Bartolotti, M. E. Smith, P. D. Boyle and S. Huo, *Inorg. Chem.*, **2011**, *50*, 8261.

(41) D. Ravindranathan, D. A. K. Vezzu, L. Bartolotti, P. D. Boyle and S. Huo, *Inorg. Chem.*, **2010**, *49*, 8922.

(42) C. F. Harris, D. A. K. Vezzu, L. Bartolotti, P. D. Boyle and S. Huo, *Inorg. Chem.*, **2013**, *52*, 11711.

(43) X. Zhang, A. M. Wright, N. J. DeYonker, T. K. Hollis, N. I. Hammer, C. E. Webster and E. J. Valente, *Organometallics*, **2012**, *31*, 1664.

(44) K. Li, X. Guan, C.-W. Ma, W. Lu, Y. Chen and C.-M. Che, *Chem. Commun.*, **2011**, *47*, 9075.

(45) K. Li, G. Cheng, C. Ma, X. Guan, W.-M. Kwok, Y. Chen, W. Lu and C.-M. Che, *Chem. Sci.*, **2013**, *4*, 2630.

(46) S. C. F. Kui, P. K. Chow, G. Cheng, C.-C. Kwok, C. L. Kwong, K.-H. Low and C.-M. Che,

Chem. Commun., **2013**, *49*, 1497.

(47) G. Cheng, P.-K. Chow, S. C. F. Kui, C.-C. Kwok and C.-M. Che, *Adv. Mater.*, **2013**, *25*, 6765.

(48) G. Cheng, S. C. F. Kui, W.-H. Ang, M.-Y. Ko, P.-K. Chow, C.-L. Kwong, C.-C. Kwok, C. Ma, X. Guan, K.-H. Low, S.-J. Su and C.-M. Che, *Chem. Sci.,* **2014**, *5*, 4819.

(49) D. A. K. Vezzu, J. C. Deaton, J. S. Jones, L. Bartolotti, C. F. Harris, A. P. Marchetti, M. Kondakova, R. D. Pike, S. Huo, *Inorg. Chem.* **2010**, *49*, 5107.

(50) H. Fukagawa, T. Shimizu, H. Hanashima, Y. Osada, M. Suzuki and H. Fujikake, *Adv. Mater.*, **2012**, *24*, 5099.

(51) S. Huo, C. F. Harris, D. A. K. Vezzu, J. P. Gagnier, M. E. Smith, R. D. Pike and Y. Li, *Polyhedron*, **2013**, *52*, 1030.

(52) X.-C. Hang, T. Fleetham, E. Turner, J. Brooks, J. Li, *Angew. Chem. Int. Ed.*, **2013**, *52*, 6753.

(53) T. Fleetham, G. Li, L. Wen, J. Li, *Adv. Mater.* **2014**, *26*, 7116.

(54) T. Fleetham, L. Huang, J. Li, *Adv. Funct. Mater.* **2014**, *24*, 6066.

(55) K.-Y. Liao, C.-W. Hsu, Y. Chi, M.-K. Hsu, S.-W. Wu, C.-H. Chang, S.-H. Liu, G.-H. Lee, P.-T. Chou, Y. Hu and N. Robertson, *Inorg. Chem.*, **2015**, *54*, 4029.

(56) M. A. Baldo, D. F. O'Brien, Y. You, A. Shoustikov, S. Sibley, M. E. Thompson and S. R. Forrest, *Nature*, **1998**, *395*, 151.

(57) H. C. Kolb, M. G. Finn, K. B. Sharpless, *Angew. Chem. Int. Ed.,* 2001, *40*, 2004.

(58) V. V. Rostovtsev, L. G. Green, V. V. Fokin, K. B. Sharpless, *Angew. Chem., Int. Ed.,* **2002**, *41*, 2596.

(59) K. S. Anseth and H.-A. Klok, *Biomacromolecules*, **2016**, *17*, 1.

(60) K. E. Beatty, F. Xie, Q. Wang and D. A. Tirrell, *J. Am. Chem. Soc.*, **2005**, *127*, 14150.

(61) J.-F. Lutz, *Angew. Chem. Int. Ed.*, **2007**, *46*, 1018.

(62) C.-F. Chang, Y.-M. Cheng, Y. Chi, Y.-C. Chiu, C.-C. Lin, G.-H. Lee, P.-T. Chou, C.-C. Chen, C.-H. Chang and C.-C. Wu, *Angew. Chem. Int. Ed.*, **2008**, *47*, 4542.

(63) S.-C. Lo, C. P. Shipley, R. N. Bera, R. E. Harding, A. R. Cowley, P. L. Burn and I. D. W. Samuel, *Chem. Mater.*, **2006**, *18*, 5119.

(64) C.-H. Yang, S.-W. Li, Y. Chi, Y.-M. Cheng, Y.-S. Yeh, P.-T. Chou, G.-H. Lee, C.-H. Wang and C.-F. Shu, *Inorg. Chem.*, **2005**, *44*, 7770.

(65) E. Orselli, G. S. Kottas, A. E. Konradsson, P. Coppo, R. Fröhlich, L. De Cola, A. van Dijken, M. Büchel and H. Börner, *Inorg. Chem.*, **2007**, *46*, 11082.

(66) Q. Wang, I. W. H. Oswald, M. R. Perez, H. Jia, B. E. Gnade and M. A. Omary, *Adv. Func. Mater.*, **2013**, *23*, 5420.

(67) Q. Wang, I. W. H. Oswald, M. R. Perez, H. Jia, A. A. Shahub, Q. Qiao, B. E. Gnade and M. A. Omary, *Adv. Func. Mater.*, **2014**, *24*, 4746.

(68) E. Orselli, R. Q. Albuquerque, P. M. Fransen, R. Frohlich, H. M. Janssen and L. De Cola, *J. Mater. Chem.*, **2008**, *18*, 4579.

(69) B. Beyer, C. Ulbricht, D. Escudero, C. Friebe, A. Winter, L. González and U. S. Schubert, *Organometallics*, **2009**, *28*, 5478.

Chapter 2

Achieving Bright Blue Phosphorescent Pt(II) Compounds with Triarylboryl-Functionalized Cyclometallating Phenyl-1,2,3-Triazole Ligands

2.1 Introduction

As mentioned in Chapter 1, one of the greatest bottlenecks in the research and the development of organic light emitting diodes (OLEDs) is to get efficient blue phosphorescent emitters with long lifetime. To date, the most studied blue phosphorescent emitters are based on cyclometalated or N^N chelated Ir(III) complexes.[1-7] To achieve blue color, the electron withdrawing fluorine atoms are commonly introduced on the aryl rings to stabilize the highest occupied molecular orbital (HOMO) of the molecule, and are known to reduce OLED device stabilities, likely caused by defluorination during the device fabrication and operation.[8,9] The use of pyridyl-triazolyl or phenyl-N-heterocyclic carbene (NHC) chelate chromophores with the proper choice of ancillary ligands has led to some fluorine-free, highly efficient deep-blue phosphorescent Ir(III) emitters.[7,10] Compared to the extensive research on blue phosphorescent Ir(III) compounds, blue phosphorescent Pt(II) compounds remain much rarer, probably due to their susceptibility towards excimer formation and intermolecular quenching owing to the flat molecular structure.[11-17] Another disadvantage of Pt(II) based emitters compared to Ir(III) ones is their slower spin-orbit coupling rates, which results in smaller radiative decay rates and lower phosphorescent quantum efficiency or longer triplet lifetimes.[18] However, phosphorescent Pt(II) compounds do possess several unique properties, including a large ligand field splitting energy and a highly tunable emission energy via MLCT and LC states. For the same chelate chromophore, the Pt(II)

compounds usually emit at a much higher energy than the corresponding Ir(III) compounds, which is beneficial for the design of deep blue emitters.[14-15, 17]

Recently, our group found a way to address the problems with Pt(II) emitters. By introducing a bulky electron-deficient dimesitylboron ($BMes_2$) group, the phosphorescent quantum efficiency of the phenylpyridine (ppy)[15,19] or phenyl-*N*-heterocyclic carbene[16] chelated Pt(II) acetylacetonates (acac) and their performance in OLEDs can be greatly improved (Figure 2.1). This drastic improvement could be attributed to the suppression of excimer formation, the greater mixing of MLCT and ^{3}LC states, and the electron transporting ability of the triarylboron unit in the $BMes_2$-functionalized compounds.[19a] For the $BMes_2$-phenylpyridine system (Bppy), bright phosphorescent Pt(II) compounds with emission maxima ranging from 470-650 nm and excellent quantum yields (0.06-0.95) are achieved and used in the fabrication of OLEDs with maximum external quantum efficiency (EQE) over 20%.[15,19] For the $BMes_2$-phenylcarbene chelate system (Bcc), highly efficient blue and blue-green phosphorescent Pt(II) compounds have been obtained and used in high-performance OLEDs.[16] However, the difficulty to further shift the emission of Pt-Bppy compounds to the blue region and the sophisticated synthetic steps and the low stability of the Pt-Bcc compounds render their limited use in blue OLEDs.

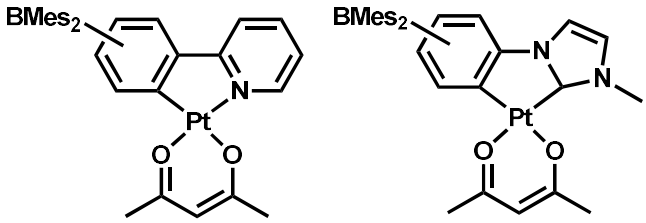

(Bppy)Pt(acac) (Bcc)Pt(acac)

Figure 2.1 Structures of dimesitylboron-functionalized Pt(II) acetylacetonates synthesized in our group.

Therefore, we initiated the investigation on new boron-containing ligands that have high triplet energy and are easy to synthesize. We found that $BMes_2$-functionalized phenyl-1,2,3-triazole ligands (Bptrz) can lead to bright blue phosphorescent C^N chelate (Bptrz)Pt(X^Y) compounds with the appropriate choice of the ancillary ligand X^Y. Compared to the Bcc chelate ligands and their Pt(II) complexes, the new Bptrz chelate ligands and their Pt(II) compounds are much simpler to prepare. In addition, we have observed that the ancillary ligands and the substituent groups have a huge impact on the emission color and the quantum efficiency of the Bptrz-Pt complexes. Further, we have found that intramolecular hydrogen bonds play a key role in determining the stereochemistry of this system. Finally, greenish blue and white electroluminescent devices have been fabricated with EQE as high as 24.0% and 15.6%, respectively.

The Pt(II) compounds we synthesized can be divided into three classes according to the ancillary ligands (Figure 2.2). In the first class (**2.1-2.3**), acac is the ancillary ligand, in the second class (**2.4-2.7**), picolinate (pic) or substituted picolinate is the ancillary ligand, and in the third class (**2.8-2.11**), 3-(2-py)-1,2,4-triazolyl (pytrz) or substituted pytrz acts as the ancillary ligand. For the acac and pic series, both *para* and *meta*-$BMes_2$ functionalized ligands ***p*-BtrzBn**, ***m*-BtrzBn** and ***m*-BtrzAd** were used in order to examine the impact of the $BMes_2$ location on emission color. For the pytrz series, we focused on the *meta*-ligands, ***m*-BtrzBn** and ***m*-BtrzAd** only since their Pt(II) chelates are blue phosphorescent. The introduction of the various substituent groups was intended to reduce excimer formations and tune the emission energy.

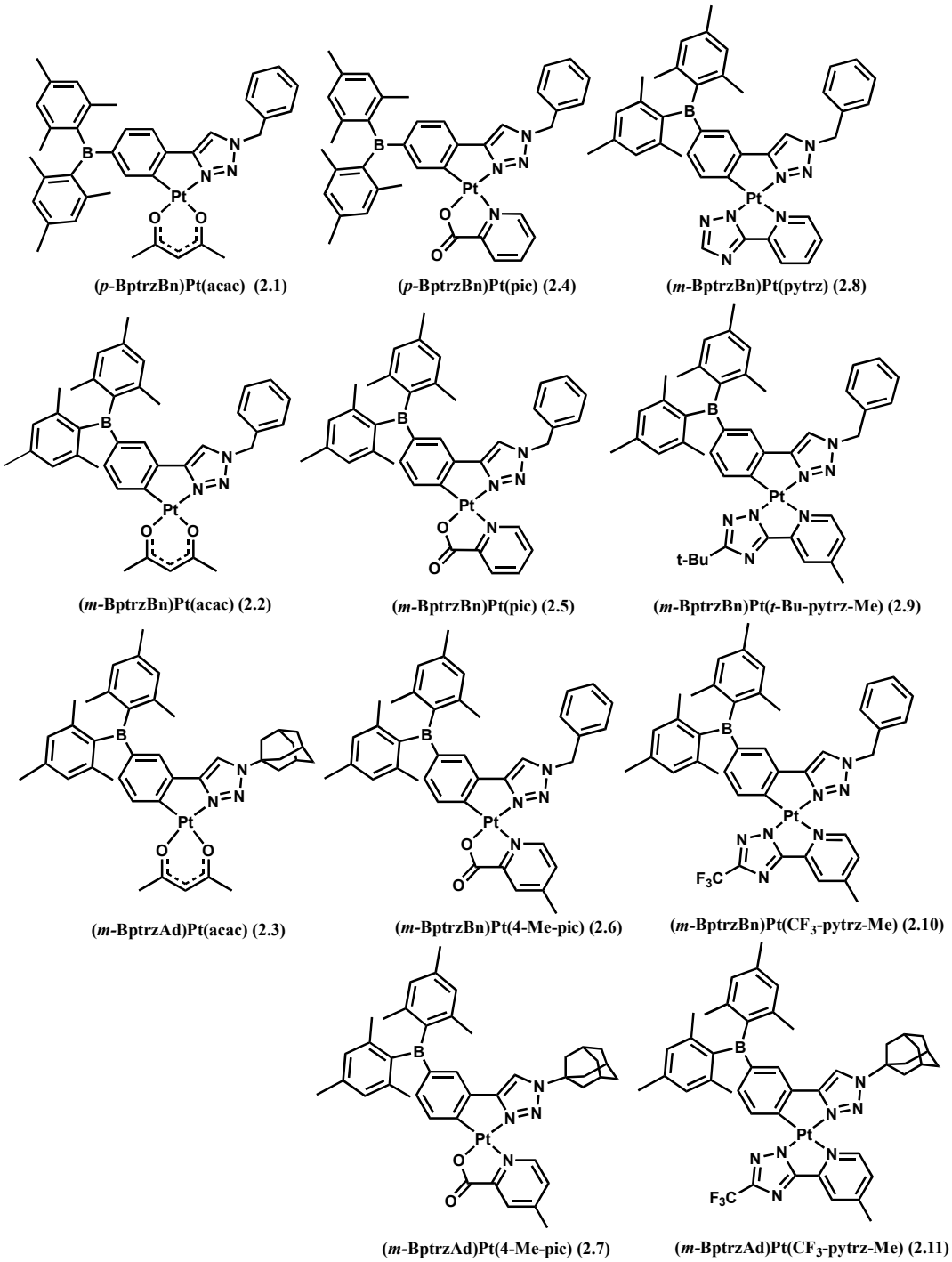

Figure 2.2 Structures of $BMes_2$-functionalized phenyl-1,2,3-triazole chelated Pt(II) compounds described in this chapter.

2.2 Results and Discussion

2.2.1 Synthesis

Ligand ***p*-BptrzBn** was synthesized by the Cu(I) catalyzed click coupling reaction between (4-ethynylphenyl)dimesitylborane and benzyl azide in CH_2Cl_2 at ambient temperature (Scheme 2.1). Diisopropylethylamine (DIPEA) was used as the base, $[Cu(CH_3CN)_4]PF_6$ along with a stabilizing ligand tris[(1-benzyl-1*H*-1,2,3-triazol-4-yl)methyl]amine (TBTA) were used as the catalyst. Similar reactions between (3-ethynylphenyl)dimesitylborane and benzyl azide or adamantyl azide led to ligands ***m*-BptrzBn** and ***m*-BptrzAd**, respectively. The introduction of the adamantyl group is based on the consideration of its sterically more demanding nature may reduce phosphorescent quenching via intermolecular interactions. The isolated yields of the new ligands are about 70-72%.

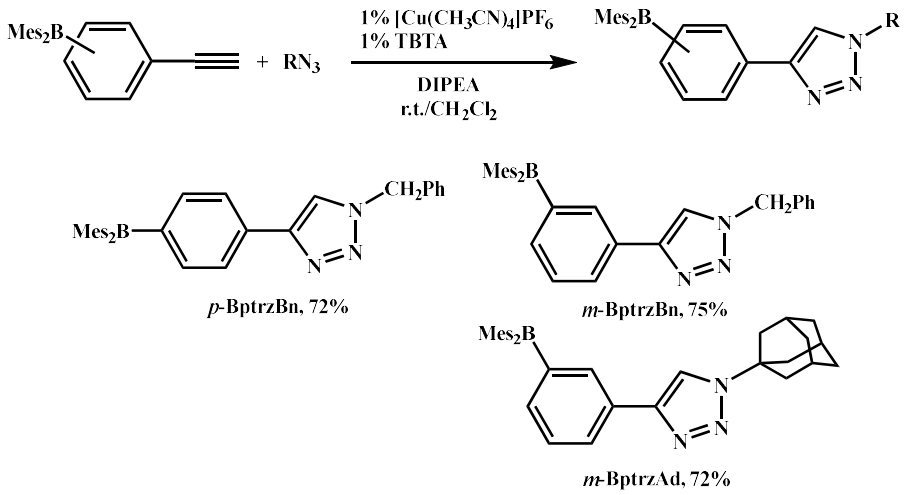

Scheme 2.1 Synthetic procedures for $BMes_2$-functionalized ligands.

The Pt(II) compounds were synthesized by a one-pot procedure developed by our group.[24] This procedure involved first the reaction of the **Bptrz** ligand with $[PtMe_2(SMe_2)]_2$ in hot acetone, followed by the addition of TsOH and the subsequent addition of Na(acac) or Na(pytrz) for compounds that use acac or pytrz or its derivatives as the ancillary ligand (Scheme 2.2 and 2.4).

Hot acetone was used instead of room temperature THF in the Pt-Bppy system because 1,2,3-trizole is a weaker σ-donor compared to pyridine, thus requiring higher temperature to overcome the energy barrier. For compounds that use picolinate as the ancillary ligand, picolinic acid can be added directly without the use of TsOH (Scheme 2.3). This simple one-pot procedure led to the isolation of the Pt(II) compounds as powdery solid in 19-30% yields. All Pt(II) compounds have been fully characterized by NMR and elemental analyses.

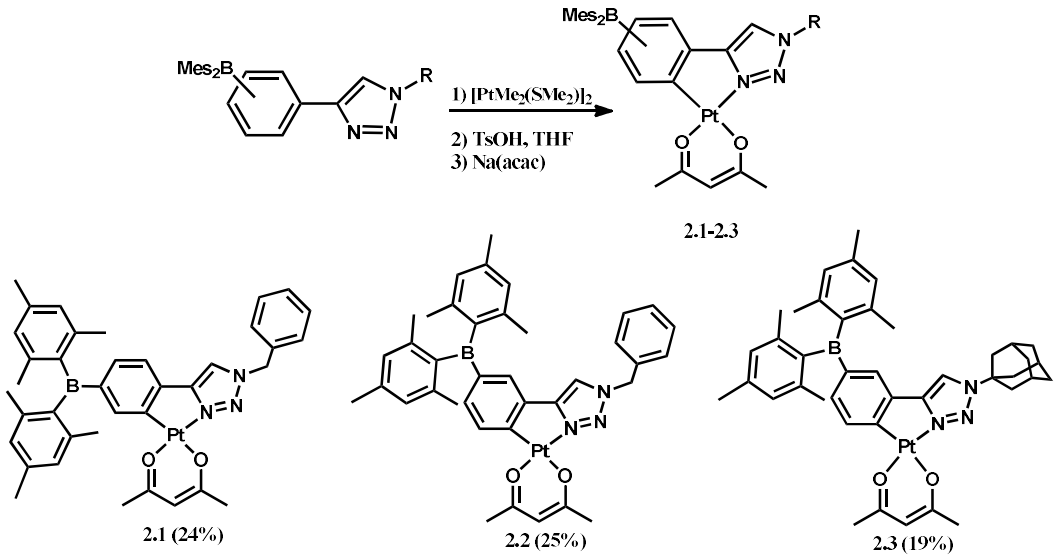

Scheme 2.2 Synthetic procedures and molecular structures of **2.1-2.3**.

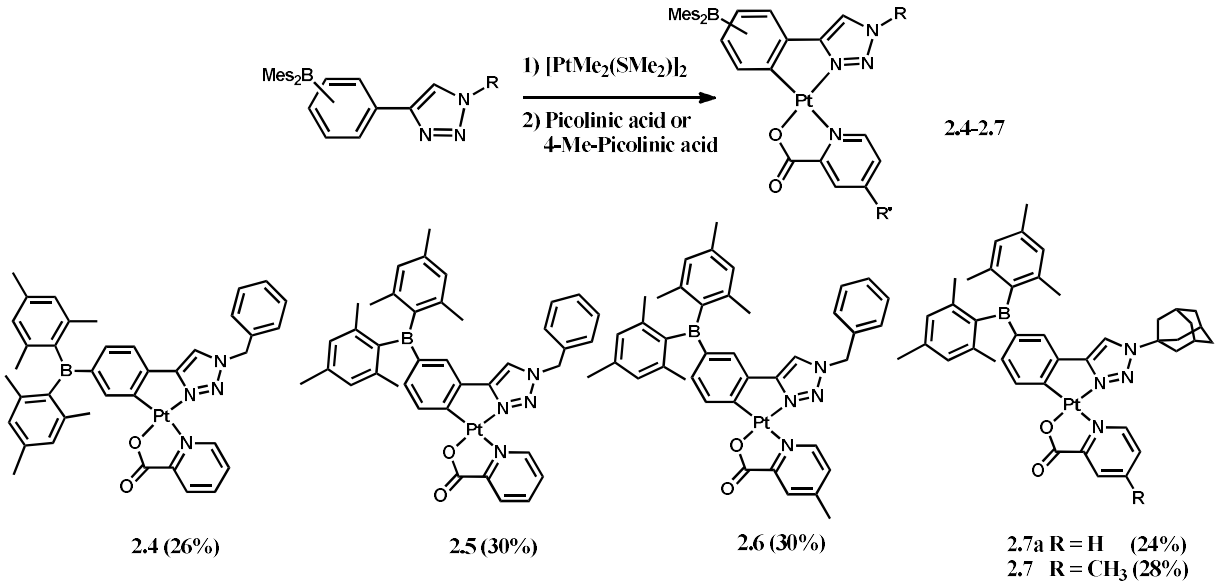

Scheme 2.3 Synthetic procedures and molecular structures of **2.4-2.7**.

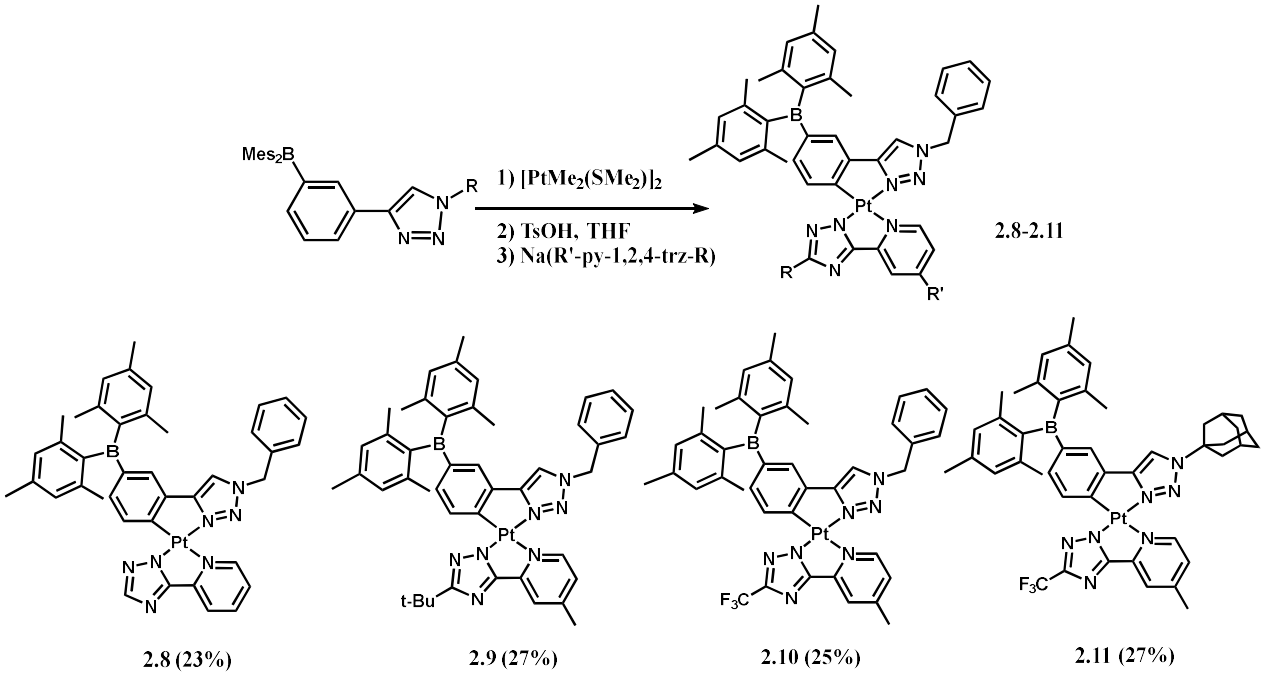

Scheme 2.4 Synthetic procedures and molecular structures of **2.8-2.11**.

2.2.2 Structures

The stereochemistry of all Pt(II) compounds were determined by NMR spectroscopic analyses. For the Pt-pic compounds **2.4-2.7** and Pt-pytrz compounds **2.8-2.11**, two geometric isomers *trans* and *cis*, as defined in Chart 2.1, are possible. ^{1}H NMR studies established that the **2.4-2.7** adopt the *cis* structure exclusively, which is in sharp contrast to the previously reported Pt(Bppy)(pic) compounds which only exhibit the *trans* form.[25] For the Pt-pytrz molecules, only the *trans* isomer was observed. The *trans* isomers of compounds **2.8-2.11** have two possible isomers, namely the N^1-*trans* and N^4-*trans* isomers, because of the tautomerism of the 1,2,4-triazole group. For previously reported metal compounds with the py-1,2,4-trz ligand, both N^1-chelate and N^4-chelate mode were observed.[26] For compound **2.8**, the N^4-*trans* isomer was found to be the major product at the early stage of the reaction while the N^1-*trans* isomer was the major product at the end of the reaction. Both N^1-*trans* and N^4-*trans* isomers of **2.8** were isolated and fully characterized by ^{1}H and 2D NMR spectroscopy (Figure 2.3-2.5), while for compounds **2.9-2.11**, the N^1-*trans* isomer was the major product while the amount of the N^4-*trans* isomer was too small to be isolated.

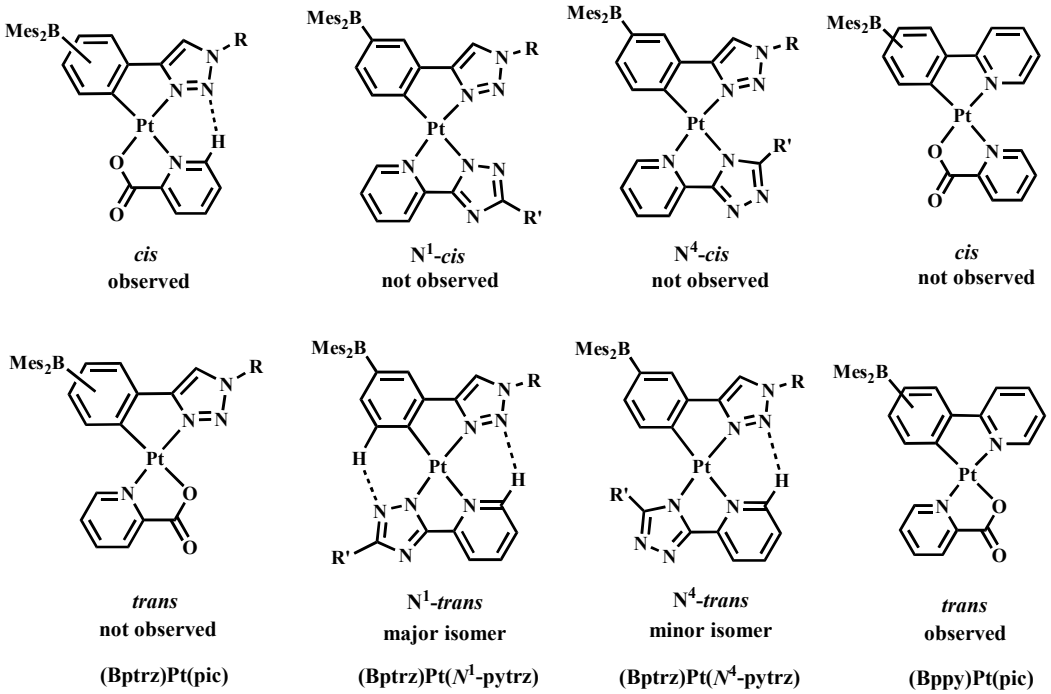

Chart 2.1 Structural isomers of (C^N)Pt(X^Y) compounds

Two determining factors of the preferential formation of the structural isomers of the Pt(II) compounds are *trans* influence and intramolecular H bonds. For the (Bppy)Pt(pic) compounds, the *trans* isomer is favored to avoid the stronger pyridyl donor of the pic ligand to be *trans* to the phenyl donor that has the strongest *trans* influence. In contrast, for (Bptrz)Pt(pic) compounds **2.4-2.7**, the *cis* isomer is favored because the intramolecular H bond between the 1,2,3-triazolyl and the pyridyl groups. The formation of the intramolecular hydrogen bond not only provides a greater stability by "linking" the C^N and N^N ligands together in the *cis* isomer but also eliminates the steric interaction between the phenyl and pyridyl hydrogens (next to the binding carbon and nitrogen atoms) in the *trans* isomer. In the ^{1}H NMR spectra of compounds **2.4-2.7**, the hydrogen atom next the pyridyl nitrogen has a chemical shift of about 9.5 ppm, which is significantly down-fielded compared to that of (Bppy)Pt(pic) compounds (8.96-9.14 ppm), supporting the *cis* structure. For the (Bptrz)Pt(pytrz) compounds **2.8-2.11**, although the *trans* influence would favor the *cis*

structure in which the two weak triazolyl donors are *cis* to each other, the formation of hydrogen bond which favors the *trans* structure clearly dominates, as none of **2.8-2.11** takes the *trans* structure. The N^4- *trans* isomer of **2.8-2.11** is less favored than the N^1-*trans* isomers because it lacks one intramolecular hydrogen bond and has the unfavorable steric interactions between the R' group of the 1,2,4-trz ring and *o*-H atom of the phenyl ring, compared to the N^1-*trans* isomer. The formation of the N^4-*trans* isomer decreases substantially as the size of the R' group increases, which explained the isolated yields of the N^4-*trans* isomer of **2.8-2.11**. The formation of two intramolecular hydrogen bonds in the N^1-*trans* isomer of **2.8-2.11** is supported by the observation of the much down-field shifted signal of the H^1 atom of the phenyl ring (~9.1 ppm) and that of the py ring of the pytrz ligand (~9.5-9.8 ppm) in the ^{1}H NMR spectra.

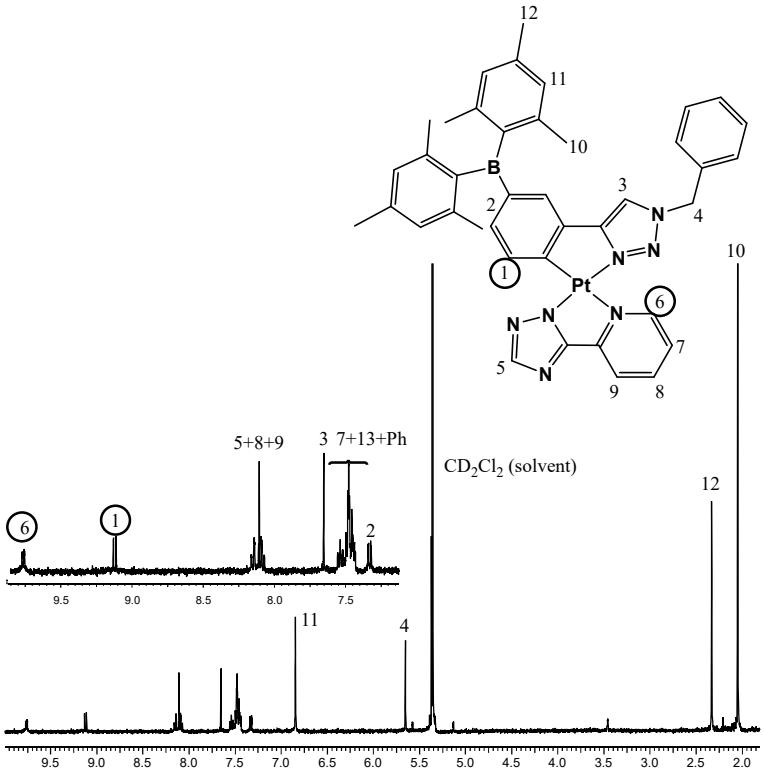

Figure 2.3 ^{1}H NMR spectrum of N^1-*trans* isomer of **2.8** in CD_2Cl_2.

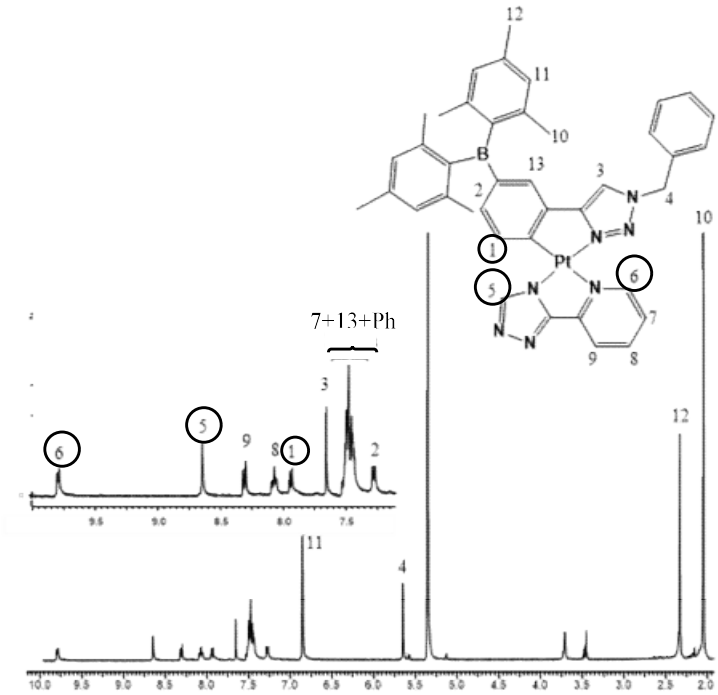

Figure 2.4 ^{1}H NMR spectrum of the *N*^{4}*-trans* isomer of **2.8** in CD_2Cl_2.

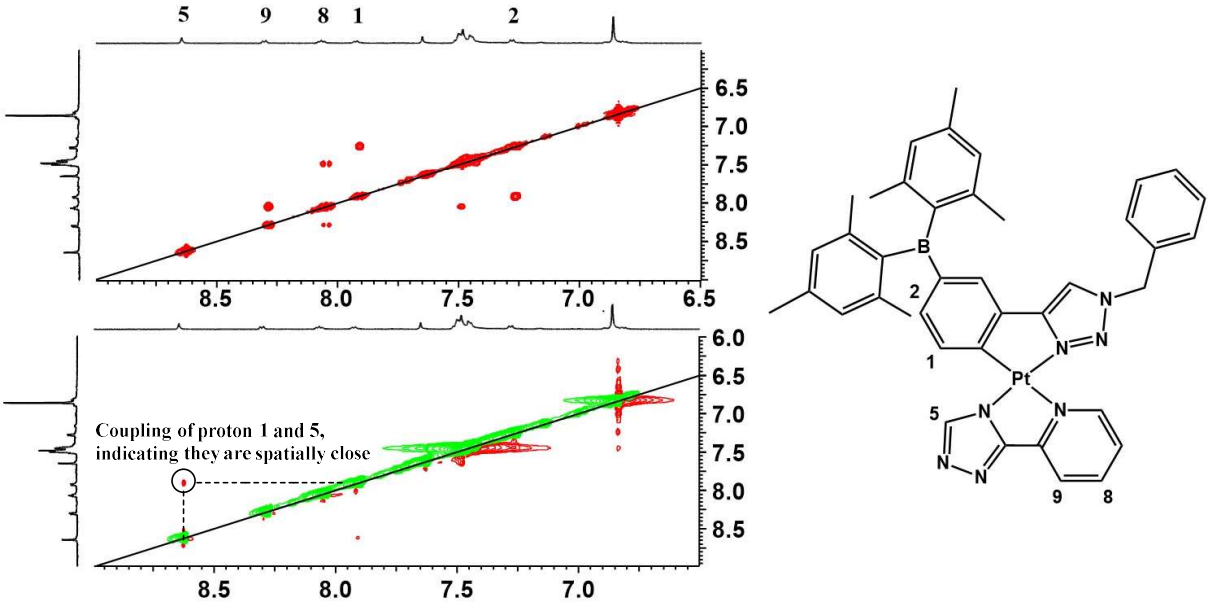

Figure 2.5 Top left: COSY NMR spectrum of of the *N*^{4}*-trans* isomer of **2.8** in CD_2Cl_2. Bottom left: ROESY NMR spectrum of the *N*^{4}*-trans* isomer of **2.8** in CD_2Cl_2.

To further establish the structural features and to examine the impact of different chromophores, different ancillary ligands and different substituent groups on intermolecular interactions of the Pt(II) compounds in the solid state, the crystal structures of **2.1**, **2.4-2.6**, **2.7a**, and **2.8-2.10** were examined by single-crystal X-ray diffraction analyses. **2.7a** is an analogue of **2.7** but without the methyl group on the pyridyl ring of the ancillary ligand. Efforts to obtain single crystals of the N^4-*trans* isomer of compound **2.8** were unsuccessful. All structures except **2.5** and **2.8**, are shown in Figure 2.6-2.10. Pt-ligand bond lengths for all compounds are summarized in Table 2.1 along with the Pt···Pt separation distances and the shortest intermolecular π stacking distances involving the central core of the Pt compounds.

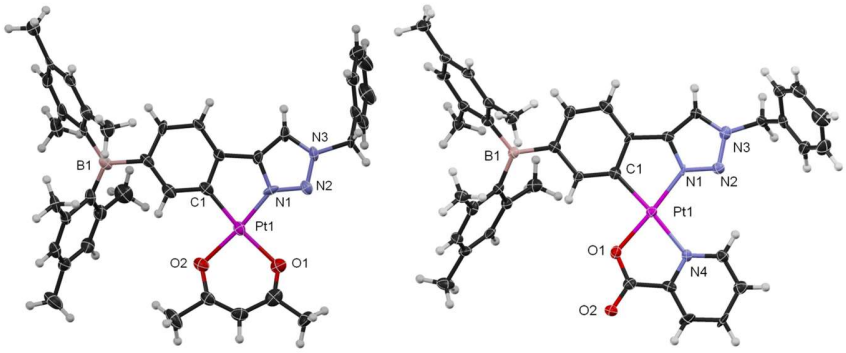

Figure 2.6 Crystal structures of **2.1** (left) and **2.4** (right) with 35% thermal ellipsoids and labeling schemes for key atoms.

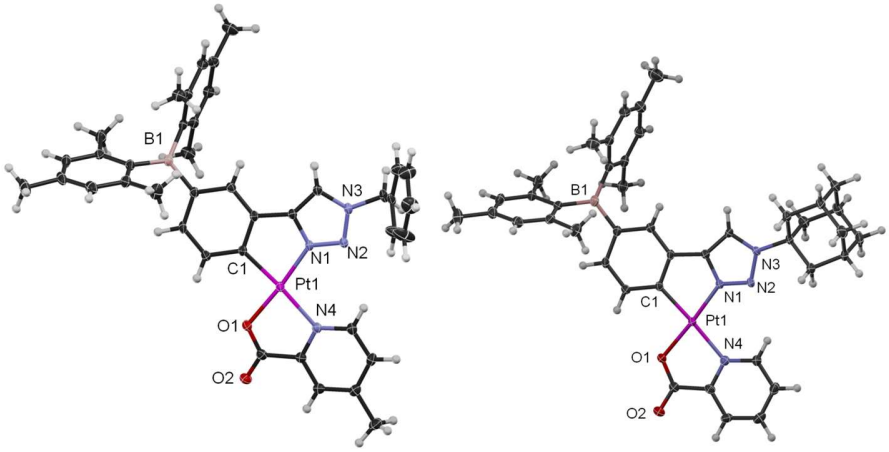

Figure 2.7 Crystal structures of **2.6** (left) and **2.7a** (right) with 35% thermal ellipsoids and labeling schemes for key atoms.

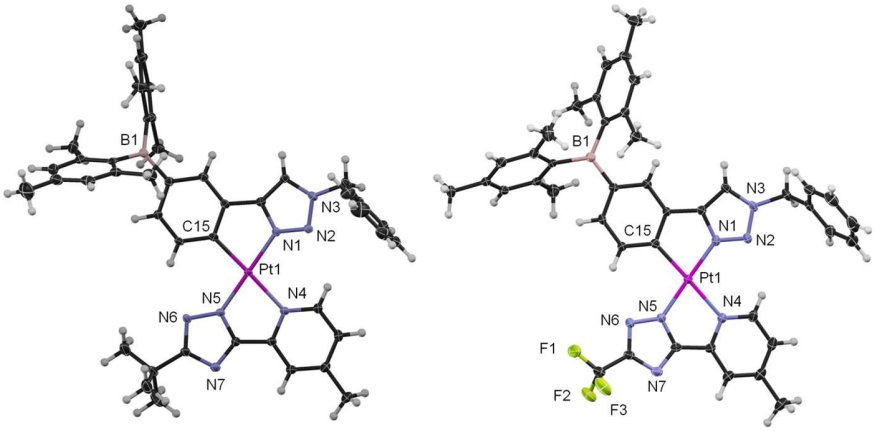

Figure 2.8 Crystal structures of **2.9** (left) and **2.10** (right) with 35% thermal ellipsoids and labeling schemes for key atoms.

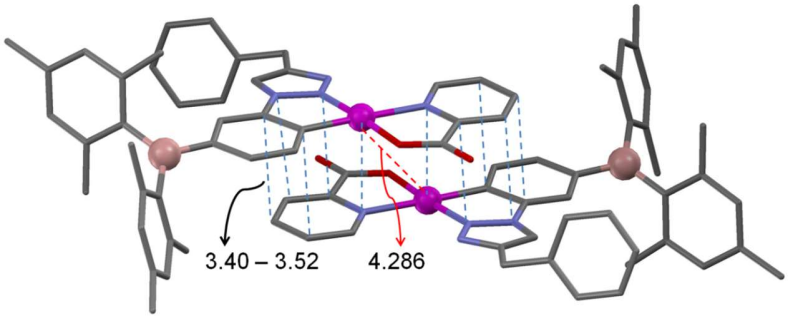

(a)

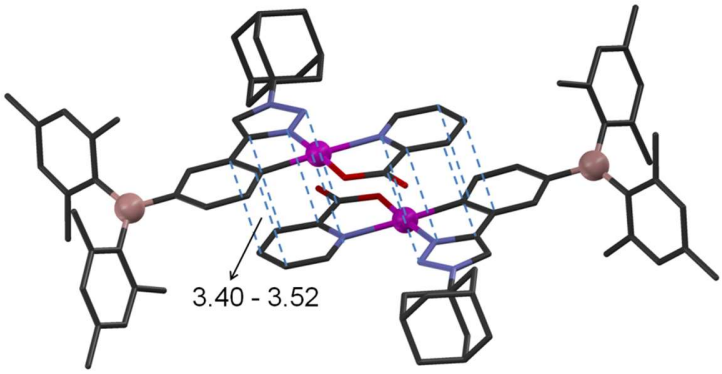

(b)

Figure 2.9 (a): A diagram showing the π-stacked dimer of **2.5** in the crystal lattice. (b): A diagram showing the π-stacked dimer of **2.7a** in the crystal lattice.

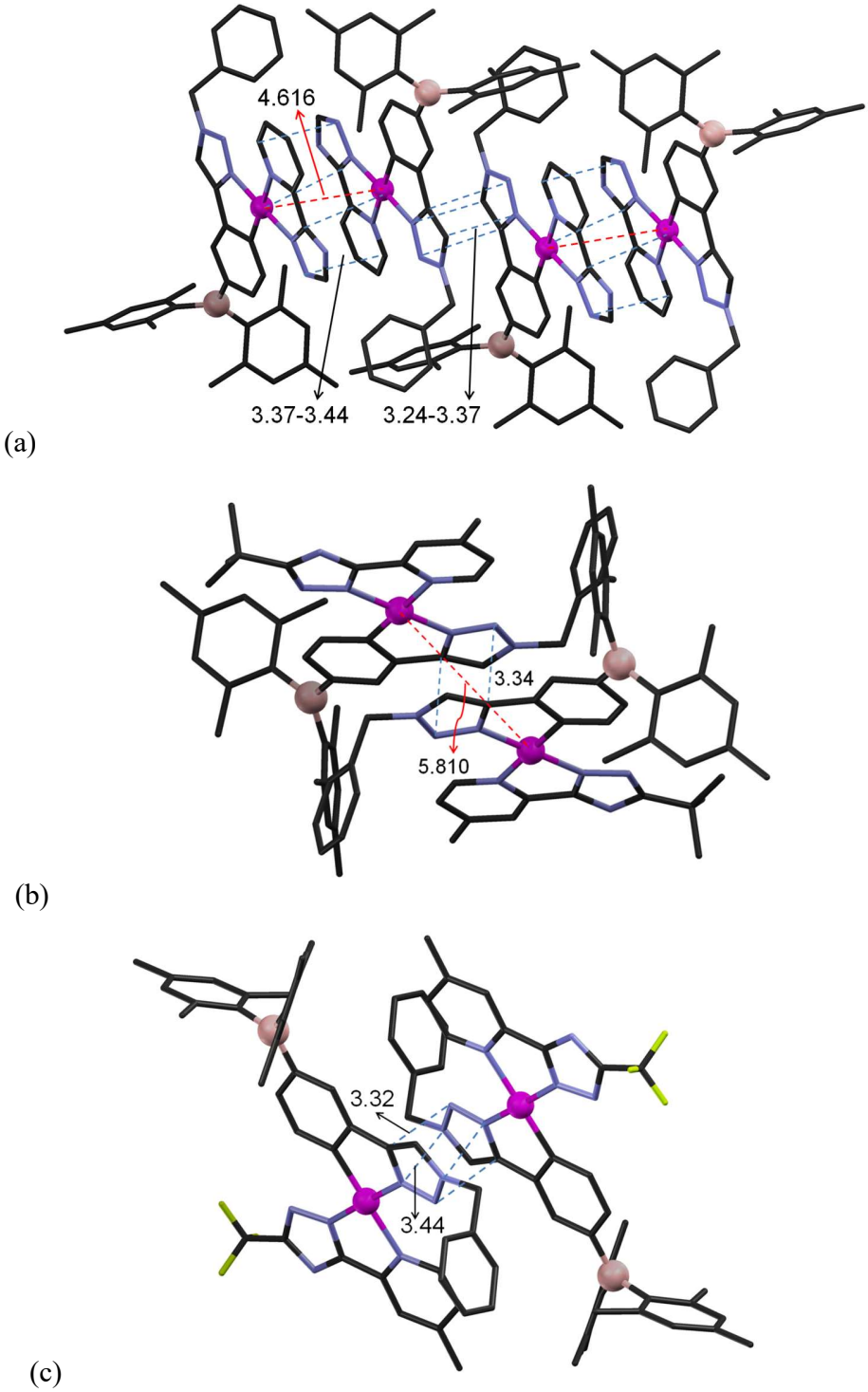

Figure 2.10 (a) A diagram showing the 1D extended π-stacking interactions of **2.8** in the crystal lattice. (b): A diagram showing the π-stacked dimer of **2.9** in the crystal lattice. (c): A diagram showing the π-stacked dimer of **2.10** in the crystal lattice.

Table 2.1 Key bond lengths and short contact distances (Å)

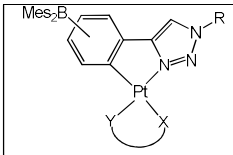	Pt-C	Pt-N (C^N)	Pt-X (dative)	Pt-Y (covalent)	Pt···Pt	Shortest π stacking distance of the central core
2.1	1.980(2) 1.980(2)	1.998(12) 2.000(2)	2.057(13) 2.028(14)	1.998(12) 1.935(12)	6.517(1) 6.320(1)	3.20(1), 3.51(1)
2.4	2.003(10) 2.004(10)	1.979(8 2.003(8))	2.107(8) 2.113(8)	2.034(7) 2.019(7)	4.143(1) 4.402(1)	3.44(1), 3.46(1) 3.48(1), 3.52(1)
2.5	2.000(3)	1.972(3)	2.099(3)	2.023(2)	4.286(1)	3.40(1), 3.52(1)
2.6	1.988(3)	1.980(2)	2.102(2)	2.009(2)	4.912(1)	3.34(1), 3.40(1)
2.7a	1.998(3)	1.976(3)	2.097(3)	2.012(2)	4.209(1)	3.46(1), 3.48(1)
2.8	2.002(7)	2.002(6)	2.129(6)	1.987(6)	4.616(1)	3.24(1), 3.37(1) (1D stacking)
2.9	2.003(4)	2.004(3)	2.147(3)	1.996(3)	5.810(1)	3.34(1), 3.53(1)
2.10	2.007(5)	1.999(4)	2.134(4)	1.995(4)	6.029(1)	3.32(1), 3.44(1)

2.2.2.1 Structural Isomers

As shown in Figure 2.7-2.10, the (Bptrz)Pt(pic) compounds indeed have the *cis*-structure while the major isomers of the (Bptrz)Pt(pytrz) compounds have the N^1-*trans* structures. The (C^N)Pt(N^O) and (C^N)Pt(N^N) central units in all compounds are planar. The crystal structures demonstrate that the *cis*-structure of (Btrz)Pt(pic) compounds and the N^1-*trans*-structure of the (Bptrz)Pt(pytrz) compounds are indeed favored by the formation of intramolecular H bonds. The intramolecular N(2)···H_{py} distances (Figure 2.6-2.7) in (Bptrz)Pt(pic) compounds **2.4**-**2.7a** range from 3.26 to 3.37 Å, adequate for the formation of an H bond between the triazoyl nitrogen atom and the proton of the pyridyl ring. The intramolecular N(2)···H_{py} distances (Figure 2.8 and 2.10) in the (Btrz)Pt(pytrz) compounds **2.8**-**2.10** are similar to those of (Bptrz)Pt(pic), ranging from 3.21

to 3.28 Å. Interestingly, however, the N(6)···H_{ph} distances in the (Bptrz)Pt(pytrz) compounds are much shorter (3.14 to 3.18 Å) than the corresponding N(2)···H_{py} distances in the same compounds. This may be attributed to the longer Pt(1)-N(4) bond, (2.129-2.147 Å), compared to the Pt(1)-N(5) bond (1.986 – 1.996 Å), caused by the strong *trans* influence of the carbon donor and the covalent nature of the Pt(1)-N(5) bond compared to the dative nature of the Pt(1)-N(4) bond.

2.2.2.2 Intermolecular Interactions

The location of the $BMes_2$ group, the ancillary ligands, and the substituent groups do have a significant impact on intermolecular interactions. For example, **2.1** and **2.4** that have a similar molecular shape but with two different ancillary ligands display distinctively different intermolecular interactions. The Pt···Pt separation distances are much greater in **2.1** (6.320, 6.517Å) than **2.4** (4.143, 4.402 Å). In addition, molecules of **2.4** form partially stacked dimers with π-stacking interactions between the pic ligand and the Bptrz chelate while the molecules of **2.1** do not have π-stacking interactions in the crystal lattice, although some short contact distances are observed between the acac and the Bptrz chelate ligand. This supports that the acac ligand is much less prone to intermolecular interactions, compared to the pic ligand. Based on the crystal structural data, both pic and pytrz ancillary ligands have a high tendency to form π-stacked dimers or 1D extended π-stacking structures in the crystal lattice, as illustrated by the stacking diagrams of **2.5, 2.7a**, **2.8**, **2.9** and **2.10** in Figure 2.9 and 2,10. This observation is not surprising since both pic and pytrz are flat chelate ligands with aryl rings. Compound **2.8** is the only molecule that displays extended 1D-parallel π stacking among all the molecules we examined in this work. The π-stacking interactions for all other molecules are limited to discrete dimmers. The introduction of a

substituent group on the ancillary ligand has been found to greatly diminish the extent of π stacking. For example, the introduction of a methyl on the pyridyl ring and a *t*-butyl group or CF_3 group on the 1,2,4-triazoyl ring reduces the 1D π-stacking in the lattice of **2.8** to dimer π-stacking only in **2.9** and **2.10**, accompanied by the substantial increase of the Pt···Pt separation distances. Another interesting aspect is that the π-stacking in the (Bptrz)Pt(pytrz) compounds always occurs between the same ligand, i.e. pytrz-pytrz stacking or Bptrz-Bptrz stacking (Figure 2.10b and 2.10c), involving mostly the trz ring. The replacement of the benzyl group on the Bptrz ligand by an adamantyl group does not appear to alter the π-stacking pattern, as evidenced by the similar π-stacked dimers and the similar Pt···Pt separation distances in the crystal lattices of **2.5** and **2.7a** (Figure 2.9a and 2.9b).

2.2.3 Luminescent Properties

The Pt(II) compounds **2.1**-**2.11** display phosphorescence in the blue-green region (Figure 2.11) and the details are summarized in Table 2.2. Compounds **2.1**-**2.11** are weakly luminescent in solution at ambient temperature, with quantum efficiencies ranging from ~0.5% to 16% (Figure 2.12-2.13). However, **2.1**-**2.11** display bright phosphorescence in 2-Me-THF glass at 77K, as neat solids or in PMMA films at ambient temperature, as shown in Figure 2.11. The emission spectra of **2.1**-**2.11** in PMMA (5 wt% or 10 wt%) all display well resolved vibronic features, an indication that the emission is mostly likely from a ^{3}LC state with MLCT contributions. The estimated Huang-Rhys ratios of the emission spectra of **2.1**-**2.11** in PMMA films are around 0.7-0.9 except **2.2** which is about 1.4. In the absorption spectra (Figure 2.14-2.16), the LC transition bands and the MLCT transition bands are not well resolved except for compound **2.1**, which displays a distinct MLCT band at 390 nm. The location of the $BMes_2$ group, the ligand field strengths of the

ancillary ligands, and the substituent groups have been found to have a significant impact on the emission color and quantum efficiency of this class of compounds.

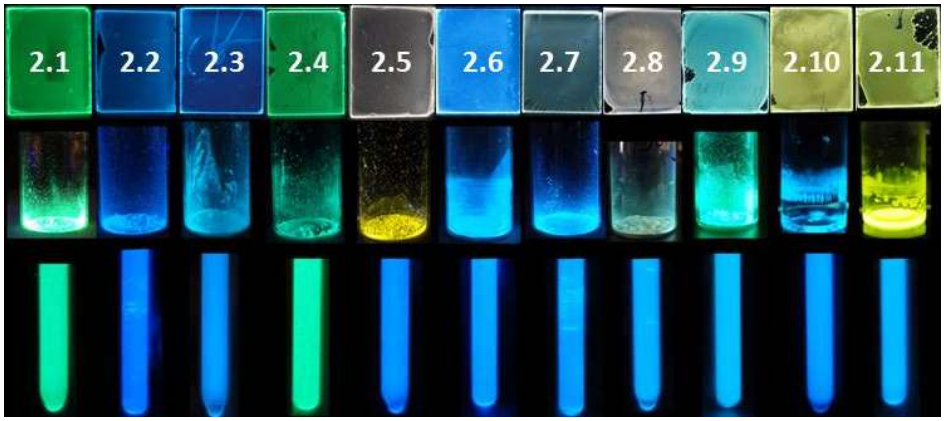

Figure 2.11 Photographs showing the emission colors of compounds **2.1-2.11** in 10 wt% PMMA films (top), as neat solids (middle) and in Me-THF glass (~1.0 x 10^{-5} M, bottom) at 77 K.

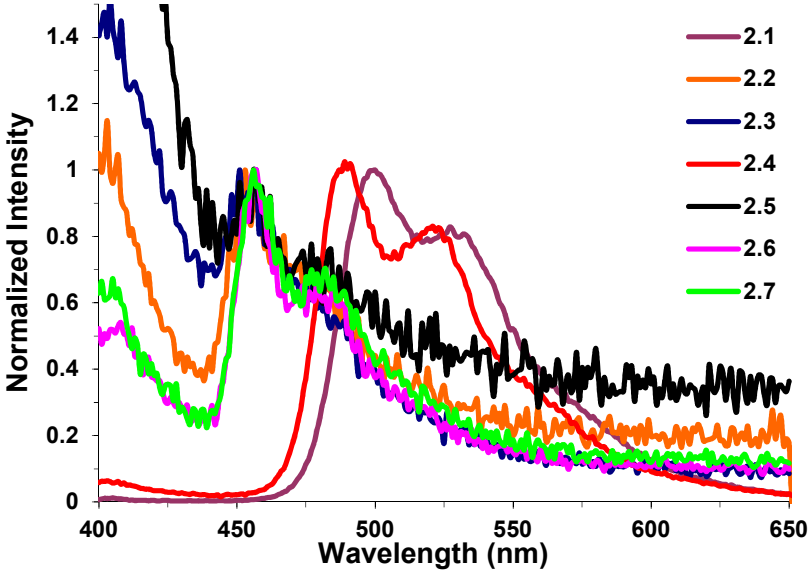

Figure 2.12 Normalized phosphorescent emission spectra of compounds **2.1-2.7** (~10^{-6} M in Me-THF) at ambient temperature.

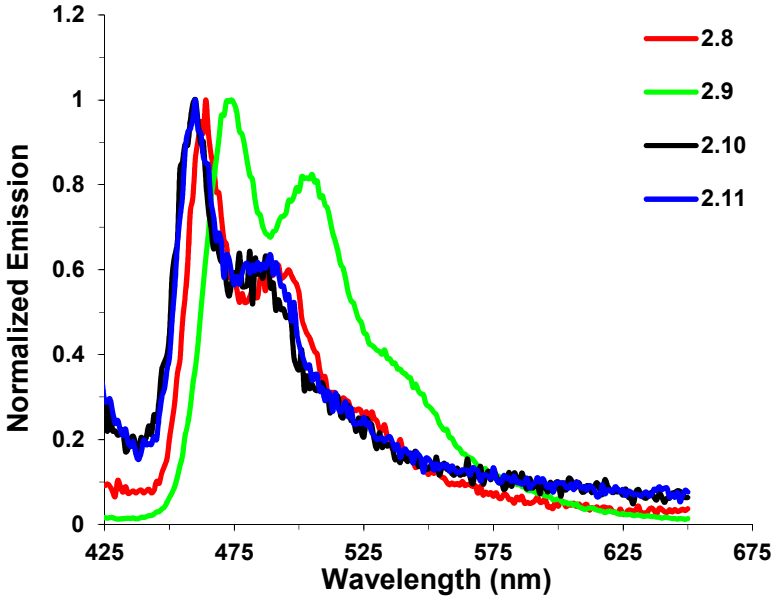

Figure 2.13 Phosphorescent spectra of compounds **2.8-2.11** (~10^{-6} M in Me-THF) at ambient temperature.

Table 2.2 Photophysical data of Pt(II) Compounds

Complex	Absorption[a] λ_{max} [nm] ε [10^4cm $^{-1}$M^{-1}]	Emission, λ_{max} [nm], 298 K						Emission 77 K[e]	
		λ_{max} [nm]			Φ_{PL} [d]			λ_{max} [nm]	τ_P [μs]
		Me-THF	PMMA 5 wt%	PMMA 10 wt%	Me-THF	PMMA 5 wt%	PMMA 10 wt%		
(*p*-BptrzBn)Pt(acac) (**2.1**)	321 (2.85), 388 (0.55)	500	493	493	0.17		0.63	491	36.1
(*m*-BptrzBn)Pt(acac) (**2.2**)	326 (2.45), 362 (2.58)	453	471	471			0.10	450	27.8
(*m*-BptrzAd)Pt(acac) (**2.3**)	325(1.79), 345 (1.73), 358(1.69)	451	455	455			0.09	450	30.2
(*p*-BptrzBn)Pt(pic) (**2.4**)	292 (2.00), 328 (2.70)	489		487	0.05		0.54	483	28.2
(*m*-BptrzBn)Pt(pic) (**2.5**)	274 (1.99), 306 (1.68), 358 (2.01)	456		455, 567			0.18	454	16.8
(*m*-BptrzBn)Pt(4-Me-pic) (**2.6**)	274 (2.21), 309 (1.72), 332 (2.03), 337 (1.97)	457	454	456		0.34	0.24	452	16.3
(*m*-BptrzAd)Pt(4-Me-pic) (**2.7**)	272 (2.18), 334 (1.96), 352 (2.03)	456	454	454, 559		0.21	0.14	453	15.7
(*m*-BptrzBn)Pt(pytrz) (**2.8**)	320 (1.95), 362 (3.00)	464	460	460	0.01	0.82	0.59	455	11.3
(*m*-BptrzBn)Pt(*t*-Bu-pytrz-Me) (**2.9**)	321 (2.24), 364 (3.97)	474	464	466	0.10	0.97	0.65	457	9.6
(*m*-BptrzBn) Pt(CF_3-pytrz-Me) (**2.10**)	312 (1.96), 355 (2.97)	460	456, 554	562	0.005	0.71	0.47	454	14.3
(*m*-BptrzAd)Pt(CF_3-pytrz-Me) (**2.11**)	270 (2.81), 340 (1.96), 355 (2.96)	460	548	556	0.005	0.27	0.20	457	14.6

[a] Measured in Me-THF at 2 x 10^{-5} M. [b] Doped into PMMA at 5 wt%. [c] Doped into PMMA at 10 wt%. [d] Phosphorescence quantum efficiency measured in Me-THF, relative to 9,10-diphenylanthracene. Solid state quantum yields were measured using an integration sphere. All quantum yields are ± 10%. [e] In Me-THF solution.

2.2.3.1 The Impact of the Bptrz Chelate Ligands and the Location of the $BMes_2$ Group on Luminescence

As shown by the photographs in Figure 2.11 and the data in Table 2.2, all $BMes_2$-functionalized Pt(II) compounds emit blue light (λ_{max} = 450-460 nm) in solution (at concentrations ≤ 1.0 x 10^{-5} M) with the exception of **2.1** and **2.4** that display greenish-blue light (λ_{max} = 480-490 nm). The chelate chromophore for **2.1** and **2.4** is *p*-BptrzBn while the chelate chromophore for all other compounds are either *m*-BptrzBn or *m*-BptrzAd. Thus, the $BMes_2$ group at the *meta* position of the phenyl ring is much more effective in achieving blue phosphorescence than at the *para* position. This observation is consistent with our earlier observation for (*p*-Bppy)Pt(acac) (λ_{max} = 538 nm)[19a] and (*m*-Bppy)Pt(acac) (λ_{max} = 481 nm)[15] and is due to the effective stabilization of the HOMO level by the electron-deficient $BMes_2$ group at the *meta*-position of the phenyl ring that increases the optical energy gap. Compared to the corresponding Pt(II) compounds with Bppy chromophores, the emission energy of Bptrz-Pt(II) compounds is about 30-50 nm blue shifted (e.g. λ_{max} = 490 nm and 538 nm for **2.1** and (*p*-Bppy)Pt(acac), respectively; 450 nm and 490 nm for **2.5** and (*m*-Bppy)Pt(pic), respectively), indicating that the Bptrz ligands are indeed effective in achieving blue phosphorescent Pt(II) compounds.

As shown by the phosphorescent spectra shown in Figure 2.15, it is also evident that compounds with the *m*-Bptrz ligand is much more prone to excimer emission. For example, among the Pt-pic compounds **2.4** – **2.7**, **2.4** is the only one that does not show significant excimer emission at 10 wt% doping level in PMMA, indicating that the bulky $BMes_2$ group is more effective in preventing intermolecular interactions at the *para* position than the *meta* position. Nonetheless, our study

focused on the *meta* substituted ligands as they lead to Pt(II) compounds with blue phosphorescence.

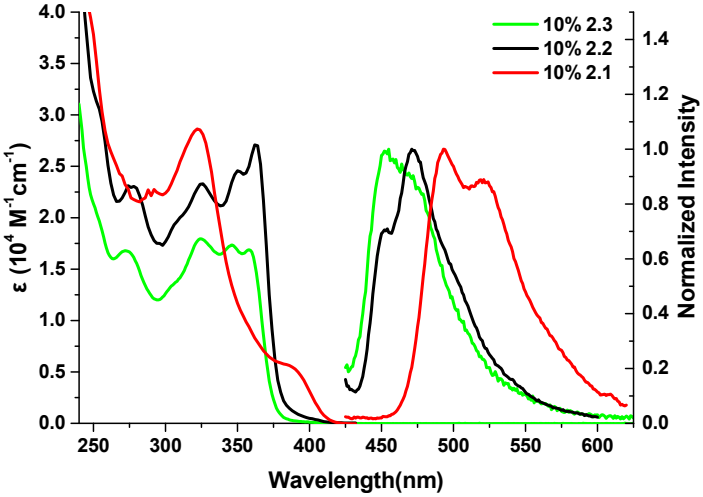

Figure 2.14 Absorption (left, recorded in THF) and phosphorescent spectra (right, in PMMA film with the doping level indicated) of compounds **2.1-2.3** at ambient temperature.

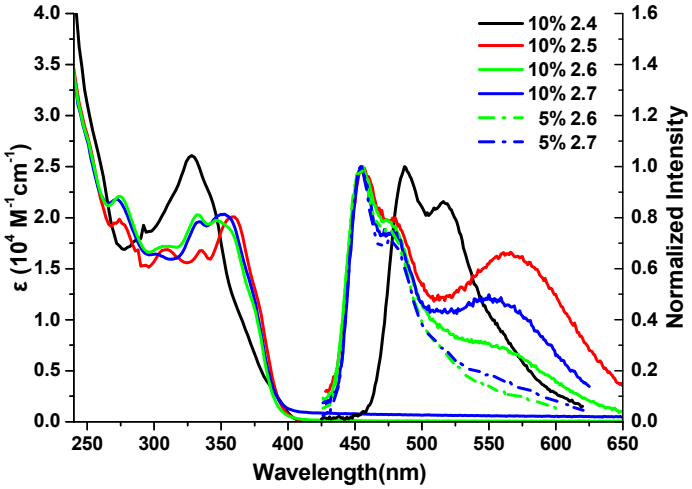

Figure 2.15 Absorption (left, recorded in THF) and phosphorescent spectra (right, in PMMA film with the doping level indicated) of compounds **2.4-2.7** at ambient temperature.

Compared to the corresponding (*p*-Bppy)Pt(acac) and (*m*-ppy)Pt(acac) (Φ_{phos} = 0.77 and 0.43, respectively in CH_2Cl_2), the emission quantum efficiencies of compounds **2.1-2.3** are much lower

(0.001-0.16 in Me-THF), which can be attributed to thermal quenching by the rotational motion of the benzyl or the adamantyl group on the trz ring in these molecules. In PMMA film (10 wt%), the quantum efficiency of **2.1** (0.63) is comparable to that of (*p*-Bppy)Pt(acac) (0.57) while those of the blue phosphorescent **2.2** and **2.3** (0.10 and 0.09, respectively) are lower than that of (*m*-Bppy)Pt(acac) (0.35). This can be attributed to the higher emission energy of **2.2** and **2.3** and the weaker ligand field of the Bptrz ligand, compared to the Bppy ligand in (*m*-Bppy)Pt(acac), which lead to a greater thermal quenching by the metal d-d state. Thus, in order to achieve bright blue phosphorescence with *m*-Bptrz ligand, it is necessary to replace the weak acac ancillary ligand by ancillary ligands with strong ligand field, such as pic and pytrz, to make the non-radiative metal d-d state thermally inaccessible.

2.2.3.2 The Impact of Ancillary Ligands on Luminescence

As shown by the data in Table 2.2 and the photographs in Figure 2.11, for the same Bptrz ligand, replacing the acac ancillary ligand with pic or pytrz or their derivatives only leads to a small change on the phosphorescence wavelength (~5-15 nm). In solution at ambient temperature, the Pt-pic and Pt-pytrz compounds still have a low emission quantum yield. However, they display bright phosphorescence in a rigid environment, such as in PMMA films, as neat solid or in Me-THF glass at 77 K. The key impact of the different ancillary ligands is on the phosphorescent efficiency and lifetime. Among the blue emitters, the phosphorescent quantum efficiency follows the order of **2.9** > **2.8** > **2.10** >> **2.6** > **2.7** ≈ **2.5** > **2.3** ≈ **2.2** and the phosphorescent lifetime follows the order of **2.9** < **2.8** < **2.10** < **2.7** < **2.6** ≈ **2.5** << **2.2** ≈ **2.3**. Compounds with the acac ancillary ligand have the lowest blue phosphorescence efficiency (~0.10 at 5-10 wt% in PMMA) and the highest phosphorescent lifetime (~30 μs) while compounds with the pytrz ancillary ligand have the highest

blue phosphorescence efficiency (0.71-0.97 in 5 wt% PMMA, ~0.50 in 10 wt% PMMA) and the lowest phosphorescent lifetime (10-15 μs). Compounds with the pic ancillary ligand have phosphorescence efficiency (0.21-0.34 in 5 wt% PMMA, ~0.20 in 10 wt% PMMA) and phosphorescent lifetime (~16 μs) in-between. As the ligand field strength of the ancillary ligands follows the order of pytrz > pic > acac, the use of a strong-field ancillary ligand leads to not only more efficient but also faster phosphorescence, which is highly desirable for blue phosphorescent emitters.

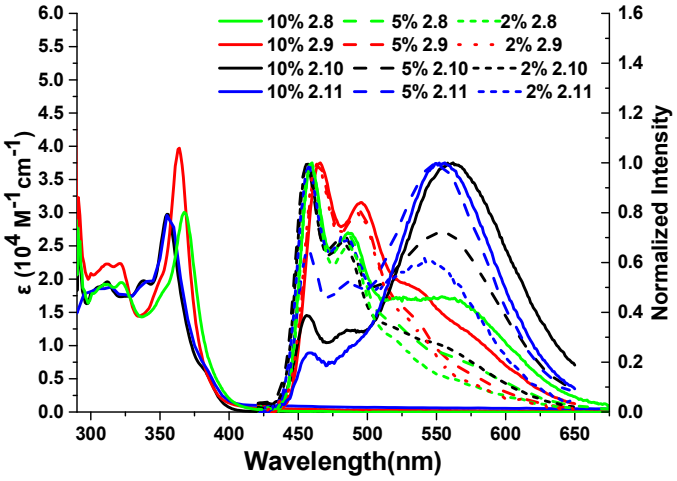

Figure 2.16 Absorption (left, recorded in THF) and phosphorescent spectra (right, in PMMA film with the doping level indicated) of compounds **2.8-2.11** at ambient temperature.

The other distinct impact by different ancillary ligands is the excimer emission caused by intermolecular interactions. As shown in Figure 2.14, Pt(II) compounds **2.1-2.3** with the acac ancillary ligands display no obvious excimer emission at 10 wt% doping level in PMMA while excimer formation is evident for all other compounds except compound **2.4** at the same doping level. This agrees with the crystal structures that revealed the presence of π-stacked dimer or 1D-structures in the crystal lattices of Pt-pic and Pt-pytrz compounds which are not observed in the Pt-acac compound **2.1**. The tendency of the Pt-pic compounds to form excimer emission was also

observed in (*m*-Bppy)Pt(pic) previously.[25] Because of the excimer formation, the quantum efficiency and color purity of Pt-pic and Pt-pytrz compounds decreases substantially with increasing doping concentrations in PMMA (Table 2.2 and Figure 2.15-2.16). Thus, to achieve bright blue emission, the excimer emission should be reduced.

2.2.3.3 The Impact of the Substituent Groups on Luminescence

For a given *C^N* ligand and the type of ancillary ligand, we have found that the nature of the substituent group on the ancillary ligand can have a subtle impact on phosphorescent energy and efficiency of the Pt(II) compounds, especially for the pic and pytrz series. For the Pt-acac compounds, because of weak intermolecular interactions, the replacement of the methyl groups by *t*-butyl groups in the acac ligand did not lead to any significant change of emission energy or efficiency. For the Pt-pic compounds, the introduction of a methyl group at the 4-position of the py ring in the pic ligand does not change the emission color significantly but substantially decreases the excimer formation and increases the emission quantum efficiency, as shown by the data for compounds **2.5** and **2.6** in Table 2.2 and the spectra in Figure 2.15. For the Pt-pytrz compounds, the introduction of a *t*-butyl group on the 1,2,4-trz ring and a methyl on the py ring reduces the excimer emission and increases the phosphorescence quantum efficiency, accompanied by a few nm red-shift of the emission energy (see data for **2.8** and **2.9** in Table 2.2). This can be attributed to the increased steric bulkiness around the metal complex that diminishes intermolecular interactions involving the central core. Surprisingly, the replacement of the *t*-butyl by a smaller electron-withdrawing CF_3 in compound **2.10** leads to a substantial increase of excimer emission and an 8 nm blueshift in emission energy, compared to that of **2.9**. Compound **2.10**, in fact, emits a white color at 5 wt% doping level and a yellow color at 10 wt% level in PMMA films,

as shown in the photographs in Figure 2.17. The increased excimer emission of **2.10** compared to **2.9** can be rationalized by the stronger intermolecular interaction between molecules of **2.10** due to the C-F···F-C and C-F···H-C interactions. Despite the excimer emission, the phosphorescent quantum yield. of compound **2.10** remains impressive (0.71 and 0.47 for 5 wt% and 10 wt%, respectively), making it a good candidate as an emitter for single-dopant white PhOLEDs.[27-28]

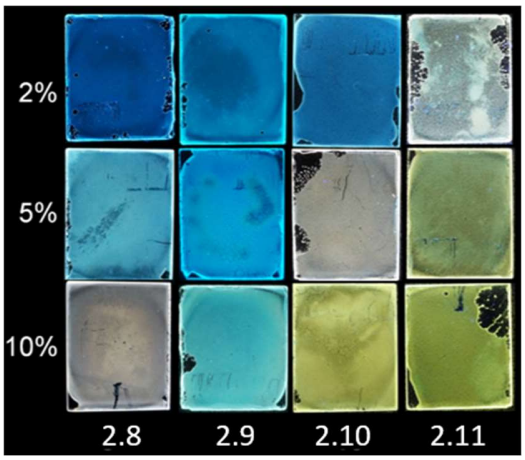

Figure 2.17 Photographs showing the emission colors of compounds **2.8-2.11** (N^1-*trans* isomers) in PMMA films at 2 wt%, 5 wt% and 10 wt% PMMA films.

To examine if the benzyl group on the 1,2,3-trz ring has any adverse effect on phosphorescent quantum efficiency it is replaced by an adamantyl group in **2.3**, **2.7** and **2.11**. As shown by the data in Table 2.2, for the Pt-acac compounds, there is little difference in emission color and efficiency between the benzyl and adamantyl substituted compounds. For the Pt-pic compounds, the adamantyl group appears to increase the excimer emission and decrease the quantum efficiency, as shown by the emission spectra of **2.6** and **2.7** in Figure 2.15 and the data in Table 2.2. For the Pt-pytrz compounds, the adamantyl group appears to have a similar effect, as illustrated by that compound **2.11** displays a greater tendency to produce excimer emission than the benzyl analogue **2.10**. Compound **2.11** displays a bright yellow emission color at 5 wt% and 10 wt% doping level

in PMMA with the excimer emission peak at ~550 nm dominating the phosphorescent spectra. At 2 wt% doping level, the emission color of **2.11** is white because of the significant contributions from the blue emission peak and the yellow excimer peak. The quantum efficiency of **2.11** also decreases significantly with the increasing doping concentration and the excimer formation (Φ_{phos} = 0.41, 0.27, 0.20 at 2 wt%, 5 wt% and 10 wt% doping level, respectively). Because of the greater excimer emission, the emission quantum efficiency of **2.11** is much lower than that of **2.10** at the same doping level. Based on the comparison of the Pt-pytrz compounds **2.10** and **2.11**, and Pt-pic compounds **2.6** and **2.7**, the adamantyl group favors excimer emission and decreases quantum efficiency, compared to the benzyl group. The impact of the substituent group and the doping level on the emission color of the Pt-pytrz compounds **2.8-2.11** are illustrated by the photographs in Figure 2.17.

2.2.3.4 The Impact of Isomerism on Luminescence

As shown in Figure 2.18, both *N^1-trans* and *N^4-trans* isomers of **2.8** have the same high energy emission peak at 460 nm. However, at the 5 wt% and 10 wt% doping concentration, in the emission spectra of the *N^4-trans* isomer, the excimer emission peak at 544 nm dominates with Φ_{phos} = 0.54 and 0.47, respectively. In contrast, for the *N^1-trans* isomer, the 460 nm peak dominates with Φ_{phos} = 0.82 and 0.59 at 5 wt% and 10 wt% doping level, respectively. This indicates that the *N^4-trans* isomer of compound **2.8** is much more prone to excimer formation than the *N^1- trans* one. The reason for this has not been understood. The double intramolecular hydrogen bonds are believed to play an important role in the exceptionally bright blue phosphorescence displayed by the *N^1-trans* isomers of compounds **2.8-2.11** since they greatly increase the rigidity of the molecules.

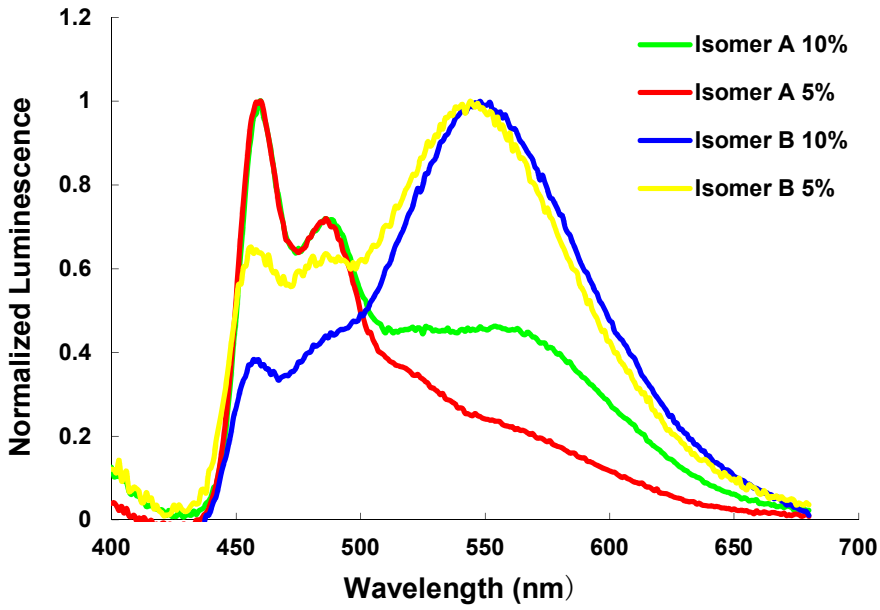

Figure 2.18 The phosphorescent spectra of the N^1-*trans* (A) and N^4-*trans* (B) isomers of compound **2.8** in 5 wt% and 10 wt% PMMA films.

2.2.4 Computational study

To further understand the photophysical properties of the Pt(II) compounds, TD-DFT calculations were performed for **2.1**, **2.2** and **2.4-2.11** and the results are summarized in Table 2.3. The experimentally estimated HOMO and LUMO energies of most of the Pt(II) compounds using the reduction potential and the optical absorption edge are also listed in Table 2.3 and Figure 2.19 for comparison. The HOMO and LUMO diagrams for selected compounds are given in Table 2.4.

Table 2.3 Experimental HOMO–LUMO energy and TD-DFT calculation results for selected compounds.

	Experimental				DFT calculation					
	[a]E_{red}	[b]HOMO (eV)	LUMO (eV)	[c]E_g (T_1)	HOMO (eV)	LUMO (eV)	H-L gap (eV)	[d]E_g (T_1)	% H → L ($S_0 \rightarrow S_1$)	f ($S_0 \rightarrow S_1$)
2.1	-2.44	-5.38	-2.36	2.53	-5.31	-1.52	3.79	2.66	88	0.0564
2.2	-2.35	-5.69	-2.45	2.76	-5.42	-1.36	4.06	2.88	78	0.3752
2.4	-2.32	-5.53	-2.48	2.58	-5.52	-1.66	3.86	2.71	70	0.0268
2.5	-2.27	-5.67	-2.53	2.75	-5.63	-1.74	3.89	2.83	80	0.1249
2.6	-2.42	-5.53	-2.38	2.74	-5.58	-1.63	3.95	2.84	83	0.1687
2.7	-2.25	-5.70	-2.55	2.74	-5.52	-1.58	3.95	2.82	84	0.1632
2.8	-2.29	-5.61	-2.51	2.73	-5.58	-1.66	3.92	2.76	86	0.0076
2.9	-2.40	-5.48	-2.40	2.71	-5.39	-1.58	3.81	2.71	88	0.0008
2.10	-2.26	-5.66	-2.54	2.73	-5.69	-1.77	3.92	2.81	79	0.0641
2.11	-2.27	-5.67	-2.53	2.71	-5.63	-1.74	3.89	2.79	82	0.0654

[a]The reduction potentials of all compounds were measured in CH_3CN/THF with 0.1 M Bu_4NPF_6 at a scan rate of either 100 mV s^{-1} or 200 mV s^{-1} (vs. Cp_2Fe/Cp_2Fe^+). [b]Cp_2Fe (4.8 eV) below the vacuum level. [c]The triplet energy value (T_1) was estimated by using the emission spectra at 77 K. [d]$S_0 \rightarrow T_1$ vertical excitation energies.

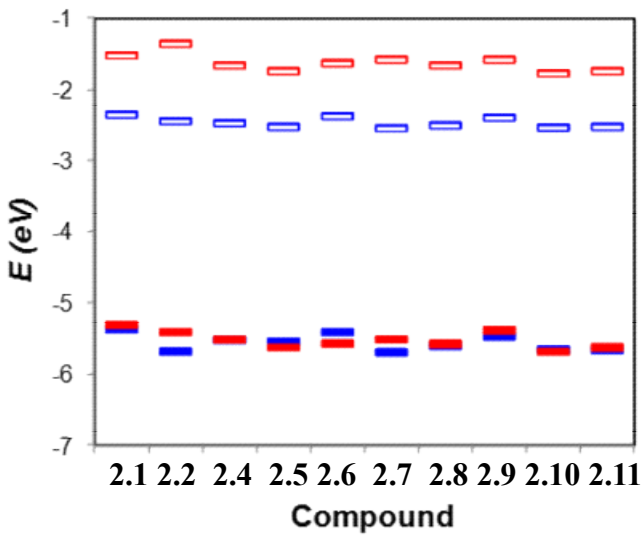

Figure 2.19 The experimental (blue) and calculated (red) HOMO and LUMO energies for selected Pt (II) compounds.

Table 2.4 The HOMO and LUMO diagrams of selected Pt(II) compounds. (isocontour value = 0.03)

	2.1	**2.2**	**2.4**	**2.5**
LUMO	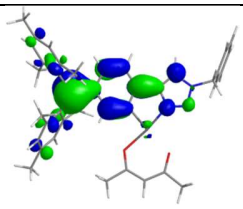	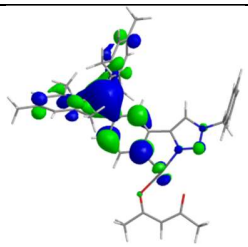	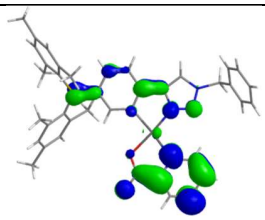	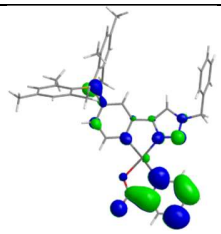
HOMO	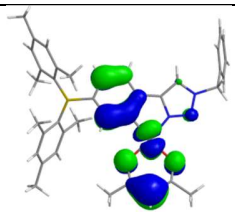	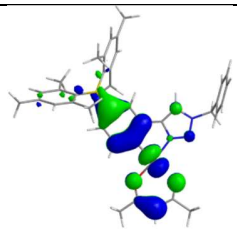	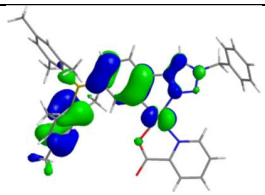	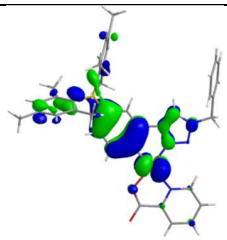
	2.6	**2.8**	**2.9**	**2.10**
LUMO	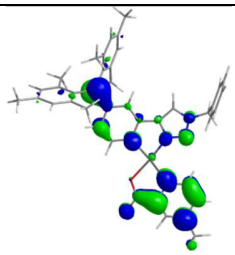	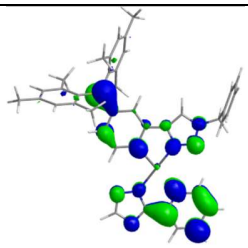	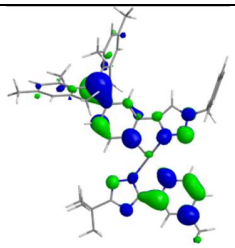	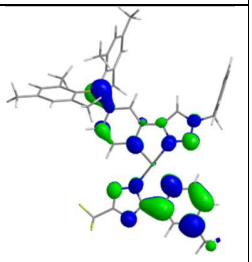
HOMO	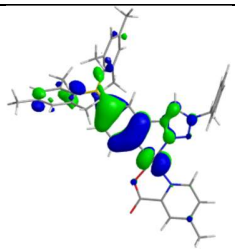	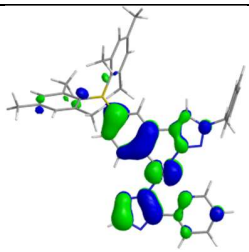	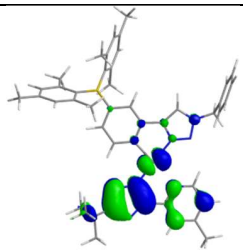	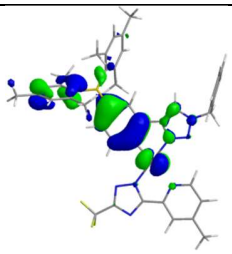

Both experimental and DFT data show that the HOMO and LUMO levels of the Pt-acac compounds are in general higher than those of Pt-pic and Pt-pytrz with **2.10** having the deepest HOMO and LUMO levels. For the Pt-acac compounds, the *m*-BptrzBn ligand causes destabilization of the LUMO and stabilization of the HOMO, leading to a wider HOMO-LUMO gap and a higher triplet energy, compared to the *p*- BptrzBn ligand (**2.2** versus **2.1**). For the Pt-pic

compounds, the *m*-BptrzBn ligand causes stabilization of both HOMO and LUMO levels but slightly more pronounced at the HOMO level, thus also leading to a higher triplet energy, compared to the *p*-BptrzBn ligand (**2.5** versus **2.4**). Electron donating substituent groups on the ancillary ligands destabilize both HOMO and LUMO levels while the electron withdrawing group CF_3 has the opposite effect (e.g. **2.5** versus **2.6**, and **2.9** versus **2.10**).

TD-DFT data established that the HOMO→LUMO transition is the main component of the $S_0 \rightarrow S_1$ and $S_0 \rightarrow T_1$ transitions for all compounds and the ancillary ligand contributes to either HOMO or LUMO or both. For the Pt-acac compounds, the HOMO has contributions mainly from the acac ligand, the Pt d orbital and the phenyl ring of the Bptrz ligand while the LUMO is localized on the Bptrz chelate with a large contribution from the boron center. For Pt-pic compounds, the HOMO involves mainly the phenyl ring,the mesityl ring of the Bptrz ligand and the Pt d orbital while the LUMO has major contributions from the pic ligand and the B atom of the Bptrz ligand. The acac contributions to the HOMO level in Pt-acac compounds is likely responsible for the higher HOMO energy level of **2.1**, relative to that of **2.4**. The involvement of the pic ligand in the LUMO level stabilizes LUMO of **2.4**, relative to that of **2.1**. For the Pt-pytrz compound **2.8**, the HOMO and LUMO are delocalized over the Bptrz and the pytrz ligand with the Pt *d* orbital contributing to the HOMO and the B p_π orbital contributing to the LUMO. The LUMO of **2.9** and **2.10** resembles that of **2.8**. However, the HOMO of **2.9** has no contribution from the Bptrz ligand while the HOMO of **2.10** has no contribution from the pytrz ligand. This can be explained by the nature of the substituent group on the pytrz ligand. The electron donating *t*-butyl group destabilizes the π orbital of the pytrz such that it dominates the HOMO, causing the slightly narrowing of the HOMO-LUMO gap of **2.9**, relative to **2.8**. In contrast, the electron withdrawing CF_3 group stabilizes the π

orbital of the pytrz such that it no longer contributes to the HOMO, causing the slightly widening of the HOMO-LUMO gap of **2.10**, relative to **2.9**. The computational data show that the replacement of the benzyl group by an adamantyl group in the Bptrz ligand causes a slight destabilization of both HOMO and LUMO levels, but more pronounced on the HOMO, leading to a slight narrowing of the HOMO-LUMO gap (e.g. **2.2** versus **2.3**, **2.5** versus **2.7**, **2.10** versus **2.11**).

2.2.5 Electrophosphorescence of 2.9 and 2.10

The study of electroluminescent (EL) properties is focused compounds **2.9** and **2.10**. **2.9** is the most efficient blue phosphorescent emitter and has the least tendency to form excimer among the (Bptrz)Pt(pytrz) compounds, thus most suitable for blue phosphorescent OLEDs. The production of white light from the combination of the deep blue monomer emission and the yellow excimer emission of **2.10**, together with its impressive quantum efficiency, make **2.10** suitable as emitter for single-dopant white OLEDs. Both **2.9** and **2.10** show high thermal stability with the decomposition temperature being > 280°C for **2.9** and ~250°C for **2.10**, based on differential scanning calorimetry results.

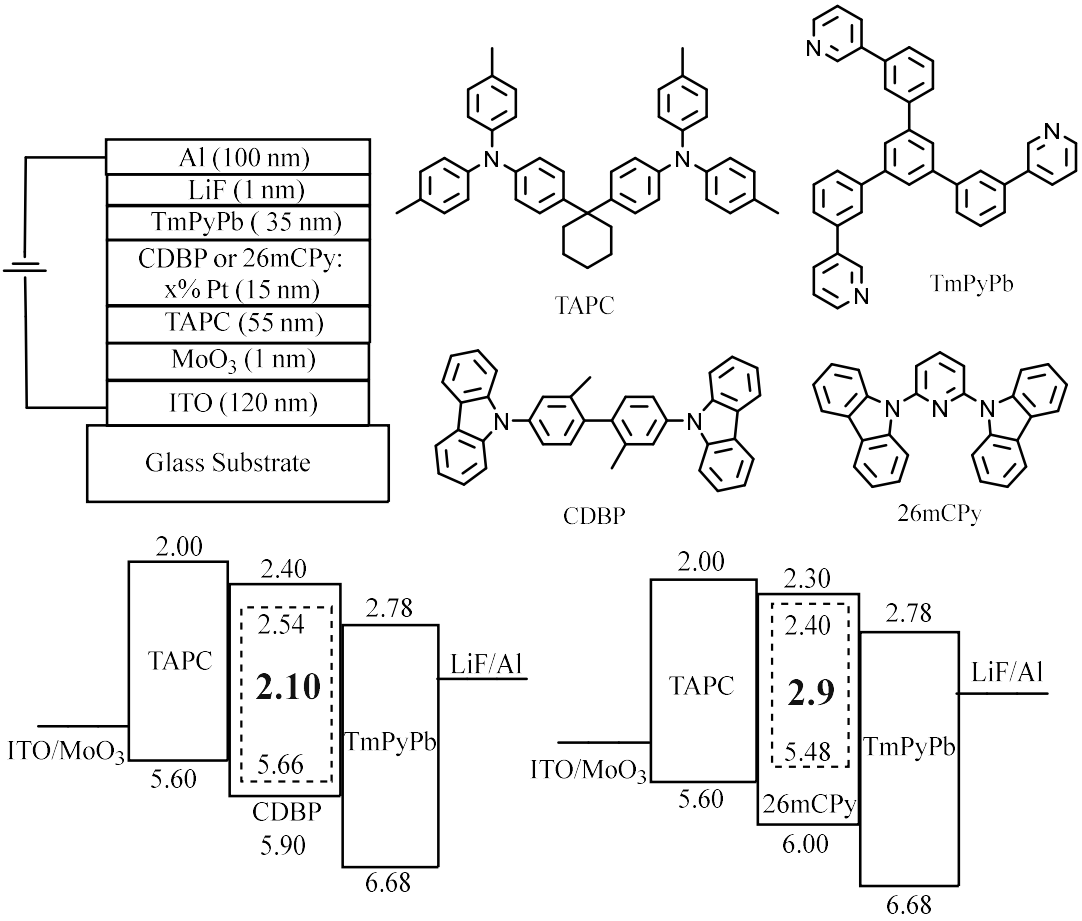

Figure 2.20 EL device structure and materials used.

The EL device structure is shown in Figure 2.20. For the electron transporting layer, both 2,2',2"-(1,3,5-benzinetriyl)-tris(1-phenyl-1-H-benzimidazole) (TPBi) and 1,3,5-tris(3-pyridyl-3-phenyl)benzene (TmPyPb) are examined. EL devices using TmPyPb as the ETL consistently give better performance, perhaps because of the higher triplet energy of TmPyPb compared to TPBi that leads to better exciton confinement.[29] For the hole transport layer, 4,4′-cyclohexylidenebis[N,N-bis(4-methylphenyl)benzene-amine] (TAPc) is used because its energy levels match well those of the host materials. Both 4,4'-bis(9-carbazolyl)-2,2'-dimethylbiphenyl (CDBP) and 2,6-bis(N-carbazolyl)pyridine (26mCPy) are chosen as the host materials because of

their high triplet energies (3.0 eV and 2.9 eV, respectively).[29] MoO_3 and LiF are chosen as the hole and electron injection material, respectively. For compound **2.9**, 26mCPy is found to be a better host than CDBP while for **2.10**, CDBP is found to produce more efficient devices. The distinct dependence of EL devices of **2.9** and **2.10** on the host material can be explained by the energy level diagrams shown in Figure 2.20, which illustrate that 26mCPy allows better charge trapping for **2.9** while the higher triplet energy of CDBP is more suitable for **2.10** which emits at a higher energy. Based on the photoluminescent data, EL devices with doping level at 2%, 5% and 10% for **2.9**, and at 2% and 5% for **2.10** were fabricated with the aim to achieve blue and white EL, respectively. The EL data for 5% and 10% devices of **2.9** and 2% and 5% devices of **2.10** are shown in Figure 2.21 and Table 2.5. The EL spectrum of the 5% device of **9** matches very well with the PL spectrum in 5 wt% PMMA or 26mCPY, producing a sky blue color with λ_{em} = 467 nm and CIE(x,y) of (0.19, 0.34). At 10% doping level, although the EL spectrum of **2.9** is still dominated by the monomer peak at 467 nm, a large excimer peak at ~555 nm appears, which is again in agreement with the PL spectrum at the same doping level. As a consequence, this EL device produces a white color with CIE (x,y) of (0.31, 0.44). For compound **2.10**, at the 2% doping level, the monomer blue peak at 456 nm dominates the EL spectrum with a large contribution of the excimer peak at ~555 nm, leading to a white color with CIE (x,y) of (0.32, 0.42). At 5% doping level, the EL spectrum of **2.10** is dominated by the excimer peak, producing a yellowish white color with CIE (x,y) shifting to (0.38, 0.48). The general trend of the EL spectral dependence of **2.10** on the doping level is in agreement with that of PL in PMMA films. However, it appears that **2.10** is more prone to excimer formation in the EL device than in PMMA since it has a greater excimer contribution at the same doping level in the device than in PMMA. In addition, the external quantum efficiency of EL devices of **2.9** and **2.10** increases significantly with the doping

level, which contradicts the trend observed for PL that decreases in efficiency with increasing doping concentration. This could be caused by more efficient exciton confinement to the excimer than the monomer emission in the device. The other possible explanation is the reduced host triplet-triplet annihilation (TTA) with increasing doping concentration, leading to higher device efficiency.[30] All devices have a low turn-on voltage of 3.0-3.2 V. The white 10% EL device of **2.9** has the most impressive performance with a maximum brightness of 3220 cd/m^2 and an external quantum efficiency of 15.6% at 100 cd/m^2. Although many examples of efficient white electrophosphorescent devices are known previously,[28] the majority of them use either multiple dopants or tandem device structures. Efficient white electrophosphorescent devices based on single dopant remain relatively rare with several examples based on Pt(II) excimers being reported recently [28d,31] The performance of the 10% EL device of **2.9** is certainly among the most efficient single-dopant white EL devices.

Table 2.5 EL device data for **2.9** and **2.10**.

Device	EL λ_{max} (nm)[a]	V_{on} (V)[b]	L (cd/m^2, V)[c]	η_{ext} (%)[d]			η_c (cd/A)[e]	η_p (lm/W)[f]	CIE (x,y)
				10 cd/m^2	100 cd/m^2	1000 cd/m^2			
5% **2.9**	467	3.2	2879, 8.4	10.4	8.3	4.6	23.6	23.2	(0.19, 0.34)
10% **2.9**	468	3.0	3220, 8.6	14.4	15.6	6.5	36.7	33.9	(0.31, 0.44)
2% **2.10**	456	3.2	865, 9.2	5.0	2.5	-	11.8	10.9	(0.32, 0.42)
5% **2.10**	563	3.2	1420, 8.0	9.3	7.3	2.1	24.7	22.9	(0.38, 0.48)

[a]Value taken at I = 20 mA. [b]The applied voltage (V_{on}) is defined as brightness of 1 cd/m^2.[c]The luminance (L) is the maximum value. [d]External quantum efficiency (EQE, η_{ext}). [e]Current efficiency (η_c) and power efficiency (η_p) are the maximum values.

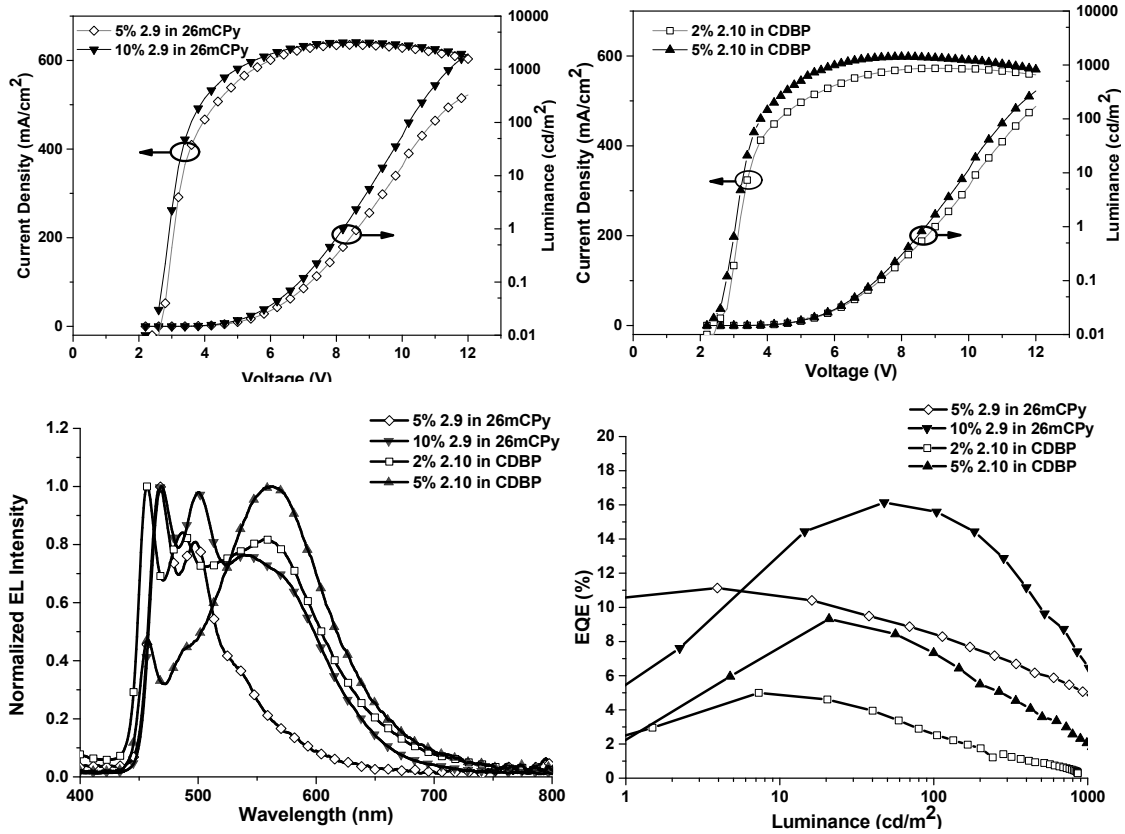

Figure 2.21 EL spectra, L-J-V and EQE-L diagrams of EL devices using **2.9** or **2.10** as the dopant.

2.2.6 Improved EL Devices for 2.9 with External Quantum Efficiency of 24.0%

In order to improve the device performance of OLEDs based on compound **2.9**, 26mCPy was replaced with a bipolar host material [(4-{1-[4-(diphenylphosphoryl)phenyl]-cyclohexyl}phenyl)bis(4-methylphenyl)amine] (POPCPA), which has a high triplet energy of 2.9 eV and a shallow HOMO level of 5.2 eV.[32] 1,3,5-tri[3-(diphenylphosphoryl)phenyl]benzene (TP3PO), with a triplet energy of 2.8 eV, a HOMO level of 6.4 eV and excellent electron-transport ability, was used as the electron transporting material.[32] The device structure, energy diagram and molecular structure of POPCPA and TP3PO were shown in Figure 2.22. The 3% and 7% EL device with structure A show impressive performance with maximum external quantum efficiency of 19.5%

and 21.9%, maximum power efficiency of 42.1 lm/W and 49.8 lm/W, respectively. However, due to the close triplet energy of **2.9** (2.71 eV) and the TP3PO (2.80 eV) and a higher hole mobility compared to electron mobility of POPCPA, the excitons were most likely generated near the POPCPA/TP3PO interface and exciton leaking to TP3PO layer is possible. In addition, as shown in Figure 2.23a, the emission of POPCPA and TP3PO overlap significantly with the ^{3}MLCT absorption band of **2.9**, which ensures efficient Förster energy transfer from POPCPA and TP3PO to **2.9**. Based on the above considerations, a new device structure B was applied by simultaneously doping compound **2.9** in both the host layer and the electron transporting layer, as shown in Figure 2.22. The 3% and 7% EL device with structure B show improved performance with maximum external quantum efficiency of 21.8% and 24.0%, maximum power efficiency of 47.9 lm/W and 55.8 lm/W, respectively, which was the highest among greenish-blue PhOLEDs at that time.

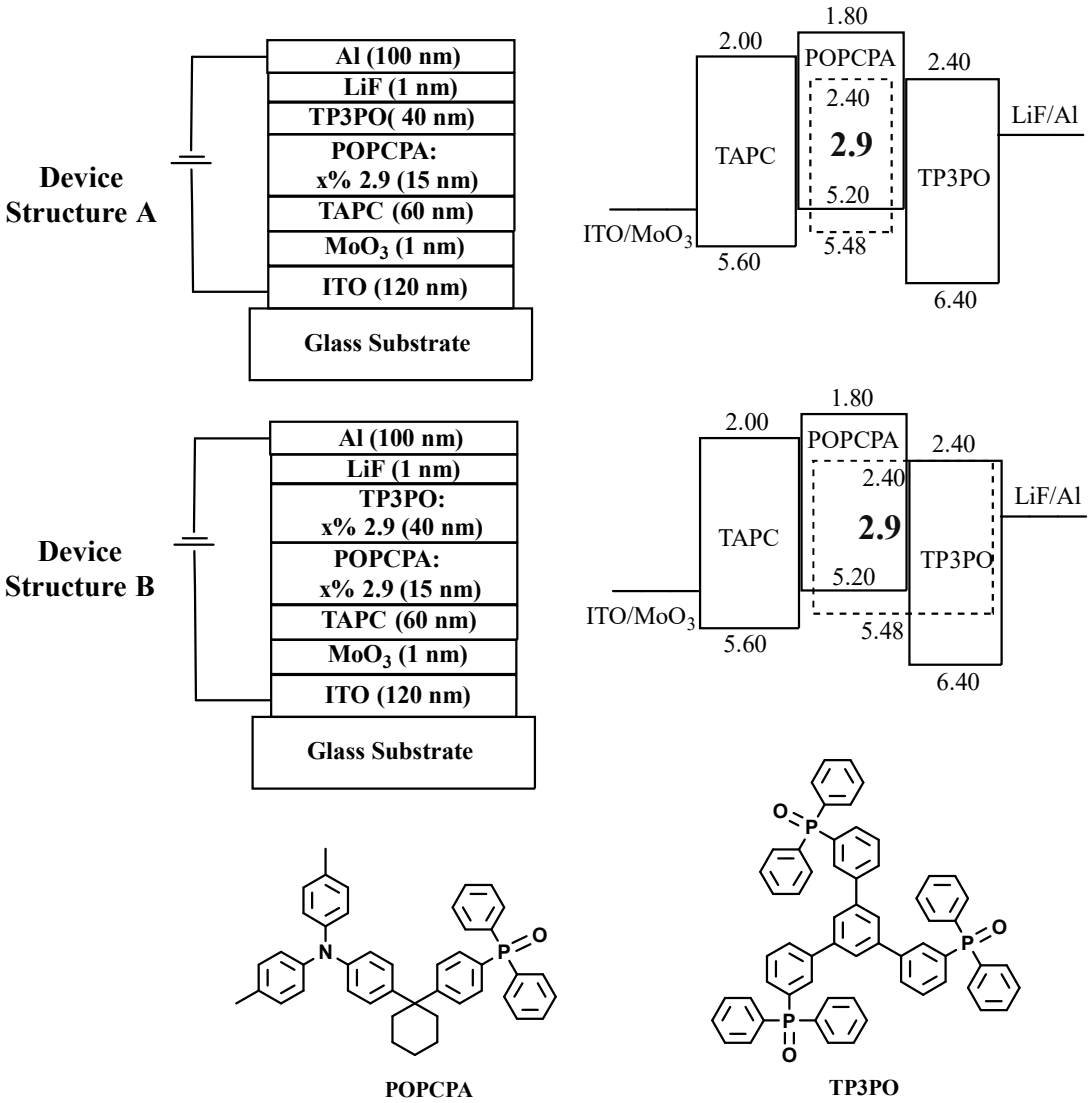

Figure 2.22 Device structures and energy diagrams of the EL devices and molecular structure of POPCPA and TP3PO.

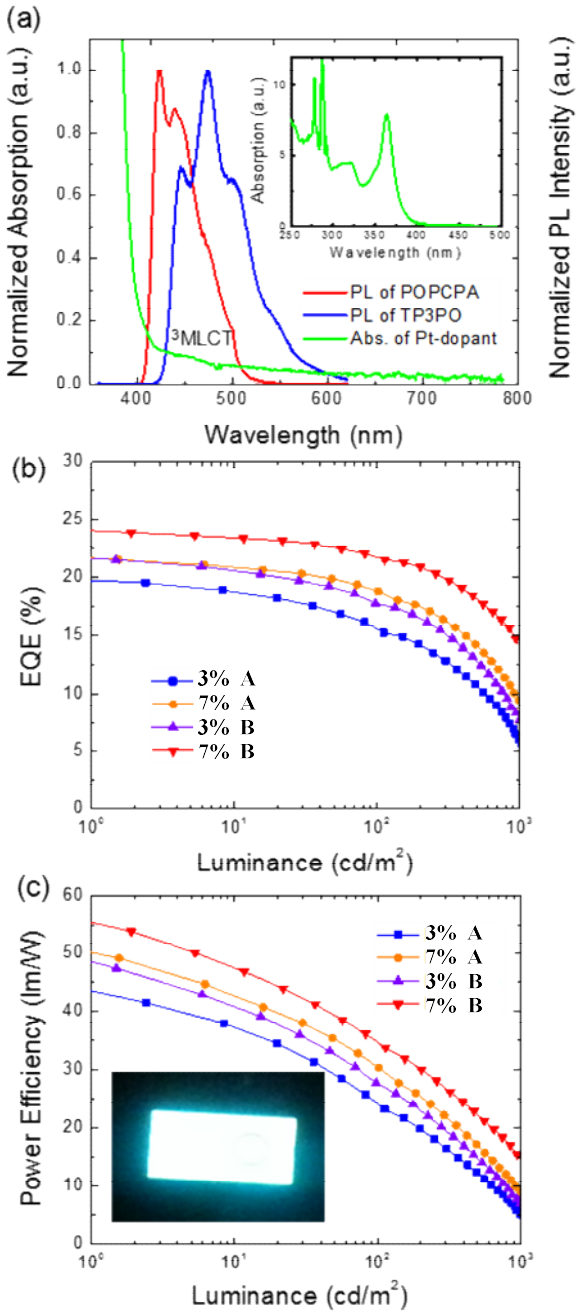

Figure 2.23 (a) Normalized emission spectra of POPCPA and TP3PO and ^{3}MLCT absorption band of 2.9. Inset: The absorption spectrum of **2.9**. (b) EQE-L diagrams of EL devices. (c) P-L diagrams of EL devices. Inset: Photograph showing device 7% B at 500 cd/m^2. (adapted from Ref. 33)

2.3 Experimental

2.3.1 General Procedures

All Reactions were carried out under a nitrogen atmosphere unless otherwise noted. Reagents were purchased from Aldrich chemical company and used as received. TLC and flash chromatography were performed on silica gel. ^{1}H and ^{13}C NMR spectra were recorded on Bruker Avance 300, 400, or 500 MHz spectrometers. Deuterated solvents were purchased from Cambridge Isotopes and used without drying. Excitation and emission spectra were obtained on a Photon Technologies International QuantaMaster Model 2 spectrometer. Phosphorescent decay lifetimes were measured using a Photon Technologies International Phosphorescent lifetime spectrometer. Solid state quantum efficiency measurements were performed using an integration sphere. Phosphorescence quantum yields of compound **2.1**, **2.4** and **2.8-2.11** were measured relative to 9,10-diphenylanthracene in degassed 2-methyltetrahydrofuran (Φ_F=0.90) at 298 K. UV-Visible spectra were recorded using a Varian Carry 50 UV/Vis spectrophotometer. Cyclic voltammetry experiments were conducted on a BAS CV-50W analyzer with a scan rate of either 150 or 200 mVs^{-1}. The electrochemical cell was a standard three-compartment cell composed of a Pt working electrode, a Pt auxiliary electrode and an Ag/AgCl reference electrode. All measurements were using 0.1M NBu_4PF_6 in DMF as the electrolyte. Ferrocene/ferrocenium was used as internal standard (E^o=0.55V). Elemental analyses were performed by University of Montreal Elemental Analysis Laboratory. Crystal structures were obtained using a Bruker AXS Apex II X-ray diffractometer. TD-DFT calculations were carried out using the Gussian 03 software at the High Performance Computing Virtual Laboratory (HPCVL) at Queen's University.[20] All computations were performed at the B3LYP level of theory using LANL2DZ as the basis set for Pt and 6-31G(d) for all other atoms.

2.3.2 Synthesis of Ligands

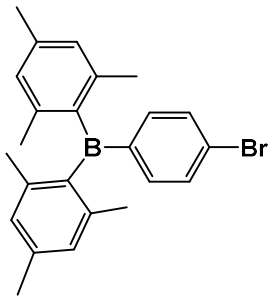

***p*-(dimesitylboryl)bromobenzene (*p*-BpBr)**: To a 100mL Schlenk flask with a stir bar was added *p*-dibromobenzene (1.0 g, 4.24 mmol) and 30mL of dry Et_2O. The solution was stirred at -78 °C for 30 minutes before 2.9 mL of 1.6 M n-Butyllithium (4.64 mmol) was slowly added. The mixture was maintained at -78°C for 1h, and dimesitylboron fluoride (1.36 g, 5.0 mmol) was added. The resulting mixture was stirred at -78 °C for another hour and then slowly warmed up to room temperature. After stirring overnight, the solvent was removed under reduced pressure and the solid was extracted with dichloromethane. The organic layer was washed with brine and water and then dried over $MgSO_4$, filtered and purified using flash chromatography on silica using hexane as eluent to afford 1.2 g of ***p*-BpBr** as white solid (70% yield). ^{1}H NMR (300 MHz, $CDCl_3$): δ7.51 (d, ^{3}J=8.1Hz, 2H), 7.38 (d, ^{3}J=8.1Hz, 2H), 6.84 (s, 4H), 2.33 (s, 6H), 2.01 (s, 12H) ppm.

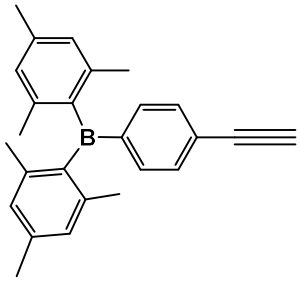

***p*-(dimesitylboryl)phenylacetylene (*p*-BpCC)**: A 100mL three-necked round bottomed flask with a stir bar and condenser was charged with ***p*-BpBr** (1.22 g, 3.03 mmol), trimethylsilylacetylene (0.45 mL, 3.44 mmol), tetrakis(triphenylphosphine)palladium(0) (0.175 g, 0.15 mmol), copper iodide (0.03 g, 0.15 mmol) and 30 mL of degassed triethylamine. The mixture was stirred at 80 °C for 20 hours and then concentrated under reduced pressure. The product was extracted with dichloromethane and sequentially washed with saturated ammonium chloride solution, brine and water. The organic layer was dried over $MgSO_4$, filtered and purified

using flash chromatography on silica using hexane as eluent. After removal of solvent by rotary evaporation, the resulting white solid was dissolved in 10mL of tetrahydrofuran and treated with sodium hydroxide in methanol (20 mL of a 2.0 M solution). After stirring for 2 hours, the resulting mixture was concentrated under reduced pressure. After extraction with dichloromethane, the organic solution was dried over $MgSO_4$, filtered and the solvent was removed by rotary evaporation to give ***p*-BpCC** as a white solid (0.67 g, 65%). ^{1}H NMR (300 MHz, $CDCl_3$): δ7.48 (s, 4H), 6.84 (s, 4H), 3.20 (s, 1H), 2.33 (s, 6H), 2.00 (s, 12H) ppm.

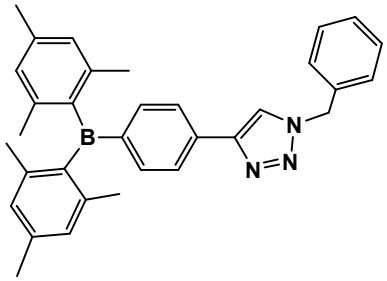

4-(4-dimesitylboryllphenyl)-1-benzyl-1H-1,2,3-triazole (*p*-BptrzBn): To a 50mL Schlenk flask with a stir bar was added ***p*-BpCC** (0.64 g, 1.84 mmol), benzyl azide (0.245 g, 1.84 mmol), diisopropylethylamine (0.475 g, 3.68 mmol), tris[(1-benzyl-1*H*-1,2,3-triazol-4-yl)methyl]amine (1 mol %) and 30 mL of dichloromethane. The solution was degassed for 20 minutes before $[Cu(CH_3CN)_4]PF_6$ (1 mol %) was added. The resulting mixture was stirred overnight. After the solvent was removed under reduced pressure, the product was extracted with dichloromethane and washed with saturated ammonium chloride solution, brine and water. The combined organic phase was dried over $MgSO_4$, filtered and purified using flash chromatography on silica (4:1 hexanes: ethyl acetate as eluent) to afford 0.64 g of ***p*-BptrzBn** as white solid (72% yield). ^{1}H NMR (400 MHz, $CDCl_3$): δ7.82 (d, ^{3}J=8.0Hz, 2H), 7.76 (s, 1H), 7.59 (d, ^{3}J=8.0Hz, 2H), 7.42-7.32 (m, 5H), 6.86 (s, 4H), 5.61 (s, 2H), 2.34 (s, 6H), 2.05 (s, 12H) ppm; ^{13}C NMR (100 MHz, $CDCl_3$): δ148.1, 145.8,141.7, 140.9, 138.7, 137.0, 134.7, 133.7, 129.2, 128.8, 128.2, 128.0, 125.2, 120.2, 54.3, 23.5, 21.3 ppm.

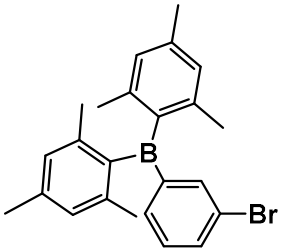

***m*-(dimesitylboryl)bromobenzene (*m*-BpBr)**: Prepared in analogy with ***p*-BpBr** by using *m*-dibromobenzene instead of *p*-dibromobenzene. (85% yield). ^{1}H NMR (300 MHz, $CDCl_3$): δ7.63 (s, 1H), 7.61 (d, ^{3}J=7.5Hz, 1H), 7.41 (d, ^{3}J=7.5Hz, 1H), 7.24 (t, ^{3}J=7.5Hz, 1H), 6.84 (s, 4H), 2.33 (s, 6H), 2.01 (s, 12H) ppm.

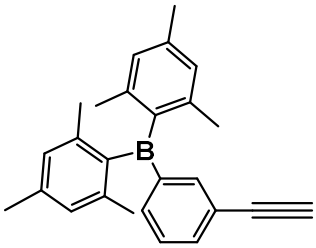

***m*-(dimesitylboryl)phenylacetylene (*m*-BpCC)**: Prepared in analogy with ***p*-BpCC** by using ***m*-BpBr** instead of ***p*-BpBr**. (63% yield). ^{1}H NMR (300 MHz, $CDCl_3$): δ7.67 (s, 1H), 7.61 (d, ^{3}J=7.5Hz, 1H), 7.50 (d, ^{3}J=7.3Hz, 1H), 7.33 (t, ^{3}J=7.3Hz, 1H), 6.84 (s, 4H), 3.05 (s, 1H), 2.33 (s, 6H), 2.00 (s, 12H) ppm.

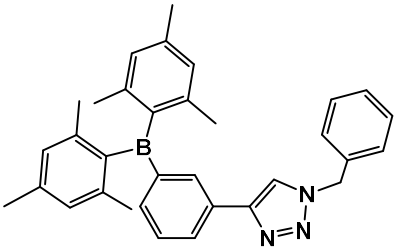

4-(3-dimesitylboryllphenyl)-1-benzyl-1H-1,2,3-triazole (*m*-BptrzBn): Prepared in analogy with ***p*-BptrzBn** by using ***m*-BpCC** instead of ***p*-BpCC**. (75% yield). ^{1}H NMR (400 MHz, $CDCl_3$): δ8.02 (d, ^{3}J=7.2Hz, 2H), 7.86 (s, 1H), 7.64 (s, 1H), 7.50-7.30 (m, 7H), 6.82 (s, 4H), 5.57 (s, 2H), 2.32 (s, 6H), 2.00 (s, 12H) ppm. ^{13}C NMR (100 MHz, $CDCl_3$): δ148.3, 140.9, 136.8, 136.1, 134.8, 132.9, 130.3, 129.3, 129.2, 128.8, 128.6, 128.3, 128.0, 119.8, 54.2, 23.5, 21.3 ppm.

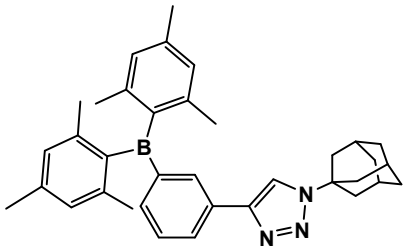

4-(3-dimesitylboryllphenyl)-1-adamantyl-1H-1,2,3-triazole (*m*-BptrzAd): Prepared in analogy with ***m*-BptrzBn** (72% yield) by using 1-adamantyl azide instead of benzyl azide. ^{1}H NMR (300 MHz, $CDCl_3$): δ8.07 (d, ^{3}J=6.2Hz, 2H), 7.94 (s, 1H), 7.79 (s, 1H), 7.50-7.40 (m, 2H), 6.85 (s, 4H), 2.40-2.20 (m, 15H), 2.04 (s, 12H), 1.83 (s, 6H) ppm. ^{13}C NMR (100 MHz, $CDCl_3$): δ145.2, 139.4, 137.2, 131.2, 127.8, 127.0, 126.7, 114.8, 103.1, 58.1, 41.5, 34.4, 28.0, 22.0, 19.7 ppm.

2.3.3 Synthesis of Pt(II) complexes

2.3.3.1 General Procedure to Synthesize Pt(II) Complexes 2.1-2.3

The **Bptrz** chelate ligand (0.10 mmol) and $[PtMe_2(u\text{-}SMe_2)]_2$ (0.055 mmol) were added to a 20 mL screw-cap vial with 5 mL of acetone. The mixture was heated at 70 ^{o}C for 3 hours before 1 mL of 0.1 M solution of tosylic acid (TsOH) in THF was added. The resulting solution was stirred for 1 hour before 2 mL of 0.1 M solution of sodium acetylacetonate in methanol was added. After stirring overnight, the solvent was removed under reduced pressure and the solid was extracted with dichloromethane. After wash with brine and water, the organic layer was dried over $MgSO_4$, filtered and purified on silica using dichloromethane as eluent.

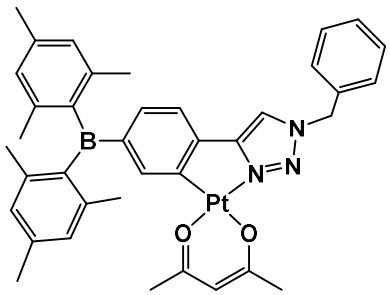

(*p*-BptrzBn)Pt(acac) (2.1): (24% yield). ^{1}H NMR (400 MHz, CD_2Cl_2): δ 7.51 (s, 1H), 7.47 (s, 1H), 7.40-7.28 (m, 5H), 7.11 (d, ^{3}J=7.6 Hz, 1H), 7.07 (d, ^{3}J=7.6 Hz, 1H), 6.74 (s, 4H), 5.49 (s, 2H), 5.37 (s,1H), 2.20 (s, 6H), 1.97 (s, 12H), 1.88 (s, 3H), 1.60 (s, 3H) ppm. Elemental analysis calcd (%) for $C_{38}H_{40}BN_3O_2Pt$: C 58.77, H 5.19, N 5.41, found: C 58.76, H 5.21, N 5.39.

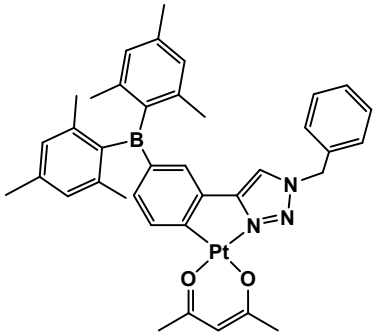

(*m*-BptrzBn)Pt(acac) (2.2): (25% yield). ^{1}H NMR (500 MHz, CD_2Cl_2): δ7.62 (d, ^{3}J=8.0 Hz, 1H), 7.52 (s, 1H), 7.50-7.38 (m, 6H), 7.20 (d, ^{3}J=8.0 Hz, 1H), 6.84 (s, 4H),5.57-5.56 (s, s, 3H), 2.32 (s, 6H), 2.04-2.03(s, s, 18H). Elemental analysis calcd (%) for $C_{38}H_{40}BN_3O_2Pt$: C 58.77, H 5.19, N 5.41, found: C 58.73, H 5.11, N 5.34.

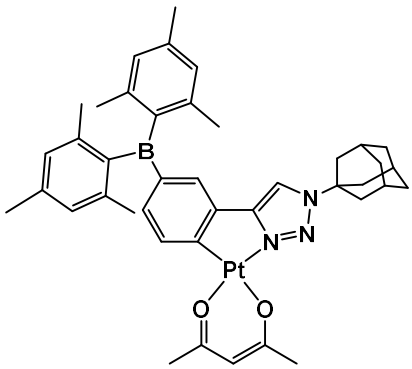

(*m*-BptrzAd)Pt(acac) (2.3): (19% yield). ^{1}H NMR (400 MHz, CD_2Cl_2): δ7.77 (s, 1H), 7.61 (d, ^{3}J=7.8 Hz, 1H), 7.44 (s, 1H), 7.19 (dd, ^{3}J=8.0 Hz, ^{4}J=1.2 Hz, 1H), 6.86 (s, 4H), 5.56 (s, 1H), 2.40-2.20 (m, 15H), 2.10-1.90(m, 15H), 1.84 (m, 3H). Elemental analysis calcd (%) for $C_{41}H_{48}BN_3O_2Pt$: C 60.00, H 5.89, N 5.12, found: C 59.30, H 6.02, N 4.68. HRMS (m/z): $[M+H]^+$ calcd for $C_{41}H_{49}BN_3O_2Pt$, 821.3565; found, 821.3561.

2.3.3.2 General Procedure to Synthesize Pl(II) Complexes 2.4-2.7

The **Bptrz** chelate ligand (0.10 mmol) and $[PtMe_2(u\text{-}SMe_2)]_2$ (0.055 mmol) were added to a 20 mL screw-cap vial with 5 mL of acetone. The mixture was heated at 70 °C for 3 hours before 2 mL of 0.1 M solution of the corresponding picolinic acid in methanol was added. The resulting solution was stirred overnight. The product was filtered and washed with hexane, diethyl ether and methanol. The product was further purified via recrystallization from THF/hexane.

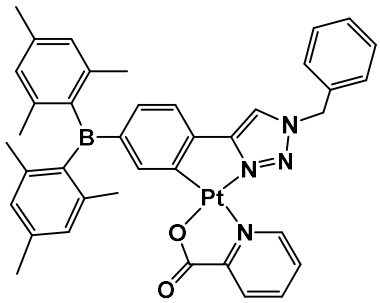

(*p*-BptrzBn)Pt(pic) (2.4): (26% yield). ^{1}H NMR (500 MHz, CD_2Cl_2): δ9.52 (d, ^{3}J=5.6 Hz, 1H), 8.14 (m, 1H), 7.80 (s, 1H), 7.70 (m, 1H), 7.62 (s, 1H), 7.50-7.42 (m, 5H), 7.27 (d, ^{3}J=7.5 Hz, 1H), 7.16 (d, ^{3}J=7.5 Hz, 1H), 6.88 (s, 4H), 5.64 (s, 2H), 2.34 (s, 6H), 2.06 (s, 12H). Elemental analysis calcd (%) for **2.4**·THF ($C_{43}H_{45}BN_4O_3Pt$): C 59.24, H 5.20 N 6.42, found: C 59.83, H 5.18, N 6.44.

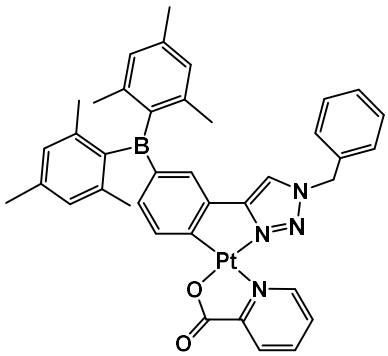

(*m*-BptrzBn)Pt(pic) (2.5): (30% yield). ^{1}H NMR (400 MHz, CD_2Cl_2): δ9.55 (d, ^{3}J=5.5 Hz, 1H), 8.18 (m, 2H), 7.79-7.75 (m, 2H), 7.58 (s, 1H), 7.50-7.40 (m, 6H), 7.25 (dd, ^{3}J=7.6 Hz, 4J=1.2 Hz, 1H), 6.84 (s, 4H), 5.61 (s, 2H), 2.33 (s, 6H), 2.04 (s, 12H). Elemental analysis calcd (%) for **2.5**·2CH_3OH ($C_{41}H_{45}BN_4O_4Pt$): C 57.01, H 5.25, N 6.49, found: C 56.98, H 5.00, N 6.08.

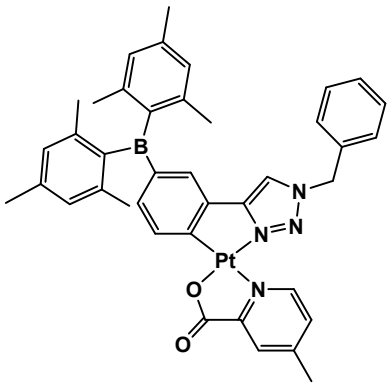

(*m*-BptrzBn)Pt(4-Mepic) (2.6): (32% yield). ^{1}H NMR (400 MHz, CD_2Cl_2):δ9.35 (d, ^{3}J=5.5 Hz, 1H), 7.99 (s, 1H), 7.75 (d, ^{3}J=7.6 Hz, 1H), 7.57 (m, 2H), 7.50-7.40 (m, 6H), 7.25 (dd, ^{3}J=7.6 Hz, 4J=1.4 Hz, 1H), 6.84 (s, 4H), 5.60 (s, 2H), 2.54 (s, 3H), 2.33 (s, 6H), 2.04 (s, 12H). Elemental analysis calcd (%) for 6·1/4CH_2Cl_2 ($C_{40.25}H_{39.5}BCl_{0.5}N_4O_2Pt$): C 57.90, H 4.77, N 6.71, found: C 57.91, H 4.53, N 6.63.

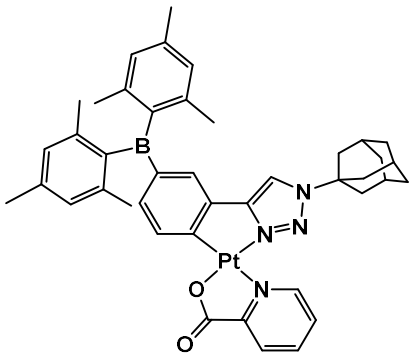

(*m*-BptrzAd)Pt(pic) (2.7a): (24% yield). ^{1}H NMR (300 MHz, CD_2Cl_2): δ9.51 (d, ^{3}J=4.8 Hz, 1H), 8.17 (m, 2H), 7.77 (m, 3H), 7.51 (s, 1H), 7.26 (d, ^{3}J=6.3 Hz, 1H), 6.87 (s, 4H), 2.34 (m, 15H), 2.07 (s, 12H), 1.88 (m, 6H. Elemental analysis calcd (%) for **2.7a**·CH_2Cl_2 ($C_{43}H_{47}B\ Cl_2N_4O_2Pt$): C 55.61, H 5.10, N 6.03, found: C 56.64, H 5.09, N 5.78.

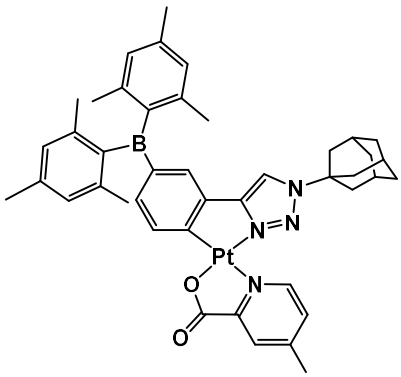

(*m*-BptrzAd)Pt(4-Mepic) (2.7): (28% yield). ^{1}H NMR (400 MHz, CD_2Cl_2):δ9.33 (d, ^{3}J=5.5 Hz, 1H), 7.99 (s, 1H), 7.80 (s, 1H), 7.75 (d, ^{3}J=7.6 Hz, 1H), 7.60 (d, ^{3}J=4Hz, 1H), 7.51 (s, 1H), 7.25 (dd, ^{3}J=7.7 Hz, 4J=1.4 Hz, 1H), 6.87 (s, 4H), 2.54 (s, 3H), 2.33 (m, 15H), 2.04 (s, 12H), 1.87 (m, 6H). Elemental analysis calcd (%) for **2.7**·CH_2Cl_2 ($C_{44}H_{49}BCl_2N_4O_2Pt$): C 56.06, H 5.24, N 5.94, found: C 55.97, H 5.22, N 5.93.

2.3.3.3 General Procedure to Synthesize Pl(II) Complexes 2.8-2.11

The ancillary ligand ***t*-Bu-pytrz-Me** and **CF_3-pytrz-Me** were synthesized according to literature procedure.[4]

The **Bptrz** ligand (0.10 mmol) and $[PtMe_2(u\text{-}SMe_2)]_2$ (0.055 mmol) were added to a 20 mL screw-cap vial with 5 mL of acetone. The mixture was heated at 70 °C for 3 hours before 1mL of 0.1M solution of TsOH in acetone was added. The resulting solution was stirred for 1 hour, then 0.13 mmol of corresponding **pytrz** ligand in acetone was added and the mixture was stirred at room temperature for 3 days. The product was filtered and washed with hexane, diethyl ether and methanol. The product was further purified via recrystallization from dichloromethane/hexane.

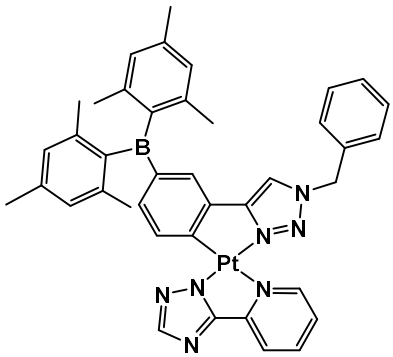

(*m*-BptrzBn)Pt(pytrz) (2.8): (23% yield). ^{1}H NMR (400 MHz, CD_2Cl_2): δ 9.76 (d, ^{3}J=6 Hz, 1H), 9.12 (d, ^{3}J=7.6 Hz 1H), 8.16-8.09 (m, 3H), 7.65 (s, 1H), 7.50-7.40 (m, 7H), 7.33 (dd, ^{3}J=7.8 Hz, 4J=1.5Hz, 1H), 6.85 (s, 4H), 5.65 (s, 2H), 2.33 (s, 6H), 2.05 (s, 12H). Elemental analysis calcd (%) for **2.8**·1/2 CH_2Cl_2 ($C_{40.5}H_{39}BClN_7Pt$): C 56.23, H 4.54, N 11.33, found: C 56.38, H 4.84, N 10.90.

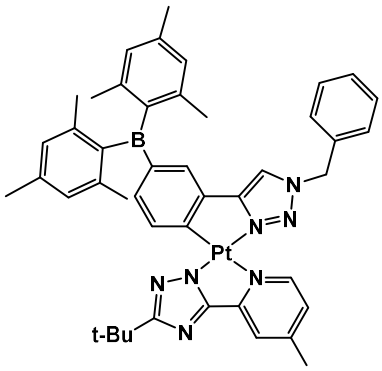

(m-BptrzBn)Pt(*t*-Bu-pytrz-Me) (2.9): (27% yield). ^{1}H NMR (400 MHz, CD_2Cl_2): δ 9.52 (d, ^{3}J=5.1 Hz, 1H), 9.19 (d, ^{3}J=7.5 Hz 1H), 7.94 (s, 1H), 7.61 (s, 1H), 7.50-7.40 (m, 6H), 7.30 (m, 2H), 6.85 (s, 4H), 5.62 (s, 2H), 2.54 (s, 3H), 2.33 (s, 6H), 2.05 (s, 12H), 1.48 (s, 9H); elemental analysis calcd (%) for $C_{45}H_{48}BN_7Pt$: C 60.54, H 5.42, N 10.98, found: C 60.64, H 5.45, N 10.87.

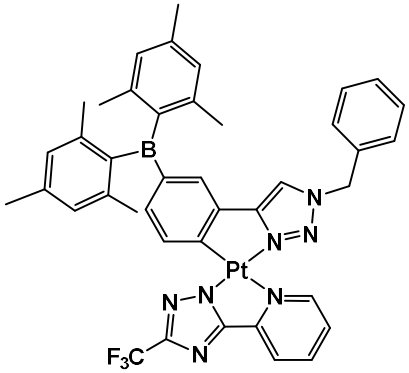

(m-BptrzBn)Pt(CF_3-pytrz-Me) (2.10): (25% yield). ^{1}H NMR (400 MHz, CD_2Cl_2): δ 9.58 (d, ^{3}J=5.7 Hz, 1H), 8.96 (d, ^{3}J=7.7 Hz 1H), 8.02 (s, 1H), 7.63 (s, 1H), 7.50-7.40 (m, 7H), 7.32 (m, 1H), 6.84 (s, 4H), 5.65 (s, 2H), 2.56 (s, 3H), 2.33 (s, 6H), 2.05 (s, 12H). Elemental analysis calcd (%) for **2.10**·CH_2Cl_2 ($C_{43}H_{41}BN_7Cl_2F_3Pt$): C 52.48, H 4.20, N 10.01, found: C 52.19, H 4.17, N 9.91.

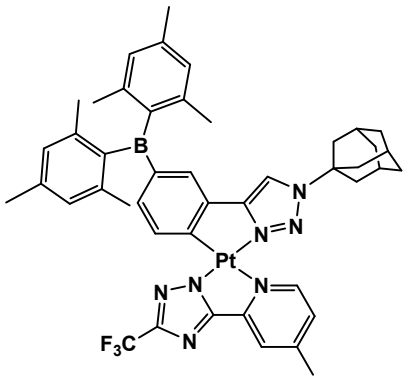

(m-BptrzAd)Pt(CF_3-pytrz-Me) (2.11): (27% yield). ^{1}H NMR (400 MHz, CD_2Cl_2): δ 9.57 (d, ^{3}J=5.6 Hz, 1H), 8.96 (d, ^{3}J=7.6 Hz 1H), 8.03 (s, 1H), 7.87 (s, 1H), 7.56 (s, 1H), 7.44 (d, ^{3}J=6.1 Hz,1H), 7.32 (dd, ^{3}J=7.8 Hz, ^{4}J=1.3 Hz, 1H), 6.88 (s, 4H), 2.57 (s, 3H), 2.36 (m, 15H), 2.08 (s, 12H), 1.89 (m, 6H). Elemental analysis calcd (%) for **2.11**·THF ($C_{49}H_{55}BN_7O_1F_3Pt$): C 57.64, H 5.45, N 9.60, found: C 57.97, H 5.49, N 9.17.

2.3.4 X-Ray Diffraction Analysis

Single crystals of **2.1**, **2.4-2.6**, **2.7a**, and **2.8-2.10** were obtained from either CH_2Cl_2 or THF by slow evaporation of the solvent. For some of the compounds, it was necessary to add either methanol or hexanes to facilitate the crystal growth. The crystals were mounted on glass fibers and the data were collected on a Bruker Apex II single-crystal X-ray diffractometer with graphite-monochromated Mo Kα radiation, operating at 50 kV and 30 mA, and at 180 K. Data were processed on a PC with the aid of the Bruker SHELXTL software package (version 6.14)[21] and corrected for absorption effects. All structures were solved using direct methods. CH_2Cl_2 solvent molecules were located in the lattices of **2.9** and **2.10** and refined successfully. THF and methanol were located in the crystal lattice of **2.5** and were modelled and refined successfully. THF solvent molecules were located in the crystal lattices of **2.6** and **2.7a**, which were all modelled and refined successfully except one disordered THF molecule in **2.7a** that was removed by the Platon Squeeze routine to improve the quality of the structural data.[22] All non-hydrogen atoms were refined anisotropically. CCDC 955635-955642 contains all the crystallographic data. These data can be obtained free of charge from The Cambridge Crystallographic Data Centre via www.ccdc. cam.ac.uk/data_request/cif.

2.3.5 EL Device Fabrication

Devices were fabricated in a three-chamber evaporator (EL-OEL cluster tool) with a base pressure of $\sim 1\times10^{-5}$ Pa without breaking vacuum. The ITO anode is commercially patterned and coated on glass substrates 50×50 mm^2 with a sheet resistance less than 15 Ω. Substrates were ultrasonically cleaned with a standard regiment of Alconox, acetone, and methanol followed by UV ozone

treatment for 15 minutes. The active area for all devices was 2 mm^2. The film thicknesses were monitored by a calibrated quartz crystal microbalance and were further verified for single-carrier devices using capacitance-voltage measurements (Agilent 4294A). I-V characteristics were measured using a HP4140B picoammeter in ambient air. Luminance measurements and EL spectra were taken using a Minolta LS-110 luminance meter and an Ocean Optics USB200 spectrometer with bare fiber, respectively. The external quantum efficiency of EL devices was calculated following the standard procedure.[23]

2.4 Conclusions

A series of new blue and blue-green phosphorescent $BMes_2$-functionalized Pt(II) compounds with C^N-coordinating Bptrz ligands are successfully synthesized and characterized. Three different types of ancillary ligands are examined and are found to have a distinct impact on the photophysical properties with the pyridyl-1,2,4-triazole (pytrz) ligand being the most effective in achieving bright blue phosphorescent Pt(II) compounds. The double intramolecular hydrogen bonds formed between pytrz and Bptrz in the complex is found to enhance the stability and the emission efficiency of the Pt(II) compounds. Substituent groups on the ancillary ligands are found to greatly impact the extent of excimer formation and the quantum efficiency. Bright white phosphorescence as a result of the monomer and excimer emission is observed in some of the Pt (II)compounds. The performance of two (Bptrz)Pt(pytrz) compounds demonstrates that they are very promising candidates in fabricating highly efficient greenish-blue or white phosphorescent OLEDs.

2.5 Notes and References

The work described in this chapter includes contributions from the following publications:

- X. Wang, Y.-L. Chang, J. S. Lu, T. Zhang, Z. H. Lu, S. Wang, *Adv. Funct. Mater.*, **2014**, 24, 1911.
- Y. L. Chang, S. Gong, X. Wang, R. White, C. Yang, S. Wang, and Z. H. Lu, *Appl. Phys. Lett.*, **2014**, 104, 173303.

References

(1) (a) H. Fu, Y.-M. Cheng, P.-T. Chou, Y. Chi, *Mater. Today*, **2011**, 14, 472 and references therein. (b) Y. Chi and P. T. Chou, *Chem. Soc. Rev.*, **2010**, *39*, 638, and references therein. (c) Y. You. S. Y. Park. *Dalton Trans.* **2009**, 1267.

(2) (a) A. B. Tamayo, B. D. Alleyne, P. I. Djurovich, S. Lamansky, I. Tsyba, N. N. Ho, R. Bau, M. E. Thompson, *J. Am. Chem. Soc.* **2003**, *125*, 7377. (b) J. Li, P. I. Djurovich, B. D. Alleyne, M. Yousufuddin, N. N. Ho, J. C. Thomas, J. C. Peters, R. Bau, M. E. Thompson, *Inorg. Chem.* **2005**, *44*, 1713. (c) R. J. Holmes, B. W. D'Andrade, S. R. Forrest, X. Ren, M. E. Thompson, *Appl. Phys. Lett.* **2003**, ***83***, 3818.

(3) S.-C. Lo, C. P. Shipley, R. N. Bera, R. E. Harding, A. R. Cowley, P. L. Burn, I. D. W. Samuel, *Chem. Mater.* **2006**, *18*, 5119.

(4) E. Orselli, G. S. Kottas, A. E. Konradsson, P. Coppo, R. Fröhlich, L. D. Cola, A. V. Dijken, M. Büchel, H. Börner, *Inorg. Chem.*, **2007**, *46*, 11082.

(5) C.-J. Chang, C.-H. Yang, K. Chen, Y. Chi, C.-F. Shu, M.-L. Ho, Y.-S. Yeh, P.-T. Chou, *Dalton Trans.*, **2007**, 1881.

(6) Y.-S. Yeh, Y.-M. Cheng, P.-T. Chou, G.-H. Lee, C.-H. Yang, Y. Chi, C.-F. Shu, C.-H. Wang, *ChemPhysChem.* **2006**, *7*, 2294.

(7) C.-F. Chang, Y.-M. Cheng, Y. Chi, Y.-C. Chiu, C.-C. Lin, G.-H. Lee, P.-T. Chou, C.-C. Chen, C.-H. Chang, C.-C. Wu, *Angew. Chem., Int. Ed.*, **2008**, *47*, 4542.

(8) V. Sivasubramaniam, F. Brodkorb, S. Hanning, H. P. Loebl, V. V. Elsbergen, H. Boerner, U. Scherf, M. Kreyenschmidt, *J. Fluor. Chem.*, **2009**, *130*, 640.

(9) (a) R. Seifert, I. R. D. Moraes, S. Scholz, M. C. Gather, B. Lüssem, K. Leo, *Org. Electronics*, **2013**, *14*, 115. (b) E. Baranoff, S. Suàrez, P. Bugnon, C. Barolo, R. Buscaino, R. Scopelliti, L. Zuppiroli, M. Graetzel, Md. K. Nazeeruddin, *Inorg. Chem*. **2008**, *47*, 6675.

(10) (a) Y.-C. Chiu, Y. Chi, J.-Y. Hung, Y.-M. Cheng, Y.-C. Yu, M.-W. Chung, G.-H. Lee, P.-T. Chou, C.-C. Chen, C.-C. Wu, H.-Y. Hsieh, *ACS Appl. Mater. Interfaces.*, **2009**, *1*, 433. (b) C.-H. Lin, Y.-Y. Chang, J.-Y. Hung, C.-Y. Lin, Y. Chi, M.-W. Chung, C.-L. Lin, P.-T. Chou, G.-H. Lee, C.-H. Chang, W.-C. Lin, *Angew. Chem. Int. Ed.* **2011**, *50*, 3182. (c) C.-H. Chang, C.-L. Ho, Y.-S. Chang, I.-C. Lien, C.-H. Lin, Y.-W. Yang, J.-L. Liao, Y. Chi, *J. Mater. Chem. C*, **2013**, *1*, 2639.

(11) X.-C. Hang, T. Fleetham, E. Turner, J. Brooks, J. Li, *Angew. Chem. Int. Ed.*, **2013**, *52*, 6753.

(12) X. Yang, Z. Wang, S. Madakuni, J. Li, G. E. Jabbour, *Adv. Mater.*, **2008**, *20*, 2405.

(13) (a) M. Cocchi, J. Kalinowski, V. Fattori, J. A. G. Williams, L. Murphy, *Appl. Phys. Lett.*, **2009**, *94*, 073309. (c) J. A. G. Williams, S. Develay, D. L. Rochester, L. Murphy, *Coord. Chem. Rev.* **2008**, *252*, 2596.(d) L. Murphy, P. Brulatti, V. Fattori, M. Cocchi and J. A. G. Williams, *Chem. Commun.* **2012**, *48*, 5817.

(14) X. Zhang, A. M. Wright, N. J. DeYonker, T. K. Hollis, N. I. Hammer, C. E. Webster, E. J. Valente, *Organometallics*, **2012**, *31*, 1664.

(15) Y. Rao, D. Schoenmakers, Y.-L. Chang, J. Lu, Z.-H. Lu, Y. Kang, S. Wang, *Chem. Eur. J.*, **2012**, *18*, 11306.

(16) Z. M. Hudson, C. Sun, M. G. Helander, Y.-L. Chang, Z.-H. Lu, S. Wang, *J. Am. Chem. Soc.*, **2012**, *134*, 13930.

(17) J. Brooks, Y. Babayan, S. Lamansky, P.I. Djurovich, I. Tsyba, R. Bau, M.E. Thompson, *Inorg. Chem.*, **2002**, *41*, 3055.

(18) H. Yersin, A. F. Rausch, R. Czerwieniec, T. Hofbeck and T. Fischer, *Coord. Chem. Rev.*, **2011**, 255, 2622.

(19) (a) Z. M. Hudson, C. Sun, M. G. Helander, H. Amarne, Z.-H. Lu, S. Wang, *Adv. Funct. Mater.* **2010**, *20*, 3426. (b) Z. M. Hudson, S. Wang, *Dalton Trans.*, **2011**, *40*, 7805. (c) Z. Wang, M. G. Helander, Z. M. Hudson, J. Qiu, S. Wang, Z. -H. Lu. *Appl. Phys. Lett.*, **2011**, *98*, 213301. (d) Z. M. Hudson, M. G. Helander, Z.-H. Lu, S. Wang. *Chem. Commun.*, **2011**, *47*, 755.

(20) M. J. Frisch, G. W. Trucks, H. B. Schlegel, G. E. Scuseria, M. A. Robb, J. R. Cheeseman, J. A. Montgomery, Jr., T. Vreven, K. N. Kudin, J. C. Burant, J. M. Millam, S. S. Iyengar, J. Tomasi, V. Barone, B. Mennucci, M. Cossi, G. Scalmani, N. Rega, G. A. Petersson, H. Nakatsuji, M. Hada, M. Ehara, K. Toyota, R. Fukuda, J. Hasegawa, M. Ishida, T. Nakajima, Y. Honda, O. Kitao, H. Nakai, M. Klene, X. Li, J. E. Knox, H. P. Hratchian, J. B. Cross, C. Adamo, J. Jaramillo, R. Gomperts, R. E. Stratmann, O. Yazyev, A. J. Austin, R. Cammi, C. Pomelli, J. W. Ochterski, P. Y. Ayala, K. Morokuma, G. A. Voth, P. Salvador, J. J. Dannenberg, V. G. Zakrzewski, S. Dapprich, A. D. Daniels, M. C. Strain, O. Farkas, D. K. Malick, A. D. Rabuck, K. Raghavachari, J. B. Foresman, J. V. Ortiz, Q. Cui, A. G. Baboul, S. Clifford, J. Cioslowski, B. B. Stefanov, G. Liu, A. Liashenko, P. Piskorz, I. Komaromi, R. L. Martin, D. J. Fox, T. Keith, M. A. Al-Laham, C. Y. Peng, A. Nanayakkara, M. Challacombe, P. M. W. Gill, B. Johnson, W. Chen, M. W. Wong, C. Gonzalez, and J. A. Pople. Gaussian 03, revision C.02; Gaussian, Inc.: Wallingford, CT, 2004.

(21) Shelxtl Version 6.14, Bruker AXS, copyright 2000-2003.

(22) (a) A. L. Spek, *Acta. Cryst*. **2009**, *D65*, 148. (b) PLATON-A multipurpose Crsytallographyic Tool, Utrecht University, Utrecht, The Netherlands, A. P. Spek, 2011.

(23) S. R. Forrest, D. D. C. Bradley, and M. E. Thompson, *Adv. Mater.* **2003**, *15*, 1043.

(24) Z. M. Hudson, B. A. Blight, S. Wang, *Org. Lett.*, **2012**, *14*, 1700.

(25) S.-B. Ko, J.-S. Lu, Y. Kang, S. Wang, *Organometallics*, 2013, *32*, 599.

(26) C. D. Pietro, S. Serroni, S. Campagna, T. Gandolfi, R. Ballardini, S. Fanni, W. R. Browne, J. G. Vos, *Inorg. Chem.*, **2002**, *41*, 2871.

(27) H. Sasabe, J. Kido, *J. Mater. Chem. C*, **2013**, *1*, 1699 and references therein.

(28) (a) Y. Sun, N. C. Giebink, H. Kanno, B. Ma, M. E. Thompson, S. R. Forrest, *Nature,* **2006**, ***440**, 908.* (b) B. W. D'Andrade, S. R. Forrest, *Adv. Mater.* **2004**, ***16**,* 1585. (c) E. L. Williams, K. Haavisto, J. Li, G. E. Jabbour, *Adv. Mater.* **2007**, ***19**,* 197 (d) M. Cocchi, J. Kalinowski, D. Virgili, V. Fattori, S. Develay, J. A. G. Williams, *Appl. Phys. Lett.* **2007**, ***90**,* 163508.

(29) (a) L. Xiao, Z. Chen, B. Qu, J. Luo, S. Kong, Q. Gong, J. Kido, *Adv. Mater*., **2011**, *23*, 926. (b) K. S. Yook, J. Y. Lee, *Adv. Mater*., **2012**, *24*, 3169.

(30) H. Z. Siboni, H. Aziz, *Org. Electronics*, **2013**, *14*, 2510.

(31) T. Fleetham, J. Ecton, Z. X. Wang, N. Bakken, J. Li, *Adv. Mater*. **2013**, *25*, 2573.

(32) S. Gong, Y.-L. Chang, K. Wu, R. White, Z.-H. Lu, D. Song and C. Yang, *Chem. Mater.*, **2014**, 26, 1463.

(33) Y. L. Chang, S. Gong, X. Wang, R. White, C. Yang, S. Wang, and Z. H. Lu, *Appl. Phys. Lett.*, **2014**, 104, 173303.

Chapter 3

Bright Phosphorescent and Thermally Stable Pt(II) Compounds Based on a Phenyl-1,2,3-triazolyl and a Pyridyl-1,2,4-triazolyl Chelate Core

3.1 Introduction

As discussed in chapter 2, we have recently shown that a dimesitylboryl unit ($BMes_2$) is highly effective in enhancing the phosphorescent and electrophosphorescent efficiency of N^C- or C^C-chelated Pt(II) compounds.[1-2] The $BMes_2$ unit was found to enhance metal-to-ligand charge transfer (MLCT) and electron transporting process in OLEDs. Another important role of the $BMes_2$ unit is to provide steric shielding to the Pt(II) unit, owing to its bulky size, that greatly reduces the formation of excimer emission. Using this approach, we have successfully developed a series of blue and blue-green phosphorescent Pt(II) compounds with a phenyl-1,2,3-triazole chromophore.[3] Among them, the best blue emitters are those shown in Chart 3.1 that contain a pyridyl-1,2,4-triazolyl (pytrz) unit as the ancillary ligand. Although these molecules display a high phosphorescent quantum efficiency (Φ_{PL}) in films (e.g. PMMA) at a low doping concentration, the excimer formation became significant, accompanied by a substantial decrease of Φ_{PL} at higher doping concentrations (e.g. R_1 = Me, R_2 = *t*Bu, Φ_{PL} = 0.97 in 5 wt% of PMMA, 0.65 in 10 wt% of PMMA; R_1 = Me, R_2 =CF_3, Φ_{PL} = 0.71 in 5 wt% of PMMA, 0.47 in 10 wt% of PMMA), which became much more pronounced in OLEDs. This is caused mainly by the propensity of the triazolyl unit to stack and the *meta*-location of the $BMes_2$ group that is less effective in shielding the central core from excimer formation compared to the *para*-location. Moving the $BMes_2$ unit to the *para*-position will produce more effective steric shielding in the cost of red-shifted emission energy. Nonetheless, our study on the *m*-$BMes_2$ functionalized Pt(II) compounds revealed that the Pt(II)

unit with the *m*-Bptrz and the pytrz chelate ligands have interesting features. For example, the two intramolecular hydrogen bonds in the central core minimize the structural distortion of the molecule in the excited state. Furthermore, computational studies suggested that the central core of this class of molecules has a triplet energy in the blue region, making them attractive for further investigation as potential blue emitters for OLEDs. One weakness of $BMes_2$-functionalized Pt(II) compounds is that they have a relatively low thermal stability (typically less than 250°C), which could make it difficult for vacuum deposition of molecules that have a relatively high molecular weight. Thus, with the aim to develop a new class of highly robust blue phosphorescent Pt(II) compounds that are relatively easy to access synthetically, we carried out the investigation on new Pt(II) compounds based on the ptrz (phenyl-1,2,3-triazolyl) and the pytrz central core, which lack the $BMes_2$ unit. The key approach we employed is to provide steric shielding for the central Pt(II) unit using non-borylated groups. Highly efficient blue, blue-green and green Pt(II) phosphorescent emitters with high thermal stability have been achieved and their performance in OLEDs has been evaluated.

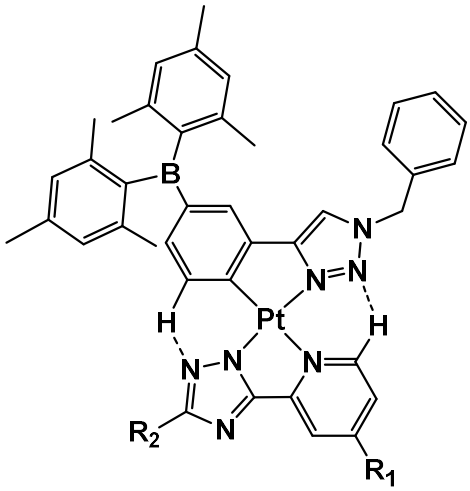

R_1 = H or Me; R_2 = H or tBu, or CF_3

Chart 3.1

3.2 Results and Discussion

3.2.1 Synthesis

Five ptrz derivative ligands containing substituents of varied steric bulkiness and electronic properties were synthesized as the chelate chromophores for the Pt(II) compounds. Four of ligands contains a benzyl group on the 1,2,3-triazole ring while the last has a diphenylmethyl group. **ptrzBn** has no substituent on the phenyl portion of the chelate while **FptrzBn** and **NptrzBn** have two fluorine atoms and a diphenylamino group on the phenyl ring, respectively, which are intended to alter the HOMO-LUMO gap in order to tune the emission color of the corresponding Pt(II) complexes. The bulky NPh_2 group at the *para*-position to the trz group in **NptrzBn** also provides steric shielding to the Pt center to minimize excimer emission. **CptrzBn** and **Cptrzp2C** contain a triphenylmethyl group at the *para*-position of the phenyl ring which is intended to increase the steric bulk around the Pt(II) unit while decreasing the electron donation to the chelate ligand, in order to prevent excimer formation and keep the emission color in the blue region. **ptrzBn** were synthesized using a modified procedure from literature, which involves the reaction of phenylacetylene or 1-ethynyl-2,4-difluorobenzene with benzyl azide in water in the presence of copper iodide in a sealed pressure tube at 50°C overnight (Scheme 3.1 top).[4] This procedure works the best for starting materials that are either liquid or have low melting points. After the reaction is finished, the product simply precipitates out and can be purified by just filtering and washing. **Nptrz** and **Cptrz** were synthesized using the procedure similar to that employed for *m*-Bptrz ligands we reported earlier (Scheme 3.1 bottom). This procedure gives higher yields (~70%), compared to the first one (~50%), but aqueous work up and column chromatography are needed to obtain the pure products. Two Me-pyridyl-1,2,4-triazole ancillary ligands (Me-pytrz) are

synthesized by previously published procedures.[5] The t-Bu and the CF_3 subtituents on the Me-pytrz ligand allows us to examine the steric and electronic effect of the ancillary ligand on the phosphorescence of the Pt(II) compounds.

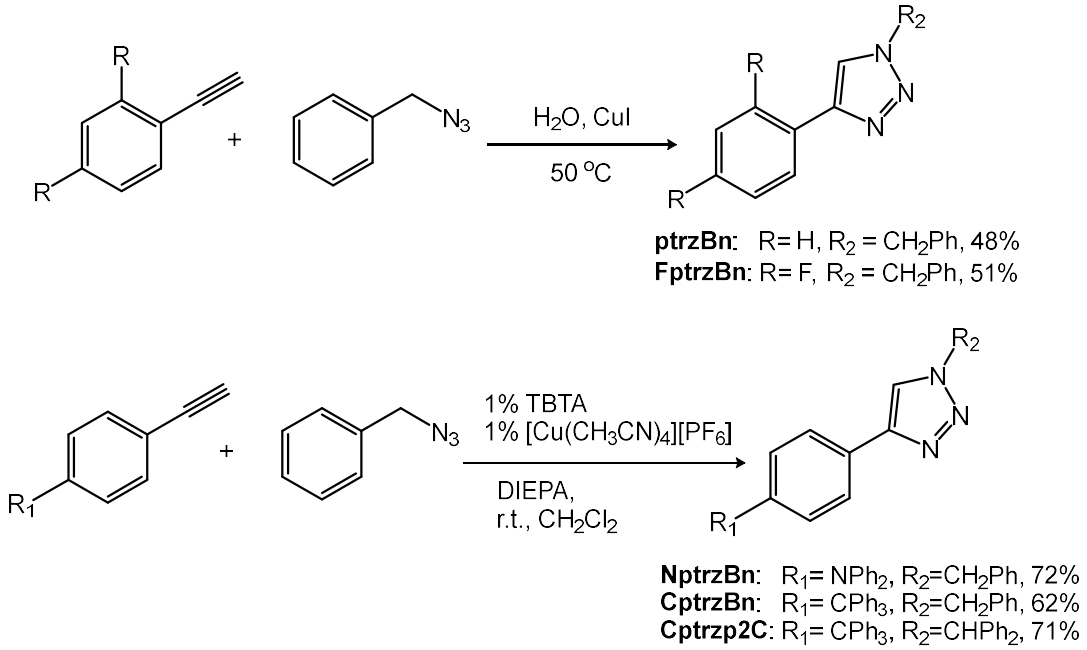

Scheme 3.1. The syntheses of ligands

Nine Pt(II) compounds with different combinations of the cyclometallating ligands and the ancillary ligands were synthesized using a modified one-pot procedure developed by our group (Scheme 3.2).[6] The appropriate ptrz ligand and $[PtMe_2(SMe_2)]_2$ are heated at 70 °C for 1 hour in acetone, followed by the addition of tosylic acid (TsOH) and the subsequent addition of the corresponding Me-pytrz ancillary ligand. After purification, the Pt(II) compounds were obtained in 14 – 46% yields. All Pt(II) compounds have been fully characterized by ^{1}H NMR and elemental analyses.

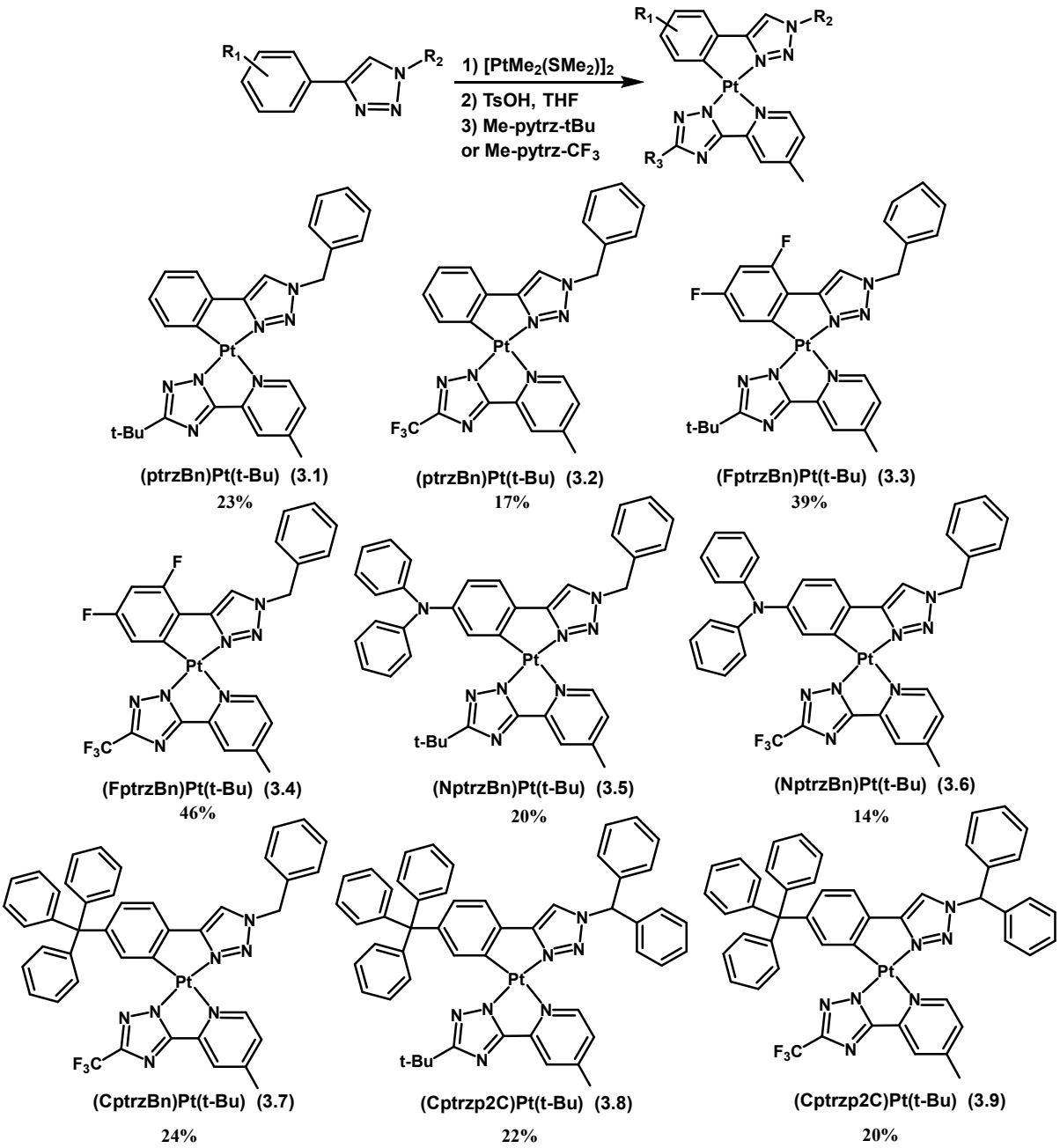

Scheme 3.2. The syntheses and structures of Pt(II) compounds

3.2.2 Crystal Structures

The crystal structures of compounds **3.4**, **3.5**, and **3.7-3.9** have been determined by single-crystal X-ray diffraction analyses. Important bond lengths and angles of these compounds are given in

Table 3.1. As shown in Figure 3.1, the molecules of **3.4** form a stacked dimer with a very short Pt···Pt separation distance (3.228(1) Å). The py-1,2,4-triazolyl ancillary ligand stacks with the ph-1,2,3-triazolyl ligand with short separation distances (3.35-3.50 Å). Between the dimers, the Pt···Pt separation distance is much larger (5.238(1) Å). Compound **3.4** exists likely as a dimer in solution as indicated by dimer peaks in the mass spectroscopic analysis. DFT computational data indicate that the HOMO and LUMO of **3.4** are localized mainly on the ptrz-Pt and the py-trz chelate unit, respectively (see the computational section below), which clearly favors intermolecular π-stacking between these two units. The attractive Pt···Pt interaction and the flat structure of **3.4** further enhance the dimer formation. Although discrete dimers are not observed for compound **3.3** in MS spectroscopic analysis, intermolecular interactions between the molecules are strong, owing to its flat and un-shielded structure.

Table 3.1 Important bond lengths and angles of the Pt(II) compounds

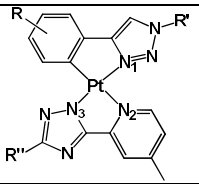	Pt-C	Pt-N_1	Pt-N_2	Pt-N_3	Pt···Pt	N_2 -Pt-C /N_1-Pt-N_3
3.4	2.024(9) 2.012(9)	2.007(7) 1.974(7)	2.120(8) 2.117(8)	1.981(7) 1.979(8)	3.2276(4)	175.8(3)/ 176.9(3) 179.3(3)/ 177.3(3)
3.5	1.978(8)	2.003(7)	2.133(7)	1.979(7)	6.508(1)	177.0(2)/178.3(3)
3.7	1.995(9)	1.979(8)	2.124(7)	1.991(8)	4.819(1)	178.8(3)/179.5(3)
3.8	2.017(3)	2.004(3)	2.133(3)	1.985(3)	4.960(1)	178.14(15)/179.23(12)
3.9	1.980(11)	2.001(7)	2.098(9)	2.002(7)	4.294(1)	178.4(3)/179.4(3)

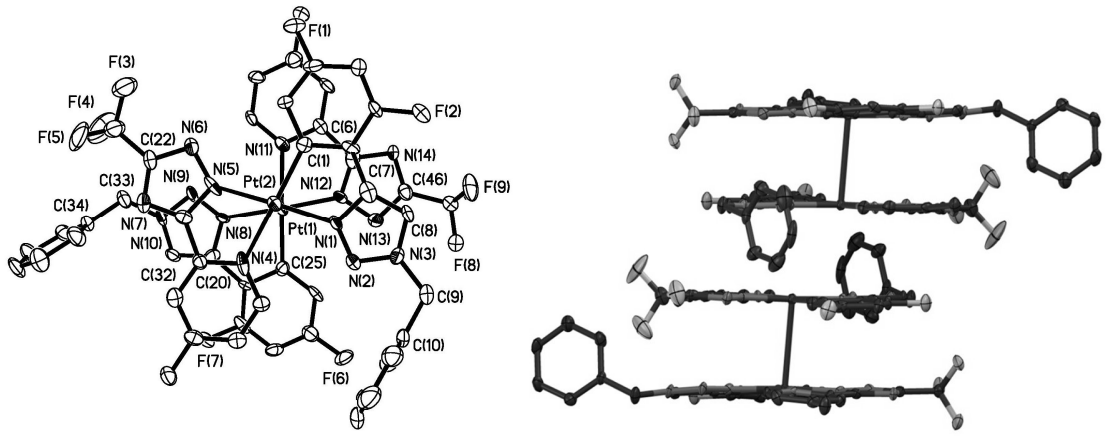

Figure 3.1 The crystal structure of compound **3.4**, showing the stacked dimer (left: top view, right: side view), with labeling schemes and 50% thermal ellipsoids. H atoms are omitted for clarity.

The crystal structures of **3.5** and **3.7** are shown in Figure 3.2 while those of **3.7** and **3.8** in Figure 3.3. In contrast to compound **3.4**, no significant intermolecular interactions are observed in the crystal lattice of **3.5** with the shortest Pt···Pt separation distance being 6.508(1) Å. The bulky NPh_2 group along with the t-butyl group is clearly effective in preventing stacking. Interestingly, despite the presence of the bulky CPh_3 group in **3.7**, extended and partial π stacking is observed in the crystal lattice of **3.7**, as shown in Figure 3.4. The Pt···Pt separation distances are 4.819(1) Å and 5.850(1) Å, respectively, between the neighboring molecules, and the shortest atomic separation distance is ~3.5 Å between the heterocyclic chelate ligands in **3.7**. This indicates that the CF_3 on the ancillary ligand is not very effective in blocking intermolecular interactions. This is further supported by the crystal structure of **3.9**, in which the benzyl group is replaced by a diphenylmethyl group. As shown in Figure 3.4, there is partial π stacking in the crystal lattice of **3.9**, leading to the formation of discrete dimers with a 4.294(1) Å Pt···Pt separation distance within the dimer. The *t*-butyl group in **3.8** appears to be more effective in reducing π-stacking interactions, as evidenced

by the larger Pt···Pt separation distance of 4.960(1) Å within the partially π-stacked dimer of **3.8** and the lack of extended π-stacking interactions (Figure 3.4).

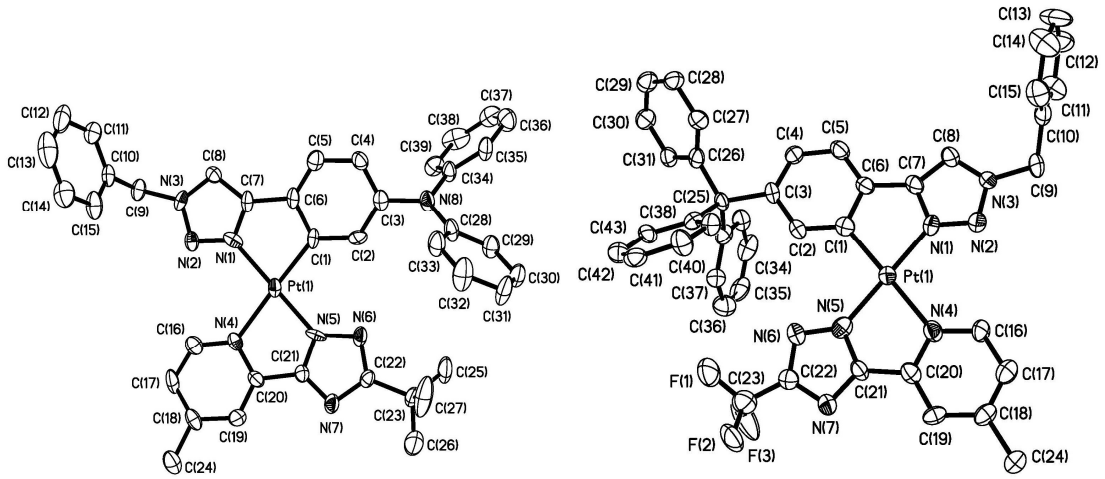

Figure 3.2 The crystal structures of compound **3.5** (left) and **3.7** (right) with labeling schemes and 50% thermal ellipsoids. H atoms are omitted for clarity.

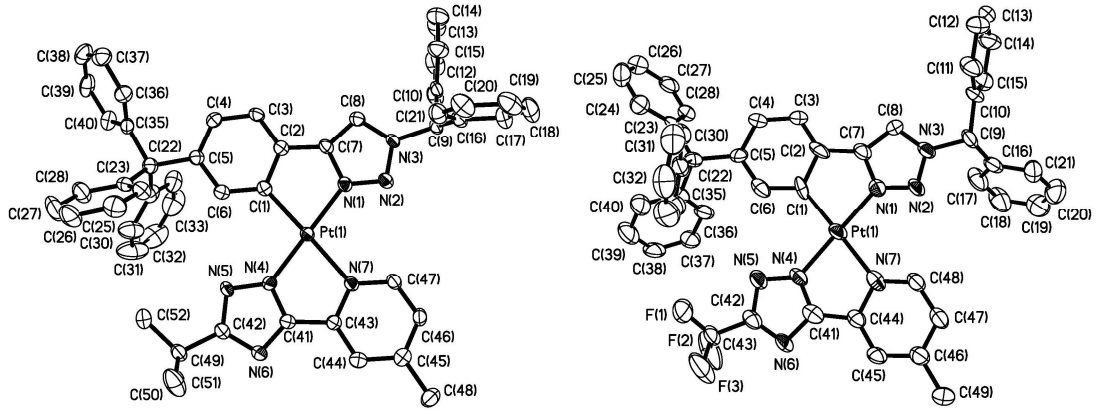

Figure 3.3 The crystal structures of compound **3.8** (left) and **3.9** (right) with labeling schemes and 50% thermal ellipsoids. H atoms are omitted for clarity.

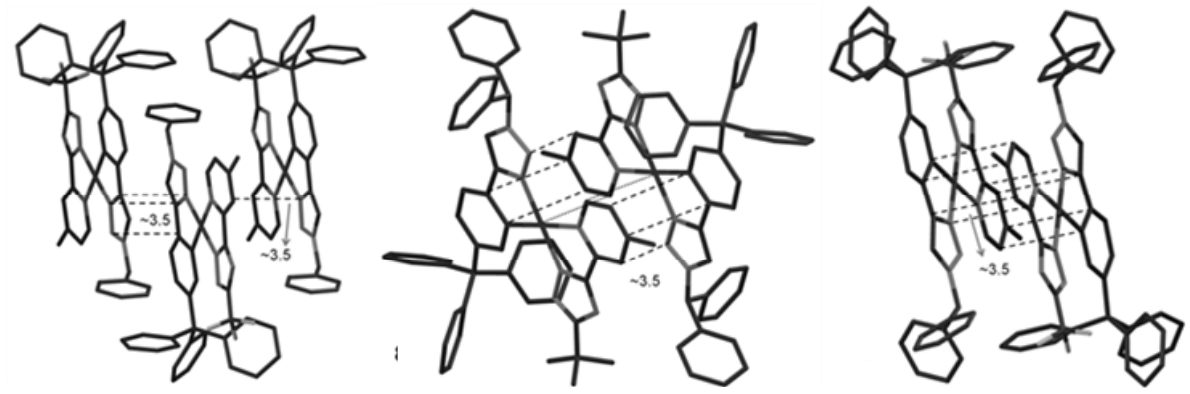

Figure 3.4 Diagram showing intermolecular π stacking interactions in the crystal lattice of **3.7** (left), **3.8** (middle) and **3.9** (right).

The crystal structural data show that the introduction of a bulky substituent group such as NPh_2 or CPh_3 on the ptrz ligand is indeed effective in substantially reducing π-stacking and Pt···Pt interactions. For the pytrz chelate ligand, a *t*-butyl group is more effective than a CF_3 group in reducing intermolecular interactions between the Pt(II) molecules.

3.2.3 Thermal stability

To examine the thermal stability of the new class of Pt(II) compounds and compare them with the $BMes_2$-functionalized compounds, thermogravimetric analysis (TGA) was performed for vacuum dried samples of compounds **3.7**-**3.9** and **2.9**. All four compounds contain solvent molecules in their crystal lattices, according to the X-ray crystal structural data (1 THF for **3.7**, 2, 2.4 and 1 CH_2Cl_2 for **3.8**, **3.9** and **2.9**, respectively). To remove these solvent molecules, all samples were kept under vacuum overnight and heated for 10 minutes at 100°C under nitrogen before recording the TGA diagrams. The TGA diagrams for these four compounds recorded under nitrogen atmosphere are shown in **Figure 3.5**. It is evident that the $BMes_2$-functionalized molecule is the

least stable thermally while compound **3.7** is the most stable and does not show any weight loss until ~400°C. Compounds **3.8** and **3.9** also display an excellent thermal stability up to ~350°C. The less than 2% weight loss of **3.8** below 350°C is likely caused by the loss of residual solvent molecules. These data confirmed the relatively low thermal stability of $BMes_2$-functionalized compounds (most likely the dissociation of the $BMes_2$ unit from the chelate ligand, corresponding to ~28% weight loss) and the robustness of the non-$BMes_2$ functionalized Pt(II) molecules.

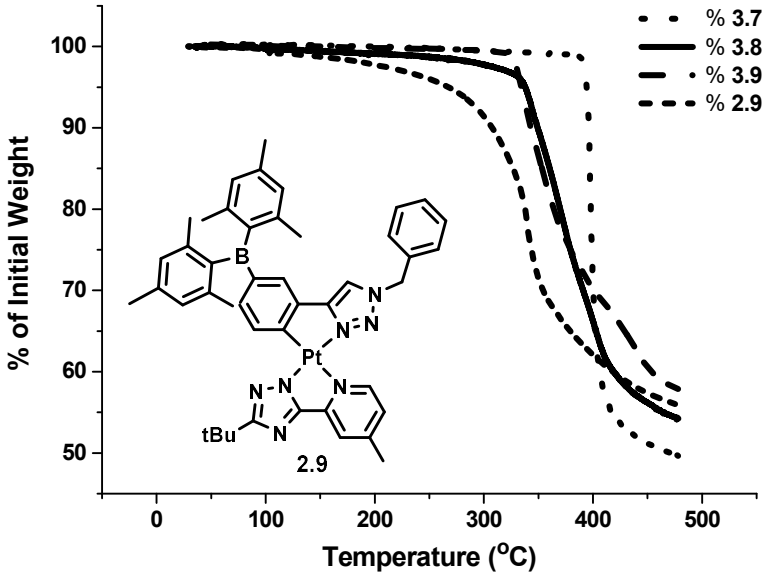

Figure 3.5 TGA diagrams for compounds **3.7-3.9** and **2.9**.

3.2.4 Luminescent Properties

The emission colors of compounds **3.1-3.9** range from blue to yellow (Figure 3.6) and their photophysical properties are listed in Table 3.2. All complexes show strong absorption bands at around 350 nm (ε= 13000-30000 M^{-1} cm^{-1}) which could be attribute to π-π* transitions (Figure 3.7). Compared to the $BMes_2$-functionalized compounds **2.9-2.10**, the π-π* transitions absorption bands of **3.1-3.9** are blue shifted by ~ 10 nm and are less intense, except for **3.5** and **3.6** which

have much larger extinction coefficients (~ 30000 M^{-1} cm^{-1}). Compounds **3.5** and **3.6** also display distinct low energy absorption bands at around 400 nm, probably due to the intramolecular charge transfer involving the electron rich diphenyl amine group.

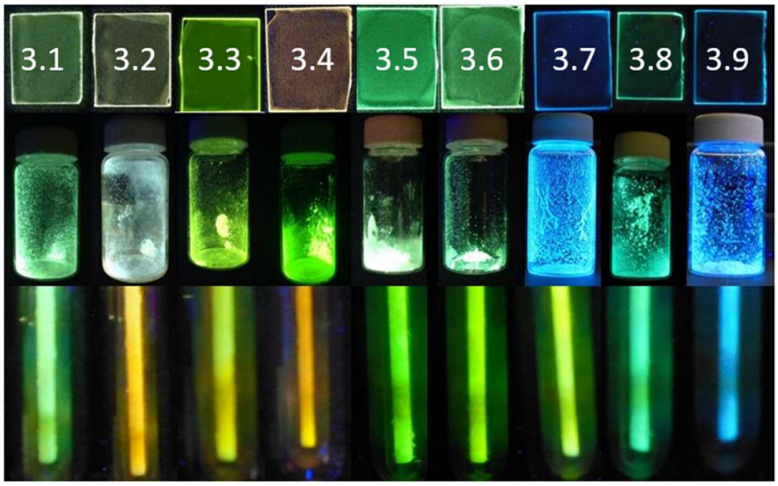

Figure 3.6 Photographs showing the emission colors of compounds **3.1-3.9** in 5 wt% PMMA films (top), as neat solids (middle) and in frozen CH_2Cl_2 glass (~2.0 x 10^{-5} M, bottom) at 77K.

Table 3.2 Photophysical data of Compounds **3.1-3.9**

	Absorption[a] λ_{max} [nm] ε [$10^4 cm^{-1} M^{-1}$]	Emission, λ_{max} [nm], 298 K						Emission 77 K[c]	
		λ_{max} [nm]			Φ_{PL}[b]			λ_{max} [nm]	τ_P [µs]
		CH_2Cl_2	PMMA (wt%)		CH_2Cl_2	PMMA (wt%)			
			5%	10%		5%	10%		
3.1	315 (1.30), 350 (1.37)	510	465,497	465,499	0.06	0.84	0.96	470	7.3
3.2	305 (0.91), 344 (1.24)	-	552	553	<0.001	0.64	0.29	440/ 556	4.2/ -
3.3	315 (1.05), 343 (1.19)	509	500	543	0.25	0.79	1.00	466/ 501	-/ 8.7
3.4	303 (0.79), 338 (1.31)	564	595	610	0.01	0.27	0.15	440/ 535	-/ 5.7
3.5	314 (3.23), 345 (3.24)	514	486	491	0.21	0.92	0.59	494	23.9
3.6	302 (2.17), 344 (3.12)	542	500	510	0.30	1.00	1.00	501/ 543	17.6/ 13.1
3.7	264 (3.34), 348 (1.16)	-	454	455	<0.001	1.00	0.89	448/ 543	7.7/ 3.6
3.8	276 (4.00), 354 (1.35)	512	468,496	468,498	0.13	0.90	0.95	460	5.3
3.9	266 (3.98), 348 (1.36)	-	452	453	<0.001	0.68	0.72	448	7.8

[a] Measured in CH_2Cl_2 at 2 x 10^{-5} M . [b] The solution quantum efficiency was determined in CH_2Cl_2 using $Ir(ppy)_3$ as the reference under nitrogen. The solid state quantum efficiency was measured using an integration sphere. All quantum yields are ± 10%. [c] Recorded in CH_2Cl_2 (~2.0 x 10^{-5} M).

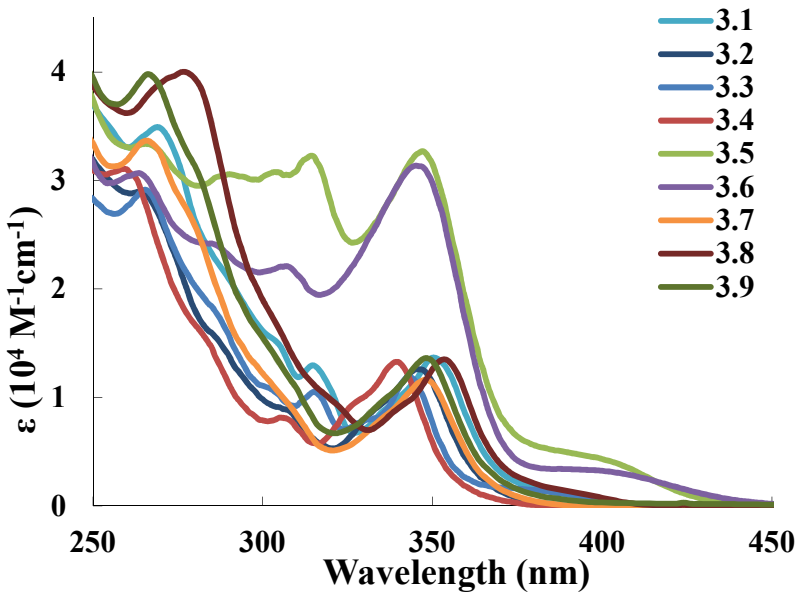

Figure 3.7 Absorption spectra of compounds **3.1-3.9** in CH_2Cl_2 at ambient temperature.

Compounds **3.1-3.9** display weak to moderate phosphorescence with quantum efficiencies up to 30% in deaerated CH_2Cl_2 solution at ambient temperature. However, all complexes show much brighter emissions in frozen CH_2Cl_2 glass at 77 K, as neat solid or in 5% or 10% doped PMMA films (Figure 3.6). The decay lifetimes of all compounds in frozen CH_2Cl_2 glass are in the microsecond range, indicating that the nature of their luminescence is phosphorescence. The electronic properties and the steric bulkiness of the substituent group play very important roles in determining the emission color and phosphorescent quantum efficiency of this type of compounds and will be discussed in details.

Compounds **3.1** and **3.2** with an unsubstituted phenyl backbone show resolved vibronic bands in frozen CH_2Cl_2 at 77K, implying that the emission is originated from a mixture of ^{3}LC and ^{1}MLCT states (Figure 3.8). However, a broad featureless band appears in the emission spectra of **3.2** in

doped PMMA films and in frozen glass at around 550 nm, which could be assigned to excimer emission due to intermolecular interactions. This is consistent with our previous observation that compounds with CF_3 group on the pytrz ligand are more prone to excimer formation than those with a t-butyl group. **3.2** also shows stronger excimer emission compared to its borylated counterpart **2.10** due to the lack of a bulkyl $BMes_2$ group that prevents short interrmolecular contacts. Compound **3.1** displays green luminescence (~500 nm) with very high quantum efficiencies (0.84 in 5 wt% PMMA, 0.96 in 10 wt% PMMA) in the solid state, which are comparable to **2.9** (0.97 in 5 wt% PMMA, 0.65 in 10 wt% PMMA). Compound **3.2** displays white color in 5 wt% PMMA and yellow color in 10 wt% PMMA with phosphorescent quantum yields of 0.64 and 0.29, respectively. It's worth noting that the λ_{max} of **3.2** in the solid state (~ 440 nm) is blue shifted by about 20 nm compared to **2.10**, implying the potential to obtain deep blue phosphoresce if the excimer emission could be eliminated.

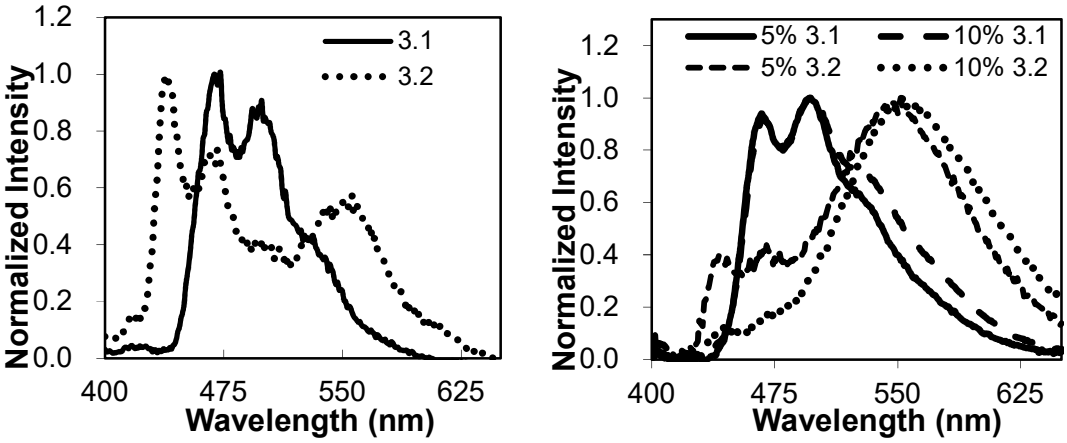

Figure 3.8 The phosphorescent emission spectra of **3.1** and **3.2** in PMMA at ambient temperature (left) and in frozen CH_2Cl_2 glass at 77 K (right).

One of the most common methods to tune the emission color of the cyclometallated Pt(II) complexes is to manipulate their HOMO/LUMO levels by introducing different functional groups.

Thompson et.al has observed a 20 nm blueshift in the emission energy by decorating the 4' and 6' positions of the phenyl ring of (ppy)Pt(acac) with two electronegative fluorine atoms.[7] Compounds **3.3** and **3.4**, with the introduction of two fluorine atoms on the ptrz ligand, display very strong excimer emission in doped PMMA film, as shown in Figure 3.9. The excimer emissions (λ_{max} = 500 nm in 5 wt% PMMA, λ_{max} = 543 nm in 10 wt% PMMA) of **3.3** in doped PMMA films are much stronger compared to **3.1,** although the quantum yields are still impressive (0.79 in 5 wt% PMMA, 1.00 in 10 wt% PMMA). Similar trend has been observed by us as **2.10** displays stronger excimer emission than **2.8** and may be explained by that the F atom favors excimer formation. In frozen CH_2Cl_2 glass, the emission spectrum of **3.3** displays more resolved bands with a lesser excimer contribution at 534 nm. When doped in PMMA films, pure excimer emissions are observed for **3.4** (λ_{max} = 595 nm in 5 wt% PMMA, λ_{max} = 610 nm in 10 wt% PMMA) with low quantum yields (0.27 in 5 wt% PMMA, 0.15 in 10 wt% PMMA). Emission spectrum at 77K reveals several less resolved bands between 400-500 nm that may be assigned to monomer emissions. The unusual high tendency for compound **3.4** to produce excimer emission can be rationalized by the formation of intrinsic dimers which are observed by both X-ray crystallography and mass spectrometry analysis.

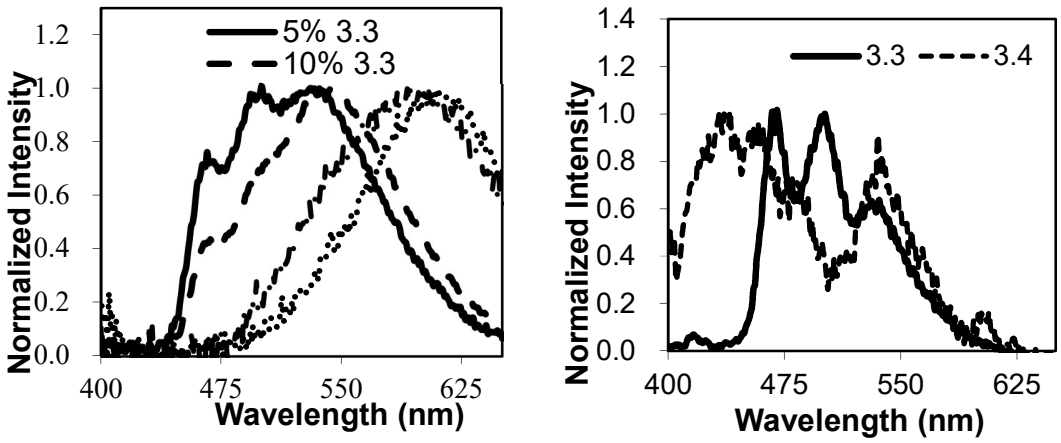

Figure 3.9 The phosphorescent emission spectra of **3.3** and **3.4** in PMMA at ambient temperature (left) and in frozen CH_2Cl_2 glass at 77 K (right).

Compounds **3.5** and **3.6**, with an electron donating diphenyl amine group on the phenyl ring, show red-shifted emission compared to **3.1** and **3.2**. Both compounds show green emissions in doped PMMA films, in frozen CH_2Cl_2 glass or in CH_2Cl_2 at ambient temperature. The most significant difference in their emission spectra of the doped PMMA films with respect to compounds **3.1-3.4** is that no excimer emission can be observed (Figure 3.10), which agrees with our previous finding that intermolecular interactions can be effectively reduced when a bulky group is introduced at the *para*-position of the phenyl ring. The decay lifetimes of **3.5** and **3.6** are substantially longer (23.9 μs for **3.5**, 17.6 μs for **3.6**) than those of the other complexes, indicating a small MLCT contribution in the excited state.[1a] The monomer emission energy of **3.5** and **3.6** is similar, in contrast to the previous pairs, in which the monomer emission peak of the CF_3 substituted molecule is always at a higher energy than the t-Butyl substituted analogue. This indicates that the phosphorescence of **3.5** and **3.6** is most likely from LC transitions localized on the Nptrz uint or LLCT transitions from the diphenylaminophenyl part of the Nptrz ligand to the pyridine part of the pytrz unit, which was confirmed by DFT calculation. Both **3.5** and **3.6** show excellent quantum

yields in doped PMMA films (0.92 / 0.59 for **3.5** in 5 wt% / 10 wt% PMMA, 1.00 for **3.6** in both 5% wt% and 10 wt% PMMA), making them good candidates as dopant for green OLEDs.

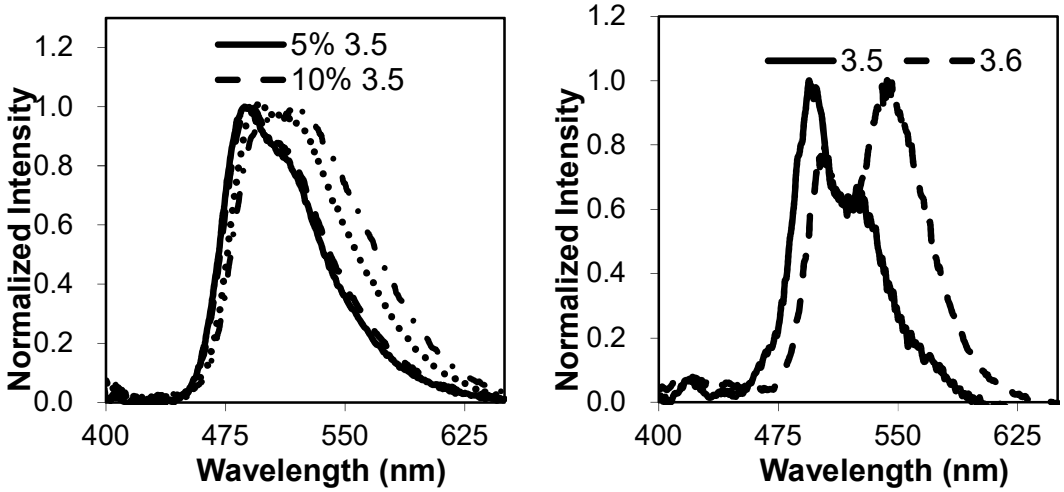

Figure 3.10 The phosphorescent emission spectra of **3.5** and **3.6** in PMMA at ambient temperature (left) and in frozen CH_2Cl_2 glass at 77 K (right).

Compounds **3.7-3.9**, bearing a bulky trityl group at the *para*-position of the phenyl ring, were synthesized based on the considerations that 1) a bulky group at the *para*-position is needed to reduce excimer emission; 2) the electron neutral triphenylmethyl group will have small impact on the HOMO-LUMO gap so that deep blue phosphorescence can be obtained. As shown in Figure 3.11, no excimer emission was found in the emission spectra of **3.7-3.9** in doped PMMA films and the emission maximum of all three compounds lie in the blue region (454 nm for **3.7**, 468 nm and 496 nm for **3.8**, and 452 nm for **3.9**) with excellent quantum efficiencies (1.00/0.89 for **3.7**, 0.90/0.95 for **3.8** and 0.68/0.72 for **3.9**, at 5 wt% and 10 wt% doping level in PMMA, respectively), indicating that this design is successful. Interestingly, an excimer peak with a decay lifetime of 3.6 μs appears in the emission spectrum of **3.7** in frozen CH_2Cl_2 glass, which is absent in the low temperature phosphorescence spectra of either **3.8** or **3.9**, indicating that the diphenyl methyl group

on the 1,2,3-triazole ring provides a better steric protection than the benzyl group, probably due to its ability to prevent interactions from both top and bottom sides of the molecule.

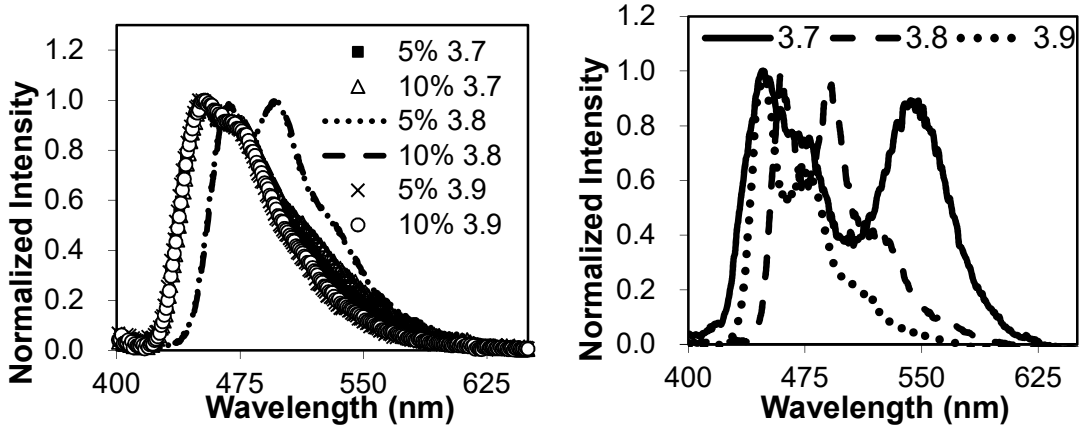

Figure 3.11 The phosphorescent emission spectra of **3.7-3.9** in PMMA at ambient temperature (left) and in frozen CH_2Cl_2 glass at 77 K (right).

3.2.5 Computational study

To further understand the photophysical properties of the Pt(II) compounds, TD-DFT calculations were performed for **3.1-3.9** using gaussian 09 software at B3LYP level of theory using LANL2DZ basis set for Pt atom and 6-31G* for the rest of the atoms.[8] The calculation results, together with the data from cyclic voltammetry analysis, are listed in Table 3.3. TD-DFT calculations show that the HOMO to LUMO transitions are dominant in S_0 to S_1 transitions (> 80%) and are the main component in S_0 to T_1 transitions (> 50%). The experimental and calculated HOMO and LUMO energies for compound **3.1-3.9** are shown in Figure 3.12. The calculated HOMO energies are in good agreement with the ones determined experimentally except for compound **3.5** and **3.6**, which is reasonable because it is known that TD-DFT produces substantial errors predicting energies with high charge-transfer contributions. The HOMO -LUMO energy gaps and the first triplet state energies are generally larger for complexes bearing CF_3 group compared to those with t-Bu group

(**3.1** versus **3.2**, **3.3** versus **3.4** and **3.8** versus **3.9**), except for compounds **3.5** and **3.6** where the t-Bu group destablizes the LUMO level of **3.5** while the CF_3 group stabilizes the LUMO level of **3.6**.

Table 3.3 Experimental HOMO–LUMO energy and TD-DFT data for compound **3.1-3.9**.

	Experimental data				TD-DFT data					
	[a]E^{red}	HOMO[b] (eV)	LUMO[b] (eV)	[c]E_g (T_1)	HOMO (eV)	LUMO (eV)	H-L gap (eV)	[d]E_g (T_1)	% H → L ($S_0 \rightarrow S_1$)	f ($S_0 \rightarrow S_1$)
3.1	-2.39	-5.50	-2.41	2.62	-5.31	-1.39	3.92	2.69	93	0.0100
3.2	-2.50	-5.58	-2.30	2.82	-5.61	-1.66	3.95	2.88	90	0.0068
3.3	-2.50	-5.35	-2.30	2.66	-5.47	-1.55	3.92	2.71	95	0.0245
3.4	-2.34	-5.88	-2.46	2.82	-5.88	-1.80	4.08	2.91	91	0.0012
3.5	-2.43	-5.25	-2.37	2.51	-4.57	-1.39	3.18	2.54	98	0.0287
3.6	-2.32	-5.30	-2.48	2.48	-4.60	-1.61	2.99	2.42	99	0.0186
3.7	-2.30	-5.61	-2.50	2.77	-5.55	-1.66	3.89	2.87	81	0.0057
3.8	-2.29	-5.52	-2.51	2.70	-5.25	-1.36	3.89	2.69	93	0.0144
3.9	-2.24	-5.67	-2.56	2.77	-5.52	-1.61	3.91	2.88	83	0.0054

[a]Recorded in CH_3CN/THF with 0.10 M Bu_4NPF_6 at a scan rate of either 100 mV s^{-1} or 200 mV s^{-1} (vs. Cp_2Fe/Cp_2Fe^+). [b]The LUMO energy was estimated using the reduction potential and the HOMO energy was calculated using the absorption edge and the LUMO energy. [c]The triplet energy value (T_1) was estimated using the emission spectra at 77 K. [d]$S_0 \rightarrow T_1$ vertical excitation energies.

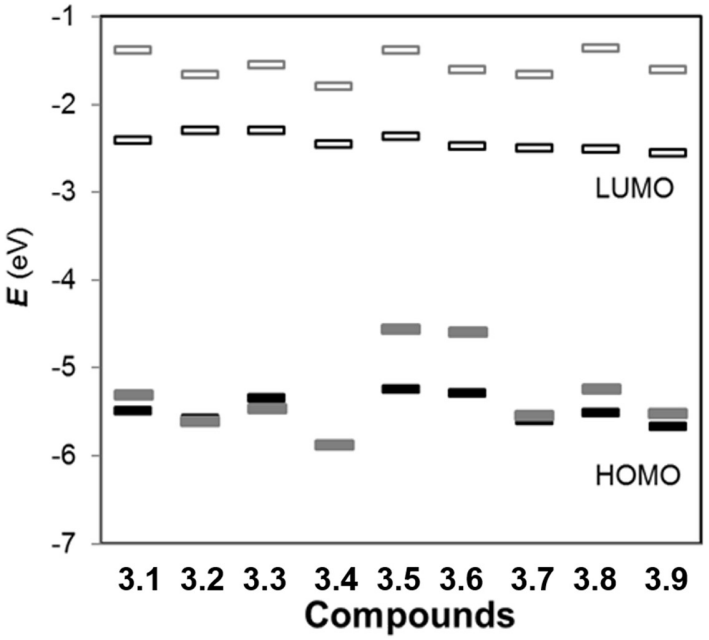

Figure 3.12 The experimental (black) and calculated (gray) HOMO and LUMO energies for compound **3.1-3.9**.

The HOMO-LUMO diagrams for **3.1**, **3.2, 3.5, 3.6, 3.8 and 3.9** are shown in Figure 3.13 while those of **3.3**, **3.4** and **3.7** resemble those of **3.1**, **3.2** and **3.9**, respectively. For compounds with CF_3-pytrz ligand, the HOMO is usually delocalized on the ptrz chelate while for the compounds with t-Bu-pytrz ligand the HOMO is mostly located on the pytrz ligand. The LUMO of compounds **3.1-3.9** involves mostly the pytrz ligand, with a small contribution from the 1,2,3-trazole ring. The Pt d orbital has a large contribution to the HOMO level of all complexes except for compounds **3.5** and **3.6**, in which the HOMO involves mainly the phenyl ring and the diphenyl amine group, which is not surprising as the electron donating group greatly destabilize the HOMO level. Based on the TD-DFT data, the phosphorescence in all complexes except **3.5** and **3.6** may be attributed to transitions involving an admixture of ^{3}LC/MLCT states while that of **3.5** and **3.6** is mainly from LLCT transitions from the Ph_2N-phenyl unit to the pytrz chelate unit, which is consistent with the long phosphorescent decay lifetimes of **3.5** and **3.6**.

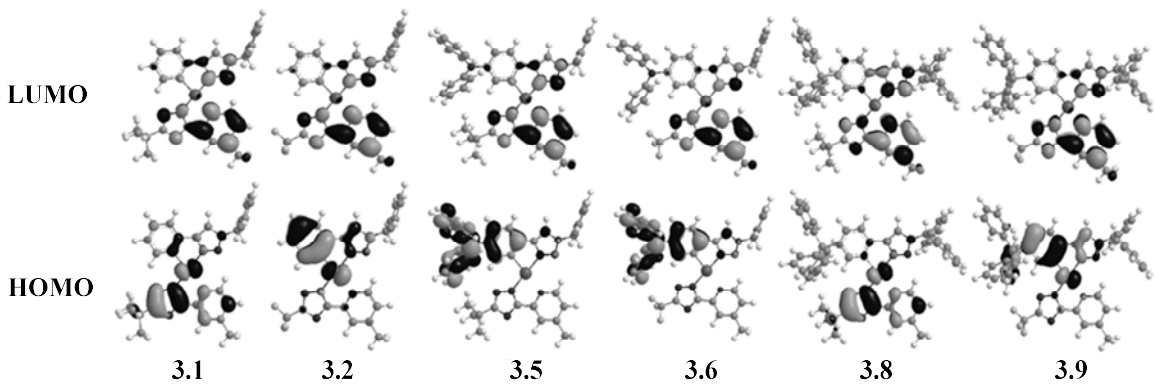

Figure 3.13 HOMO and LUMO diagrams of selected compounds (isocontour value = 0.03).

3.2.6 Electrophosphorescence of 3.7-3.9

Based on the excellent phosphorescent quantum efficiency, the blue or blue-green emission colors and the least tendency of excimer formation, compounds **3.7-3.9** are chosen for electrophosphorescence evaluation. EL devices with various host and charge transport materials are fabricated for these three compounds. The two typical device structures used in the investigation are **A**: ITO (70 nm)/MoO_3 (1 nm)/TAPC (60 nm)/POPCPA : x% Pt dopant (15 nm)/Tm3PyPb (40 nm)/LiF (1 nm)/Al (100 nm)) and **B**: ITO (70 nm)/MoO_3 (1 nm)/TAPC (60 nm)/26mCPy : x% Pt dopant (15 nm)/Tm3PyPb (40 nm)/LiF (1 nm)/Al (100 nm), as listed in Figure 3.14 and 3.15. The electron transport material 1,3,5-tri(*m*-pyrid-3-yl-phenyl)benzene (Tm3PyPb) and the hole transport material 1,1-bis[(di-4-tolylamino)phenyl] cyclohexane (TAPC) are selected because of their high triplet energy and suitable HOMO and LUMO energy levels.[9] The host material (4-{1-[4-(diphenylphosphoryl)phenyl]cyclohexyl}phenyl)-bis(4-methylphenyl) amine (POPCPA) and 2,6-bis(N-carbazolyl)pyridine (26mCPy) are selected because of their high triplet energy (2.93 eV and 2.80 eV, respectively) and their relatively high LUMO level which is higher than those of **3.7-3.9** (triplet energy = ~2.7 eV), thus can potentially facilitate the transfer

of the triplet exciton to the Pt(II) compounds.[10] Unfortunately, however, the EL devices for the CF_3-substituted compounds **3.7** and **3.9** are dominated by either excimers of the Pt(II) compound or exciplexes formed likely between the dopant and the host molecule or the charge transport molecule with a low brightness and efficiency (Figure 3.16-3.19). This may be caused by the high triplet energy of compounds **3.7** and **3.9**, the poor match of the energy level with the host material, and their tendency to form excimers as indicated by the 77 K phosphorescent spectrum of **3.7**. A similar trend was observed previously in $BMes_2$-functionalized Pt-ptrz compounds with a CF_3 substituted pytrz ancillary ligand. For the *t*-Bu substituted compound **3.8**, greenish-blue electroluminescent spectra (λ_{max} = 475 nm) that matches very well with the phosphorescent spectrum of **3.8** are obtained using both device structure **A** and **B** with the doping level of **3.8** up to 10% in the device. Nonetheless, the device **B** structure is found to be more efficient than **A** for **3.8** (EQE maximum = 11.7% at 10% doping level, Figure 3.20). Therefore, the discussion will be focused on EL devices of compound **3.8** using the structure **B**.

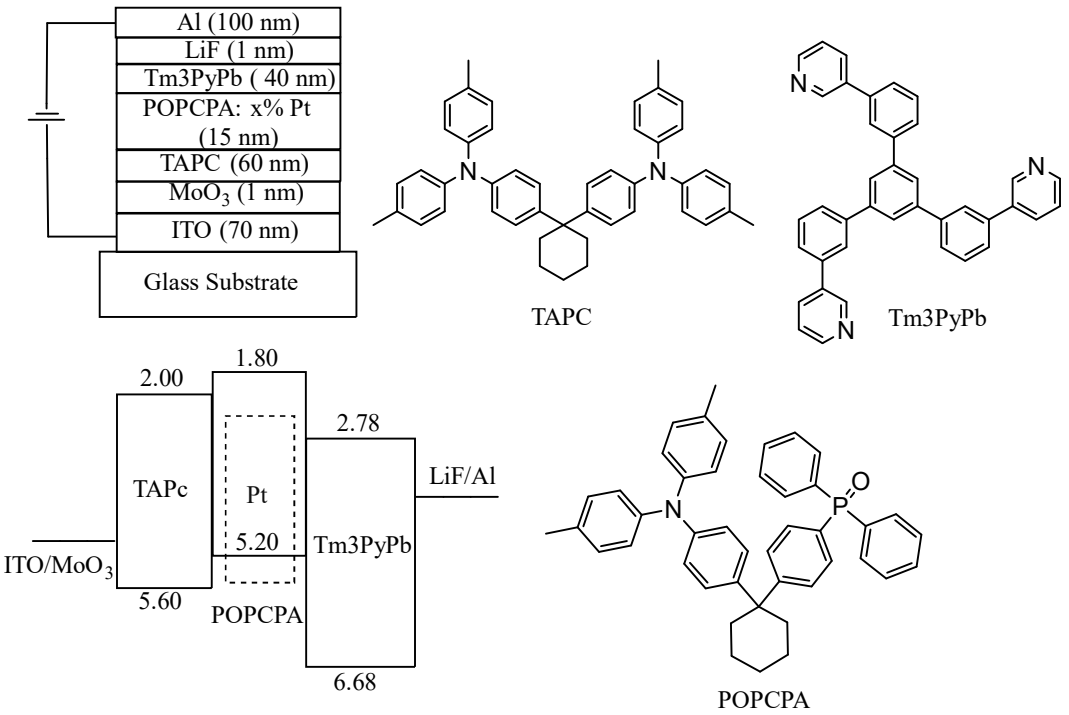

Figure 3.14 The structure **A** for the EL devices using POPCPA as host material

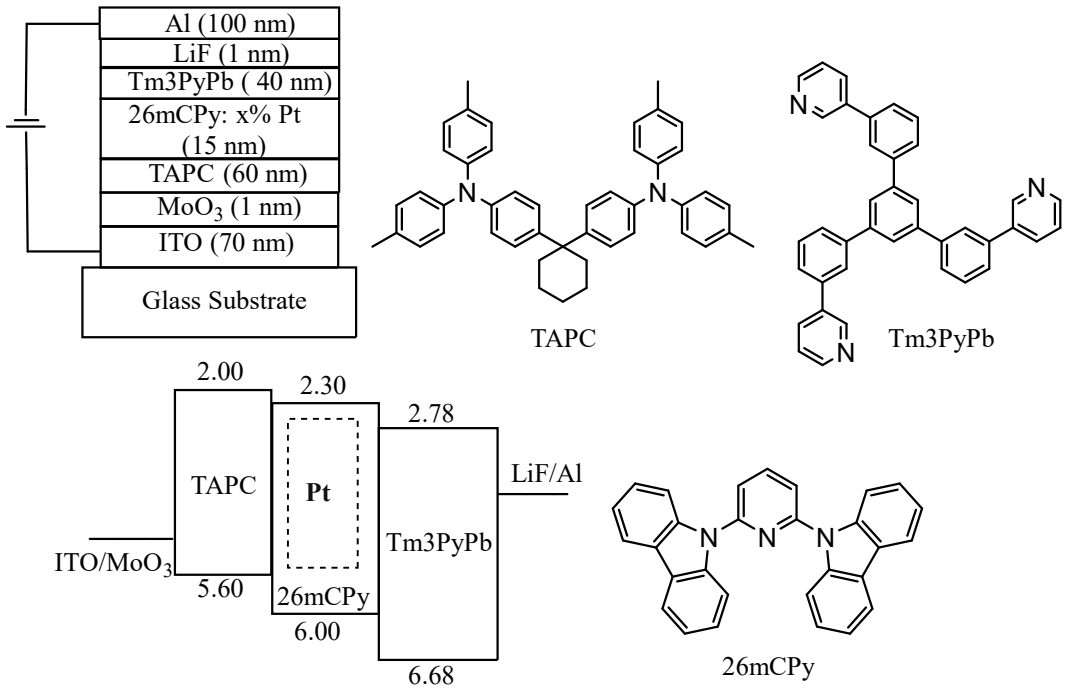

Figure 3.15 The structure **B** for the EL devices using 26mCPy as host material.

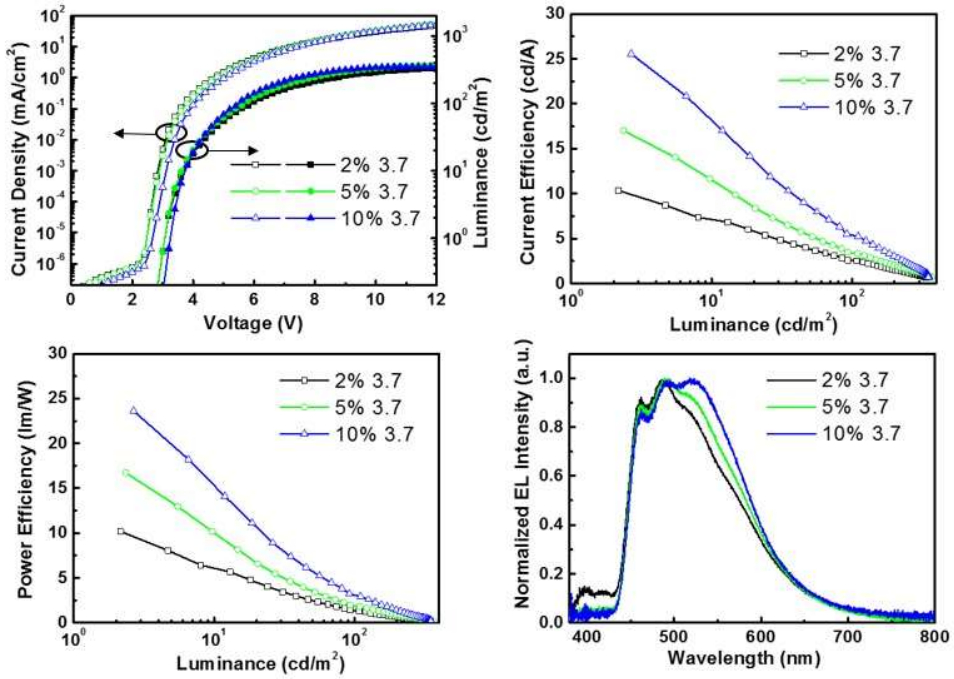

Figure 3.16. L-J-V and current efficiency, power efficiency, EL spectra of EL devices based on 3.7 and device structure **B**.

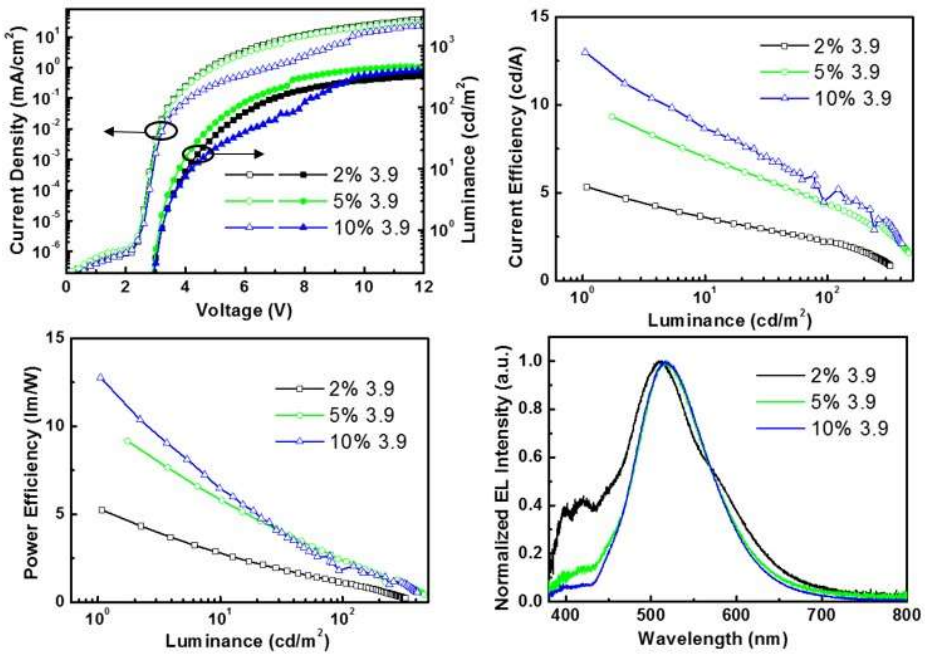

Figure 3.17 L-J-V and current efficiency, power efficiency, EL spectra of EL devices based on 3.9 and device structure **B**.

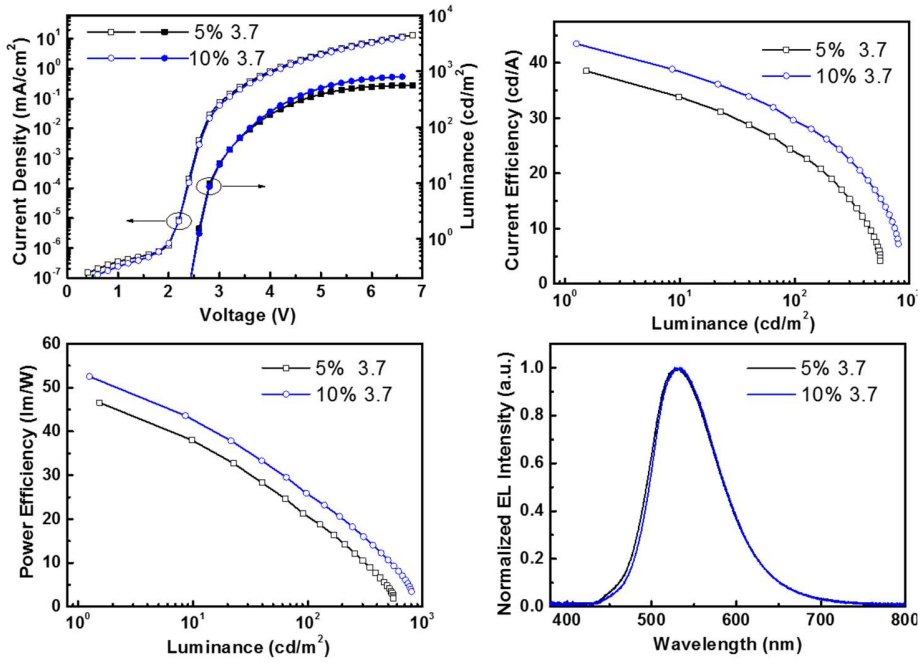

Figure 3.18 L-J-V and current efficiency, power efficiency, EL spectra of EL devices based on 3.7 and device structure **A**.

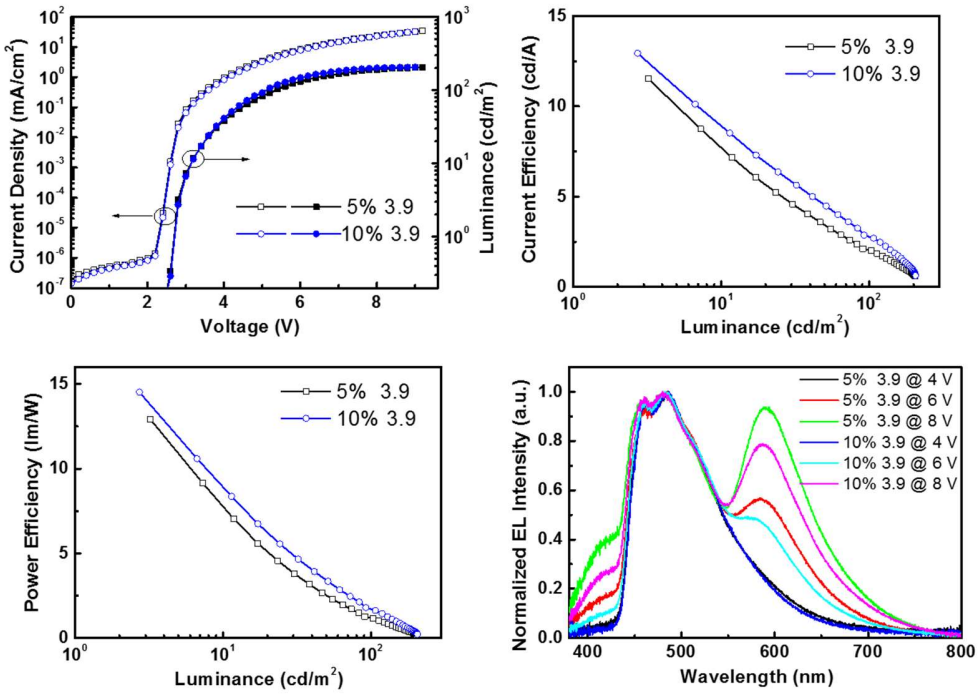

Figure 3.19 L-J-V and current efficiency, power efficiency, EL spectra and EQE-L diagram of EL devices based on 3.9 and device structure **A**.

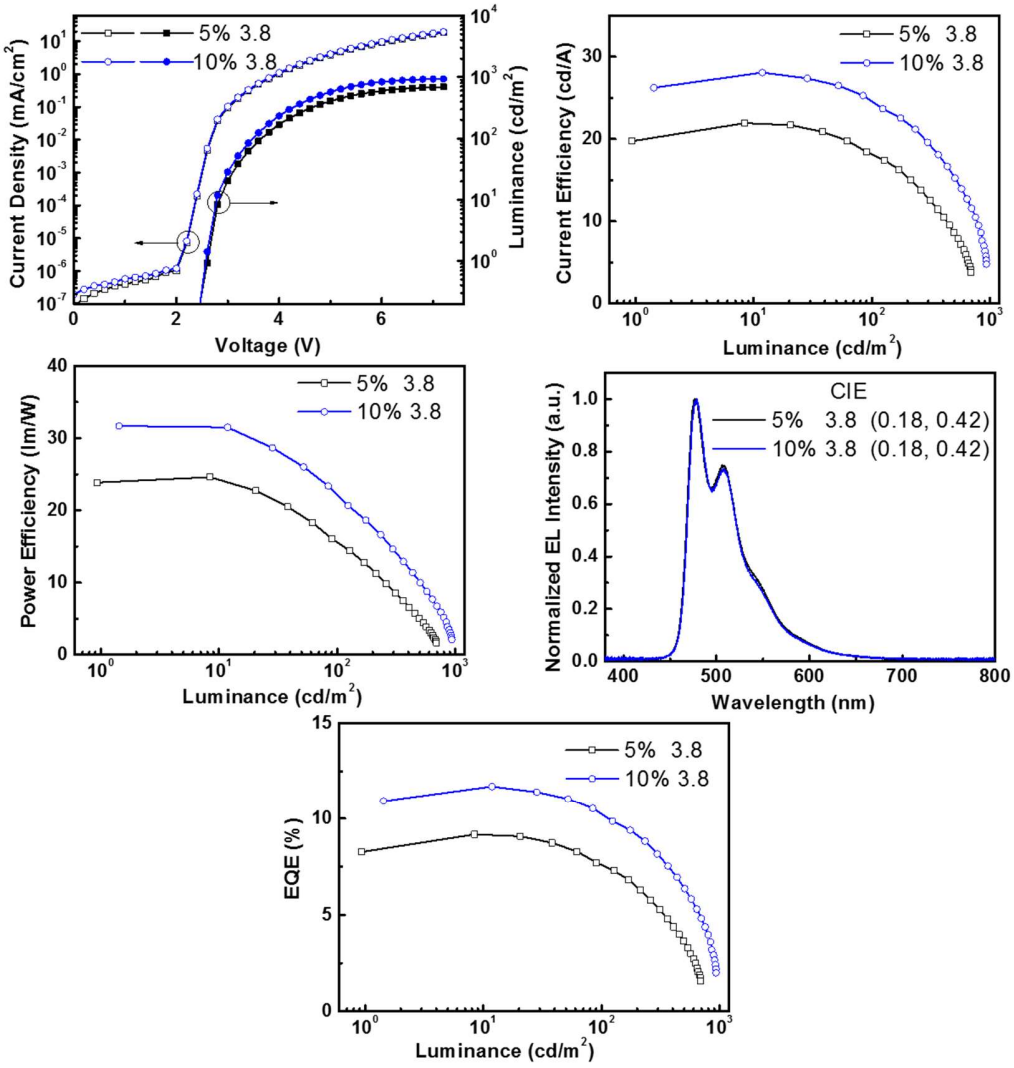

Figure 3.20 L-J-V and current efficiency, power efficiency, EL spectra of EL devices based on **3.8** and device structure **A**.

Three sets of devices using device structure **B** with compound **3.8** at doping level 2%, 5% and 10% are examined and the data are shown in Figure 3.21 and Table 3.4. It can be seen that the EL spectra remain the same as the doping concentration increased from 2% to 10%, producing a greenish blue color with λ = 477 nm and CIE (x, y) of (0.18, 0.42). This, compared to the EL spectra of the device based on **2.9**,[3] clearly demonstrates that the effectiveness of introducing a

bulky group on the 4' position of the phenyl ring on reducing excimer emission. The current efficiency, power efficiency and external quantum efficiency increase as the doping concentration increases, probably due to reduced triplet-triplet annihilation of the host material. Device with 10% **3.8** shows peak current efficiency, power efficiency and external quantum efficiency of 40.1 cd/A, 39.4 lm/W and 16.7%, which remain at 31.1 cd/A, 22.2 lm/W and 12.9 % at 100 cd/m^2. These preliminary results are pretty good for a newly developed greenish blue Pt(II) compound and future work will be carried out on optimizing the device structure for compound **3.8** and testing the performance of compound **3.7** and **3.9** as dopant for deep blue OLEDs.

Table 3.4 EL device data for **3.8**.

Device	EL λ_{max} (nm)[a]	V_{on} (V)[b]	L (cd/m^2, V)[c]	η_{ext} (%)[d]			η_c (cd/A)[e]	η_p (lm/W)[f]	CIE (x,y)
				10 cd/m^2	100 cd/m^2	1000 cd/m^2			
2% **3.8**	476	3.0	2192, 12.0	7.3	6.4	4.8	20.0	21.0	(0.18, 0.41)
5% **3.8**	477	3.0	2559, 12.0	11.1	9.1	6.3	29.6	31.0	(0.18, 0.42)
10% **3.8**	477	3.0	2735, 12.0	15.9	12.9	8.0	40.1	39.4	(0.18, 0.43)

[a]Value taken at I = 20 mA. [b]The applied voltage (V_{on}) is defined as brightness of 1 cd/m^2.[c]The luminance (L) is the maximum value. [d]External quantum efficiency (EQE, η_{ext}). [e]Current efficiency (η_c) and power efficiency (η_p) are the maximum values.

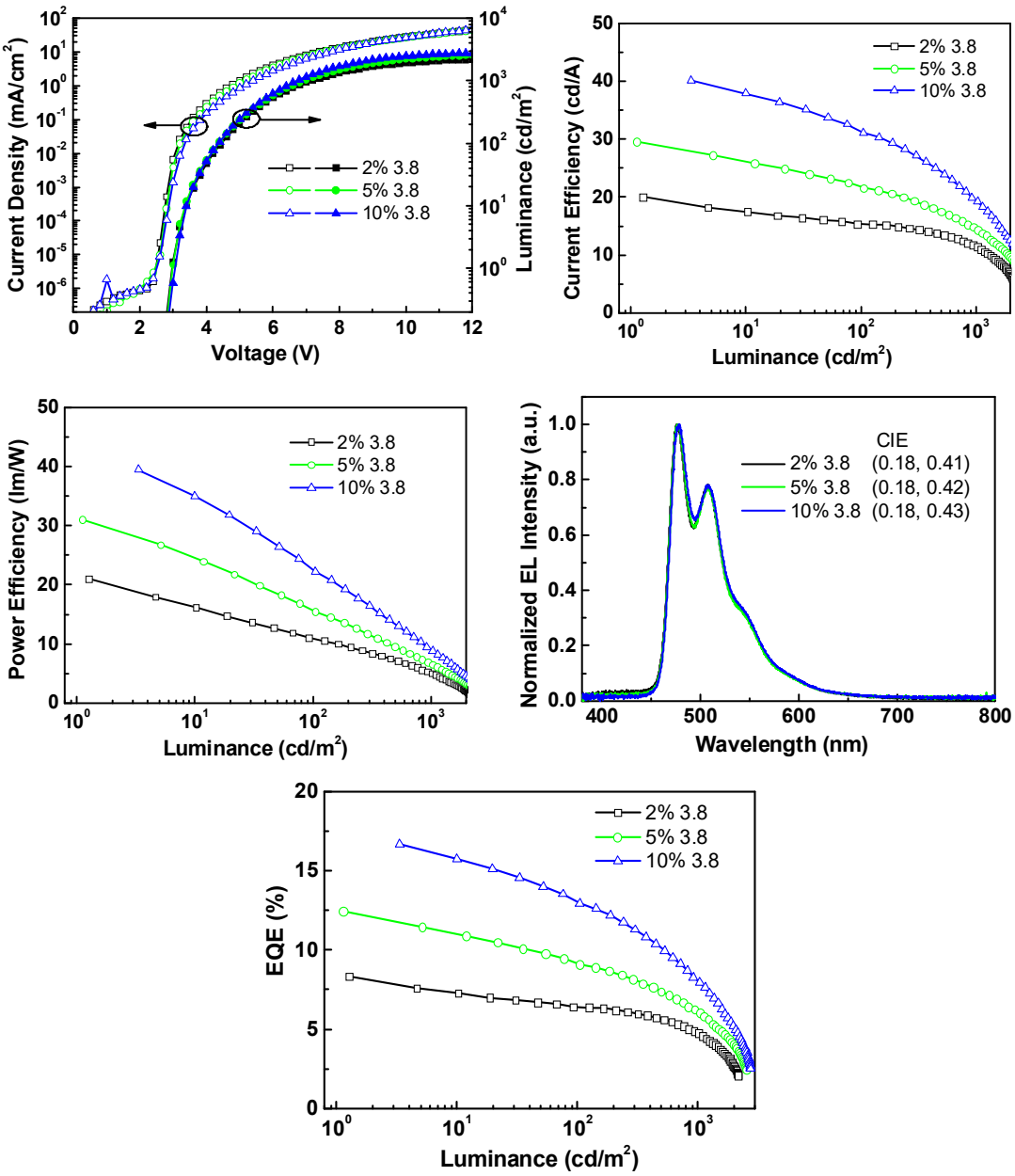

Figure 3.21 L-J-V and current efficiency, power efficiency, EL spectra and EQE-L diagrams of EL devices based on **3.8** device structure **B**.

3.3 Experimental

3.3.1 General Procedures

All Reactions were carried out under a nitrogen atmosphere unless otherwise noted. Reagents were purchased from Aldrich chemical company and used as received. TLC and flash chromatography were performed on silica gel. ^{1}H and ^{13}C NMR spectra were recorded on Bruker Avance 300 or 400 MHz spectrometers. Deuterated solvents were purchased from Cambridge Isotopes and used without drying. Excitation and emission spectra were obtained on a Photon Technologies International QuantaMaster Model 2 spectrometer. Solid state quantum efficiency measurements were performed using the same spectrometer with an integration sphere. Phosphorescent decay life times were measured with a Photon Technologies International Phosphorescent lifetime spectrometer using a xenon flash lamp as excitation source. Solution phosphorescence quantum yields of compound **3.1**, **3.3-3.6** and **3.8** were measured relative to $Ir(ppy)_3$ in degassed dichloromethane (Φ_{Phos}=0.95) at 298 K. UV-Visible spectra were recorded using a Varian Carry 50 UV/Vis spectrophotometer. Cyclic voltammetry experiments were conducted on a BAS CV-50W analyzer with a scan rate of either 100 or 200 mVs^{-1}. The electrochemical cell was a standard three-compartment cell composed a Pt working electrode, a Pt auxiliary electrode and an Ag/AgCl reference electrode. All measurements were using 0.1M NBu_4PF_6 in acetonitrile/tetrahydrofuran mixture as the supporting electrolyte. Ferrocene/ferrocenium was used as internal standard (E^o=0.55V). TGA was performed using a TA Q5000 instrument under nitrogen. The samples were heated to 100 ^oC at a speed of 10 ^oC/min. The temperature was maintained for 10 min before further heating to 480 ^oC at 10 ^oC/min. Elemental analyses were performed by University of Montreal Elemental Analysis Laboratory. Crystal structures were obtained using a Bruker AXS Apex II X-ray diffractometer. TD-DFT calculations were carried out using the Gaussian 09

software at the High Performance Computing Virtual Laboratory (HPCVL) at Queen's University. All computations were performed at the B3LYP level of theory using LANL2DZ as the basis set for Pt and 6-31G(d) for all other atoms.

3.3.2 Synthesis of Ligands

1-Benzyl-4-phenyltriazole (ptrzBn) and 1-Benzyl-4-(2,4-difluorophenyl)-1H-1,2,3-triazole (FptrzBn) were prepared according to literature procedure.[4] (4-ethynylphenyl)diphenylamine, ((4-ethynylphenyl)methanetriyl)tribenzene N,N- diphenyl-4-(1-benzyl-1H-1,2,3-triazol-4-yl) aniline (NptrzBn), 1-benzyl-4-(4-tritylphenyl)-1H-1,2,3-triazole (CptrzBn) and 1-(diphenylmethyl)-4-(4-tritylphenyl)-1H-1,2,3-triazole (Cptrzp2C) were prepared according to our previous report.[3] The ancillary ligand *t*-Bu-pytrz-Me and CF_3-pytrz-Me were synthesized according to literature procedure.[5]

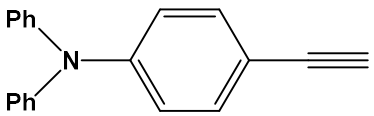

(4-ethynylphenyl)diphenylamine (NpCC): To a 100 mL three-necked round bottomed flask equipped with a magnetic stir bar and a condenser was added (4-bromophenyl)diphenylamine (1 g, 3.08mmol), trimethylsilylacetylene (0.6mL, 4.62mmol), bis(triphenylphosphine) palladium dichloride (0.11g, 0.3 mmol), copper iodide (0.03g, 0.15mmol) and 40 mL of degassed THF/triethylamine (v:v= 3:1). The mixture was stirred at 80°C for 20 hours, and then concentrated under reduced pressure. The product was dissolved in dichloromethane and washed sequentially with saturated ammonium chloride solution, water and brine. The organic layer was dried over $MgSO_4$, filtered and the solvent was removed under reduced pressure. The solid was then purified using flash chromatography through silica using 4% ethyl acetate in hexane as eluent. The resulting white solid was dissolved in 10 mL of

tetrahydrofuran and treated with sodium hydroxide in methanol (20 mL of a 2.0 M solution). After stirring for 2 hours, the resulting mixture was concentrated under reduced pressure. After extraction with dichloromethane, the organic layer was dried over $MgSO_4$, filtered and the solvent was removed under reduced pressure to give the product **NpCC** as a white solid (0.5g, 60% Yield). ^{1}H NMR (300 MHz, $CDCl_3$): δ 7.50-7.00 (m, 14H), 3.04 (s, 1H).

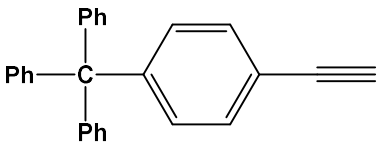

((4-ethynylphenyl)methanetriyl)tribenzene (**CpCC**): Prepared using the same procedure as **NpCC** except replacing (4-bromophenyl)diphenylamine with ((4-iodophenyl)methanetriyl)tribenzene (74% Yield). ^{1}H NMR (300 MHz, $CDCl_3$): δ 7.40 (d, J = 8.5 Hz, 2H), 7.35-7.05 (m, 17H), 3.06 (s, 1H).

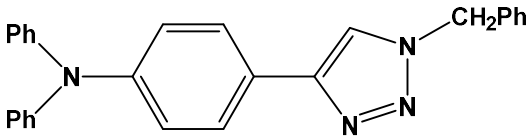

***N,N*-diphenyl-4-(1-benzyl-1H-1,2,3-triazol-4-yl) aniline (NptrzBn)**: To a 50 mL Schlenk flask equipped with a magnetic stir bar was added (4-ethynylphenyl)diphenylamine (0.5g, 1.86mmol), benzyl azide (0.29g, 2.21mmol), diisopropylethylamine (0.475g, 3.68mmol), tris[(1-benzyl-1H-1,2,3-triazol-4-yl)- methyl]amine (1 mol %) and 30 mL of dichloromethane. The resulting solution was bubbled with nitrogen gas for 20 minutes. $[Cu(CH_3CN)_4]PF_6$ (1 mol %) was added as a catalyst. The resulting mixture was stirred overnight, after which the solvent was removed under reduced pressure. The crude product was redissolved in dichloromethane and washed with saturated ammonium chloride solution, water and brine. The organic layer was dried over $MgSO_4$, filtered and the solvent was removed

under reduced pressure. The product was then purified using flash chromatography through silica (1:1 hexanes:ethyl acetate as eluent) to afford 0.54 g **NptrzBn** as white solid (72% yield). ^{1}H NMR (300 MHz, $CDCl_3$): δ 7.68 (d, J = 8.8 Hz, 2H), 7.60 (s, 1H), 7.45-7.36 (m, 3H), 7.35-7.20 (m, 6H), 7.19-6.98 (m, 8H), 5.59 (s, 2H).

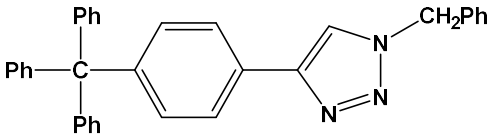

1-benzyl-4-(4-tritylphenyl)-1H-1,2,3-triazole (CptrzBn): Prepared using the same procedure as **NptrzBn** except replacing (4-ethynylphenyl)diphenylamine with ((4-ethynylphenyl)-methanetriyl)tribenzene (62% Yield). ^{1}H NMR (300 MHz, $CDCl_3$) δ 7.79 (d, J = 8.3 Hz, 2H), 7.63 (s, 1H), 7.45-7.10 (m, 22H), 5.59 (s, 2H).

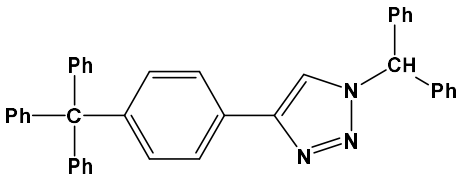

1-benzhydryl-4-(4-tritylphenyl)-1H-1,2,3-triazole (Cptrzp2C): Prepared using the same procedure as **CptrzBn** except replacing benzyl azide with (azidomethylene)dibenzene (71% Yield). ^{1}H NMR (300 MHz, $CDCl_3$) δ 7.71 (d, J = 8.0 Hz, 2H), 7.59 (s, 1H), 7.45-7.10 (m, 28H)

3.3.3 Synthesis of Pt(II) complexes

The general synthetic procedures for the Pt(II) compounds are provided below. ^{13}C NMR spectra were not recorded for all Pt(II) compounds because of their poor solubility. The Pt(II) compounds have the tendency to co-crystallize with solvent molecules such as THF and CH_2Cl_2. For some of the compounds, the solvent molecules were positively identified in the crystal lattice of the Pt(II)

compounds. For elemental analysis, all samples were dried under vacuum at ambient temperature. Nonetheless, many of the compounds still show solvent molecules trapped inside the crystal lattice.

General procedure for the synthesis of Pt(II) compounds: The **ptrz** chelate ligand (0.20 mmol) and $[PtMe_2(u\text{-}SMe_2)]_2$ (0.11 mmol) were added to a 20 mL screw-cap vial with 5 mL of acetone. The mixture was heated at 70 °C for 1 hours before 1 mL of 0.1 M solution of tosylic acid (TsOH) in THF was added. The resulting solution was stirred for 1 hour before 0.22 mmol of corresponding pytrz ligand in acetone was added and the mixture was stirred at room temperature for 2 days. After the solvent was removed under reduced pressure, the product was extracted with dichloromethane, and then washed with water and brine. The combined organic phase was dried over $MgSO_4$, filtered and purified on silica.

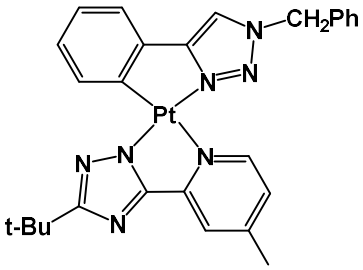

(ptrzBn)Pt(t-Bu) (**3.1**): Yield 23%. ^{1}H NMR (300 MHz, CD_2Cl_2) δ 9.35 (d, J = 4.9 Hz, 1H), 9.00 (d, J = 7.7 Hz, 1H), 7.81 (s, 1H), 7.49-7.26 (m, 6H), 7.25-6.95 (m, 4H), 5.49 (s, 2H), 2.41 (s, 3H), 1.40 (s, 9H). Anal. calcd for **3.1** ($C_{27}H_{27}N_7Pt$): C 50.07, H 4.12 N 14.99; found: C 50.31, H 4.22, N 15.21.

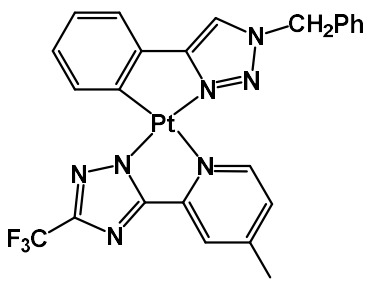

(ptrzBn)Pt(CF_3) (**3.2**): Yield 17%. ^{1}H NMR (400 MHz, CD_2Cl_2) δ 9.32 (d, J = 5.6 Hz, 1H), 8.69 (d, J = 7.6 Hz, 1H), 7.79 (s, 1H), 7.45-7.29 (m, 6H), 7.18 (d, J = 5.6 Hz, 1H), 7.14 (dd, J = 7.3 Hz, 1.3 Hz, 1H), 7.08 (td, J = 7.5 Hz, 1.5 Hz, 1H), 7.01 (td, J = 7.3 Hz, 1.1 Hz, 1H), 5.51 (s, 2H), 2.41 (s, 3H). Anal. calcd for **3.2**·1/2 THF ($C_{26}H_{22}F_3N_7O_{0.5}Pt$): C 45.09, H 3.20 N 14.16; found: C 44.84, H 2.70, N 14.30.

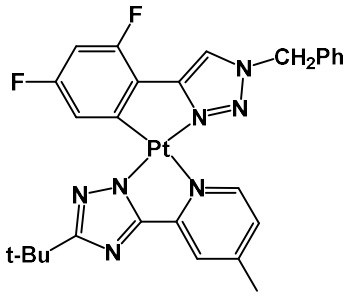

(FptrzBn)Pt(t-Bu) (**3.3**): Yield 39%. ^{1}H NMR (400 MHz, CD_2Cl_2) δ 9.26 (d, J = 5.8 Hz, 1H), 8.66 (dd, J = 10.2 Hz, 2.4 Hz, 1H), 7.77 (s, 1H), 7.47 (d, J = 1.1 Hz, 1H), 7.41-7.30 (m, 5H), 7.10 (dd, J = 5.6 Hz, 1.3 Hz, 1H), 6.51 (ddd, J = 10.0 Hz, 9.0 Hz, 2.4 Hz, 1H), 5.51 (s, 2H), 2.42 (s, 3H), 1.40 (s, 9H). Anal. calcd for **3.3**·1 THF ($C_{31}H_{33}F_2N_7OPt$): C 49.46, H 4.42 N 13.03; found: C 49.38, H 4.24, N 13.37.

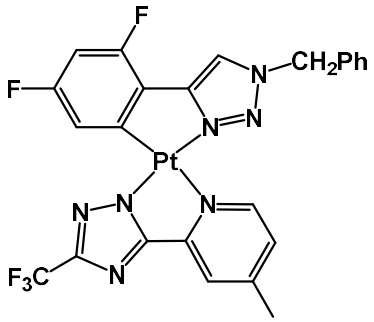

(FptrzBn)Pt(CF_3) (**3.4**): Yield 46%. ^{1}H NMR (400 MHz, THF-d_8) δ 9.44 (d, J = 5.7 Hz, 1H), 8.52 (dd, J = 9.9 Hz, 2.3 Hz, 1H), 8.15 (s, 1H), 7.95 (s, 1H), 7.55-7.30 (m, 6H), 6.66 (m, 1H), 5.76 (s, 2H), 2.53 (s, 3H). HRMS (ESI) for C24H17N7F5Pt $[M+H]^+$: calcd. 693.1113, found 693.1132; $[M_2]^+$: 1384.2066, found 1384.2135. Anal. calcd for **3.4** ($C_{24}H_{16}F_5N_7Pt$): C 41.63, H 2.33 N 14.16; found: C 41.86, H 2.16, N 13.64.

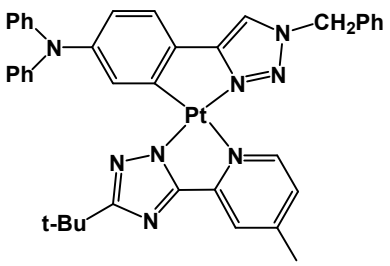

(NptrzBn)Pt(t-Bu) (**3.5**): Yield 20%. ^{1}H NMR (300 MHz, CD_2Cl_2) δ 9.39 (d, J = 5.9 Hz, 1H), 8.85 (s, 1H), 7.78 (s, 1H), 7.51-7.26 (m, 6H), 7.25-6.98 (m, 10H), 6.90 (t, J = 7.2 Hz, 2H), 6.70 (d, J = 8.2 Hz, 1H), 5.51 (s, 2H), 2.40 (s, 3H), 1.06 (s, 9H). Anal. calcd for **3.5** ($C_{39}H_{36}N_8Pt$): C 57.70, H 4.47 N 13.80; found: C 57.27, H 4.31, N 13.45.

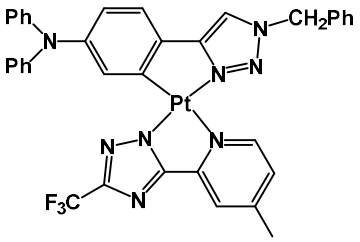

(NptrzBn)Pt(CF$_3$) (**3.6**): Yield 14%. ^{1}H NMR (400 MHz, CD_2Cl_2) δ 9.42 (d, J = 5.6 Hz, 1H), 8.51 (d, J = 2.3 Hz, 1H), 7.84 (s, 1H), 7.40 (s, 1H), 7.39-7.31 (m, 5H), 7.27-7.14 (m, 5H), 7.12-7.01 (m, 5H), 6.96 (t, J = 7.3 Hz, 2H), 6.75 (dd, J = 8.2 Hz, 2.1 Hz, 1H), 5.51 (s, 2H), 2.41 (s, 3H). Anal. calcd for **3.6**·1 hexane ($C_{42}H_{41}F_3N_8Pt$): C 55.44, H 4.54, N 12.31; found: C 54.89, H 4.23, N 12.29.

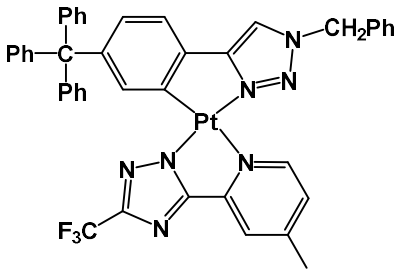

(CptrzBn)Pt(CF$_3$) (**3.7**): Yield 24%. ^{1}H NMR (400 MHz, CD_2Cl_2) δ 9.38 (d, J = 5.8 Hz, 1H), 8.87 (d, J = 1.8 Hz, 1H), 7.86 (s, 1H), 7.45-6.95 (m, 24H), 5.46 (s, 2H), 2.41 (s, 3H). Anal. calcd for **3.7**·1 THF ($C_{47}H_{40}F_3N_7OPt$): C 58.14, H 4.15N 10.10; found: C 58.39, H 4.18, N 10.39.

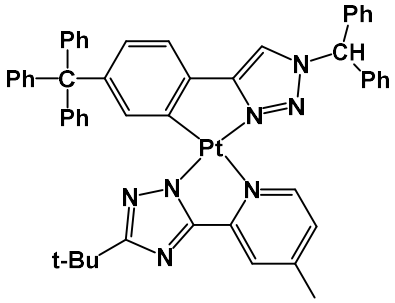

(Cptrzp2C)Pt(t-Bu) (**3.8**): Yield 22%. ^{1}H NMR (400 MHz, CD_2Cl_2) δ 9.12 (d, J = 5.6 Hz, 1H), 9.07 (d, J = 1.8 Hz, 1H), 7.72 (s, 1H), 7.49 (s, 1H), 7.45-7.00 (m, 28H), 6.98 (d, J = 4.5 Hz, 1H), 2.35 (s, 1H), 1.03 (s, 9H). Anal. calcd for **3.8** ($C_{49}H_{36}N_7Pt$): C 64.85, H 4.71 N 10.18; found: C 65.11, H 4.64, N 10.09.

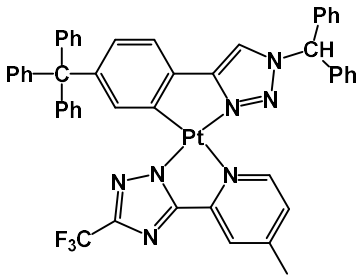

(Cptrzp2C)Pt(CF$_3$) (**3.9**): Yield 20%. ^{1}H NMR (400 MHz, CD_2Cl_2) δ 9.16 (d, J = 5.6 Hz, 1H), 8.87 (d, J = 1.5 Hz, 1H), 7.83 (s, 1H), 7.51 (s, 1H), 7.45-6.95 (m, 29H), 2.38 (s, 3H). Anal. calcd for **3.9**·1 THF ($C_{53}H_{44}F_3N_7OPt$): C 60.80, H 4.24 N 9.36; found: C 60.96, H 3.87, N 9.34.

3.3.4 X-Ray Diffraction Analysis

Single crystals of **3.4, 3.5, 3.7-3.9** were obtained from either CH_2Cl_2 or THF by slow evaporation of the solvent. For some of the compounds, it was necessary to add either methanol or hexanes to facilitate the crystal growth. The crystals were mounted on glass fibers and the data were collected on a Bruker Apex II single-crystal X-ray diffractometer with graphite-monochromated Mo K_α radiation, operating at 50 kV and 30 mA, and at 180 K. Data were processed on a PC with the aid of the Bruker SHELXTL software package (version 6.14) and corrected for absorption effects.[11] All structures were solved using direct methods. The crystals of **3.4** and **3.8** belong to the triclinic space group P-1, those of **3.7** and **3.9** belong to the monoclinic space group $P2_1/n$, while **3.5** belongs to the monoclinic space group C2/c. CH_2Cl_2 solvent molecules were located in the lattices of **3.8** (two CH_2Cl_2 per molecule of **3.8**) and **3.9** (2.4 CH_2Cl_2 per molecule of **9**) and refined

successfully. THF solvent molecules were found in the lattice of **3.7** (1 THF per molecule of **7**) and refined successfully. All non-hydrogen atoms were refined anisotropically. CCDC 1013543 (**3.4**), 1013542 (**3.5**), 1013541 (**3.7**), 1013539 (**3.8**), and 1013540 (**3.9**) contain the crystallographic data. These data can be obtained free of charge from The Cambridge Crystallographic Data Centre via www.ccdc.cam.ac.uk/data_request/cif.

3.3.5 EL Device Fabrication

Devices were fabricated in a three-chamber evaporator (EL-OEL cluster tool) with a base pressure of ~1×10^{-7} Pa without breaking vacuum. The ITO anode is commercially patterned and coated on glass substrates 50 x 50 mm^2 with a sheet resistance less than 15 Ω. Substrates were ultrasonically cleaned with a standard regiment of Alconox®, acetone, and methanol followed by UV ozone treatment for 15 min. The active area for all devices was 2 mm^2. The film thicknesses were monitored by a calibrated quartz crystal microbalance and were further verified for single-carrier devices using capacitance-voltage measurements (Agilent 4294A). I-V characteristics were measured using a HP4140B picoammeter in ambient air. Luminance measurements and EL spectra were taken using a Minolta LS-110 luminance meter and an Ocean Optics USB200 spectrometer with bare fiber, respectively. The external quantum efficiency of EL devices was calculated following the standard procedure.[12]

3.4 Conclusion

A series of bright luminescent Pt(II) compounds based on a ptrz and a pytrz chelate core have been successfully synthesized. The attachment of bulky substituents such as NPh_2 and CPh_3 at the *para*-position of the ptrz ligand was found to be highly effective in reducing excimer emission and

enhancing the phosphorescent quantum efficiency. Green and blue phosphorescent Pt(II) compounds with near unity quantum efficiency have been achieved with the introduction of NPh_2 and CPh_3 group, respectively. Bluish-green EL devices based on one of the new Pt(II) emitters have been demonstrated to have external efficiencies comparable to those of the meta-BMes2 substituted analogue, but with much less excimer or no excimer emission. Furthermore, the new non-borylated Pt(II) compounds was found to have a much higher thermal stability than the meta-$BMes_2$ substituted analogues. For the new deep blue emitters, better host and charge transport materials are necessary in order to fabricate blue EL devices with no excimer emission,

3.5 Notes and References

The work described in this chapter includes contributions from the following publication:

- X. Wang, S. L. Gong, D. Song, Z. H. Lu, and S. Wang, *Adv. Funct. Mater.*, **2014**, *24*, 7257.

References

(1) (a) Z. M. Hudson, C. Sun, M. G. Helander, H. Amarne, Z.-H. Lu, S. Wang, *Adv. Funct. Mater.* **2010**, *20*, 3426. (b) Z. M. Hudson, S. Wang, *Dalton Trans.*, **2011**, *40*, 7805. (c) Z. Wang, M. G. Helander, Z. M. Hudson, J. Qiu, S. Wang, Z. -H. Lu. *Appl. Phys. Lett.*, **2011**, *98*, 213301. (d) Z. M. Hudson, M. G. Helander, Z.-H. Lu, S. Wang. *Chem. Commun.*, **2011**, *47*, 755.

(2) Z. M. Hudson, C. Sun, M. G. Helander, Y.-L. Chang, Z.-H. Lu, S. Wang, *J. Am. Chem. Soc.*, **2012**, *134*, 13930.

(3) X. Wang, Y.-L. Chang, J. S. Lu, T. Zhang, Z. H. Lu, S. Wang, *Adv. Funct. Mater.*, **2014**, *24*, 1911.

(4) C. Zhang, B. Huang, Y. Chen, D.-M. Cui, *New Journal of Chemistry* **2013**, *37*, 2606.

(5) E. Orselli, G. S. Kottas, A. E. Konradsson, P. Coppo, R. Fröhlich, L. D. Cola, A. V. Dijken, M. Büchel, H. Börner, *Inorg. Chem.*, **2007**, *46*, 11082.

(6) Z. M. Hudson, B. A. Blight, S. Wang, *Org. Lett.*, **2012**, *14*, 1700.

(7) J. Brooks, Y. Babayan, S. Lamansky, P.I. Djurovich, I. Tsyba, R. Bau, M.E. Thompson, *Inorg. Chem.*, **2002**, *41*, 3055.

(8) M. J. Frisch, G. W. Trucks, H. B. Schlegel, G. E. Scuseria, M. A. Robb, J. R. Cheeseman, J. A. Montgomery, Jr., T. Vreven, K. N. Kudin, J. C. Burant, J. M. Millam, S. S. Iyengar, J. Tomasi, V. Barone, B. Mennucci, M. Cossi, G. Scalmani, N. Rega, G. A. Petersson, H. Nakatsuji, M. Hada, M. Ehara, K. Toyota, R. Fukuda, J. Hasegawa, M. Ishida, T. Nakajima, Y. Honda, O. Kitao, H. Nakai, M. Klene, X. Li, J. E. Knox, H. P. Hratchian, J. B. Cross, C. Adamo, J. Jaramillo, R. Gomperts, R. E. Stratmann, O. Yazyev, A. J. Austin, R. Cammi, C. Pomelli, J. W. Ochterski, P. Y. Ayala, K. Morokuma, G. A. Voth, P. Salvador, J. J. Dannenberg, V. G. Zakrzewski, S. Dapprich, A. D. Daniels, M. C. Strain, O. Farkas, D. K. Malick, A. D. Rabuck, K. Raghavachari, J. B. Foresman, J. V. Ortiz, Q. Cui, A. G. Baboul, S. Clifford, J. Cioslowski, B. B. Stefanov, G. Liu, A. Liashenko, P. Piskorz, I. Komaromi, R. L. Martin, D. J. Fox, T. Keith, M. A. Al-Laham, C. Y. Peng, A. Nanayakkara, M. Challacombe, P. M. W. Gill, B. Johnson, W. Chen, M. W. Wong, C. Gonzalez, and J. A. Pople. Gaussian 03, revision C.02; Gaussian, Inc.: Wallingford, CT, 2004.

(9) (a) L. Xiao, Z. Chen, B. Qu, J. Luo, S. Kong, Q. Gong, J. Kido, *Adv. Mater.*, **2011**, *23*, 926.
(b) K. S. Yook, J. Y. Lee, *Adv. Mater.*, **2012**, *24*, 3169.

(10) S. Gong, Y.-L. Chang, K. Wu, R. White, Z.-H. Lu, D. Song, C. Yang, *Chem. Mater.* **2014**, *26*, 1463.

(11) Shelxtl Version 6.14, Bruker AXS, copyright 2000-2003.

(12) S. R. Forrest, D. D. C. Bradley, and M. E. Thompson, *Adv. Mater.* **2003**, *15*, 1043.

Chapter 4

Stable and Efficient Deep Blue Phosphorescent Pt(II) Compounds Based on Tetradentate and Macrocyclic Phenyltriazole Ligands

4.1 Introduction

The development of organic light-emitting diodes (OLEDs) has attracted tremendous research efforts as OLED technology has broad applications in flat-panel displays and lighting devices.[1]As mentioned in chapter 1, green and red phosphorescent OLEDs (PHOLEDs), which have a theoretical internal quantum yield of 100% and long device lifetime, have already been commercialized successfully.[2] Achieving efficient and stable deep blue phosphorescent emitters still remains as one of the greatest challenges in OLEDs research.[3] To date, the most well-studied blue phosphorescent emitters are based on Ir(III) compounds that contain either fluorine-substituted ligands or an N-heterocyclic carbene (NHC) moiety to ensure a wide energy gap.[4-6] These deep blue Ir(III) compounds do have some shortcomings, such as defluorination or ligand dissociation through one of the weaker Ir-N bonds during the device fabrication/operation,[5] or the difficulty to find suitable electron/exciton-blocking or host materials due to the high-lying HOMO and LUMO levels of the Ir(III)-NHC compounds.[7]

Compared to the extensive research on blue phosphorescent Ir(III) compounds, deep blue phosphorescent Pt(II) compounds remain underexplored, mainly because of the flat square-planar geometry that leads to strong intermolecular stacking interactions, the formation of excimers/exciplexes, the bathochromic shift of emission wavelength, and the decrease of emission efficiency.[8] In chapter 3, we have demonstrated that the aboved problems can be solved by introducing a sterically bulky and electron neutral trityl group at the *para*-position of the phenyl

ring to the 1,2,3-trazole, as shown in Chart 4.1. Bright phosphorescent Pt(II) compounds **3.7-3.9** with emission maxima ranging from 454-468 nm and excellent quantum yields (0.68-1.00) are achieved and used in the fabrication of OLEDs with maximum external quantum efficiency (EQE) of 16.7%.[8e] However, there are three problems with this type of molecules. First, although compounds **3.7-3.9** have excellent thermal stability (> 350 ºC), their high molecular weight makes them very difficult to vaporize. In the OLED fabrication process, the temperature required to evaporate these molecules are quite close to their decomposition temperatures. Second, the electroluminescence of these compounds are not in the deep blue region, which is within the Commission Internationale de L'Eclairage (CIE) coordinates of (0.15, 0.15). The CF_3 substituted compounds **3.7** and **3.9** still display strong excimer emission in the OLED devices, indicating that the trityl group is not enough to eliminate intermolecular stackings in the EL devices. For the tBu substituted compounds **3.8**, its emission energy is not blue enough, due to the stabilization of its HOMO level by the electron donating tBu group. Finally, during the collaboration with the Aziz group at the University of Waterloo and the Cambridge Display Technology Ltd., we found that this type of bidentate Pt(II) complexes are not photochemically and electrochemically stable, as they decompose rapidly under UV irradiation or in the electroluminescent devices. This is due to the distortion of the platinum center from square-planar geometry in the excited states, which is common issue with the Pt(II)-based emitters.[9] Consequently, only a few examples of deep blue electrophosphorescent Pt(II) complexes with Commission Internationale de L'Eclairage (CIE) coordinates near deep blue (0.15, 0.15) were reported in the literature.[10]

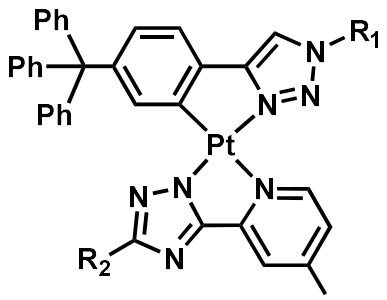

R_1 = CH_2Ph or $CHPh_2$; R_2 = tBu or CF_3

Chart 4.1

Recently, the development of Pt(II)-based deep blue emitters has gained a great momentum recently after the successful demonstration of using tetradentate chelate ligands as an effective strategy in achieving efficient Pt(II) emitters for OLEDs by a number of research teams.[10,11] The representative examples of blue and blue-green Pt(II) emitters with tetradentate ligands are shown in Scheme 4.1. Impressive deep blue OLEDs based on compound E[10b, 10c] and white light OLEDs based on compound B[11d] with high external quantum efficiencies (EQE) have been reported. Nonetheless, in addition to poor color purity for some of the tetradentate chelate Pt(II) compounds, the previously reported blue/blue-green Pt(II) emitters have various deficiencies such as a highly distorted non-planar structure (e.g. A,[11a] D[10b] and E[10c]), or a low emission quantum efficiency at ambient temperature (e.g. C[11b, 11c]), or a great tendency to form excimers (e.g. B, F[11e]), which limit their use as deep-blue emitters in OLEDs. Therefore, it is necessary to design and develop new deep blue emitters of Pt(II) compounds that can address these problems. Based on these considerations and the prior work, we have designed and synthesized a new class of highly efficient deep-blue phosphorescent Pt(II) compounds F shown in Scheme 4.1.

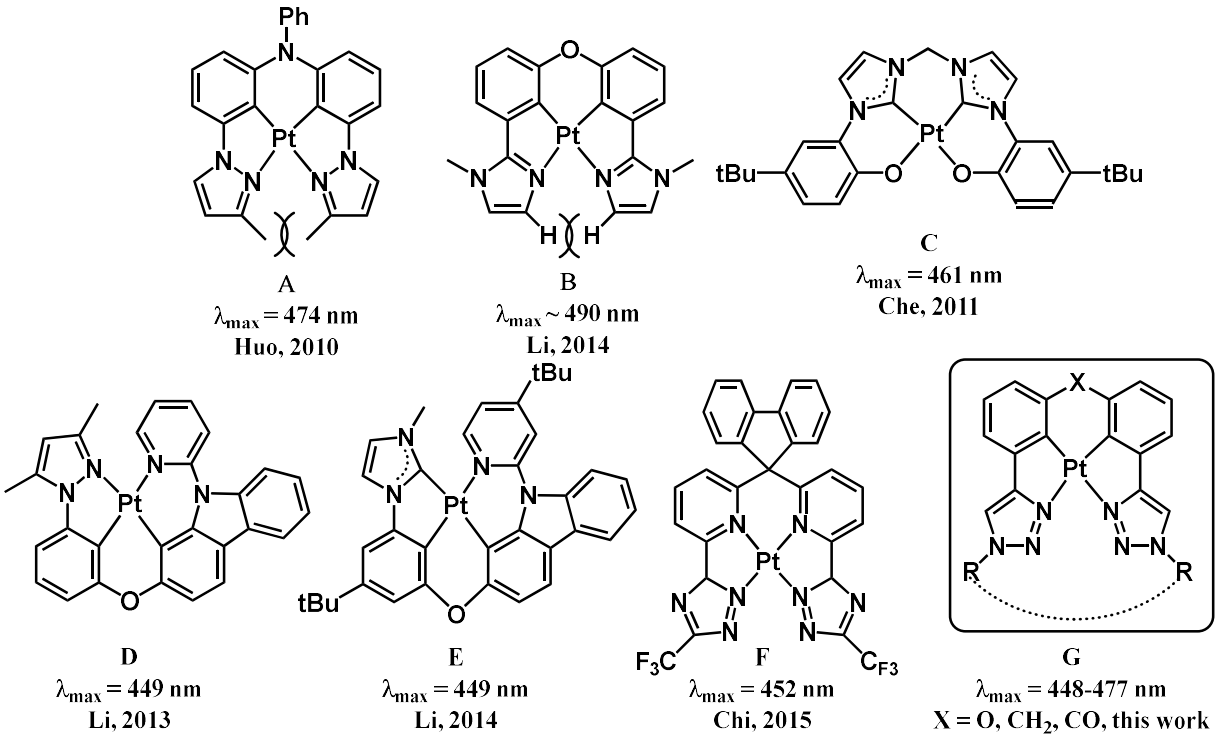

Scheme 4.1 Representative examples of tetradentate blue/blue green Pt(II) emitters.

The design of molecules G was inspired by Huo and Li's molecules A[11a] and B.[11d] Although the central core of compounds G resembles those of A and B, there are important differences between them. First, compounds A and B are blue-green emitters with two pyrazolyl or two *N*-methyl-imidazolyl rings in the central core, while in G, there are two 1,2,3-triazolyl rings in the central core, which would be critical to move the blue-green emission to deep blue, based on TD-DFT computational data. Secondly, there are two *ortho* methyl groups in A, two *ortho* H atoms (H_1) and two *N*-methyls in B which cause structural distortion due to intramolecular steric interactions. This problem could, however, be eliminated in the new molecules G, which lack the *ortho* substituents on the triazolyl ring, thus enhancing the structural stability of the Pt(II) compounds. Lastly, molecules F allow us to add additional steric constraint via a linker between the two N atoms of the triazolyl rings, thus creating macrocyclic tetradentate chelate ligands to further

enhance the structural stability in the excited state. Another key advantage offered by the 1,2,3-triazolyl unit is that the syntheses and functionalization of 1,2,3-triazoles can be achieved readily via the well-established Cu(I) catalysed "click" coupling reaction.

Based on the new ligand design, a series of bright blue phosphorescent tetradentate and macrocyclic Pt(II) compounds have been achieved. The macrocyclic Pt(II) molecules were found to indeed have a better thermal stability, higher phosphorescence quantum efficiency, higher photostability and undergo little structural change in the excited state, compared to the non-macrocyclic tetradentate molecules. Finally, bright deep-blue OLEDs have been successfully fabricated.

4.2 Results and Discussion

4.2.1 Synthesis

Seven tetradentate N^C^C^N ligands were synthesized as the chelate chromophores for the Pt (II) compounds. Three different units, oxygen atom (**L4.1, L4.2, L4.5-L4.7**), a methylene group (**L4.3**) or a carbonyl group (**L4.4**), which link the two phenyl-1,2,3-triazolyl units of the chelate backbone were employed in order to establish the impact of the linking unit on the structure and the photophysical properties of the resulting Pt(II) compounds. To examine the influence of the R group on the 1,2,3-triazolyl ring on the properties of the Pt(II) compounds, various R groups were introduced. In compounds **L4.2**, **L3.3** and **L4.4**, the two R groups are *n*-hexyl groups while in **L4.1** they are benzyl groups. Compound **L4.5** is asymmetric with one methyl and one hexyl group on the two triazole rings, respectively. In **L4.6** and **L4.7**, the two triazolyl rings are connected by a dodecamethylene chain and a 3,6,9-trioxaundecamethylene chain, respectively. **L4.1-L4.4** were

synthesized using the procedure similar to that we reported earlier for related bidentate ligands[8d] (Scheme 4.2), in which the corresponding dialkyne and the monoazide were reacted in CH_2Cl_2 at ambient temperature overnight. Diisopropylethylamine was used as the base, $[Cu(CH_3CN)_4]PF_6$ along with tris[(1-benzyl-1*H*-1,2,3-triazol-4-yl)methyl]amine (TBTA) was used as the catalyst. For macrocyclic molecules **L4.6** and **L4.7**, the concentrations of all reagents and catalysts were reduced to one sixth of that for **L4.1**-**L4.4** and the reaction time was increased to 6 days. The yields of **L4.6** and **L4.7** (17% - 24%) are substantially lower than those of **L4.1**-**L4.4** (53% - 74%), which is not surprising as the polymerization of the dialkyne and the diazide was competing with the ring closing reaction. In fact, a large quantity of insoluble polymer products precipitated out during the reaction even at the reduced concentration. Further dilution of the solution would result in prolonged reaction time without significant improvement on yield. For **L4.5**, due to its asymmetric nature, a different method was used, namely, a Cu(I) catalyzed etherification of aryl halides and phenols.[12] The reaction between the bromine substituted phenyl-triazole and the phenol generated **L4.5** in good yield (77%).

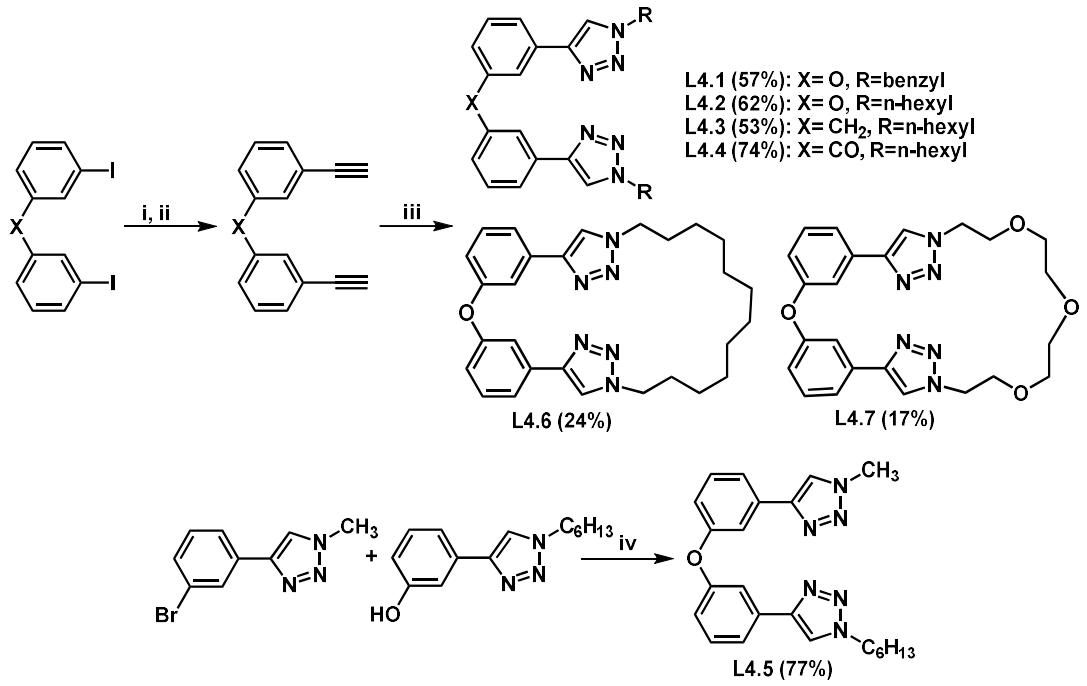

Scheme 4.2 Synthetic procedures of ligands **L4.1**-**L4.7**. Reagents and conditions: i) $PdCl_2(PPh_3)_2$, CuI, THF/Et_3N (3:1 v/v), r.t.; ii) TBAF, THF; iii) $(i\text{-Pr})_2NEt$, $[Cu(CH_3CN)_4]PF_6$, TBTA, CH_2Cl_2, RN_3, r.t.; iv) K_3PO_4, CuI, 2-picolinic acid, DMSO, 90 °C, 4 days.

The new Pt(II) compounds with the seven tetradentate chelate ligands were synthesized using a procedure shown in Scheme 4.3. The tetradentate ligand, the phase transfer reagent NBu_4Br and K_2PtCl_4 were stirred at 25 °C for 1 day in glacial acetic acid, followed by heating at 140 °C for 4 days. After purification, the Pt(II) compounds were obtained in 11 – 52% yields. All Pt(II) compounds were characterized by NMR and HRMS analyses. The crystal structures of all Pt(II) compounds except **4.4** were determined by single-crystal X-ray diffraction analyses.

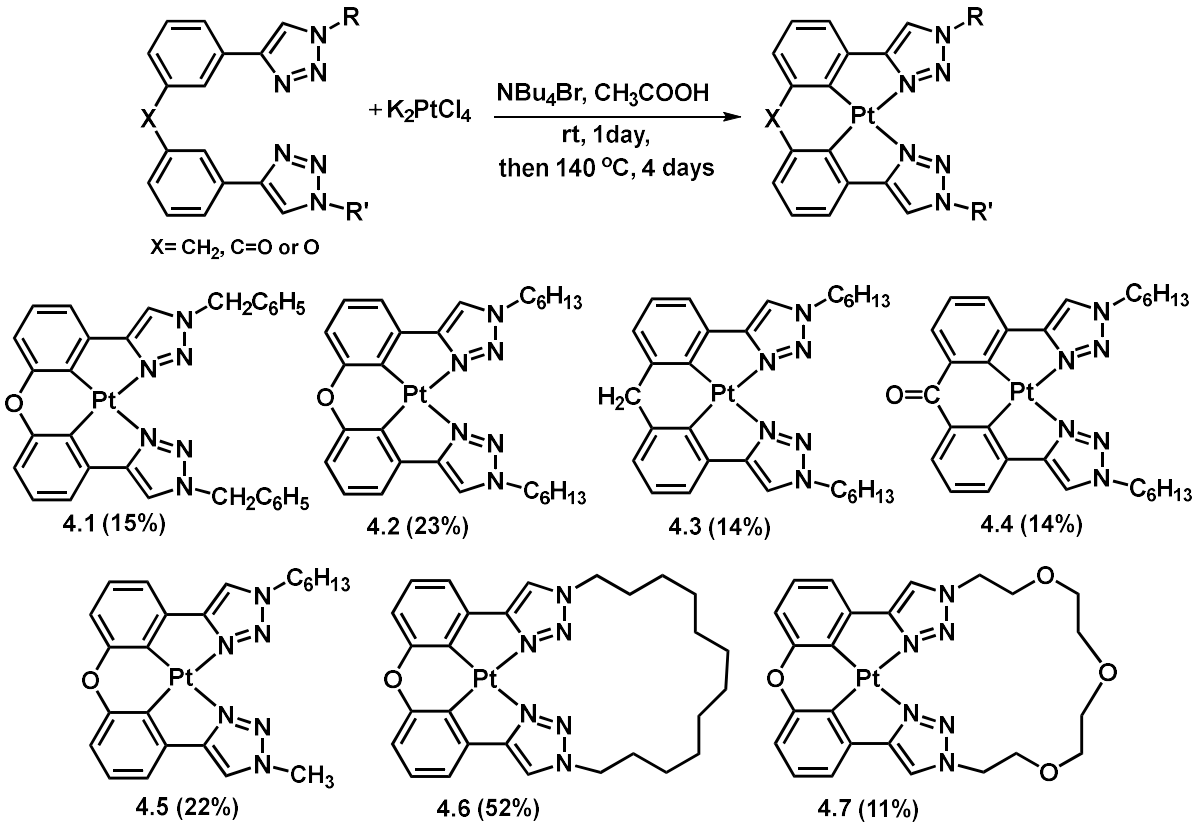

Scheme 4.3 Synthetic procedure and structures of tetradentate Pt(II) compounds **4.1-4.7**.

4.2.2 Crystal Structures

The crystal structures of **4.1**-**4.3** and **4.5-4.7** are shown in Figure 4.1 and the important bond lengths and angles are given in Table 4.1. The geometry of the Pt(II) unit in all molecules displays a significant deviation from an ideal square plane as evidenced by the C(1) –Pt(1) – N(4)/C(7) – Pt(1) – N(1) angles (~172°) and the N(1) – Pt(1) – N(4) angle (~106 ° – 107.0 °) in **4.1**, **4.2** and **4.5-4.7** , which may be explained by the significant bond length difference between the Pt-N bonds (2.05 – 2.08 Å) and the Pt-C bonds (1.96-1.97 Å) in these structures. For **4.3**, however, the structure is less deviated from an ideal square plane as shown by C(1) –Pt(1) – N(4)/C(7) – Pt(1) – N(1) angles (~175°) and the N(1)-Pt1-N(4) angle (~104 °), which can be attributed to the much longer

bonds between the CH_2 linker and the phenyl rings (1.507(5) Å, 1.519(5) Å), compared to those between the O(1) linker and the phenyl rings in other molecules (~1.370 – 1.390 Å). For structures that have the oxygen atom as the linker, the central core has a flat structure and the O(1) atom is in the plane of the central core as shown by the side view of the crystal structures in Figure 4.1. However, for **4.3**, its CH_2 linker is out of the plane of the central core with considerable puckering, as shown by the side view of the crystal structure of **4.3**. The two phenyl rings connecting the methylene group in **4.3** are slightly bent compared to those in other tetradentate molecules. The long alkyl/polyether chains/linkers in **4.2**, **4.3**, **4.5-4.7** are considerably puckered and out of the plane of the Pt(II) unit, which is believed to reduce intermolecular π stacking. In fact, crystal structures revealed that in the crystal lattice, only molecule **4.5** shows extended π stacking interactions as shown in Figure 4.2 while molecules **4.1** and **4.6** form a partially stacked dimer via the triazolyl rings. Therefore, to minimize π-stacking interactions, it is necessary to have either a long alkyl group on each of the triazolyl N atoms or a long alkyl or polyether linker. These crystal structural data support that the use of 1,2,3-triazolyl in the tetradentate ligand is an effective approach in achieving planar tetradentate/macrocyclic Pt(II) compounds.

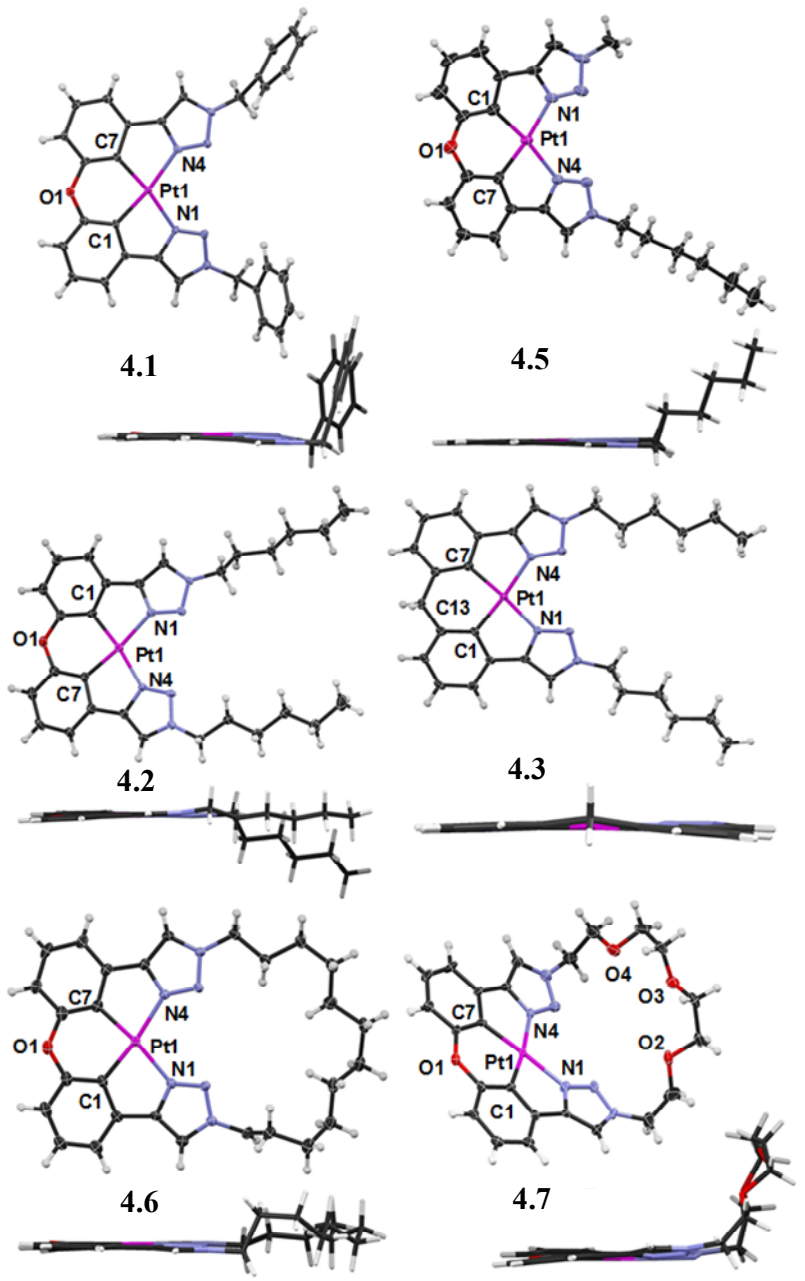

Figure 4.1 Top view and side view of the crystal structures of compounds **4.1-4.3** and **4.5-4.7**. For **4.3**, the side view shows the puckering of the CH_2 linker.

Table 4.1 Important Bond Lengths (Å) and Angles (°) for compounds 4.1-4.7 (except 4.4)

	X – C_{Ph}	Pt(1)–C(1)/C(7)	Pt(1)–N(1)/N(4)	N(1)–Pt(1)–C(7)/ N(4)–Pt(1)–C(1)	N(1)–Pt(1)–N(4)
4.1	1.389(7)/1.407(7)	1.962(6)/1.954(6)	2.095(5)/2.096(5)	171.4(2)/172.1(2)	107.5(2)
4.2	1.380(6)/1.392(6)	1.963(6)/1.968(5)	2.076(4)/2.076(4)	172.3(2)/172.34(2)	107.3(2)
4.3	1.507(5)/1.519(5)	1.989(3)/1.986(4)	2.079(3)/2.080(3)	175.1(1)/175.0(1)	104.3(1)
4.5	1.387(6)/1.396(7)	1.957(5)/1.957(4)	2.081(4)/2.089(4)	172.2(2)/172.3(2)	107.3(2)
4.6	1.387(5)/1.389(5)	1.967(4)/1.964(4)	2.078(3)/2.069(3)	172.9(2)/172.2(2)	106.6(1)
4.7	1.369(11)/1.388(11)	1.977(9)/1.967(9)	2.071(8)/2.050(8)	173.3(4)/172.8(4)	105.9(3)

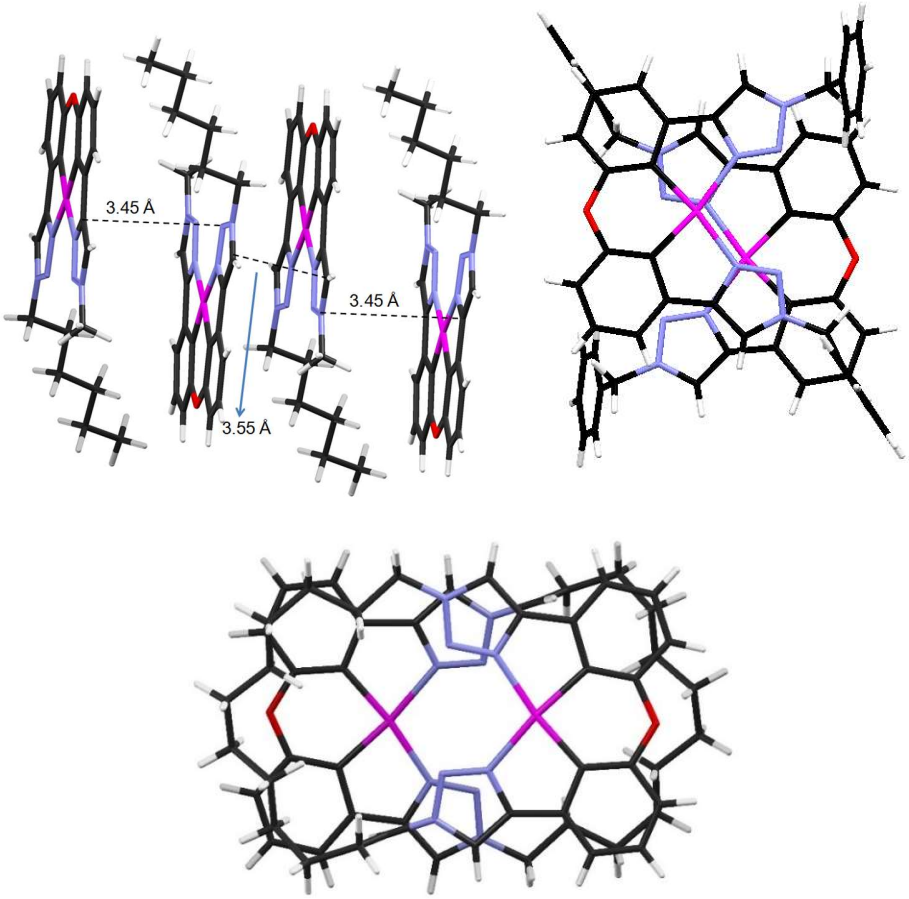

Figure 4.2 Diagrams showing the stacking of compound **4.1**, **4.5** and **4.6** in the crystal lattice. Top left: extended π-stacking of compound **4.5**; Top right: partially stacked discrete dimer of **4.1**; Bottom: partially stacked discrete dimer of **4.6**.

4.2.3 Thermal stability

To examine the thermal stability of the new class of Pt(II) compounds, thermogravimetric analysis (TGA) was performed for vacuum dried samples of **4.2** and **4.6**. To remove potential solvent molecules in the samples, both compounds were kept under vacuum overnight and then heated for 10 minutes at 100°C under nitrogen before recording the TGA diagrams under nitrogen. Although both **4.2** and **4.6** have the same total number of carbon atoms (12) in the R groups attached to the 1,2,3-triazolyl N atom, the TGA diagrams (Figure 4.3) show that compound **4.6** is thermally more stable than **4.2**, as **4.2** starts to decompose at about 325°C while **4.6** is stable up to 400 °C. The less than 2% weigh loss of **4.6** below 400°C is likely caused by the loss of residual solvent molecules. These data indicate that the thermal stability of the tetradentate Pt (II) complexes can be enhanced by adopting the macrocyclic structure.

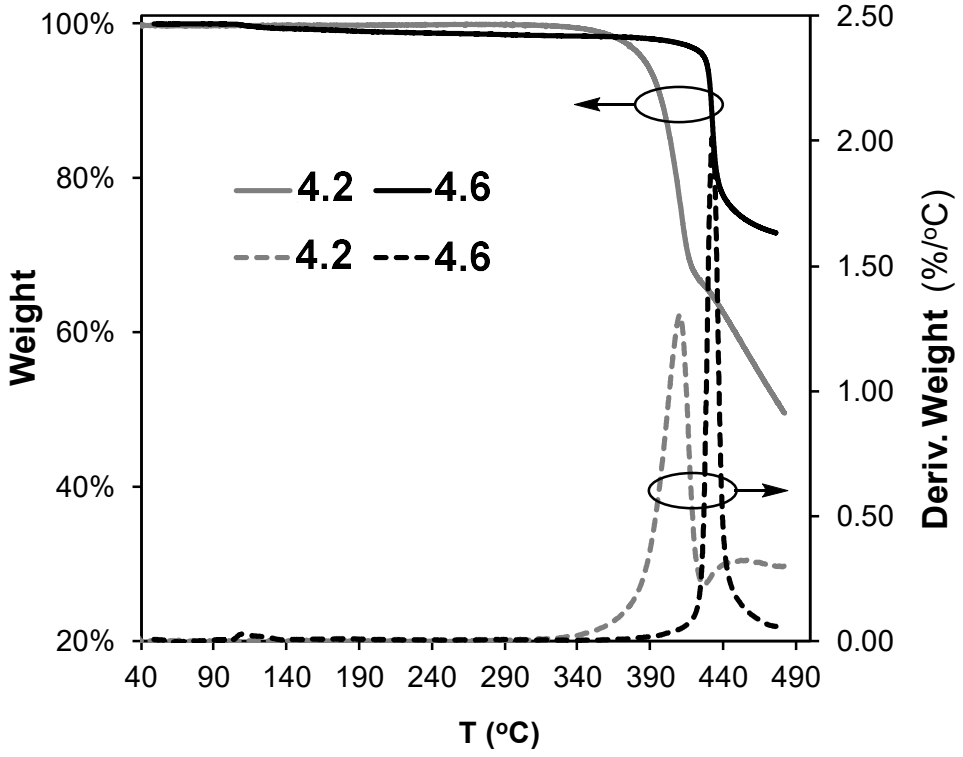

Figure 4.3 TGA diagrams for compounds **4.2** and **4.6**.

4.2.4 Luminescent Properties

The photophysical properties of **4.1-4.7** are summarized in Table 4.2. The phosphorescent and absorption spectra of 4.1-4.7 are shown in Figure 4.4. All complexes have strong absorption bands at around 345 nm (ε = 10,000 – 23,000 M^{-1} cm^{-1}) which could be attributed to π-π^* transitions. The weaker bands (ε = 1,500-6,000 M^{-1} cm^{-1}) at around 400 nm may be assigned as metal-to-ligand charge transfer (MLCT) transitions. For compound **4.3**, this low energy band is very weak and appears as a shoulder band.

Table 4.2 Photophysical Data of Compounds **4.1-4.7**

Compd	Absorption[a] λ_{max} [nm] ε [$10^4 cm^{-1} M^{-1}$]	Emission, λ_{max} [nm], 298 K						Emission, 77 K[c]	
		λ_{max} [nm]			Φ_{PL} [b]			λ_{max} [nm]	τ_P [μs]
		CH_2Cl_2	PMMA (wt%)		CH_2Cl_2	PMMA (wt%)			
			5%	10%		5%	10%		
4.1	331 (1.41), 344 (2.35), 387 (0.29)	450	447	448	0.39	0.46	0.27	443	4.1 (58%), 9.5 (42%)
4.2	333 (1.40), 344 (2.35), 386 (0.29)	450	447	448	0.46	0.97	0.62	443	4.5 (63%), 9.7 (37%)
4.3	323 (0.77), 349 (1.84)	445	442	443	0.14	0.38	0.15	439	5.0 (48%), 9.3 (52%)
4.4	316 (1.10), 347 (1.00), 404 (0.68)	477	467	470	0.18	0.50	0.16	457	15.0 (100%)
4.5	331 (1.15), 344 (1.91), 386 (0.26)	449	446	446	0.57	0.60	0.69	443	4.6 (62%), 9.7 (38%)
4.6	335 (1.28), 344 (2.23), 390 (0.24)	448	447	447	0.58	0.83	0.95	442	4.6 (63%), 9.9 (37%)
4.7	331 (1.05), 344 (1.82), 386 (0.21)	449	446	446	0.62	0.84	0.48	443	4.7 (63%), 9.7 (37%)

[a] Measured in CH_2Cl_2 at 2 x 10^{-5} M . [b] The solution quantum efficiency was determined in CH_2Cl_2 using 9,10-diphenylanthracene as the reference under nitrogen. The solid state quantum efficiency was measured using an integration sphere. All quantum yields have an estimated error of ~10%. [c] Recorded in 2-Methyl THF (~2.0 x 10^{-5} M).

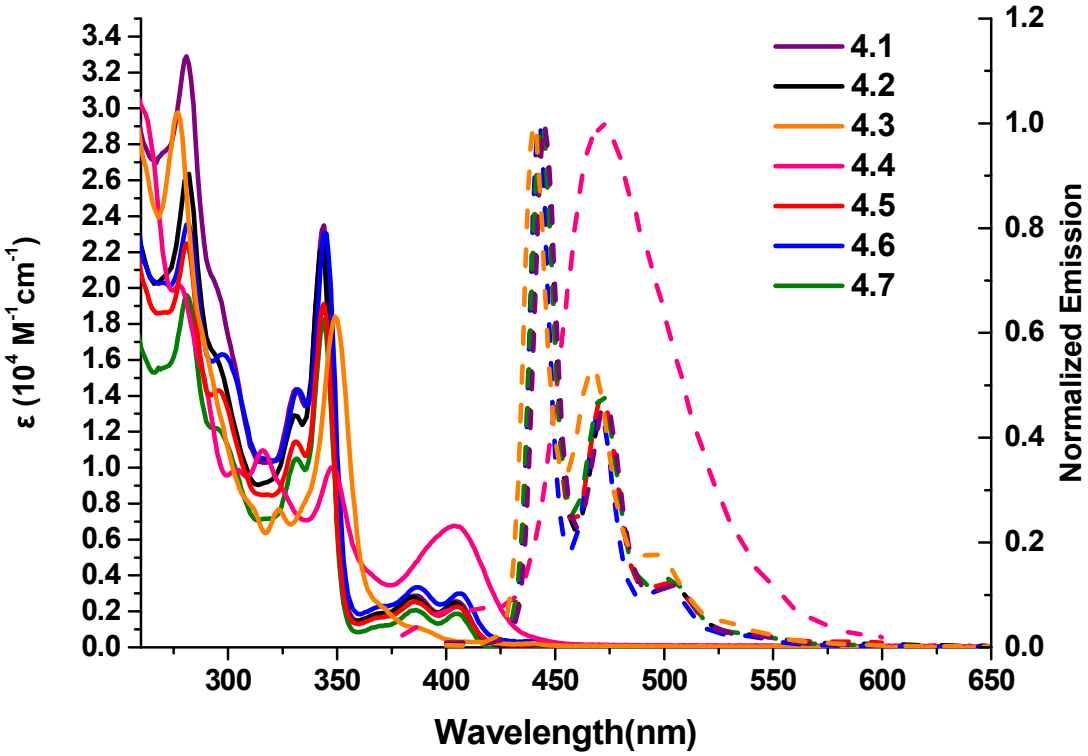

Figure 4.4 UV-Vis (solid lines) and phosphorescent (dashed lines) spectra of compounds **4.1-4.7** in CH_2Cl_2 at ambient temperature.

As shown in Figure 4.4 and 4.5, all complexes display blue emission color in solution and in PMMA film with the emission maxima at about 450 nm (except compound **4.4**) at room temperature, which are blue shifted by about 5 nm at 77 K. The decay lifetimes of all compounds in 2-methyl THF at 77 K are in the microsecond range, indicating that the nature of the luminescence is phosphorescence. The emission spectra of all compounds except **4.4** display well resolved vibronic features, indicating that the emission is likely originated from admixture of ^{3}LC and ^{1}MLCT states. Huang-Rhys ratios of around 0.4-0.5 were estimated for **4.1-4.7** (except **4.4**) in CH_2Cl_2 at ambient temperature and in doped PMMA films, suggesting very small structural displacement in the excited state and a large improvement compared to the bidentate Pt(II) compounds discussed in chapter 2 and 3 (Figure 4.6).

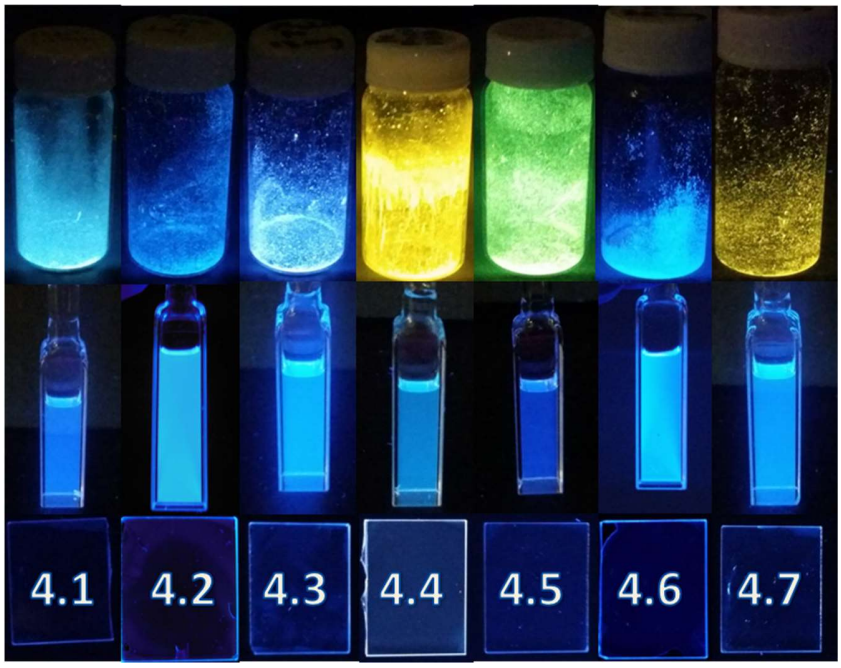

Figure 4.5 Photographs showing the emission colours of compounds **4.1-4.7** as neat solid (top), in CH_2Cl_2 (middle) and in 5% PMMA film at ambient temperature.

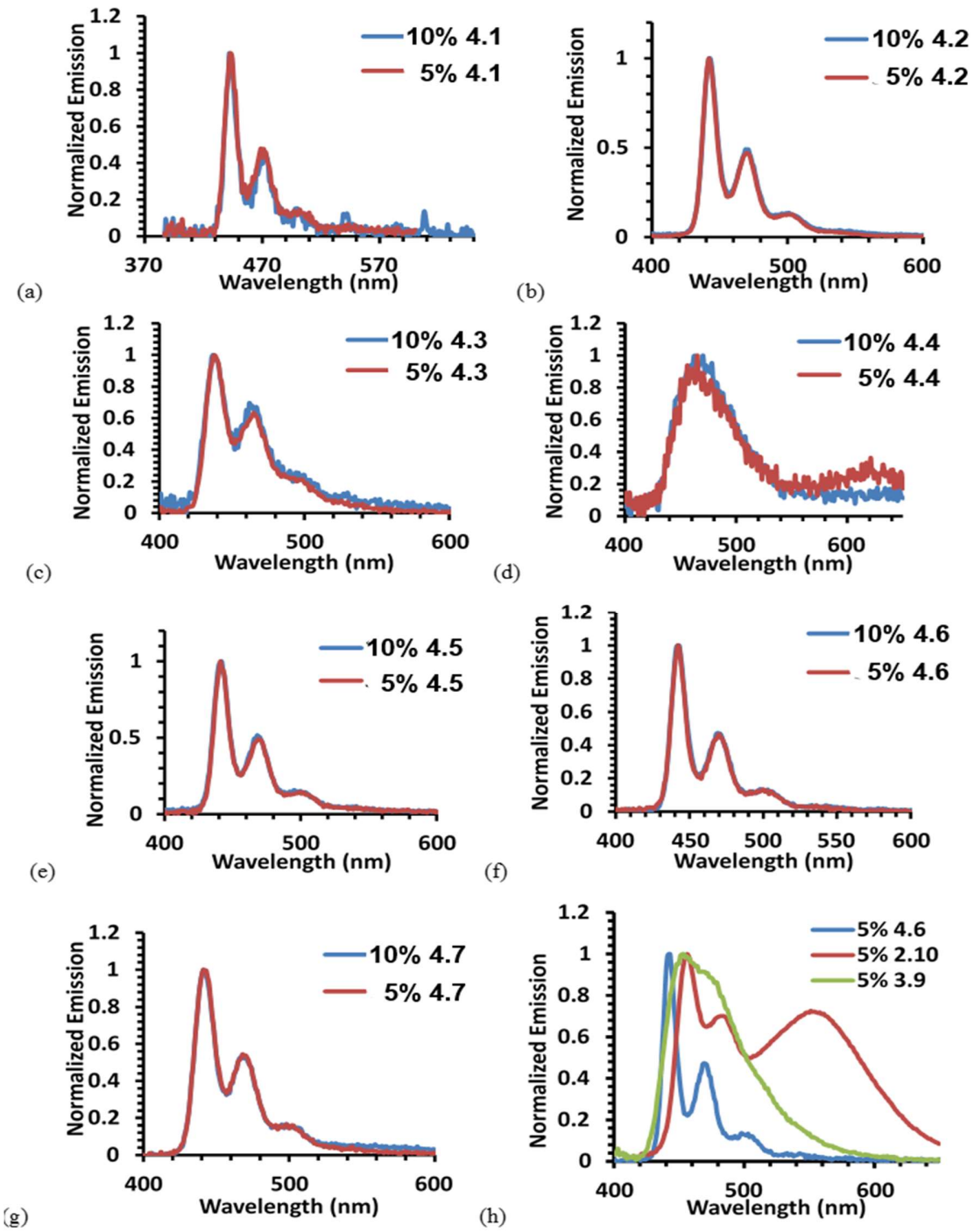

Figure 4.6 (a)-(g): Phosphorescent emission spectra of **4.1-4.7** in doped PMMA films; (h) Phosphorescent emission spectra of **4.6**, **2.10** and **3.9** in 5% PMMA films.

The linker X group has a significant impact on phosphorescence of the Pt(II) complexes, as demonstrated by the luminescent properties of compounds **4.3** and **4.4**. The emission peak of **4.3** is about 5 nm blue shifted from those of **4.1**, **4.2**, and **4.5-4.7**, which is clearly caused by the lack of π-conjugation between the two phenyl rings in the chelate ligand owing to the CH_2 linker. Furthermore, the photoluminescent quantum efficiency (Φ_{PL}) of **4.3** is the lowest (0.14 in CH_2Cl_2 and 0.38 in 5% PMMA film) among the all seven Pt(II) compounds, which is attributed to the non-rigidity of the central core due to the puckering of the CH_2 linker as revealed by the crystal structure, which could enhance non-radiative decay from the excited state. In fact, the Huang-Rhys ratio of **4.3** is the highest among compounds **4.1-4.3** and **4.5-4.7**, suggesting that the excited state structure of **4.3** is the least stable among these complexes. In contrast to the blue emission peaks of **4.1-4.3**, and **4.5-4.7** that have well resolved vibronic features, the emission peak of **4.4** in doped PMMA films and in CH_2Cl_2 at 298K is red shifted by 20-30 nm, and is broad and featureless. This may be explained by the lack of MLCT character in the excited state of **4.4** which is dominated by the ligand centered π-π* transitions and intra ligand charge transfer transitions, as indicated by long decay lifetime of **4.4** (15 μs) compared to the other complexes. Compound **4.4** also has a low Φ_{PL} as shown in Table 4.2, which can be attributed to its low radiative decay rate due to the low MLCT contributions in the excited state.

Compounds **4.1**, **4.2**, **4.5-4.7** have very impressive Φ_{PL}, from 0.39 (**4.1**) to 0.62 (**4.7**) in deaerated CH_2Cl_2 at ambient temperature, which increase significantly in 5% or 10% doped PMMA films, owing to much reduced thermal motion/solvent quenching in a rigid environment. The emission spectra of **4.1**, **4.2**, **4.5-4.7** are essentially identical, indicating that the substituent groups on the 1,2,3-triazole ring have very little effect on the emission energy of these molecules. The substituent

groups on the 1,2,3-triazolyl do have a significant impact on intermolecular interactions, solubility and phosphorescent efficiency. For example, compound **4.1** contains two benzyl groups, which gives it a poor solubility in most common organic solvents except CH_2Cl_2 and $CHCl_3$. In solution, the rotational motion of the benzyl group on the triazole ring contributes to thermal quenching of the phosphorescence, leading to the relatively low Φ_{PL} of **4.1**. The benzylic hydrogens in **4.1** are also susceptible to attacks by radicals, which could be produced during the operation of OLED devices. On the other hand, the steric bulkiness of the benzyl group can reduce intermolecular interactions, making the molecule less prone to excimer formation. Molecules **4.2** and **4.5**, with both substituent groups being alkyl groups, have a much better solubility and higher Φ_{PL} than **4.1**. However, as shown in Figure 4.5, the emission color of **4.5** as neat solid is green, while it emits a blue color in dilute solution or in doped PMMA films. The difference in emission color of **4.5** can be rationalized by intermolecular π stacking interactions in the solid state, as revealed by the crystal data of **4.5**, which leads to excimer emission in the solid state (Figure 4.7). Compounds **4.4** and **4.7** emit yellow and orange color (Figure 4.5 and 4.7), respectively, in the solid state, which is also likely caused by intermolecular interactions in the solid state, although π-stacking interactions are not observed in the crystal lattice of **4.7**.

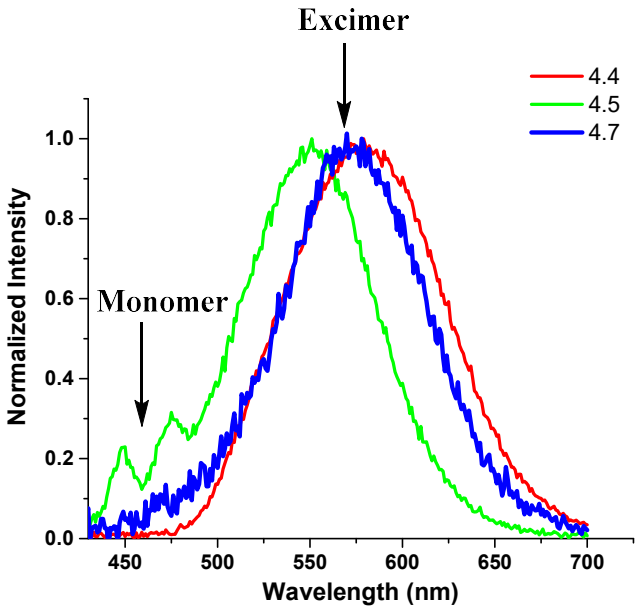

Figure 4.7 Phosphorescent emission spectra of **4.4**, **4.5** and **4.7** as neat powder.

Molecules **4.6** and **4.7** with the macrocyclic chelate ligands have a significantly higher Φ_{PL} (0.58, 0.62, respectively) in solution than the related non-macrocyclic compound **4.2** (0.42), which can be attributed to the greater structural rigidity imposed by the macrocyclic ligands in **4.6** and **4.7**. In 10% doped PMMA films, compound **4.6** has the highest Φ_{PL}, 0.95, while those of **4.2** (0.62) and **4.7** (0.48) are much lower. The persistent deep blue emission color and high Φ_{PL} make compound **4.6** a good candidate as a emitter for deep blue OLEDs.

4.2.5 Stability towards UV Irradiation

UV stability tests for emitters are a standard practice to evaluate the stability of emitters in the excited state.[13] Molecules that are unstable toward UV irradiation at a wavelength near its excitation energy are certainly not suitable as emitters in OLEDs. Therefore, to study the stability of the new tetradentate Pt(II) compounds in the excited state, we examined the stability of

compounds **4.2** and **4.6** toward UV irradiation. PMMA films of compound **4.2** and **4.6** were prepared at a 5% doping level and exposed to continuous UV irradiation at 350 nm and 352 nm (within the first low energy band in each molecule), respectively, at which both molecules have a similar extinction coefficient. The emission intensity change of these two compounds with time was monitored for a total of 300 minutes under ambient conditions. For comparison, the same experiment was also performed for 5% doped PMMA films of the well-known green emitter $Ir(ppy)_3$, an Ir(III) blue emitter Firpic and a sterically protected bis-chelate blue Pt(II) emitter **3.8**, at the irradiation wavelength of 393 nm, 364 nm, and 364 nm, respectively. At the selected irradiation wavelength, these compounds have approximately the same molar absorptivity of ~7000 M^{-1} cm^{-1}. Under these experimental conditions, it was found that the bis-chelate compound **3.8** is the least stable among the compounds tested as its emission intensity dropped to 68% of the initial value after being irradiated for 5 hours, while 13%, 14%, 13%, and 13% intensity losses were observed for **4.2**, **4.6** and $Ir(ppy)_3$, and Firpic, respectively, (Figure 4.8). The same experiments were also performed in polystyrene films and similar results were obtained. The photographs of the polymer films before and after UV irradiation are also shown in Figure 4.8. A darkened area that corresponds to the area exposed to the irradiation light was visible at the centre of the films of **3.8**, $Ir(ppy)_3$ and Firpic, indicating photodegradation of these materials after UV irradiation. Interestingly, however, there is no obvious darkening for the films of **4.2** and **4.6**. Similar results were also obtained for irradiation at 350 nm for these compounds. In a collaboration with Cambridge Display Technology Ltd., We found that the photostability of **4.6** in doped polystyrene films is about 5 times higher than that of **4.2**, demonstrating that the phosostability of the molecule could also be enhanced using the macrocyclic ligand instead of the non-macrocyclic tetradentate ligand. These data support that the photostability of the tetradentate Pt(II) compounds

are much higher than the bidentate compound and are at least comparable to or better than that of $Ir(ppy)_3$ and Firpic under ambient conditions, further strengthening the case of the new tetradentate Pt(II) compounds as deep blue emitters for OLEDs.

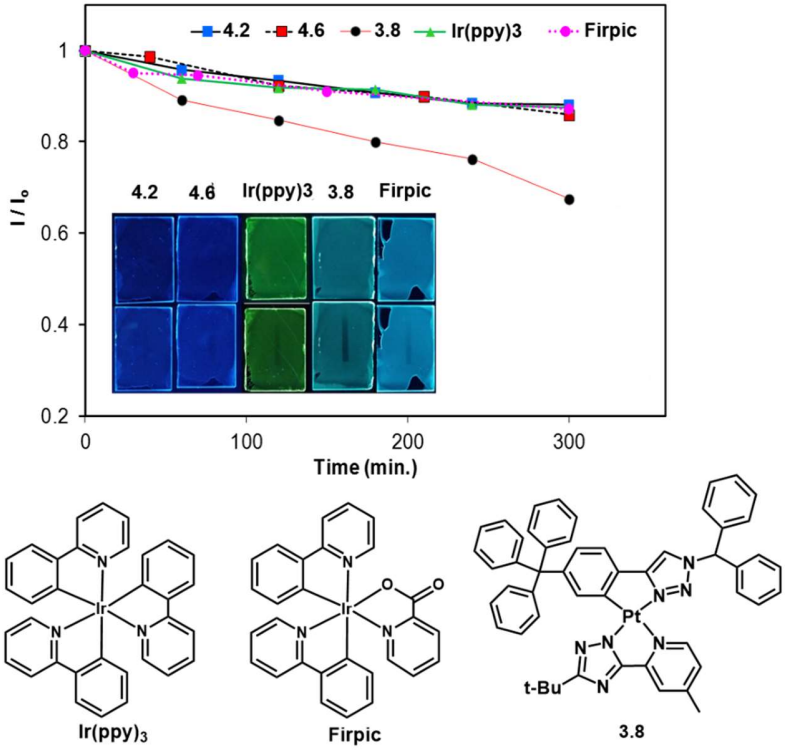

Figure 4.8 A diagram showing the emission intensity decay of the peak at λ_{max} with time for representative compounds in 5 wt% PMMA films under continuous UV irradiation under air and at ambient temperature. Inset: photographs showing the emission color of the PMMA films before and after UV exposure.

4.2.6 Computational Studies

To gain a deeper insight into the luminescent properties of the new tetradentate Pt(II) complexes, TD-DFT calculations were performed using Gaussian 09 software at B3LYP level of theory using LANL2DZ basis set for Pt atom and 6-31G* for all other atoms.[14] The results are summarized in Table 4.3. The compositions of HOMO and LUMO of **4.1**, **4.2**, **4.5**, **4.6** and **4.7** are similar with the HOMO located on the phenyl rings and having a large contribution from the bridging oxygen

atom and the Pt(II) core, while the LUMO delocalized over the entire ligand backbone (Table 4.4). The aliphatic chains have no contributions to HOMO and LUMO, which is not surprising as the absorption and emission spectra of this group of compounds show little difference. TD-DFT computational data confirmed that the vertical excitation to the S_1 state involves mainly HOMO → LUMO transition for all compounds. The calculated energy and the oscillator strengths for the $S_0 \rightarrow S_1$ transition agree well with the observed extinction coefficients of the low energy absorption bands in the UV-Vis spectra of the Pt(II) compounds. The HOMO → LUMO transition is also the major component of the $S_0 \rightarrow T_1$ vertical excitation (> 70%, see Table 4.3) for all compounds except **4.4**, whose first triplet excited state mainly involves HOMO-2 → LUMO (93%), transitions (Table 4.4). For compound **4.4** there is a large contribution from the carbonyl linker to both the HOMO-2 and the LUMO, which gives a significant ligand centered π-π* and intra ligand charge transfer character in the first triplet excited state, in good agreement with the featureless phosphorescent spectrum of **4.4** and its long decay lifetime due to the lack of MLCT contributions. For **4.3**, the bridging methylene group has little contributions in the HOMO compared to the oxygen-containing ones, as the carbon atom is sp^3 hybridized and breaks the conjugation.

Table 4.3 TD-DFT data for compounds **4.1-4.7**

Compd	HOMO (eV)	LUMO (eV)	H – L gap (eV)	$^{a}E_g$ (S_1)	$^{b}E_g$ (T_1)	% H → L ($S_0 \rightarrow S_1$)	f ($S_0 \rightarrow S_1$)	% H → L ($S_0 \rightarrow T_1$)
4.1	-4.65	-0.82	3.83	3.12	2.53	88	0.0364	87
4.2	-4.63	-0.77	3.86	3.12	2.53	94	0.0339	89
4.3	-4.82	-0.66	4.16	3.33	2.37	98	0.0115	75
4.4	-5.19	-1.20	3.99	3.34	2.23	85	0.0765	< 1
4.5	-4.66	-0.77	3.89	3.14	2.54	94	0.0319	90
4.6	-4.63	-0.79	3.84	3.10	2.52	94	0.0365	90
4.7	-4.81	-1.03	3.78	3.06	2.47	88	0.0395	90

$^{a}S_0 \rightarrow S_1$ vertical excitation energies, calculated using the optimized structure at S_0. $^{b}T_1 \rightarrow S_0$ emission energies, calculated using the optimized structure at the T_1 state.

Table 4.4 MO diagrams of **4.1-4.7** (isocontour value = 0.03).

	4.1	**4.2**	**4.3**	**4.4**
LUMO	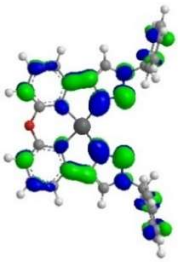	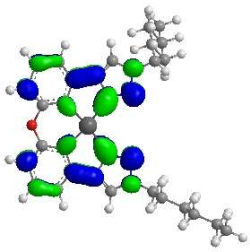	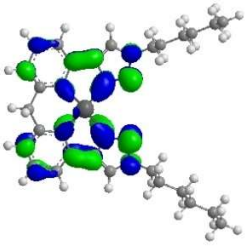	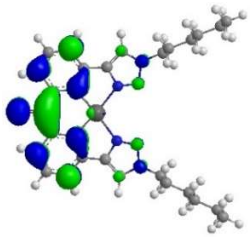
HOMO	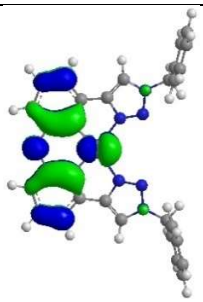	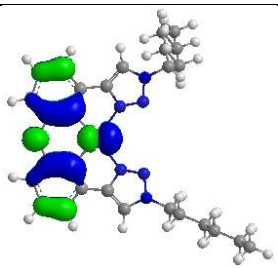	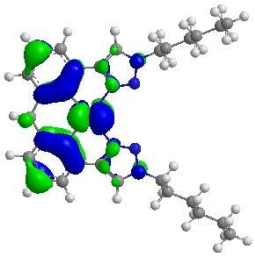	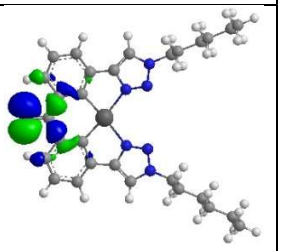 **(HOMO-2)**
	4.5	**4.6**	**4.7**	
LUMO	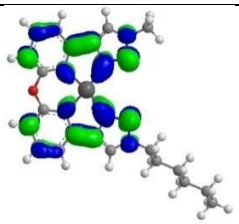	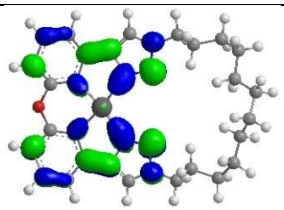	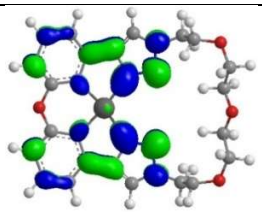	
HOMO	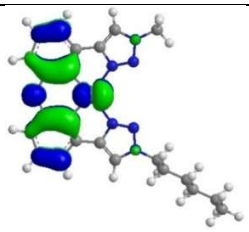	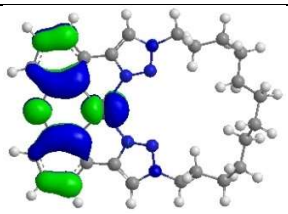	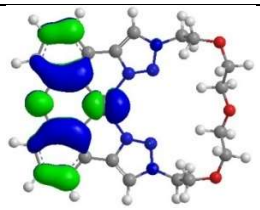	

Computational analysis was also employed to examine the structural stability of the tetradentate Pt(II) compounds **4.7** and the bidentate Pt(II) compound **3.8** in the excited state. In biology, root mean square deviation (RMSD) is commonly used to compare the structural similarity of two

proteins.[15] Here we use RMSD to determine the structural difference of compound **4.1-4.7** and **3.8** at the S_0 and T_1 state. The formula is：

$$\mathrm{RMSD} = \sqrt{\frac{1}{N}\sum_{i}^{natom}[(x_i - x_i')^2 + (y_i - y_i')^2 + (z_i - z_i')^2]}$$

where (x_i, y_i, z_i) and (x_i', y_i', z_i') denote the coordinates of the *i*th atom in the optimized ground and the first triplet excited state structure. The optimized S_0 and T_1 structures of **4.1-4.7** and **3.8** and the calculated RMSD are provided in Table 4.5. The RMSD values of **4.6** and **4.7** (0.064 and 0.043) were found to be substantially smaller compared to that of **4.1** and **4.2** (0.408 and 0.351), indicating that the macrocyclic molecules undergo less structural distortion at the T_1 state, which could be responsible for the higher phosphorescence quantum yields of **4.6** and **4.7** in solution, compared to **4.1** and **4.2** shown in Table 4.2.

It is well known that one of the degradation processes in Ir(III) based OLEDs involves ligand dissociation, in which one of the binding site of the emitter is opened up after electronic excitation.[5, 16] Similar reactions could also take place for bis-chelate Pt(II) based complexes, but would be less favorable by changing the bidentate ligands to tetradentate ligands, due to the increased chelate effect and structural constraint. To verify this hypothesis, TD-DFT analysis was used to examine and compare the possible structural change of **4.2** and **3.8** in the excited state. The input structures of **4.2** and **3.8** were varied from their optimized configuration and geometry optimizations were performed. Although the optimized structure at the T_1 state retains the square planar geometry for compound **3.8**, six other stable configurations were found for **3.8** at the T_1 state (Table 4.6), in which the square-planar geometry is lost and replaced by either a distorted tetrahedral or pyramidal geometry with considerably lengthened Pt-N_{py} bonds, which are believed to be responsible for the

relatively poor stability of **3.8** in the excited state. In contrast, similar structural distortion and local minima were not found at all for **4.2** at the T_1 state. In fact, no structural distortion pathway involving the central core was found for **4.2** in the excited state, which supports that the tetradentate ligand's constraint on the Pt(II) structure can indeed greatly enhance the structural stability of the molecule in the excited state.

Table 4.5 Optimized S_0 and T_1 structures and RMSD values of **4.1-4.7** and **3.8**

compd	**4.1**	**4.2**	**4.3**	**4.4**
T_1	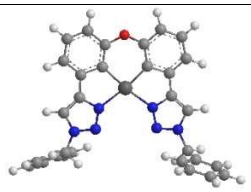	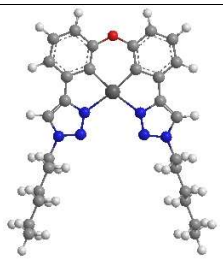	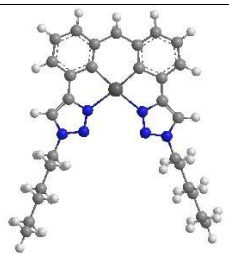	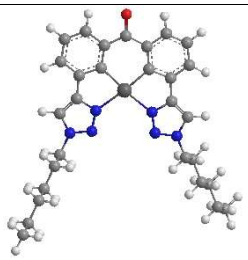
S_0		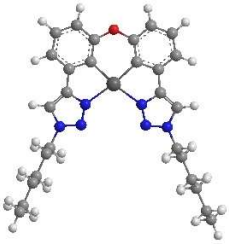	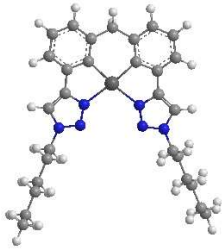	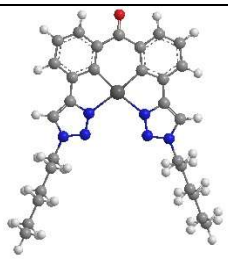
RMSD	0.408	0.351	0.118	0.088
compd	**4.5**	**4.6**	**4.7**	**3.8**
T_1	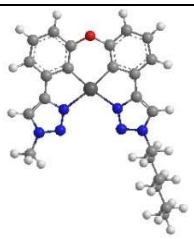	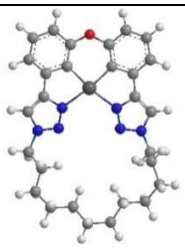	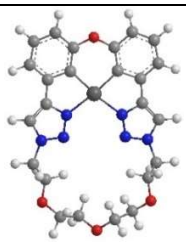	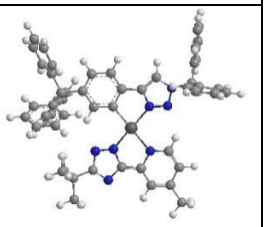
S_0		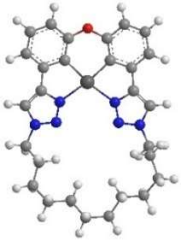	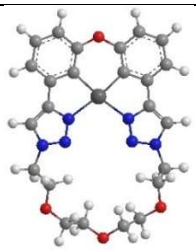	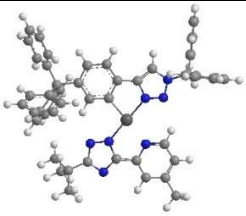
RMSD	0.390	0.064	0.043	

Table 4.6 Six stable geometries of **3.8** at the T_1 state

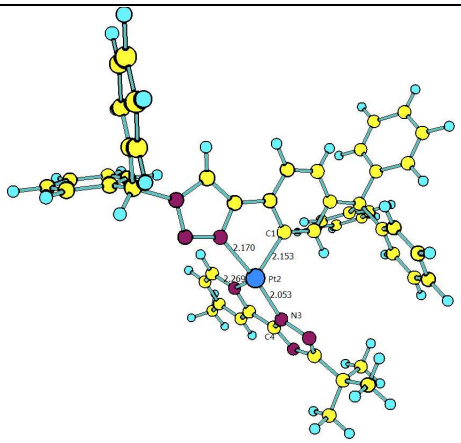	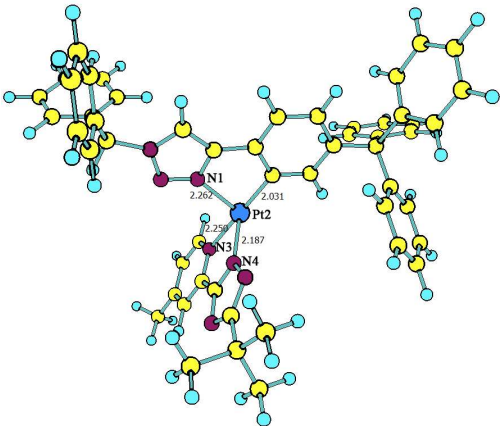
3.8-a	**3.8-b**
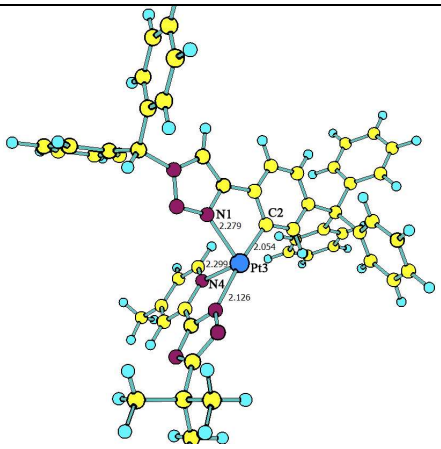	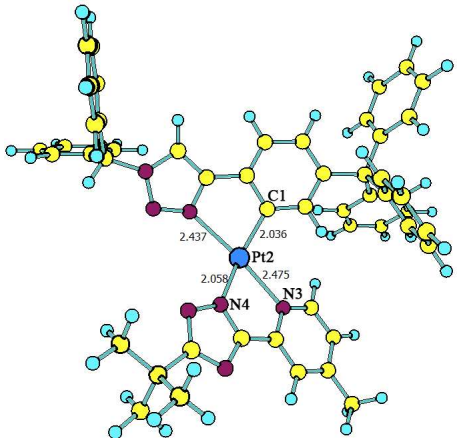
3.8-c	**3.8-d**
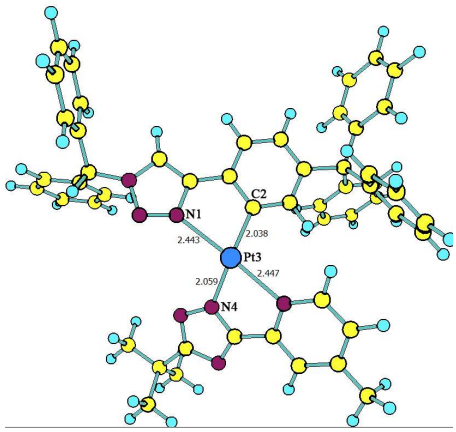	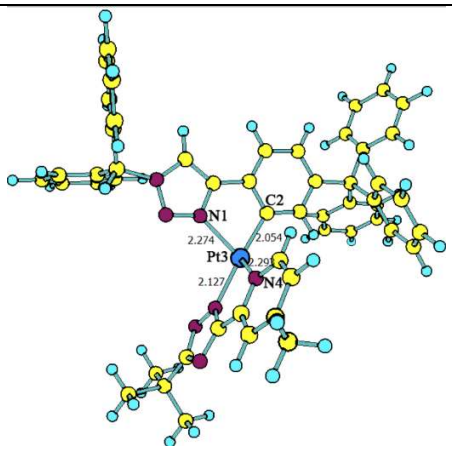
3.8-e	**3.8-f**

4.2.7 Electroluminescence

Based on the excellent phosphorescent quantum efficiency, the deep blue emission color and the high thermal stability, compound **4.6** was selected to evaluate electroluminescent (EL) performance. EL devices with various combinations of hosts and charge transport materials were fabricated and examined. The best device structure that produces color-stable deep-blue EL at various driving voltages was found to be ITO/NPB (50 nm) / mCP (10 nm) / BCPO:**4.6** x% (20nm) / DPEPO (10 nm) / TPBi (30nm) / LiF (1 nm) / Al (100 nm) shown in Scheme 4.4, where *N,N′*-di(1-naphthyl)-N,N′-diphenyl-(1,1′-biphenyl)-4,4′-diamine (NPB) and 1,3,5-tris(1-phenyl-1H-benzimidazol-2-yl)benzene (TPBi) are the hole transport layer and the electron transport layer, respectively. Because of the high triplet energy, 1,3-bis(*N*-carbazolyl)benzene (mCP, 2.90 eV) and bis[2-(diphenylphosphino)phenyl] ether oxide (DPEPO, 3.00 eV)[17] were synthesized and used as the hole transport and electron transport/exciton blocking material, respectively. The host material 9,9′-(4,4′-(phenylphosphoryl)bis-(4,1-phenylene))bis(9H-carbazole) (BCPO)[18] was synthesized and used because of its high triplet energy (3.01 eV) and the bipolar nature, which could improve the carrier balance within the emitting layer. To optimize the device efficiency, three devices, A1, B1 and C1 with 2%, 5% and 10% of **4.6** doped in BCPO employed as the emitting layer, respectively, were fabricated first. The energy diagram and the molecular structures of the materials used in the devices are shown in Scheme 4.4. A good carrier trapping can be expected in these devices as the HOMO and LUMO levels of **4.6** are all within those of the host materials BCPO. The EL characteristics of all devices were recorded under ambient conditions without encapsulation of the devices owing to the limitation of the facility in our laboratory. The EL, *L-J-V* (*L* = luminance, *J* = current density, *V* = voltage) and EQE-*L* (EQE = external quantum efficiency)

diagrams for these three devices are shown in Figure 4.9, and the EL data are summarized in Table 4.7.

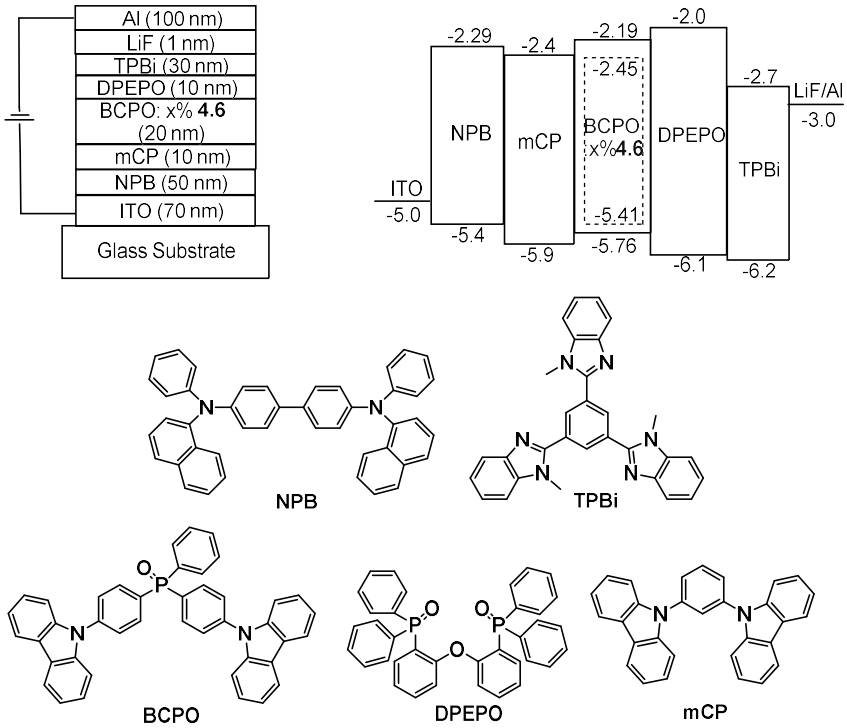

Scheme 4.4 The structures and energy diagram of the EL device and the host and charge transport materials used in the devices.

Table 4.7 EL device data of Compound **4.6**

Device (x% **4.6**)	EL λ_{max} (nm)[a]	V_{on} (V)[b]	Max. *L* (cd/m^2) / V	EQE (%)				η_c (cd/A)[c]	η_p (lm/W)[c]	CIE (x,y)[a]
				Max. EQE / *L*	10 cd/m^2	100 cd/m^2	1000 cd/m^2			
A1 (2%)	452	3.2	6342 / 10.0	7.4 / 1.5	6.9	6.0	4.8	7.1	7.0	(0.11, 0.14)
B1 (5%)	452	3.2	8798 / 11.5	7.5 / 1.4	7.2	6.5	5.4	8.4	8.2	(0.14, 0.13)
C1 (10%)	452	3.2	10676 / 12.5	9.7 / 1.6	9.5	9.1	7.6	11.0	10.8	(0.14, 0.14)
C2 (10%)	451	5.2	3163 / 11.6	15.4 / 490	5.2	12.3	13.0	18.9	14.1	(0.15, 0.17)
D1 (15%)	451	4.4	2304 /12.0	13.6 / 210	2.5	12.1	11.5	20.4	17.8	(0.15, 0.16)
E1 (20%)	451	4.4	3133 / 12.0	14.1 /218	2.2	11.2	11.5	20.4	16.9	(0.16, 0.16)

[a]Value taken at V = 12 V. [b]The applied voltage (V_{on}) is defined as brightness of 1 cd/m^2. [c]Current efficiency (η_c) and power efficiency (η_p) are the maximum values.

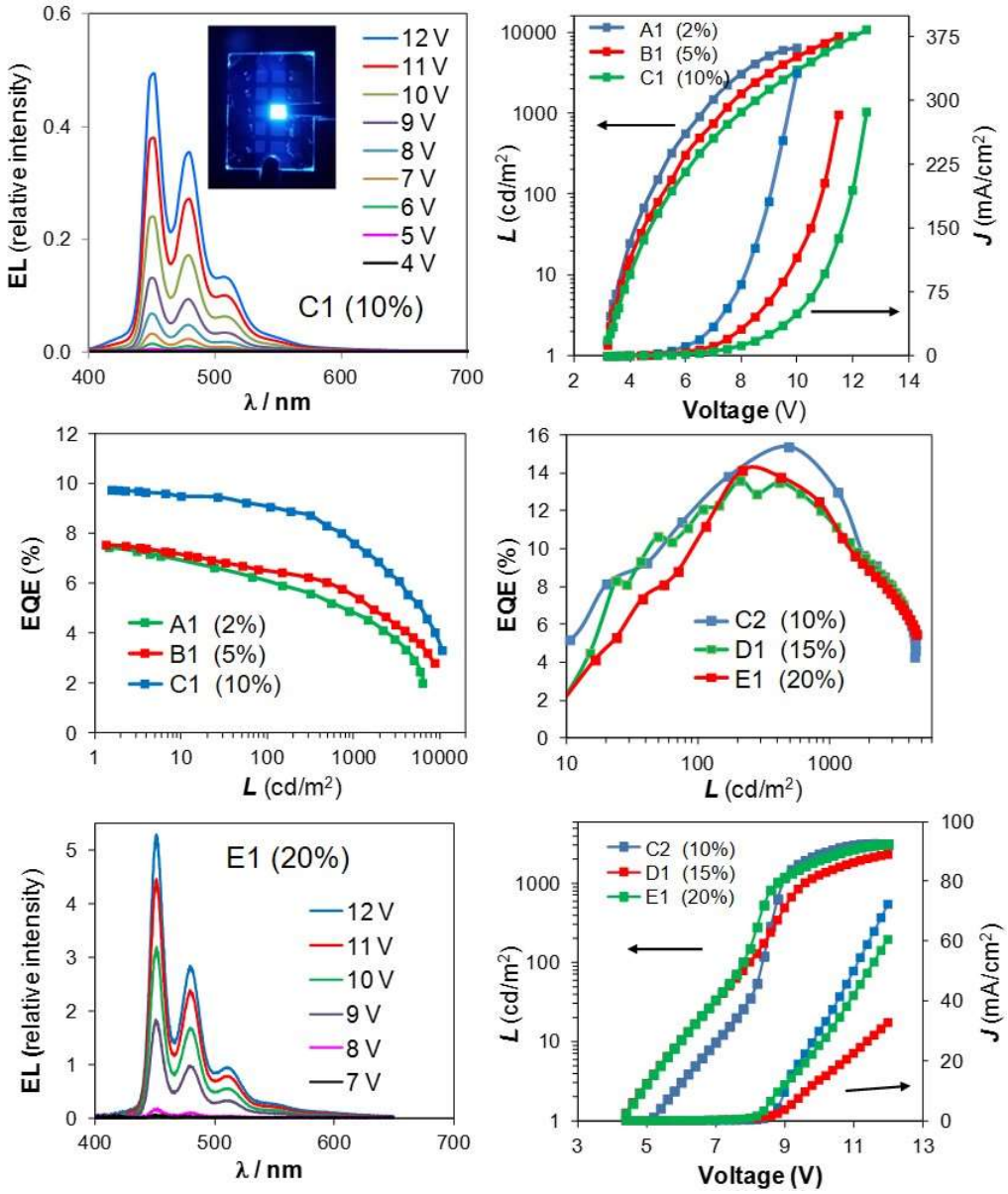

Figure 4.9 EL spectra of devices C1 and E1 at various driving voltages, *L*-*J*-*V* diagrams of all devices, and EQE-*L* diagrams of all devices. Inset: a photograph showing the emission color of the EL device.

The performance of this set of EL devices is very good. The EL spectra produced by the three devices are the same with λ = 452 nm that do not change with the doping level of **4.6** and match well with the PL spectrum of **4.6**, which can be attributed to the efficient triplet confinement of

the exciton blocking layers. Commission Internationale de L'Eclairage (CIE) coordinates of all three devices are in the deep blue region with (x + y) < 0.30 as shown in Table 4.7. Significantly, all three devices exhibit stable EL emission within the entire range of the driving voltage as shown by the EL spectra of the device C1 in Figure 4.9. All of the devices exhibited rather low turn-on voltage at 3.2 V. The best performance was achieved for device C1 with 10% doped emitter **4.6**, which reached maximum brightness, current efficiency and power efficiency of 10,680 cd m^{-2}, 11.0 cd/A and 10.8 lm/W, respectively. The EQE of 9.1% and 7.5% were achieved at the brightness of 100 and 1000 cd m^{-2}, respectively for device C1. Although the maximum EQE (9.7%) of C1 is not very high, compared to some of the recently reported deep blue Pt(II)-based EL devices, C1 is certainly among the brightest deep blue Pt(II) EL devices. Furthermore, C1 has a relatively low EQE roll-off curve at brightness below 1000 cd/m^2, as shown in Figure 4.9. These preliminary data support that the new phosphorescent dopant **4.6** is very promising for high efficiency and high brightness deep blue OLEDs.

To investigate if the device efficiency can be improved further by using a more sophisticated and advanced device fabrication facility, we prepared a second set of devices at Professor Lu's laboratory in University of Toronto. The new devices employed the same structure as that shown in scheme 4.4 with the doping level of **4.6** at 10% (C2), 15% (D1) and 20% (E1), respectively. Again, we were not able to record EL test data under inert atmosphere or encapsulate the devices. The three new devices display similar EL spectra as those of devices A1, B1 and C1 with the CIE coordinates being shifted somewhat but still in the deep blue region. The device E1 that has a 20% doped compound **4.6** in the emitting layer has an excellent color/emission stability over the entire driving range as shown by the EL spectra in Figure 4.9. The performance of device C2 that has the

same doping level and the same structure as C1 is quite different from C1. C2 is less bright than C1. For example, at 10 V, the brightness of C1 is 3395 cd m^2 while that of C2 is 2339 cd m^{-2}. The maximum brightness of C2 is also much lower than C1 (Table 4.7). However, device C2 is much more efficient than C1 as evidenced by its max. EQE of 15.4% achieved at the brightness of 490 cd m^{-2}. The device D1 and E1 are also more efficient than C1 with max EQE of 14.1% and 13.6% being achieved at a brightness of 218 cd m^{-2} and 210 cd m^{-2}, respectively. The EQE roll off of devices C2, D1 and E1 is much steeper than that of A1, B1 and C1. The contrasting EL performance of C1 and C2 illustrates that the EL testing data can be highly dependent on the fabrication and testing facility. Subtle difference in the device fabrication process seems also making a big difference in device performance. Furthermore, because all device data were recorded under ambient conditions without encapsulation, the environmental factors such as humidity level and temperature likely also have a significant impact on the device performance data. Despite the limitation of our testing facilities, the preliminary EL data clearly support that compound **4.6** is a highly promising deep blue dopant for OLEDs.

4.3 Experimental

4.3.1 General Procedures

All Reactions were carried out under a nitrogen atmosphere unless otherwise noted. Reagents were purchased from Aldrich chemical company and used as received. TLC and flash chromatography were performed on silica gel. ^{1}H spectra were recorded on Bruker Avance 300, 400 and 500 MHz spectrometers. Deuterated solvents were purchased from Cambridge Isotopes and used without drying. Excitation and emission spectra were obtained on a Photon Technologies International QuantaMaster Model 2 spectrometer. Solid state quantum efficiency measurements were performed using the same spectrometer with an integration sphere. Phosphorescent decay life

times were measured with an Edinburgh Instrument FLS980 spectrophotometer. Solution phosphorescence quantum yields were measured relative to 9,10-diphenylanthracene in degassed dichloromethane at 298 K. UV-Visible spectra were recorded using a Varian Carry 50 UV/Vis spectrophotometer. High-resolution mass spectra (HRMS) were obtained from an Applied Biosystems Qstar XL spectrometer. TD-DFT calculations were carried out using the Gaussian 09 software at the High Performance Computing Virtual Laboratory (HPCVL) at Queen's University. All computations were performed at the B3LYP level of theory using LANL2DZ as the basis set for Pt and 6-31G(d) for all other atoms.

4.3.2 Synthesis of Ligands

3,3'-oxydianiline[19], bis(3-iodophenyl)methane[20], bis(3-iodophenyl)methanone[21], 4-(3-bromophenyl)-1- methyl-1H-1,2,3-triazole[8d] and 3-(1-hexyl-1H-1,2,3-triazol-4-yl)phenol[22] were prepared according to literature procedures.

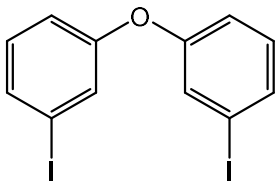

3,3'-oxybis(iodobenzene): In a 250 mL round-bottomed flask, 3,3'-oxydianiline (4g, 20.0 mmol) was dissolved in 100 mL of acetone. To the flask 21 mL of concentrated HCl in 30 mL of water was added dropwise. The solution was cooled to 0 °C and sodium nitrite (8.4 g, 121.8 mmol) in 50 mL of water was added slowly. The solution was stirred at 0 °C for another hour before potassium iodide (25 g, 150.6 mmol) in 50 mL water was added dropwise. The solution was stirred at 0 °C for 2h, then at 60 °C for 4h. Upon cooling, sodium bisulfite was added until all iodine in the solution was consumed. The mixture was then concentrated under reduced pressure. The product was dissolved

in dichloromethane and washed sequentially with water and brine. The organic layer was dried over $MgSO_4$, filtered and the solvent was removed under reduced pressure. The solid was then purified using flash chromatography through silica using hexane as eluent to give 6.09 g 3,3'-oxybis(iodobenzene) as white powder (72% yield). ^{1}H NMR (300 MHz, CHLOROFORM-d, δ, ppm): 7.55 - 7.42 (m, 2H), 7.41 - 7.30 (m, 2H), 7.15 - 7.03 (m, 2H), 7.03 - 6.90 (m, 2H).

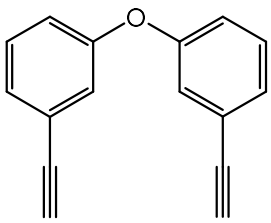

3,3'-oxybis(ethynylbenzene): A 250 mL Schlenk flask was charged with 3,3'-oxybis(iodobenzene) (5.6 g, 13.3 mmol), trimethylsilylacetylene (5.2 mL, 36.8 mmol), $PdCl_2(PPh_3)_2$ (0.94g, 1.34 mmol), triphenylphosphine (0.7 g, 2.67 mmol) copper iodide (0.38g, 2.00 mmol) and 80 mL of degassed THF/triethylamine (v:v= 3:1). The mixture was stirred at room temperature overnight, and then concentrated under reduced pressure. The product was dissolved in dichloromethane and washed sequentially with saturated ammonium chloride solution, water and brine. The organic layer was dried over $MgSO_4$, filtered and the solvent was removed under reduced pressure. The solid was then purified using flash chromatography through silica using 10% dichloromethane in hexane as eluent. The resulting white solid was dissolved in 40 mL of tetrahydrofuran and treated with tetrabutylammonium fluoride in THF (40 mL of a 1.0 M solution). After stirring overnight, the resulting mixture was concentrated under reduced pressure. After extraction with dichloromethane, the organic layer was dried over $MgSO_4$, filtered and the solvent was removed under reduced pressure. The solid was then purified using flash chromatography through silica using 10% dichloromethane in hexane as eluent to afford 2.74 g 3,3'-oxybis(ethynylbenzene) as white solid (94% yield). ^{1}H NMR (300 MHz, CHLOROFORM-d, δ, ppm): 7.39 - 7.23 (m, 4H), 7.13 (s, 2H), 7.03 (td, J = 2.0, 7.6 Hz, 2H), 3.10 (s, 2H).

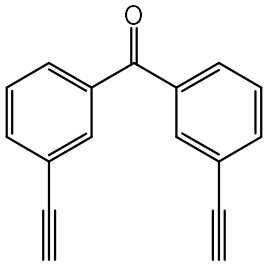

bis(3-ethynylphenyl)methanone: Prepared using the same procedure as 3,3'-oxybis(ethynylbenzene) except replacing 3,3'-oxybis(iodobenzene) with bis(3-iodophenyl)methanone (70% yield). ^{1}H NMR (300 MHz, CHLOROFORM-d, δ, ppm): 7.91 (s, 2H), 7.76 (dd, J = 7.7, 14.8 Hz, 4H), 7.56 - 7.42 (m, 2H), 3.15 (s, 2H).

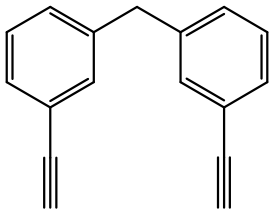

bis(3-ethynylphenyl)methane: Prepared using the same procedure as 3,3'-oxybis(ethynylbenzene) except replacing 3,3'-oxybis(iodobenzene) with bis(3-iodophenyl)methane (88% yield). ^{1}H NMR (300 MHz, CHLOROFORM-d, δ, ppm): 7.41 - 7.31 (m, 16H), 7.31 - 7.23 (m, 15H), 7.22 - 7.13 (m, 9H), 3.95 (s, 9H), 3.07 (s, 8H).

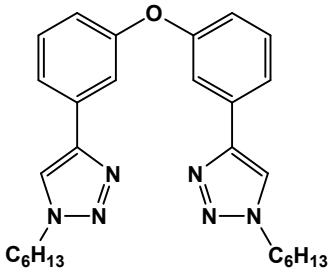

4,4'-(oxybis(3,1-phenylene))bis(1-hexyl-1H-1,2,3-triazole) (L4.2): To a 50 mL Schlenk flask equipped with a magnetic stir bar was added 3,3'-oxybis(ethynylbenzene) (0.4 g, 1.83 mmol), 1-azidohexane (0.7 g, 5.78 mmol), diisopropylethylamine (0.95 g, 7.32 mmol), tris[(1-benzyl-1*H*-1,2,3-triazol-4-yl) methyl]amine (1 mol %) and 40 mL dichloromethane. The resulting solution was bubbled with nitrogen gas for 20 minutes. $[Cu(CH_3CN)_4]PF_6$ (1 mol %) was added as a catalyst. The resulting mixture was stirred overnight, after which the solvent was removed under reduced pressure. The crude product was dissolved in dichloromethane and washed with saturated ammonium chloride solution, water and brine. The organic layer was dried over $MgSO_4$, filtered and the solvent was removed under reduced pressure. The product was then purified using

flash chromatography through silica (8:1 dichloromethane:ethyl acetate as eluent) to afford 0.48 g 4,4'-(oxybis(3,1-phenylene))bis (1-hexyl-1H-1,2,3-triazole) as white solid (57 % yield). ^{1}H NMR (300 MHz, CHLOROFORM-d, δ, ppm): 7.73 (s, 2H), 7.64 (d, *J* = 7.7 Hz, 2H), 7.52 (t, *J* = 1.9 Hz, 2H), 7.42 (t, *J* = 7.9 Hz, 2H), 7.03 (dd, *J* = 1.5, 8.1 Hz, 2H), 4.40 (t, *J* = 7.3 Hz, 4H), 1.94 (d, *J* = 7.2 Hz, 4H), 1.34 (br. s., 12H), 0.98 - 0.81 (m, 6H).

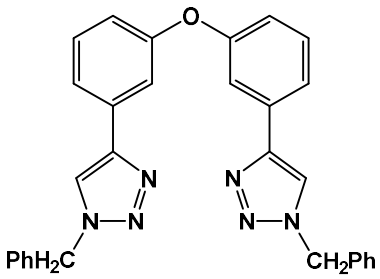

4,4'-(oxybis(3,1-phenylene))bis(1-benzyl-1H-1,2,3-triazole) (L4.1): Prepared using the same procedure as **L4.2** except replacing 1-azidohexane with benzyl azide (62% yield). ^{1}H NMR (300 MHz, CHLOROFORM-d, δ, ppm): 7.73 - 7.52 (m, 4H), 7.51 - 7.32 (m, 12H), 6.99 (d, *J* = 6.6 Hz, 2H), 5.58 (s, 4H).

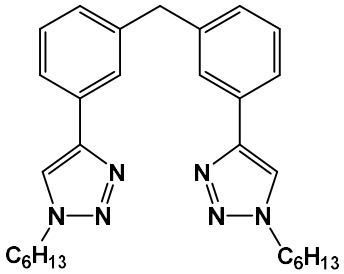

bis(3-(1-hexyl-1H-1,2,3-triazol-4-yl)phenyl)methane (L4.3): Prepared using the same procedure as **L4.2** except replacing (3,3'-oxybis(ethynylbenzene) with bis(3-ethynylphenyl)methane (53% yield). ^{1}H NMR (300 MHz, CHLOROFORM-d, δ, ppm): 7.80 (s, 2H), 7.76 (br. s., 2H), 7.69 (d, *J* = 7.0 Hz, 2H), 7.39 (t, *J* = 7.6 Hz, 2H), 7.24 (d, *J* = 7.7 Hz, 2H), 4.39 (t, *J* = 7.3 Hz, 4H), 4.12 (s, 2H), 1.95 (br. s., 4H), 1.36 (br. s., 12H), 0.92 (br. s., 5H).

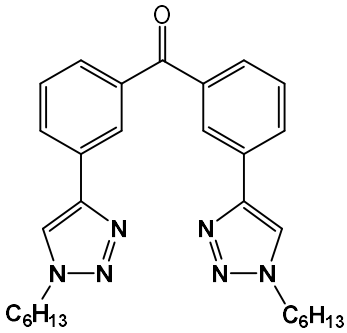

bis(3-(1-hexyl-1H-1,2,3-triazol-4-yl)phenyl)methanone (L4.4): Prepared using the same procedure as **L4.2** except replacing (3,3'-oxybis(ethynylbenzene) with bis(3-ethynylphenyl)methanone (74% yield). ^{1}H NMR (300 MHz, CHLOROFORM-d, δ, ppm): 8.28 - 8.14 (m, 4H), 7.85 (s, 2H), 7.79 (d, *J* = 7.6 Hz, 2H), 7.66 - 7.50 (m, 2H), 4.43 (t, *J* = 7.2 Hz, 4H), 1.96 (d, *J* = 6.9 Hz, 4H), 1.36 (br. s., 12H), 1.01 - 0.79 (m, 6H).

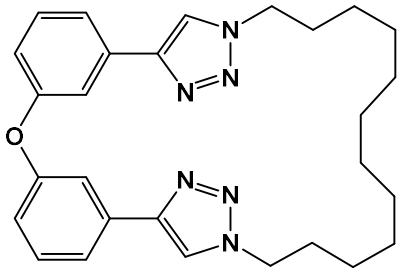

(1^4Z,5^4Z)-1^1H,5^1H-3-oxa-1,5(4,1)-ditriazola-2,4(1,3)-dibenzenacycloheptadecaphane (L4.6): To a 500 mL Schlenk flask equipped with a magnetic stir bar was added 3,3'-oxybis(ethynylbenzene) (0.4g, 1.83 mmol), 1,12-diazidododecane (0.49 g, 1.92 mmol), diisopropylethylamine (0.95 g, 7.32 mmol), tris[(1-benzyl-1*H*-1,2,3-triazol-4-yl)methyl]amine (1 mol %) and 240 mL of dichloromethane. The resulting solution was bubbled with nitrogen gas for 30 minutes. $[Cu(CH_3CN)_4]PF_6$ (1 mol %) was added as a catalyst. The resulting mixture was stirred at room temperature for 6 days, after which the solvent was removed under reduced pressure. The crude product was dissolved in dichloromethane and washed with saturated ammonium chloride solution, water and brine. The organic layer was dried over $MgSO_4$, filtered and the solvent was removed under reduced pressure. The product was then purified using flash chromatography through silica (5:1 dichloromethane:ethyl acetate as eluent) to afford 0.2 g (1^4Z,5^4Z)-1^1H,5^1H-3-oxa- 1,5(4,1)-ditriazola-2,4(1,3)-dibenzenacycloheptadecaphane as white solid (24% yield). ^{1}H NMR (300 MHz, CHLOROFORM-d, δ, ppm): 7.74 - 7.60 (m, 4H), 7.48 (t, *J* = 7.8 Hz, 2H), 7.33 (s, 2H), 7.19 (d, *J* = 8.1 Hz, 2H), 4.39 (t, *J* = 6.5 Hz, 4H), 1.88 (br. s., 4H), 1.35 - 1.05 (m, 16H).

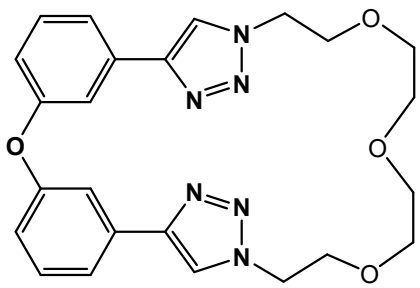

(1^4Z,5^4Z)-1^1H,5^1H-3,8,11,14-tetraoxa-1,5(4,1)-ditriazola-2,4(1,3)-dibenzenacyclohexadecaphane (L4.7): Prepared using the same procedure as **L4.6** except replacing 1,12-diazidododecane with Tetraethylene glycol bisazide (17% yield). ^{1}H NMR (300 MHz, CHLOROFORM-d, δ, ppm): 7.84 - 7.72 (m, 4H), 7.50 (t, *J* = 7.9 Hz, 2H), 7.25 - 7.11 (m, 4H), 4.55 (t, *J* = 5.3 Hz, 4H), 385 (t, *J* = 5.3 Hz, 4H), 3.48 (t, *J* = 5.3 Hz, 4H), 3.41 (t, *J* = 5.3 Hz, 4H).

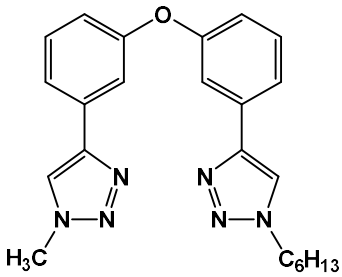

1-hexyl-4-(3-(3-(1-methyl-1H-1,2,3-triazol-4-yl)phenoxy)phenyl) -1H-1,2,3-triazole (L4.5): A 100 mL three-necked round bottomed flask, equipped with a magnetic stir bar and a condenser, was charged with 4-(3-bromophenyl)-1-methyl-1H-1,2,3-triazole (0.4 g, 1.68 mmol), 3-(1-hexyl-1H-1,2,3-triazol-4-yl) phenol (0.45 g, 1.84 mmol), K_3PO_4 (0.71 g, 3.36 mmol), copper iodide (0.032 g, 0.17 mmol), 2-picolinic acid (0.041 g, 0.34 mmol) and 50 mL of degassed DMSO. The mixture was stirred at 90°C for 4 days before 75 mL of water was added. The mixture extracted with ethyl acetate and then washed sequentially with saturated ammonium chloride solution, water and brine. The organic layer was dried over $MgSO_4$, filtered and the solvent was removed under reduced pressure. The solid was then purified using flash chromatography through silica(8:1 dichloromethane:ethyl acetate as eluent) to afford 0.52 g 1-hexyl-4-(3-(3-(1-methyl-1H-1,2,3- triazol-4-yl)phenoxy)phenyl)-1H-1,2,3-triazole as white solid (77% yield). ^{1}H NMR (300 MHz, CHLOROFORM-d, δ, ppm): 7.74 – 7.72 (m, 2 H), 7.67 - 7.57 (m, 2H), 7.55 - 7.47 (m, 2H), 7.40 (t, *J* = 7.9 Hz, 2H), 7.02 (dd, *J* = 1.7, 8.1 Hz, 2H), 4.38 (t, *J* = 7.2 Hz, 2H), 4.13 (s, *3*H), 1.93 (d, *J* = 7.0 Hz, 2H), 1.45 - 1.20 (m, 6H), 0.98 - 0.79 (m, 3H).

4.3.3 Synthesis of Pt(II) complexes

The general synthetic procedure and the characterization data for the Pt(II) compounds **4.1-4.7** are given below. The Pt(II) compounds have the tendency to co-crystallize with solvent molecules such as THF and CH_2Cl_2. For some of the compounds, the solvent molecules were positively identified in the crystal lattice of the Pt(II) compounds.

General procedure for the synthesis of Pt(II) compounds: The ligand (0.12 mmol), tetrabutylammonium bromide (0.006 g) and K_2PtCl_4 (0.126 mmol) were added to a sealed tube with 10 mL dry degassed acetic acid. The mixture was stirred at room temperature for 1 day, and then heated at 140 ^oC for 4 days. 10 mL of water was added to the resulting solution and the precipitate was collected via vacuum filtration. The solid was then dissolved in dichloromethane and washed with water and brine. The combined organic phase was dried over $MgSO_4$, filtered and purified on using flash chromatography through silica (dichloromethane as eluent). The Pt(II) compounds were characterized by ^1H NMR (see fully assigned ^1H NMR spectra in the supporting information) and HRMS analyses. ^{13}C NMR spectra were not obtained due to the poor solubility of the Pt(II) compounds.

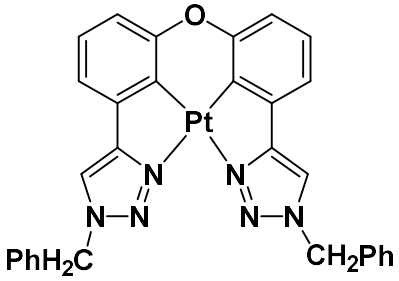

4.1: Yield 15%. ^{1}H NMR (400 MHz, CD_2Cl_2, δ, ppm): 7.68 (s, 2 H), 7.50 - 7.35 (m, 8 H), 7.24 - 7.05 (m, 8 H), 5.68 (s, 4 H). HRMS (ESI) calculated for $C_{30}H_{23}N_6OPt$ $[M+H]^+$: calcd, 678.1576; found, 678.1575.

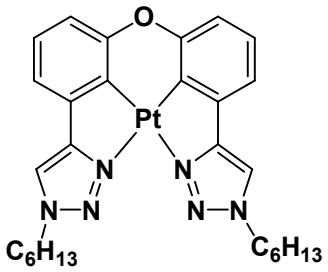

4.2: Yield 23%. ^{1}H NMR (400 MHz, CD_2Cl_2, δ, ppm): 7.76 (s, 2 H), 7.29- 7.24 (m, 2 H), 7.24 - 7.18 (m, 2 H), 7.10 (d, *J*=8.1 Hz, 2 H), 4.47 (t, *J*=7.3 Hz, 4 H), 2.10 – 1.98 (m, 4 H), 1.49 - 1.29 (m, 12 H), 0.91 ppm (t, *J*=6.9 Hz, 6 H). HRMS (ESI) calculated for $C_{28}H_{35}N_6OPt$ $[M+H]^+$: calcd, 666.2515; found, 666.2533.

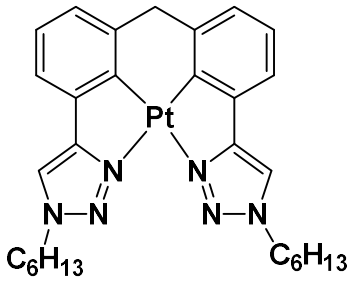

4.3: Yield 14%. ^{1}H NMR (400 MHz, CD_2Cl_2, δ, ppm): 7.76 (d, *J* = 1.5 Hz, 2 H), 7.37 (d, *J* = 7.3 Hz, 2 H), 7.29 - 7.09 (m, 4 H), 4.91 (s, 2 H), 4.50 (t, *J* = 7.4 Hz, 4 H), 2.07 (quin, *J* = 7.1 Hz, 4 H), 1.53 - 1.30 (m, 12 H), 0.95 (t, *J* = 6.2 Hz, 6 H). HRMS (ESI) calculated for $C_{29}H_{37}N_6Pt$ $[M+H]^+$: calcd, 664.2722; found, 664.2681.

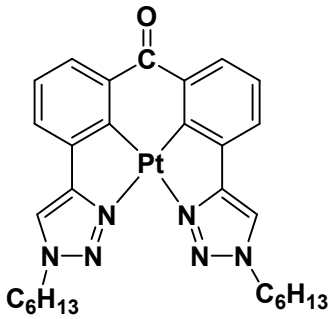

4.4: Yield 14%. ^{1}H NMR (400 MHz, CD_2Cl_2, δ, ppm): 8.21 (dd, *J* = 1.3, 8.1 Hz, 2 H), 7.80 (s, 2 H), 7.61 (dd, *J* = 1.4, 7.2 Hz, 2 H), 7.27 (t, *J* = 7.7 Hz, 2 H), 4.50 (t, *J* = 7.4 Hz, 4 H), 2.05 (t, *J* = 7.6 Hz, 4 H), 1.50 - 1.24 (m, 12 H), 0.98 - 0.83 (m, 6 H). HRMS (ESI) calculated for $C_{29}H_{35}N_6OPt$ $[M+H]^+$: calcd., 678.2515; found, 678.2513.

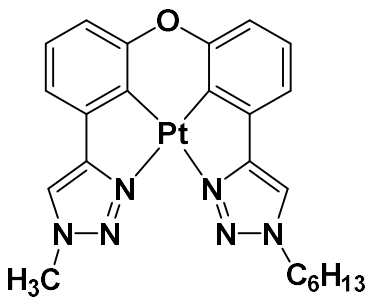

4.5: Yield 22%. ^{1}H NMR (500 MHz, CD_2Cl_2, δ, ppm): 7.77 (s, 1 H), 7.76 (s, 1H), 7.30- 7.05 (m, 6 H), 4.48 (t, *J*=7.3 Hz, 2 H), 4.22 (s, 3 H), 2.09 – 1.98 (m, 2 H), 1.46 - 1.30 (m, 6 H), 0.92 ppm (m, 3 H). HRMS (ESI) calculated for $C_{23}H_{25}N_6OPt$ $[M+H]^+$: calcd, 596.1732; found, 596.1730.

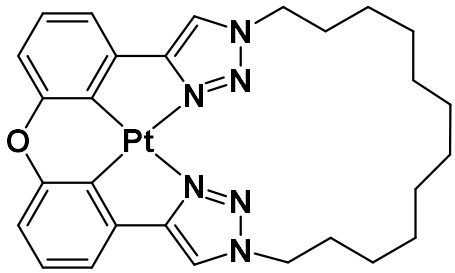

4.6: Yield 52%. ^{1}H NMR (400 MHz, CD_2Cl_2, δ, ppm): 7.74 (s, 2 H), 7.30 - 7.23 (m, 2 H), 7.23 - 7.17 (m, 2 H), 7.15 (s, 2 H), 4.51 (t, *J*=6.4 Hz, 4 H), 2.12 – 1.98 (m, 4 H), 1.50 - 1.23 ppm (m, 16 H). HRMS (ESI) calculated for $C_{28}H_{33}N_6OPt$ $[M+H]^+$: calcd., 664.2358; found, 664.2333.

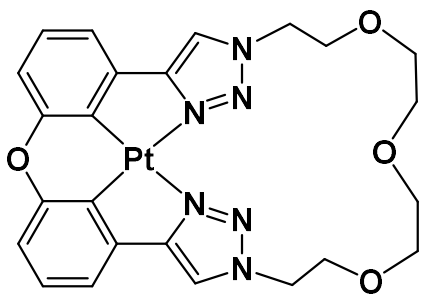

4.7: Yield 11%. ^{1}H NMR (400 MHz, CD_2Cl_2, δ, ppm): 7.73 (s, 2 H), 7.30 - 7.24 (m, 2 H), 7.24 - 7.18 (m, 2 H), 7.18 - 7.03 (m, 2 H), 4.70 - 4.60 (m, 4 H), 3.98 - 3.91 (m, 4 H), 3.64 ppm (s, 8 H). HRMS (ESI) calculated for $C_{24}H_{25}N_6O_4Pt$ $[M+H]^+$: calcd, 656.1580; found, 656.1592.

4.3.4 X-Ray Diffraction Analysis

Single crystals of **4.1**, **4.2**, **4.3**, and **4.5-4.7** were obtained from either CH_2Cl_2 or THF solution with hexanes by slow evaporation of the solvents. The crystals were mounted on glass fibers and the data were collected on a Bruker Apex II single-crystal X-ray diffractometer with graphite-monochromated Mo K_α radiation, operating at 50 kV and 30 mA, and at 180 K. Data were processed on a PC with the aid of the Bruker SHELXTL software package (version 6.14)[20] and

corrected for absorption effects. All structures were solved using direct methods. The crystals of **4.1**, **4.5** and **4.6** belong to the monoclinic space group $P2_1/c$; those of **4.2** and **4.3** belong to the orthorhombic space group Pbca while that of **4.7** belongs to the monoclinic space group Cc. All non-hydrogen atoms were refined anisotropically. Complete crystal structural data have been deposited at the Cambridge Crystallographic Data Centre [CCDC No. 1455641 (**4.1**), 1455643 (**4.2**), 1455642 (**4.3**), 1479415 (**4.5**), 1455644 (**4.6**), 1455645 (**4.7**)]. These data can be obtained free of charge from The Cambridge Crystallographic Data Centre via www.ccdc.cam.ac.uk/data_request/cif.].

4.3.5 EL Device Fabrication

Fabrication and evaluation of EL devices A1, B1 and C1: The ITO (indium-tin oxide) glass (20Ω/square) were routinely cleaned by sonicating in detergent solutions, rinsing with acetone, isopropanol, and then de-ionized water. The substrates were dried in vacuum oven between each cleaning step above. To increase the value of work function, the surfaces of ITO substrates were treated with atmospheric air plasma using a Plasma Cleaner (PDC-32G-2, 100 W). All organics were thermally evaporated at a rate of 1.0 Å S^{-1} at a base pressure of around 3.5 x 10^{-4} Pa using a deposition system manufactured by Shenyang Sida Vacuum Technology Research Institute of China. A LiF layer (0.5 nm) was deposited at a rate of 0.2 Å S^{-1}. The Al electrode (cathode) was deposited at a rate of 10 Å S^{-1}. The active area of the diode segments was 2 × 2 mm^2. The EL spectra, brightness, CIE coordinates and the current–brightness–voltage characteristics of the devices were measured with a rapid scan system using a spectrophotometer (PR-650, Photo Research) with a computer-controlled programmable direct-current power supply Keithley model 2400 voltage-current source under ambient condition.

Fabrication and evaluation of EL devices C2, D1 and E1: Devices were fabricated in a three-chamber evaporator (EL-OEL cluster tool) with a base pressure of ~3 x 10^{-7} Torr without breaking vacuum. The ITO anode is commercially patterned and coated on glass substrates 50 x 50 mm^2 with a sheet resistance less than 15 Ω. Substrates were ultrasonically cleaned with a standard regiment of Alconox®, acetone, and methanol followed by UV ozone treatment for 15 min. The active area for all devices was 2 mm^2 and the film thicknesses were 1.1 mm. I-V characteristics were measured using a HP4140B picoammeter in ambient air. Luminance measurements and EL spectra were taken using a Minolta LS-110 luminance meter and an Ocean Optics USB200 spectrometer with bare fiber, respectively. The CIE coordinates were determined from the corresponding EL spectra using MATLAB software. The external quantum efficiency of EL devices was calculated following the standard procedure.[23]

4.4 Conclusion

The synthesis of a new class of Pt(II) complexes based on tetradentate chelate ligands has been accomplished. Most members of this class of molecules have been found to display deep blue phosphorescence with very high quantum efficiencies. Comparative study established that the tetradentate Pt(II) compounds have a much greater stability toward UV irradiation and structural distortion in the excited state than the bidentate bis-chelate Pt(II) compound. Macrocyclic tetradentate ligands that provide a full steric constraint on the structure of the molecule have been found to enhance the thermal, UV stability and phosphorescent quantum efficiencies, demonstrating that this is an effective approach in designing new and stable blue phosphorescent emitters for OLEDs. Efficient and bright deep blue EL devices have been fabricated successfully

for the first time using emitters developed in our lab, which support that the new Pt(II) compounds are a very promising class of deep blue emitters for OLEDs.

4.5 **Notes and References**

The work described in this chapter includes contributions from the following publications:

- X. Wang, T. Peng, C. Nguyen, Z. H. Lu, N. Wang, W. J. Wu, Q. S. Li and S. Wang, *Adv. Funct. Mater.*, accepted. DOI: 10.1002/adfm.201604318

References

(1) (a) M. A. Baldo, D. F. O'Brien, Y. You, A. Shoustikov, S. Sibley, M. E. Thompson and S. R. Forrest, *Nature* **1998**, *395*, 151; (b) W. C. Choy, W. K. Chan and Y. Yuan, *Adv. Mater.* **2014**, *26*, 5368; (c) L. Xiao, Z. Chen, B. Qu, J. Luo, S. Kong, Q. Gong and J. Kido, *Adv. Mater.* **2011**, *23*, 926; (d) M. Hack, W.-Y. So, P. A. Levermore, M. S. Weaver and J. J. Brown, *Sid. Symp. Dig. Tec.* **2011**, *42*, 606; (e) P. A. Levermore, A. B. Dyatkin, Z. M. Elshenawy, H. Pang, R. C. Kwong, R. Ma, M. S. Weaver and J. J. Brown, *Sid. Symp. Dig. Tec.* **2011**, *42*, 1060.

(2) H. Fu, Y.-M. Cheng, P.-T. Chou, Y. Chi, *Mater. Today* **2011**, *14*, 472.

(3) (a) N. C. Giebink, B. W. D'Andrade, M. S. Weaver, P. B. Mackenzie, J. J. Brown, M. E. Thompson and S. R. Forrest, *J. Appl. Phys.* **2008**, *103*, 044509; (b) Y. Chi, P. T. Chou, *Chem. Soc. Rev*. **2010**, *39*, 638, and references therein; (c) Y. You. S. Y. Park, *Dalton Trans.* 2009, 1267; (d) C.-L. Ho, W.-Y. Wong, *New. J. Chem*. **2013**, *37*, 1665; (e) G. J. Zhou, C. L. Ho, W. Y. Wong, Q. Wang, D. G. Ma, L. X. Wang, Z. Y. Lin, T. B. Marder, A. Beeby, *Adv. Funct. Mater.* **2008**, *18*, 499; (f) M. Cocchi, D. Virgili, V. Fattori, D. L. Rochester, J. A. G. Williams, *Adv. Funct. Mater.* **2007**, *17*, 285.

(4) (a) S. Yoshiyuki, O. Tomohiro, I. Hiroto, H. Kunihisa, K. Hiroshi, *Sci. Technol. Adv. Mater.* **2014**, *15*, 054202; (b) K. Dedeian, J. Shi, N. Shepherd, E. Forsythe and D. C. Morton, *Inorg. Chem.* **2005**, *44*, 4445; (c) J. Li, P. I. Djurovich, B. D. Alleyne, M. Yousufuddin, N. N. Ho, J. C. Thomas, J. C. Peters, R. Bau, M. E. Thompson, *Inorg. Chem.* **2005**, *44*, 1713; (d) S.-C. Lo, C. P. Shipley, R. N. Bera, R. E. Harding, A. R. Cowley, P. L. Burn, I. D. W. Samuel, *Chem. Mater.* **2006**, *18*, 5119; (e) E. Orselli, G. S. Kottas, A. E. Konradsson, P. Coppo, R. Fröhlich, L. De Cola, A. van Dijken, M. Büchel, H. Börner, *Inorg. Chem.* **2007**, *46*, 11082; (f) C.-F. Chang, Y.-M. Cheng, Y. Chi, Y.-C. Chiu, C.-C. Lin, G.-H. Lee, P.-T. Chou, C.-C. Chen, C.-H. Chang, C.-C. Wu, *Angew. Chem. Int. Ed.* **2008**, *47*, 4542; (g) Y.-C. Chiu, Y. Chi, J.-Y. Hung, Y.-M. Cheng, Y.-C. Yu, M.-W. Chung, G.-H. Lee, P.-T. Chou, C.-C. Chen, C.-C. Wu, H.-Y. Hsieh, *ACS. Appl. Mater. Interfaces* **2009**, *1*, 433; (h) Y. Kang, Y.-L. Chang, J.-S. Lu, S.-B. Ko, Y. Rao, M. Varlan, Z.-H. Lu, S. Wang, *J. Mater. Chem. C* **2013**, *1*, 441; (i) S. Lee, S.-O. Kim, H. Shin, H.-J. Yun, K. Yang, S.-K. Kwon, J.-J. Kim , Y.-H. Kim, *J. Am. Chem. Soc.* **2013**, *135*, 14321.

(5) (a) I. R. de Moraes, S. Scholz, B. Lüssem, K. Leo, *Appl. Phys. Lett.* **2011**, *99*, 053302; (b) I. R. d. Moraes, S. Scholz, B. Lüssem, K. Leo, *Org. Electron.* **2011**, *12*, 341; (c) V. Sivasubramaniam, F. Brodkorb, S. Hanning, H. P. Loebl, V. van Elsbergen, H. Boerner, U. Scherf, M. Kreyenschmidt, *J. Fluorine Chem.* **2009**, *130*, 640; (d) K. P. Klubek, C. W. Tang, L. J. Rothberg, *Org. Electron.* **2014**, *15*, 1312.

(6) (a) K.-Y. Lu, H.-H. Chou, C.-H. Hsieh, Y.-H. O. Yang, H.-R. Tsai, H.-Y. Tsai, L.-C. Hsu, C.-Y. Chen, I. C. Chen, C.-H. Cheng, *Adv. Mater.* **2011**, *23*, 4933; (b) H. Sasabe, J.-i. Takamatsu, T. Motoyama, S. Watanabe, G. Wagenblast, N. Langer, O. Molt, E. Fuchs, C. Lennartz, J. Kido, *Adv. Mater.* **2010**, *22*, 5003.

(7) J. Lee, H.-F. Chen, T. Batagoda, C. Coburn, P. I. Djurovich, M. E. Thompson, S. R. Forrest, *Nat. Mater.* **2016**, *15*, 92.

(8) (a) L. Murphy, P. Brulatti, V. Fattori, M. Cocchi and J. A. G. Williams, *Chem. Commun.* **2012**, *48*, 5817; (b) X. Yang, Z. Wang, S. Madakuni, J. Li, G. E. Jabbour, *Adv. Mater.* **2008**, *20*, 2405; (c) L.-M. Huang, G.-M. Tu, Y. Chi, W.-Y. Hung, Y.-C. Song, M.-R. Tseng, P.-T. Chou, G.-H. Lee, K.-T. Wong, S.-H. Cheng, W.-S. Tsai *J. Mater. Chem. C* **2013**, *1*, 7582; (d) X. Wang, Y.-L. Chang, J.-S. Lu, T. Zhang, Z.-H. Lu, S. Wang, *Adv. Funct. Mater.* **2014**, *24*, 1911; (e) X. Wang, S.-L. Gong, D. Song, Z.-H. Lu, S. Wang, *Adv. Funct. Mater.* **2014**, *24*, 7257.

(9) (a) W. H. Lam, E. S.-H. Lam, V. W.-W. Yam, *J. Am. Chem. Soc.* **2013**, *135*, 15135; (b) A. F. Rausch, L. Murphy, J. A. G. Williams, H. Yersin, *Inorg. Chem.* **2012**, *51*, 312; (c) A. Tronnier, G. Wagenblast, I. Münster, T. Strassner, *Chem.-Eur. J.* **2015**, *21*, 12881; (d) Z. M. Hudson, C. Sun, M. G. Helander, Y.-L. Chang, Z.-H. Lu, S. Wang, *J. Am. Chem. Soc.* **2012**, *134*, 13930; (e) Y. L. Chang, S. Gong, X. Wang, R. White, C. Yang, S. Wang, Z. H. Lu, *Appl. Phys. Lett.* **2014**, *104*, 173303; (f) Y. Unger, D. Meyer, O. Molt, C. Schildknecht, I. Münster, G. Wagenblast, T. Strassner, *Angew. Chem. Int. Ed.* **2010**, *49*, 10214.

(10) (a) T. Fleetham, Z. Wang, J. Li, *Org. Electron.* **2012**, ***13***, 1430; (b) X.-C. Hang, T. Fleetham, E. Turner, J. Brooks, J. Li, *Angew. Chem. Int. Ed.*, **2013**, *52*, 6753; (c) T. Fleetham, G. Li, L. Wen, J. Li, *Adv. Mater.* **2014**, *26*, 7116.

(11) (a) D. A. K. Vezzu, J. C. Deaton, J. S. Jones, L. Bartolotti, C. F. Harris, A. P. Marchetti, M. Kondakova, R. D. Pike, S. Huo, *Inorg. Chem.* **2010**, *49*, 5107; (b) K. Li, X. Guan, C.-W. Ma, W. Lu, Y. Chen, C.-M. Che, *Chem. Commun*. **2011**, *47*, 9075; (c) K. Li, G. Cheng, C. Ma, X.

Guan, W.-M. Kwok, Y. Chen, W. Lu, C.-M. Che, *Chem. Sci.* **2013**, *4*, 2630. (d) T. Fleetham, L. Huang, J. Li, *Adv. Funct. Mater.* **2014**, *24*, 6066. (e) K.-Y. Liao, C.-W. Hsu, Y. Chi, M.-K. Hsu, S.-W. Wu, C.-H. Chang, S.-H. Liu, G.-H. Lee, P.-T. Chou, Y. Hu and N. Robertson, *Inorg. Chem.*, **2015**, 54, 4029.

(12) D. Maiti and S. L. Buchwald, *J. Am. Chem. Soc.* **2009**, *131*, 17423.

(13) (a) M. J. Jurow, A. Bossi, P. I. Djurovich, M. E. Thompson, *Chem. Mater.* **2014**, *26*, 6578; (b) S. Schmidbauer, A. Hohenleutner, B. König, *Beilstein J. Org. Chem.* **2013**, *9*, 2088; (c) X. Zhang, A. M. Wright, N. J. DeYonker, T. K. Hollis, N. I. Hammer, C. E. Webster, E. J. Valente, *Organometallics* **2012**, *31*, 1664; (d) R. Seifert, I. Rabelo de Moraes, S. Scholz, M. C. Gather, B. Lüssem, K. Leo, *Org. Electron.* **2013**, *14*, 115.

(14) M. J. Frisch, G. W. Trucks, H. B. Schlegel, G. E. Scuseria, M. A. Robb, J. R. Cheeseman, G. Scalmani, V. Barone, B. Mennucci, G. A. Petersson, H. Nakatsuji, M. Caricato, X. Li, H. P. Hratchian, A. F. Izmaylov, J. Bloino, G. Zheng, J. L. Sonnenberg, M. Hada, M. Ehara, K. Toyota, R. Fukuda, J. Hasegawa, M. Ishida, T. Nakajima, Y. Honda, O. Kitao, H. Nakai, T. Vreven, J. A. Montgomery Jr., J. E. Peralta, F. Ogliaro, M. J. Bearpark, J. Heyd, E. N. Brothers, K. N. Kudin, V. N. Staroverov, R. Kobayashi, J. Normand, K. Raghavachari, A. P. Rendell, J. C. Burant, S. S. Iyengar, J. Tomasi, M. Cossi, N. Rega, N. J. Millam, M. Klene, J. E. Knox, J. B. Cross, V. Bakken, C. Adamo, J. Jaramillo, R. Gomperts, R. E. Stratmann, O. Yazyev, A. J. Austin, R. Cammi, C. Pomelli, J. W. Ochterski, R. L. Martin, K. Morokuma, V. G. Zakrzewski, G. A. Voth, P. Salvador, J. J. Dannenberg, S. Dapprich, A. D. Daniels, Ö. Farkas, J. B. Foresman, J. V. Ortiz, J. Cioslowski and D. J. Fox in Gaussian 09, Vol. Gaussian, Inc., Wallingford, CT, USA, 2009.

(15) V. N. Maiorov, G. M. Crippen, *J. Mol. Biol.* **1994**, *235*, 625.

(16) S. Scholz, D. Kondakov, B. Lüssem, K. Leo, *Chem. Rev.* **2015**, *115*, 8449 and references therein.

(17) C. Han, Y. Zhao, H. Xu, J. Chen, Z. Deng, D. Ma, Q. Li, P. Yan, *Chem.-Eur. J.* **2011**, *17*, 5800.

(18) K. S. Yook, J. Y. Lee, *Adv. Mater.* **2012**, *24*, 3169.

(19) A. V. Anzalone, T. Y. Wang, Z. Chen and V. W. Cornish, *Angew. Chem. Int. Ed*, **2013**, 52, 650.

(20) A. Avellaneda, C. A. Hollis, X. He and C. J. Sumby, *Beilstein J. Org. Chem*, **2012**, 8, 71.

(21) J. R. Cox, J. H. Simpson and T. M. Swager, *J. Am. Chem. Soc*, **2013**, 135, 640.

(22) C. Menendez, A. Chollet, F. Rodriguez, C. Inard, M. R. Pasca, C. Lherbet and M. Baltas, *Eur. J. Med. Chem*, **2012**, 52, 275.

(23) S. R. Forrest, D. D. C. Bradley, and M. E. Thompson, *Adv. Mater.* **2003**, *15*, 1043.

Chapter 5

Conclusion and Future Work

In this thesis three series of phenyl-1,2,3-triazole containing Pt(II) complexes were prepared in order to achieve highly stable and efficient deep blue phosphorescent emitters, as shown in Scheme 5.1.

The first type of compounds was the BMes-containing Pt(II) complexes and was mentioned in Chapter 2. Compared to compound **1.14**, which was synthesized previously in our group, the replacement of the phenyl-pyridine backbone by the phenyl-triazole backbone in compound **2.2** blueshifted the emission energy. By changing the acetylacetonate ligand in **2.2** by a pyridyl-1,2,4-triazole ancillary ligand with stronger ligand field, the emission quenching metal d-d state in compound **2.9** was deactivated, resulting a drastic improvement of phosphorescent quantum efficiency. OLED devices containing **2.9** reached EQE_{max} as high as 24.0%.

The second type of compounds was the non-boron containing bischelate Pt(II) complexes demonstrated in Chapter 3. When the $BMes_2$ group in **2.9** was replaced by the bulky trityl group, the thermal stability of **3.8** was improved and its excimer formation was reduced. OLED devices based on **3.8** showed impressive efficiency and no excimer emission.

The third type of compounds was the tetradentate Pt(II) complexes discussed in Chapter 4. The full steric constraint strategy that confines the platinum molecule in a stable and non-distorted structure at the emissive state leaded to the highly efficient and stable deep blue phosphorescent emitters **4.6**. Bright and efficient deep blue OLEDs with high color purity were successfully

fabricated using **4.6** as the dopant, demonstrating a brand-new approach to stable and efficient deep blue phosphorescent emitters.

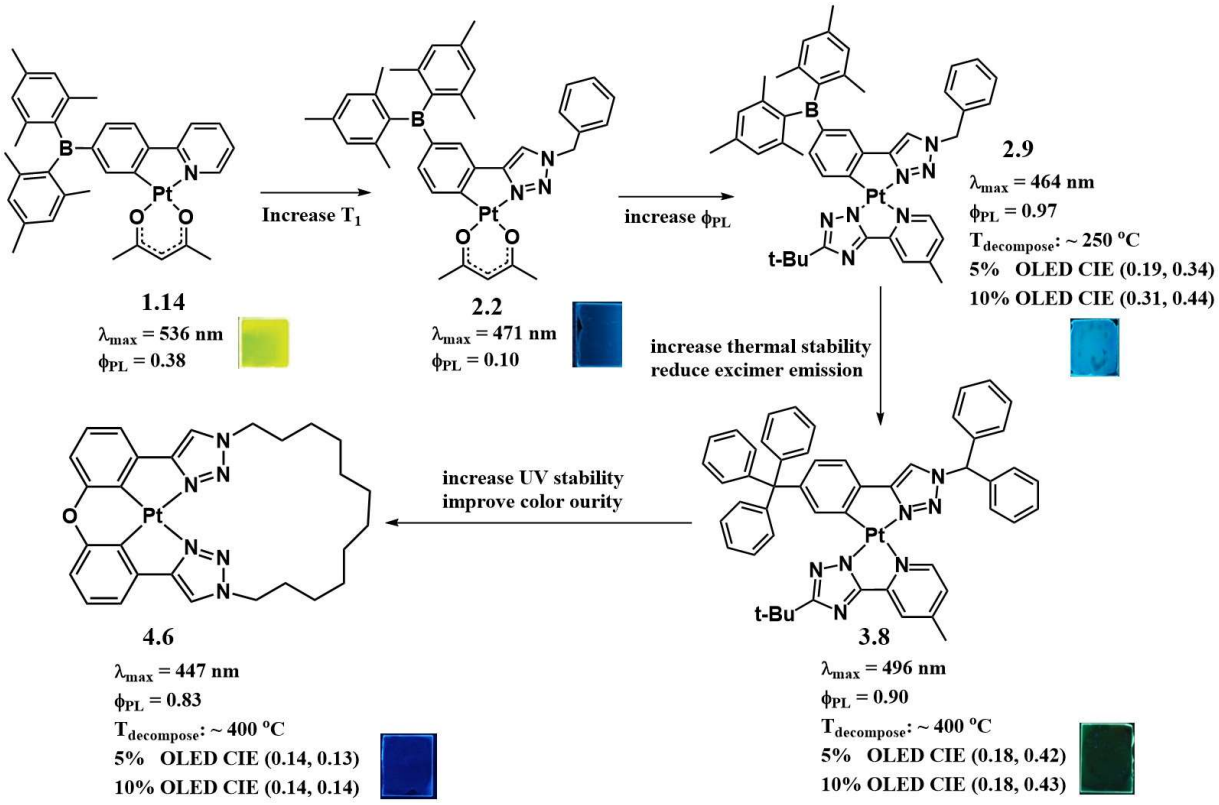

Scheme 5.1 Summary of photophysical properties, thermal properties and OLED performance of Pt(II) complexes described in the previous chapters.

Although we have made tremendous progress in blue phosphorescent Pt(II) emitters, much work can still be done. First, to fully confirm the stability of compound **4.6** in OLED devices, optimization of the device structure must be done and the EL measurements must be performed under inert atmosphere. Second, the synthetic procedure of **L4.6** need to be modified to reduce the reaction time and improve the yield. Third, the luminous efficiency (power efficiency) of the OLED devices mentioned in the thesis (~ 20 – 30 lm/W) need to be improved to be comparable to the fluorescent tubes and high-intensity discharge light bulbs, as shown in table 5.1. Finally, up till now, we focused on using the Pt(II) complexes as emitters in OLEDs. However, many of the Pt(II)

compounds have other interesting properties, such as piezochromic and thermochromic properties, as shown in Figure 5.1. Detailed studies on these phenomena may reveal their origins.

Table 5.1 Luminous efficiency of various light sources. (adapted from Ref. 1)

Light Source	Luminous Efficiency (lm/W)
Incandescent light bulbs	1-25
Fluorescent tubes	50-80
High-intensity discharge light bulbs	50-140

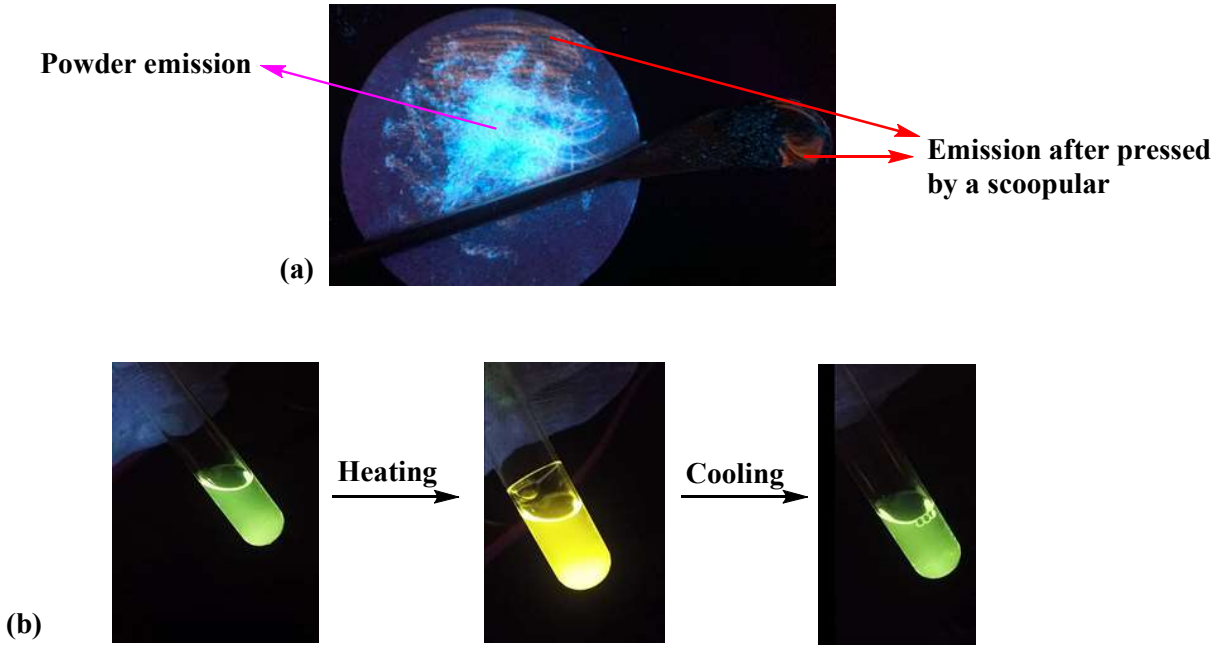

Figure 5.1 (a) Photograph showing the piezochromic property of compound **3.7**; (b) Photographs showing the thermochromic property of compound **3.4** in THF.

References

(1) E. F. Schubert, Light-Emitting Diodes, 2003, Cambridge Univ. Press.